

UCLA

UCLA Electronic Theses and Dissertations

Title

Atomic Layer Etching of Magnetic and Noble Metals

Permalink

<https://escholarship.org/uc/item/28m072gc>

Author

Altieri, Nicholas Dominic

Publication Date

2018

Peer reviewed|Thesis/dissertation

UNIVERSITY OF CALIFORNIA

Los Angeles

Atomic Layer Etching of Magnetic and Noble Metals

A dissertation submitted in partial satisfaction of the
requirements for the degree Doctor of Philosophy
in Chemical Engineering

by

Nicholas Altieri

2018

© Copyright by

Nicholas Altieri

2018

ABSTRACT OF THE DISSERTATION

Atomic Layer Etching of Magnetic and Noble Metals

by

Nicholas Altieri

Doctor of Philosophy in Chemical Engineering

University of California, Los Angeles, 2018

Professor Jane Pei-Chen Chang, Chair

This work has focused on the study and development of atomic layer etching for metallic and intermetallic thin films commonly used in front and back end of line applications. A thermodynamic equilibrium based framework consisting of minimization of Gibbs free energy and volatility assessment was used in screening and selecting promising plasma modification and chemical etchants. Challenges, such as the nonvolatility of metal etch products in front end of line processing of Cu for use in interconnects as well as back end of line patterning of magnetic and noble metals such as Co, Fe, CoFeB and Pt used in MRAM devices were addressed using the aforementioned approach to identify and develop reactive ion and atomic layer etch processes in parallel. The efficacy of modification chemistries, including inductively coupled O₂ and Cl₂ plasmas, was assessed first for Cu. Alternating Cl₂/H₂ plasma exposure has been predicted and subsequently validated in literature to be capable of etching Cu at sufficiently high rates. Assessment of the Cl₂ and subsequent H₂ plasma exposure were predicted to enhance the vapor

pressure of volatile etch products for patterning CoFeB as well as Pt. Experimental studies resulted in up to a 36% enhancement in etch rate while surface characterization indicated the removal of the non-volatile metallic chloride surface upon exposure to H₂ discharge. For CoFeB specifically, damage to the static magnetic properties was shown to also have been recovered to nearly 70% of its original value, suggesting that this process could also be viable with additional optimization.

In order to achieve a self-limiting etch process for use in atomic scale patterning, O₂ plasma modification in conjunction with the use of organic solution and vapor chemistries was studied as well. In concentrated solutions of acetylacetone, hexafluoroacetylacetone, acetic acid, and formic acid, CuO was observed to etch selectively over metallic Cu at values up to 285, confirming thermodynamic calculations. Formic acid vapor was subsequently found to etch CuO at rates up to 18 nm/min while no etch of metallic Cu was observed, indicating near infinite selectivity. Incorporating this formic acid chemistry with inductively coupled plasma oxidation resulted in etch rates up to 3.5 nm/cycle at 80 °C and 148 Torr. Similar self-limited chemical vapor etch of modified oxide layers were observed for Fe, Pt, Pd, and Co with etch rates of up to 4.8, 0.5, 1.1, and 2.8 nm/cycle and were shown to depend on the thickness of the modified metal oxide layer, giving rise to a route for controlling the etch rate. Reduction in etch per cycle through controlled oxidation was subsequently demonstrated for highly selective etch of CoFeB, resulting in a self-limited etch rate of 1.8 nm/cycle and subsequent chemical confirmation of selective oxide surface removal. Anisotropic etch profiles for patterned 70 nm × 10 μm lines of Cu and Co and 1 μm × 1 μm Cu square pads were achieved through application of a -100 and -200 V bias during the modification step and demonstrated that directional atomic layer etching can be achieved for patterning metallic thin films through precise control of ion energy, modification time, and subsequent chemical vapor etch.

The dissertation of Nicholas Altieri is approved.

Puneet Gupta

Vasilios Manousiouthakis

Dante A. Simonetti

Jane Pei-Chen Chang, Committee Chair

University of California, Los Angeles

2018

Dedicated to the loving memory of my grandmother

Laura Altieri

TABLE OF CONTENTS

Chapter 1 : Motivation and Background	1
1.1 Nano-scale patterning.....	1
1.2 Challenges of Metal Etch	8
1.3 Dry etching of metals	12
1.4 Thermodynamic Approach for Screening Viable Etch Chemistries	23
1.5 Atomic Layer Etching	29
1.6 Scope and Organization	38
Chapter 2 : Experimental Setup	42
2.1 Ultra-High Vacuum Transfer Tube and Load Lock	43
2.2 Inductively Coupled Plasma Reactor	46
2.3 Vapor Etch Chamber Coupled with ICP Reactor.....	49
2.4 Ion Beam Etch Reactor	52
2.5 Organic Solution Etching	54
2.6 Sample Preparation	55
2.7 Etch Rate Quantification	57
2.8 Etch Product Identification.....	67
2.9 Plasma Diagnostics	74
2.10 Thin Film Analysis.....	81
Chapter 3 : Organic Chemical Etch of Cu and CuO.....	89
3.1 Beyond the Damascene Process	89
3.2 Thermodynamic analysis of organic etchants for Cu and CuO	94
3.3 Solution and Vapor Phase Etch of Cu and CuO.....	96
3.4 Plasma Modification for Enabling Selectivity in Cu Etch	98
3.5 Cyclical Oxidation and Organic Vapor Etch for Patterning Cu Thin Films	102
Chapter 4 : Reactive Ion Etch and Atomic Layer Etch of Co, Fe, and CoFeB	107
4.1 Thermodynamic assessment of Co, Fe, and B in Cl ₂	108
4.2 Experimental validation of thermodynamic assessment	114
4.3 Organic chemical etch of Co, Fe, and CoFeB.....	120
4.4 Cyclical oxidation and chemical vapor etch of Co, Fe, and CoFeB	127
Chapter 5 : Controlled Pt Etch through Tunable Surface Modification	140
5.1 Controlled modification of metallic Pt surfaces.....	140
5.2 Etch of metallic and modified Pt.....	155
Chapter 6 : Summary	167
Appendices.....	174
Bibliography	293

LIST OF FIGURES

Figure 1-1. Patterned magnetic tunnel junctions ($AR \approx 14$) (Song 2013) in comparison to One World Trade Center ($AR \approx 7$), the tallest building in the Western Hemisphere, sixth tallest in the world.	2
Figure 1-2. Periodic table with highlighted elements studied in this work. With the exception of boron, each of these are considered etch-resistant materials by current standards and also include ferromagnetic alloys such as CoFe, CoFeB, and CoPt.	3
Figure 1-3. Schematic of 3D MRAM memory element showing information storage through the control of spin in ferromagnetic layers (Xiufeng, H. et al., 2013).	5
Figure 1-4. Cross sectional SEM and TEM images of ion beam etched MTJ stacks with (a) no wafer tilt—note the rounding of the stack profile—and (b) optimal 45° angle (Sugiura 2009).	7
Figure 1-5. Measured thickness changes for Co and Fe films etched in solutions of a) 68% HNO_3 and (b) 85% H_3PO_4 in water at $25^\circ C$. Reproduced from (Jung 1997).	9
Figure 1-6. Measured dissolved mass of Pd and Pt in $SOCl_2$ /pyridine post-etch solution as a function of etch time. Reproduced from (Lin 2010).	11
Figure 1-7. Sputter yield of various elements as a function of atomic number for 400 eV Ar^+ ion beam. Note the bolded elements of interest all having sputtering yields around unity. Adapted from (Laegreid 1961).	13
Figure 1-8. Schematic of hfac ligand adsorbed to oxidized copper surface resulting in chelation Adapted from (Nigg and Masel 1999).	15
Figure 1-9. (a) Dependence of etch rate of 250 nm Pt films on sample temperature under atmosphere of 22% Cl_2 in CO and (b) XPS survey scan of Pt film surface before and after chemical dry etch at $220^\circ C$ with 22% Cl_2 . (Kim 1998)	16
Figure 1-10. Scanning electron micrographs of (a,b) pre-etch patterned CoFe films, (c,d) after 4 min 500W/100W Ar plasma, (e,f) 2 min 500W/50W Cl_2 plasma, and (g,h) subsequent 4 min 500W/50W H_2 plasma exposure (Kim 2015).	19
Figure 1-11. (a) Measured etch rates of CoFeB and Ti as well as the calculated selectivity of CoFeB/Ti as a function of methanol concentration in Ar. Films were etched using 800 W source power, 300 V bias, and 5 mTorr. Reproduced from (Xiao 2011). (b) Etch rates of CoFeB and TiN at varying concentrations of H_2O in Ar plasma. Etch 1 was run under 800 W power and 300 V bias at 5 mTorr. Etch 2 was run under 900 W power with 400 V bias at 1 mTorr. Reproduced from (Lee 2013).	21

Figure 1-12. Complete volatility diagram of Cu-Cl ₂ system at 50°C constructed based on the chemical reactions listed in Table 1-3. Reproduced with slight modifications from (Kulkarni 2002).	25
Figure 1-13. (a) XPS spectrum of 400nm Cu film before etching and after etching for 10 cycles of 2 min Cl ₂ and 5 min H ₂ at 12-15 °C with 500W source power and 150 bias power and (b) thickness measurement of 400nm Cu as a function of number of cycles (Tamirisa 2007)	27
Figure 1-14. (a) Calculated partial pressure of etch products generated from reaction of CoCl ₂ and FeCl ₃ with atomic Br, O, and H. (b) Etched thickness of CoFe as a function of chlorine and hydrogen plasma cycles. Each cycle consisted of one 20 second half-cycle of Cl ₂ and a second 20 second half-cycle of H ₂ (Kim 2015).	28
Figure 1-15. (a) Schematic of discretized atomic layer etching steps (Athavale 1995), and (b) atomic layer etch rate as a function of chlorine adsorption step at different applied bias conditions for 140W Ar plasma with 15 mTorr Ar pressure and chlorine partial pressure of 2.4 mTorr (Athavale 1996).	31
Figure 1-16. (a) Particle-in-cell simulation of atomic layer etching of SiO ₂ with Ar and C ₄ F ₈ (Agarwal 2009), and (b) in-situ ellipsometry measurements of SiO ₂ thickness over time in continuous Ar plasma with pulsed C ₄ F ₈ (Metzler 2014).	32
Figure 1-17. Reaction of fluorinated aluminum surface through donation of acac ligand from Sn(acac) ₂ to form Al(acac) ₃ and subsequent introduction of HF from HF-pyridine facilitates removal of SnF(acac) and water to regenerate AlF ₃ surface (Lee 2015).	33
Figure 1-18. (a) Comparison of chemical vapor deposition (CVD) to plasma etching and the corresponding analogy of atomic layer etch (ALE) as reversing the ALD process (Marchack 2011) (b) Saturation curves detailing the self-limiting (a, b) nature of first step adsorption. (c) Energy regimes for etching, removal energy remains constant in ALE window due to threshold energy required to removed modified surface without damaging underlying layers (Kanarik 2015).	34
Figure 1-19. Flowchart summarizing the key objectives presented in this work for studying reactive ion etch and atomic layer etch for patterning metallic and intermetallic thin films.	39
Figure 2-1. Schematic of ultra-high vacuum transfer tube.	44
Figure 2-2. Schematic of integrated ion beam chamber, inductively coupled plasma reactor, and UHV transfer tube with <i>in situ</i> XPS.	45
Figure 2-3. Schematic of inductively coupled plasma (ICP) etcher showing division between upper and lower sections.	47
Figure 2-4. Schematic of inductively coupled plasma (ICP) etcher with attached gate valve and vapor etch chamber and commercial vaporizer.	49
Figure 2-5. Schematic of ion beam chamber.	53

Figure 2-6. Scanning electron micrographs of 20 nm platinum film (a) pre-processing and (b) after exposure to inductively coupled O₂ plasma with 500 W source power, no applied bias, 5 mTorr, and 120 seconds. (c) Summary of measured thicknesses of 20 nm films post time-dependent exposure to 5 mTorr O₂ plasma at 500 W source power and 0 W bias power. 58

Figure 2-7. Overlayer model for the formation of cobalt oxide on metallic platinum after inductively coupled O₂ plasma exposure. As the oxide is generated, the total thickness of metallic Pt decreases while the growth of less dense PtO₂ results in an overall thickness greater than that of the initial pre-processed Pt. Adapted from (Blackstock 2003). 59

Figure 2-8. High resolution x-ray photoelectron spectra of (a) Pt 4f, (b) O 1s regions and (c) survey scan of elements on the sample surface for as deposited 30 nm Pt before and after 150s exposure to Ar/O₂ plasma at an applied bias of 10V. 60

Figure 2-9. Inelastic mean free path for PtO₂, FeO, and CoO as a function of the photoelectron kinetic energy. The kinetic energies of photoelectrons for each of the corresponding metallic bonding states are also shown. 62

Figure 2-10. (a) Extinction coefficient (k) and refractive index (n) as a function of wavelength for CoFeB using Bruggeman Effective Medium Approximation and (b) measured amplitude (Ψ) and phase (Δ) data for a 30nm CoFeB film with corresponding Ψ and Δ model fitting. 64

Figure 2-11. (a) Schematic of contact profilometer with an enlarged portion detailing the contact of the stylus tip with the original sample surface, and (b) raw data of a profilometry scan performed on 250 nm CoFeB after etching in 500 W Ar plasma with 50 W bias power for 1 minute. 66

Figure 2-12. (a) Schematic of ICP-MS operation, and (b) raw data from characterized post-etch solution of 95% formic acid used in 10 min liquid phase etching of chlorinated Pd, CoPd, and CoPt thin films. 68

Figure 2-13. Periodic table of elements measured by ICP-MS along with their corresponding detection limit ranges for ELAN series mass spectrometers. All of the elements studied in this work have limit ranges between 0.1-10 parts per trillion. (Image courtesy of PerkinElmer, Inc.) 69

Figure 2-14. (a) Schematic and high speed photograph of Taylor cone, jet, and plume formation for ESI-MS sample introduction (Nemes 2007) and (b) sample spectra of hexafluoroacetylacetone solution after etch of Co and Fe thin films, indicating substantial amount of Fe(hfac)₃ complex in solution with the corresponding isotope pattern. (Chen 2017) 71

Figure 2-15. Mass spectra of (a) inductively coupled O₂ plasma at 500 W source power, 0 V applied bias, and 16 mTorr indicating presence of main ¹⁶O and ³²O₂ species as well as residual water (¹⁸H₂O) and (b) CH₄ after opening the gas line valve and in an inductively coupled CH₄ plasma at 500 W source power, 0 V applied bias and 9 mTorr indicating characteristic cracking pattern. All sets of data are collected with the ionization filament current (I_{fil}) of 1.0 mA and a 70 V potential. 73

Figure 2-16. Sample I-V curves for inductively coupled Ar (black) and O₂ (red) plasmas taken from ICP reactor described previously at 500 W source power, 0 V bias voltage, and 10 mTorr pressure. 76

Figure 2-17. (a) Optical emission spectrum for inductively coupled N₂ plasma at 500 W source power, 0 V applied bias, 6 mTorr, and 5% Ar actinometer feed and (b) calculated percentage of excited molecular N₂ and atomic N increasing as a function of increasing source power. 80

Figure 2-18. High resolution x-ray photoelectron spectra of (a) Co 2p, (b) Fe 2p, and (c) Cl 2p and B1s for 30 nm CoFeB before processing (black), after 30 second exposure to Cl₂ plasma (red) as well as (d) binding energies of interest for constituent elements studied in this work. 83

Figure 2-19. SQUID magnetometer hysteresis loop measurement of 30 nm CoFeB before plasma treatment (black, dotted) and post 30 s exposure to 500 W_s Cl₂ plasma (red, dashed). The total magnetization measured by the SQUID magnetometer is normalized by the saturation magnetization (M_s) and shown on the y-axis with the applied field shown on the x-axis. The coercivity, H_c, is measured as the absolute value difference between 0 Oe field value (point 1) to the intersection of the sample hysteresis with M/M_s=0 value (point 2), and indicates the field necessary to change the magnetization direction. The measurement has been repeated and shown for the coercivity (H_{c,Cl2}) of the sample exposed to 30 s Cl₂ plasma as the absolute value difference between points 1 and 3. 87

Figure 3-1. (a) Process steps for integration of damascene plating process, and (b) typical evolution profiles observed in damascene plating. 90

Figure 3-2. (a) Etch rates of Cu and CuO_x in liquid phase acac, hfac, acetic acid and formic acid are shown as measured at 80°C. Shown in comparison are results from etching Cu and CuO_x thin films in formic acid vapor at 150 °C and 10 Torr for 5 min. SEM cross-sections (b) before and (c) after etching CuO_x thin films in formic acid vapor. The asterisk (*) denotes a zero etch rate as measured in this work. 98

Figure 3-3. Measured etched thickness per cycle for copper as a function of a cyclic process alternating between O₂ plasma and organic vapor exposure (the dotted lines are linear regressions with R² values >0.98). 99

Figure 3-4. X-ray photoelectron spectra of (a) high resolution Cu 2p region and (b) survey of all elements present on the surface of Cu film after exposure to ICP O₂ surface modification and subsequent formic acid vapor etch. 100

Figure 3-5. (First column) SEM cross-section and EDS spectrum of pre-process Cu (35 nm) on 35 nm of low-k material and 200 nm of SiO₂. (a) SEM cross-section of 35 nm Cu etched under 15 cycles consisting of alternating plasma oxidation (500 W, -100 V, 2 min) and formic acid vapor etch (50 s). (b) Energy dispersive x-ray spectrum (EDS) of sample surface after exposure to 15 cycles. The interface between the mask and copper is outlined with a dashed line to help guide the eyes for comparison. 101

Figure 3-6. Bird eye view scanning electron micrographs of patterned (a) 60 nm × 10 μm lines with 70 nm pitch, (b) 60 nm × 10 μm lines with 120 nm pitch, and (c) 60 nm × 10 μm lines with 100 nm pitch after exposure to 4 cycles of alternating O ₂ plasma (500W, -200 V bias, 2 min) and formic acid vapor (15, 50, and 90 s, respectively).....	103
Figure 3-7. (First column) As-patterned 1 μm×1 μm pads and 70 nm×10 μm lines of 40 nm Ta hard mask (HM) patterned 35 nm Cu films, in cross-sectional and birds-eye views. The interface between the mask and copper is outlined with a dashed line to help guide the eyes for comparison. (a-b) SEM images of patterned copper etched in formic acid (500 s) in solution (no oxidation). (c-d) SEM images of patterned copper etched by 10 cycles of alternating O ₂ plasma (500 W, -100 V bias, 2 min) and formic acid vapor (50 s), terminating with a final exposure to O ₂ plasma.	104
Figure 3-8. Energy dispersive x-ray spectra for (a) Ta hard masked and (b) exposed regions of Cu patterned by 70 nm × 10 μm lines pre-processing, after 2 cycles of plasma oxidation and formic acid vapor etch, and after 6 cycles of plasma oxidation and vapor etch.....	105
Figure 4-1. Product distribution of (a) Co-Cl, (b) Fe-Cl, and (c) B-Cl systems simulated through minimization of Gibbs free energy scheme to determine gaseous and condensed phase species present at thermodynamic equilibrium as a function of temperature (K).....	109
Figure 4-2. Volatility diagrams for Co, Fe, and B in Cl ₂ at 300, 350, 400, 450, and 500 K.....	113
Figure 4-3. Atomic percentage of Co, Fe, B, O, and C measured in 30 nm Co ₃₀ Fe ₄₅ B ₂₅ as a function of etch depth for XPS depth profile using 1 keV Ar ⁺	115
Figure 4-4. Etched thickness as a function of time for 30 nm CoFeB and 800 nm Co and Fe films etched in alternating exposures of Cl ₂ and H ₂ plasmas. Co (□) and Fe (○) were etched under sequential 20 s exposures to Cl ₂ and H ₂ plasma (800 W source power, 100 W bias power). CoFeB (Δ) was etched under sequential 30 s exposures to Cl ₂ and H ₂ plasma (800 W source power, 50 W bias power). Dashed lines have been added to guide the eye.	116
Figure 4-5. High resolution x-ray photoelectron spectra of (a) Co 2p, (b) Fe 2p, (c) Cl 2p and B 1s of pre-process CoFeB, CoFeB after 30 s of Cl ₂ plasma, and CoFeB after a single cycle of alternating Cl ₂ and H ₂ plasma, each for 30 s.	117
Figure 4-6. High resolution x-ray photoelectron spectra of (a) O 1s and (b) a survey scan of all elements present on the surface of pre-process CoFeB, CoFeB after 30s of Cl ₂ plasma, and CoFeB after a single cycle of alternating Cl ₂ and H ₂ plasma.....	118
Figure 4-7. Magnetic measurement of (a) 30 nm CoFeB blank film (black), following 30s of Cl ₂ plasma (red), and following single cycle of sequential Cl ₂ and H ₂ plasma (magenta) and (b) 50 nm CoFe blank blank film (black), following 30s of Cl ₂ plasma (red), and following single cycle of sequential Cl ₂ and H ₂ plasma (magenta). Note the order of magnitude change in x-axis due to increasing magnetic hardness of CoFe compared to CoFeB due to high concentration of boron.	119

Figure 4-8. Volatility diagrams for Co-acac, Co-hfac, Fe-acac, and Fe-hfac systems at 300 K with the corresponding dashed line at 10^{-8} atm as the threshold for observable etch. 122

Figure 4-9. Etched thickness of Co and Fe etched in pure acac and hfac solutions at 80 °C as a function of time. 123

Figure 4-10. Electrospray ionization mass spectra for post etch solutions of Co etched in solutions of (a) acac and (b) hfac as well as Fe etched in solutions of (c) acac and (d) hfac at 80 °C. Vertical dashed lines indicate the typical isotope distribution for Co(acac)_2 , Co(hfac)_3 , Fe(acac)_3 , and Fe(hfac)_3 124

Figure 4-11. Etched thickness of 30 nm CoFeB in acac, hfac, formic acid, and mixtures of acac/hfac for etch times up to 120 s. 126

Figure 4-12. Thicknesses of CoO and Fe_2O_3 as a function of plasma oxidation time for O_2 plasma at 500 W source power and -100 V applied bias. 129

Figure 4-13. High resolution x-ray photoelectron spectra of (a) Co 2p, (b) O 1s, and (c) C 1s binding energy regions for 30 nm Co samples pre-processing, after exposure to electron beam driven O_2 plasmas with increasing applied bias voltages of 0, 10, 30, and 50 V for 600 s, and after plasma oxidation at 50 V bias with separate subsequent exposure to concentrated formic acid solutions (>97%) at 80 °C for 5 s and 15 min. 132

Figure 4-14. Etched thickness of CoO and Fe_2O_3 as a function of oxidation and formic acid vapor etch cycles. Cycles consisted of O_2 plasma at 500 W source power and -100 V applied bias for 5 min followed by formic acid vapor at 80 °C, 148 Torr for 50 s. 133

Figure 4-15. Etched thickness of CoFeB as a function of oxidation and formic acid vapor etch cycles as well as equivalent time exposures of only plasma oxidation and only formic acid vapor. Each cycle consisted of O_2 plasma at 500 W source power and -100 V applied bias for 2 min followed by formic acid vapor at 80 °C and 148 Torr for 50 s. 135

Figure 4-16. High resolution x-ray photoelectron spectra of (a) Co 2p, (b) Fe 2p, (c) B 1s binding energy regimes for pre-process CoFeB, CoFeB after oxidation in 500 W_s, -100 V_b O_2 plasma for 2 min, and oxidation with subsequent formic acid vapor at 80 °C and 148 Torr for 50 s. 136

Figure 4-17. Simulated etch profiles and corresponding SEM images of 40 nm TiN hard mask (HM) and 10 nm SiN, patterned on 30 nm Co, with a 10 nm barrier layer (BL) on Si before and after processing. The boundary between each layer is outlined with a thin dashed line. The cyclical etch process was comprised of exposure to an O_2 plasma (500 W, 5 min) and formic acid vapor (50 s). Etch profiles of patterned Co after (a) 6 cycles of oxidation (0 V bias) and formic acid vapor exposure, and (b) 4 alternating cycles of oxidation (-200 V bias) and formic acid vapor exposure. 138

Figure 5-1. Example synthesis route for Pd(acac)_2 using sequential oxidation, chlorination, and reaction with acetylacetone (acac). A similar approach was taken for surface modification and organic chemical etch of Pt. 142

Figure 5-2. Product distribution of Pt-O-acac system simulated through minimization of Gibbs free energy scheme to determine gaseous and condensed phase species present at thermodynamic equilibrium as a function of temperature (K). 143

Figure 5-3. Volatility diagrams for Pt-O-formic acid (HCOOH) system at 300 K with the corresponding dashed line at 10^{-8} atm as the threshold for observable etch..... 144

Figure 5-4. Summary of Pt^{X+}/Pt^0 ratio for 60 nm Pt films processed under inductively coupled Cl_2 and Cl_2+Ar plasmas at 200 and 800 W source powers and 10 and 30 W bias powers. 146

Figure 5-5. Summary of Pt^{4+}/Pt^0 ratio for 60 nm Pt processed under inductively coupled plasma mixtures of O_2 and Ar as well as O_2 with subsequent Cl_2 exposure..... 148

Figure 5-6. High resolution x-ray photoelectron spectra of (a) Pt 4f, (b) Cl 2p, and (c) O 1s binding energy regimes for Pt films processed under mixtures of $O_2:Ar$ as well as sequential exposure to O_2/Cl_2 149

Figure 5-7 XPS spectrum of Pt films before processing and after exposure to oxygen ion beams with ion energies of 50, 100, 200, and 500 eV for 300 seconds. 151

Figure 5-8. Fraction of oxidized Pt as a function of ion energy for 30 nm Pt films exposed to 50, 100, 200, and 500 eV oxygen ion beam for 10 min..... 152

Figure 5-9. Etch rate of 30 nm Pt films as a function of ion energy for samples processed at 50, 100, 200, and 500 eV under oxygen ion beam. 153

Figure 5-10. Oxide thickness as a function of plasma oxidation time for Pt thin films exposed to O_2 plasma with 500 W source power and -100 V applied bias. The curve corresponds to the inverse log model used to fit the oxide thickness..... 154

Figure 5-11. Etched thickness of 60 nm Pt films as a function of etch cycle under Cl_2 and Cl_2/H_2 alternating chemistry. Both Cl_2 and H_2 plasmas were held at 800 W source power and 50 W bias power..... 157

Figure 5-12. High resolution x-ray photoelectron spectra of (a) Pt 4f and (b) Cl 2p binding energy regimes as well as (c) survey scan of all elements present on the surface pre-processing, after exposure to 800 W source power Cl_2 plasma with 50 W bias power for 30 s, and after subsequent exposure to 800 W source power H_2 plasma with 50 W bias for 30 s..... 158

Figure 5-13. High resolution x-ray photoelectron spectra of (a) Pt 4f, (b) O 1s, and (c) C 1s binding energy regions for 30 nm Pt samples with 5 nm Ti adhesion layer pre-processing, after exposure to electron beam driven O_2 plasma with increasing applied bias voltages of 0, 10, 30, and 50 V for 600 s, and after plasma oxidation at 50 V bias with separate subsequent exposure to concentrated formic acid solutions (>97%) at 80 °C for 5 s and 15 min. 160

Figure 5-14. Percentge of Pt in metallic Pt⁰ and oxidized Pt²⁺ and Pt⁴⁺ oxidation states for as deposited, oxidized, and after formic acid (FA) solution etch as a function of applied bias during plasma oxidation. 161

Figure 5-15. Measured thickness of oxide for as-deposited, oxidized, and formic acid (FA) etched Pt as a function of applied bias during plasma oxidation. 162

Figure 5-16. (a) High resolution x-ray photoelectron spectra of 20 nm Pt pre-processing, after exposure to plasma oxidation, and after subsequent exposure to formic acid vapor. (b) Etched thickness of Pt as a function of cycle for alternating plasma oxidation and formic acid vapor etch and equivalent cycles of plasma oxidation alone..... 164

Figure 5-17. Etched thickness as a function of cycles consisting of plasma oxidation and formic acid vapor etch. 165

Figure 6-1. Etched thickness per cycle as a function of oxide thickness for plasma oxidized and formic acid vapor etched Pt, Pd, Co, Cu, and Fe. Each material falls on or close to the dashed line with a slope of 1, indicating that alternating oxidation and formic acid vapor etch exhibits selective removal of the metal oxide as well as the ability to control the etch thickness by controlling the modified layer thickness. 170

LIST OF TABLES

Table 1-1. Summary of boiling and melting points used to assess the volatility of select metal fluorides, chlorides, and metalorganic complexes related to this work. Melting point was used for assessing metalorganic complexes due to decomposition at elevated temperatures. (NIST 2013, Sigma-Aldrich 2015, HSC Chemistry 2013)	4
Table 1-2. Summary of plasma etch chemistries reported for CoFeB, Pt, and Pd	18
Table 1-3. Reactions used for creating volatility diagram shown in Figure 1-12 for the Cu-Cl system.	24
Table 1-4. Summary of reported atomic layer etching of materials	37
Table 2-1. Process gases available for use in inductively coupled plasma reactor with their corresponding purities and maximal flow rates.	48
Table 2-2. Organic etchants chosen for testing in the vapor phase with their corresponding molecular structures, purities, vapor pressures, and boiling points.	51
Table 2-3. Thin film sample materials, source purities, deposited film thicknesses, and patterned feature sizes.....	56
Table 2-4. Parameters necessary for calculation of the photoelectron inelastic mean free path (λ) in metal oxides (Tanuma 2011).	61
Table 3-1 Reactive ion etch chemistries reported for copper and the corresponding etch rates, temperatures, masks used, and selectivity, where reported.	93
Table 3-2. Gibbs free energies for reaction of metallic copper with liquid and gas phases of acetylacetone and hexafluoroacetylacetone at 300 K and 1 atm.*	94
Table 3-3. Gibbs free energies for reaction of copper oxide with liquid and gas phases of acetylacetone and hexafluoroacetylacetone at 300 K and 1 atm.*	96
Table 4-1. Reactions used for creating volatility diagram shown in Figure 4-1 for Co-Cl, Fe-Cl, and B-Cl systems.	112
Table 4-2. Reactions used for creating volatility diagram shown in for Co-acac/hfac and Fe-acac/hfac systems.....	121
Table 4-3. Reactions and corresponding ΔG_{rxn} values for Co, CoO, Fe, and Fe ₂ O ₃ reacting with vapor phase formic acid (HCOOH) at 300 K.	128
Table 5-1. Summary of experimental conditions and XPS analysis of chlorinated 30 nm Pt thin films under Cl ₂ and Cl ₂ with varying amounts of Ar.....	145

Table 5-2 Summary of experimental conditions and XPS quantification of oxidized 30 nm Pt thin films. Additional experiments investigated oxidation as a primary step to ultimately achieve chlorination. 147

Table 5-3. Conditions for 30 nm Pt samples processed under electron beam generated Ar/O₂ discharge with increasing terminal anode bias voltages. 159

Table 6-1. Summary of etch rate, selectivity (for metal oxide to metal as well as to hard mask materials), and directionality for etching Cu, Co, and Pt by an oxidation process followed by formic acid etch. Cu and Co thin films were patterned using Ta and TiN hard masks; however, Pt patterned samples were unavailable. 172

ACKNOWLEDGEMENTS

First and foremost, I'd like to thank Professor Jane P. Chang for serving as my research advisor. Over the last five years she has shaped me into a capable researcher while also instilling in me the importance of a strong work ethic and meticulous attention to detail. Her insight and advisement have forever influenced the way I approach and communicate my research.

I would also like to thank the members of my committee, Professors Vasilios Manousiouthakis, Dante Simonetti, and Puneet Gupta, as well as the generous funding support from the SRC-ERC for Environmentally Benign Semiconductor Manufacturing, IMPACT+ program, C-DEN, and Intel Corporation. I owe a special debt of gratitude to Lam Research, especially Drs. Meihua Shen and Thorsten Lill who served as professional mentors during my time at UCLA; I look forward to continuing my career with you both in the future.

I count myself extremely fortunate for the close-knit cadre of lab mates, past and present, with whom I had the pleasure of spending my graduate career. Gary, even though our time together was brief, I truly enjoyed discussing our research and laying the groundwork for your upcoming doctoral studies. Adrian, you have an incredible sense of motivation and a strong intellect. Ernest, it was a pleasure getting to teach and work with you over the last couple years. You have taught me so much and have been an indispensable resource on all things related to the larger world of semiconductor manufacturing. I have the greatest confidence in your ability to usher in a new era of the Etch Crew. Ryan, I'll forever remember and cherish our trips to Monkish in spite of awful traffic. Kevin, thank you for accompanying me during the weekends and late nights spent in the office and lab. You have a brilliant intellect, and I cannot wait to see what you accomplish in your

future endeavors. Jeff, you have been my constant companion through these past five years and made the most trying of times tolerable. Here we are now; we have finally made it!

To all of my former lab mates, Dr. Colin Rementer, Dr. Cyrus Cheung, Dr. Jay Cho, Dr. Calvin Pham, and Dr. Taeseung Kim, thank you all for your incredible friendship. A special thank you to my mentor, Dr. Jack Chen, who patiently taught me most of what I now know about vacuum technology, plasma etching, and a slew of other analytical techniques. I look forward to working with you in the future!

Thank you to all of my collaborators over the years. Professor H.-S. Philip Wong, Dr. Scott Fong, and Chris Neumann at Stanford University—my work on phase change materials would be impossible without your advice and generosity. Thank you to the Naval Research Laboratory, especially Dr. Scott Walton for his discussion, insight, and work on helping me further understand and address challenges in this new era of atomic layer processing as well as his generosity in touring me through the Naval Research Lab facilities in Washington, D.C.

I would not have been able to do this without the support of my friends. Madison—you've been one of my very best friends since our time at Tulane and will forever be my PLP. Thank you for the innumerable wonderful memories of our time living together in Los Angeles. Ray, thank you for always being there for me, and listening to me talk endlessly about my days in lab. I truly admire your charisma, uniqueness, nerve, and talent. Anthony, you have been a beacon of hope and guidance during our careers here at UCLA. As we sashay away, I am excited to embark upon the next chapter of our lives in San Mateo.

Finally, I would like to thank my family for their support throughout this entire experience. To my mom, Denise, and stepdad, Rod. Both of you have put me before yourselves at every point

throughout my life, and I will be forever grateful for all the sacrifices you have made. I am where I am today because of you. To my dad, Chris, thank you for instilling in me the importance of academic excellence and the motivation to strive for it from an early age. To my cousins, Jenna and Nhadia, I adore you both. Thank you for the abundant laughs and emotional support. Finally, to my Grandma and Bobbo, the two of you have had an incredibly large role in shaping the person I am today. I carry all of our wonderful memories and the countless lessons you have taught me in my heart wherever I may go. I love you both dearly.

VITA

- 2013 B. S. E., Chemical Engineering
Tulane University
New Orleans, LA
- 2013-2018 Graduate Student Researcher
Department of Chemical and Biomolecular Engineering
University of California, Los Angeles
Los Angeles, CA
- 2016 Teaching Assistant
Department of Chemical and Biomolecular Engineering
University of California, Los Angeles

AWARDS

- 2009-2013 Presidential Scholar
2012 Randall K. Nichols Award in Chemical Engineering
2013 Francis M. Taylor Award in Chemical Engineering
Tulane University
- 2017 AVS Coburn and Winters Award Finalist
64th AVS International Symposium and Exhibition
Tampa, FL

PUBLICATIONS

- N. D. Altieri**, J. K. Chen, L. Minardi, and J. P. Chang, "Plasma-surface interactions at the atomic scale for patterning metals," *J. Vac. Sci. Technol. A*, 35 (5) (2017) 05C203
- J. K. Chen, **N. D. Altieri**, T. Kim, T. Lill, M. Shen, and J. P. Chang, "Directional etch of magnetic and noble metals. I. Role of surface oxidation states," *J. Vac. Sci. Technol. A*, 35 (5) (2017) 05C304
- J. K. Chen, **N. D. Altieri**, T. Kim, E. Chen, T. Lill, M. Shen, and J. P. Chang, "Directional etch of magnetic and noble metals. II. Organic chemical vapor etch," *J. Vac. Sci. Technol. A*, 35 (5) (2017) 05C305
- J. K. Chen, T. Kim, **N. D. Altieri**, E. Chen, and J. P. Chang, "Ion beam assisted organic chemical vapor etch of magnetic thin films," *J. Vac. Sci. Technol. A*, 35 (3) (2017) 031304
- X. Li, K. Fitzell, D. Wu, C. T. Karaba, A. Buditama, G. Yu, K. L. Wong, **N. D. Altieri**, C. Grezes, N. Kioussis, S. Tolbert, "Enhancement of voltage-controlled magnetic anisotropy through precise

control of Mg insertion thickness at CoFeB|MgO interface,” *Appl. Phys. Lett.*, 110 (5) (2017) 052401

PRESENTATIONS

N. D. Altieri, E. Chen, and J. K. Chen, and J. P. Chang, “Enabling Atomic Layer Etching of Magnetic and Noble Metal Alloys,” AVS 64th International Symposium & Exhibition, Tampa, FL, November 1, (2017) (Oral Presentation – Nominated for Coburn and Winters Award)

N. D. Altieri, E. Chen, and J. P. Chang, “Patterning Nickel Thin Films for EUV Mask Applications,” C-DEN Workshop, San Jose, CA, October 27, (2017)

N. D. Altieri, L. Minardi, E. Chen, and J. P. Chang, “Thermodynamic Prediction and Experimental Verification of Etch Selectivity for EUV Mask Materials,” C-DEN Workshop, San Jose, CA, May 26, (2017)

N. D. Altieri, J. K. Chen, L. Minardi, E. Chen, and J. P. Chang, “Organic Etchants Toward Atomic Layer Etching of Magnetic Metals,” AVS 63rd International Symposium & Exhibition, Nashville, TN, November 9, (2016)

N. D. Altieri, L. Minardi, E. Chen, and J. P. Chang, “Enabling Nano-Fabrication with Atomic Precision in Etch Directionality and Selectivity,” C-DEN Workshop, San Jose, CA, November 4, (2016)

L. Minardi, J. K. Chen, **N. D. Altieri**, and J. P. Chang: “Thermodynamic prediction and experimental verification of etchant selectivity for tantalum-based materials,” IMPACT+ Workshop, San Jose, CA, November 24, (2015)

N. D. Altieri, J. K. Chen, L. Minardi, M. Paine, and J. P. Chang, “Non-PFC Plasma Chemistries for Patterning Low-k Dielectric Materials,” AVS 62nd International Symposium & Exhibition, San Jose, CA, October 20, (2015)

J. K. Chen, **N. D. Altieri**, M. Paine, and J. P. Chang, “Non-PFC Plasma Chemistries for Patterning Low-k Dielectric Materials,” AVS 61st International Symposium & Exhibition, Baltimore, MD, November 10, (2014)

Chapter 1 : Motivation and Background

This chapter serves as an introduction to the various materials and complex structures used in the semiconductor industry for furthering advances in areas of logic and memory devices. Emphasis is placed on a review of past studies found in literature focusing on patterning of memory devices as well as an introduction to the thermodynamic methods explored in this work for chemistry selection for enabling reactive ion and atomic layer etch processes. The creation of a chemical contrast between the material surface and underlying film is crucial to realizing selectivity in the removal process. The depth to which this modified layer can be formed is dependent on not only the modification time, but also through manipulated of the energetic collisions of ions striking the surface. Since chemical etching, whether in solution or gas phase, removes material equally in all directions (isotropic), directional surface modification of patterned structures must be implemented to achieve anisotropic etching.

1.1 Nano-scale patterning

The advent of the International Technology Roadmap for Semiconductors in 1998 has provided the suggested direction for furthering the fabrication technology of semiconductors and their associated components in accordance with the continuation of Moore's Law. However, continual accommodation of this trend has proven difficult.

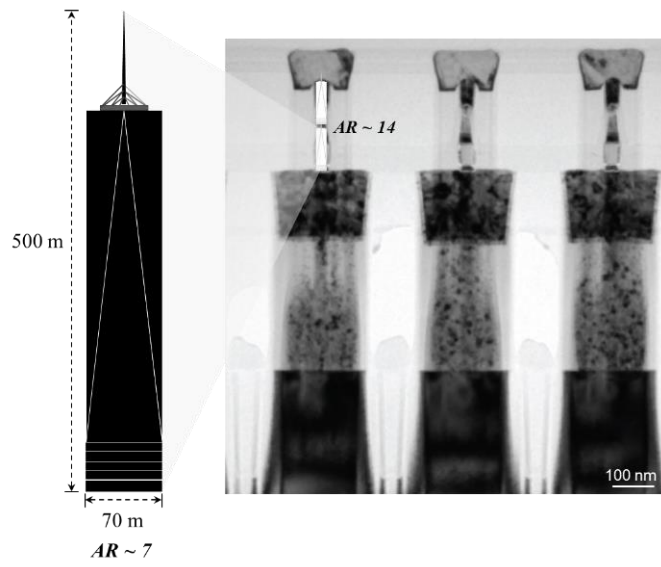


Figure 1-1. Patterned magnetic tunnel junctions ($AR \approx 14$) (Song 2013) in comparison to One World Trade Center ($AR \approx 7$), the tallest building in the Western Hemisphere, sixth tallest in the world.

Increased device density requires reduced feature sizes, while introduction of novel materials and device architectures has resulted in processing bottlenecks due to reduced effectiveness in chosen patterning chemistries overcoming the chemically inert nature of selected metallic elements and added structural complexity. One such application of novel and etch-resistant materials is in the development of new forms of memory. With the expected increase in computational power, there is a resulting surge in the desire for further improvements in the application of memory. One such specific form of memory is deemed non-volatile, that is, the information stored within each unit is not lost as soon as electrical power is turned off. This non-volatile aspect can be seen, for example, in the use of hard disk drives (HDD). The enabling factor behind many of these forms of memory is the use of complex materials and structures that are examined in greater detail in this work.

A number of these materials are deemed difficult to etch due to their lack of both chemical reactivity and volatile etch products. Figure 1-2 shows elements pertinent to this work highlighted in blue. With the exception of boron, these elements are considered etch-resistant.

Periodic Table of the Elements

1 IA 1A	2 IIA 2A											13 IIIA 3A	14 IVA 4A	15 VA 5A	16 VIA 6A	17 VIIA 7A	18 VIIIA 8A	
1 H Hydrogen 1.008	3 Li Lithium 6.941	4 Be Beryllium 9.012											5 B Boron 10.811	6 C Carbon 12.011	7 N Nitrogen 14.007	8 O Oxygen 15.999	9 F Fluorine 18.998	10 Ne Neon 20.180
11 Na Sodium 22.990	12 Mg Magnesium 24.305	3 IIIB 3B	4 IVB 4B	5 VB 5B	6 VIB 6B	7 VIIB 7B	8 VIII 8	9 VIII 8	10 VIII 8	11 IB 1B	12 IIB 2B	13 Al Aluminum 26.982	14 Si Silicon 28.086	15 P Phosphorus 30.974	16 S Sulfur 32.065	17 Cl Chlorine 35.453	18 Ar Argon 39.948	
19 K Potassium 39.098	20 Ca Calcium 40.078	21 Sc Scandium 44.956	22 Ti Titanium 47.867	23 V Vanadium 50.942	24 Cr Chromium 51.996	25 Mn Manganese 54.938	26 Fe Iron 55.845	27 Co Cobalt 58.933	28 Ni Nickel 58.693	29 Cu Copper 63.546	30 Zn Zinc 65.38	31 Ga Gallium 69.723	32 Ge Germanium 72.631	33 As Arsenic 74.922	34 Se Selenium 78.971	35 Br Bromine 79.904	36 Kr Krypton 84.798	
37 Rb Rubidium 84.468	38 Sr Strontium 87.62	39 Y Yttrium 88.906	40 Zr Zirconium 91.224	41 Nb Niobium 92.906	42 Mo Molybdenum 95.96	43 Tc Technetium 98.907	44 Ru Ruthenium 101.07	45 Rh Rhodium 102.905	46 Pd Palladium 106.42	47 Ag Silver 107.868	48 Cd Cadmium 112.414	49 In Indium 114.818	50 Sn Tin 118.711	51 Sb Antimony 121.760	52 Te Tellurium 127.6	53 I Iodine 126.904	54 Xe Xenon 131.294	
55 Cs Cesium 132.905	56 Ba Barium 137.328	57-71 Lanthanide Series	72 Hf Hafnium 178.49	73 Ta Tantalum 180.948	74 W Tungsten 183.84	75 Re Rhenium 186.207	76 Os Osmium 190.23	77 Ir Iridium 192.221	78 Pt Platinum 195.085	79 Au Gold 196.967	80 Hg Mercury 200.592	81 Tl Thallium 204.383	82 Pb Lead 207.2	83 Bi Bismuth 208.980	84 Po Polonium [208.982]	85 At Astatine 209.987	86 Rn Radon 222.018	
87 Fr Francium 223.020	88 Ra Radium 226.025	89-103 Actinide Series	104 Rf Rutherfordium [261]	105 Db Dubnium [262]	106 Sg Seaborgium [266]	107 Bh Bohrium [264]	108 Hs Hassium [265]	109 Mt Meitnerium [268]	110 Ds Darmstadtium [271]	111 Rg Roentgenium [272]	112 Cn Copernicium [277]	113 Uut Ununtrium unknown	114 Fl Flerovium [289]	115 Uup Ununpentium unknown	116 Lv Livermorium [293]	117 Uus Ununseptium unknown	118 Uuo Ununoctium unknown	
			57 La Lanthanum 138.905	58 Ce Cerium 140.116	59 Pr Praseodymium 140.908	60 Nd Neodymium 144.242	61 Pm Promethium 144.913	62 Sm Samarium 150.36	63 Eu Europium 151.964	64 Gd Gadolinium 157.25	65 Tb Terbium 158.925	66 Dy Dysprosium 162.500	67 Ho Holmium 164.930	68 Er Erbium 167.259	69 Tm Thulium 168.934	70 Yb Ytterbium 173.055	71 Lu Lutetium 174.967	
			89 Ac Actinium 227.028	90 Th Thorium 232.038	91 Pa Protactinium 231.036	92 U Uranium 238.029	93 Np Neptunium 237.048	94 Pu Plutonium 244.064	95 Am Americium 243.061	96 Cm Curium 247.070	97 Bk Berkelium 247.070	98 Cf Californium 251.080	99 Es Einsteinium [254]	100 Fm Fermium 257.095	101 Md Mendelevium 258.1	102 No Nobelium 259.101	103 Lr Lawrencium [262]	

Figure 1-2. Periodic table with highlighted elements studied in this work. With the exception of boron, each of these are considered etch-resistant materials by current standards and also include ferromagnetic alloys such as CoFe, CoFeB, and CoPt.

This lack of volatility is summarized by comparing the vapor pressures of a wide range of metal fluorides and chlorides. The use of metalorganics as an approach to formation of volatile metal complexes is an attractive option. Listed below (Table 1-1) are the boiling and melting points of metal fluorides, chlorides, and metalorganics of transition metals highlighted in Figure 1-2.

Table 1-1. Summary of boiling and melting points used to assess the volatility of select metal fluorides, chlorides, and metalorganic complexes related to this work. Melting point was used for assessing metalorganic complexes due to decomposition at elevated temperatures. (NIST 2013, Sigma-Aldrich 2015, HSC Chemistry 2013)

<i>Element</i>	<i>Fluoride</i> $T_b(^{\circ}C)$	<i>Chloride</i> $T_b(^{\circ}C)$	<i>Metalorganic</i> $T_m(^{\circ}C)$
Fe	FeF _{2(g)} : decomp.	FeCl ₂ : 1023	Fe(acac) ₃ : 184
	FeF _{3(g)} : decomp.	FeCl ₃ : 316	Fe(hfac) ₃ : 97
Co	CoF ₂ : 1400	CoCl ₂ : 1049	Co(acac) ₂ : 170
			Co(hfac) ₃ : 94
Pd	PdF ₂ : 1227	PdCl ₂ : 1028	Pd(acac) ₂ : 200
Pt	PtF ₆ : 69	PtCl ₂ : decomp.	Pt(acac) ₂ : 239
			Pt(hfac) ₂ : 144

A large portion of etch resistant materials exist in the transition metal series. These d-block elements exhibit significant chemical inertness due to the nature of their metallic bonds. In comparison to the covalent bond, wherein an electron pair is shared and thus localized to two atoms, metallic bonds allow for the electrons to exist in a delocalized form. This delocalization can be thought of through the rudimentary description of a “sea of electrons” provided by the Drude Model. While simplistic, this approximation allows for a contrast to be drawn between the delocalized nature of the metallic bond and the localized covalent bond. Delocalized electrons are able to move around the entirety of a metallic lattice whereas localized electrons in a covalent bond allow the bond to be targeted and cleaved.

Further complications arise when multiple etch resistant materials are utilized in complex structures. The current trend in memory devices, for example, looks to use multiple thin layers of different metallic and oxide based films to take advantage of coupling magnetic properties with electrical properties in order to control information storage through the use of electric fields. These structures are designed to use nanometer thick layers of materials that can be exploited for their

ferromagnetic behavior. Shaping these complex multi layered structures into usable devices is an added challenge. Figure 1-3 shows a generalized schematic of the MRAM stack that would allow for coupled magnetic and electric behaviors to allow for improved memory devices (Xiufeng, H. et al., 2013).

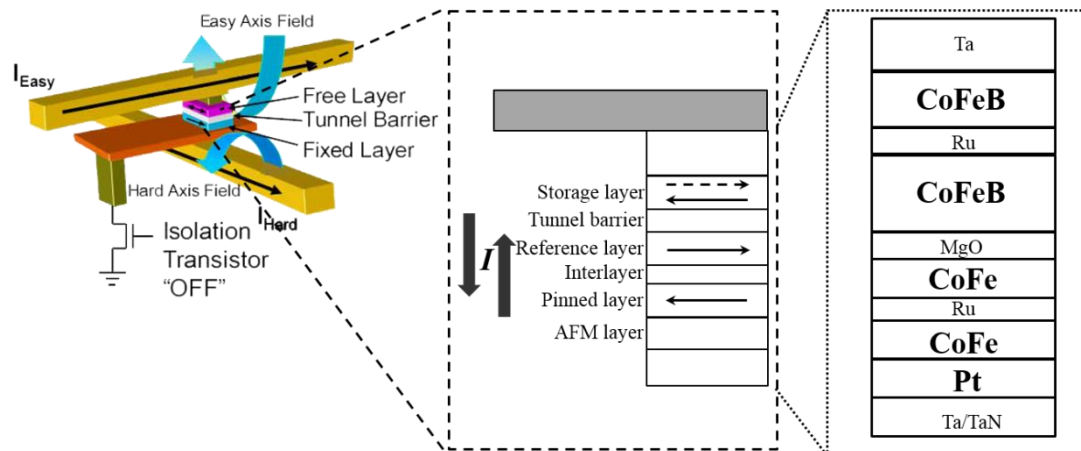


Figure 1-3. Schematic of 3D MRAM memory element showing information storage through the control of spin in ferromagnetic layers (Xiufeng, H. et al., 2013).

The enabling material behind the current trend in MRAM devices is the magnetic alloy CoFeB. Until recently, CoFe was utilized as the magnetic alloy of choice due to the existence of perpendicular magnetic anisotropy, the directional dependence of the magnetic moment. This anisotropy is unique to materials such as CoFe and CoFeB and results in the ability to exploit the alignment of the magnetic domain as parallel or antiparallel in relation to a reference layer, resulting in the storage of information in the form of a bit (Donahue 2002). There are two advantages to using CoFeB. First, compared to CoFe, CoFeB has a much lower coercivity, meaning that the magnetic field required to switch the domain between parallel and antiparallel—or storing information as “0” or “1” values—is approximately 30% of that for an equivalent thickness of CoFe. Second, in conjunction with the tunneling barrier, MgO, the incorporation of boron results in changes within the structure of CoFeB that make a much more stable interface,

which is key for proper device functionality at smaller scales (Ikeda 2010). Additional attractive features of CoFeB for use in perpendicular MTJs include much higher thermal stability, resulting in less interlayer mixing at increased temperatures, as well as the ability to use much lower switching currents when inducing magnetic fields for switching the free magnetic layer in writing operations.

In addition to CoFeB, platinum is also used in portions of the stack either in the form of an alloy with magnetic elements Co and Fe or, at times, in the antiferromagnetic layer near the bottom of the structure. Due to the high-Z nature of Pt, it is a prime candidate for mixing with Co and Fe, resulting in the perpendicular magnetic anisotropy that CoFeB also exhibits. However, whereas CoFeB is a homogeneous mixture maintaining consistent stoichiometry, CoPt and FePt exhibit alternating multilayer structures in crystalline L10 phase (Zeper 1989).

Despite the attractive magnetic material properties of both CoFeB and Pt, modern etch techniques tend to falter when patterning extremely small devices on the order of tens of nanometers. Due to the nanometer thick layers utilized in magnetic tunnel junction fabrication, etching chemistries capable of patterning metallic thin films generally require increased temperature, which, despite the enhanced thermal stability, are too high for use with these stack structures. Furthermore, selectivity tends to suffer from processes that rely largely on physical bombardment to either directly sputter the material or induce chemical reaction through reactive ion etching.

Current industrial techniques utilize ion beam etching (IBE), known also as ion beam milling, to fabricate highly anisotropic features from the constituent materials of the MTJ stack (Parkin 2004, Sugiura 2009). Material removal is accomplished by bombarding the surface with

highly directional and energetic ionic species—typically noble gases to mitigate any chance of reaction upon contact with the surface—resulting in ejection of the thin film materials. However, a large concern within this processing technology is the issue of sidewall redeposition. As the aspect ratio and feature density increases, the ejected material ultimately redeposit onto the sidewalls, causing degradation of device performance.

Methods for overcoming this issue of sidewall redeposition have been formulated by a number of groups. A common technique seen in literature requires tilting and rotating the wafer stage during exposure to Ar^+ ions (Sugiura 2009). Wafers processed using this tilt and rotate technique have resulted in improvement more in line with the desired anisotropic feature profiles. Cross sectional SEM and TEM images in Figure 1-4 show the effects of wafer tilting at an optimized 45° angle.

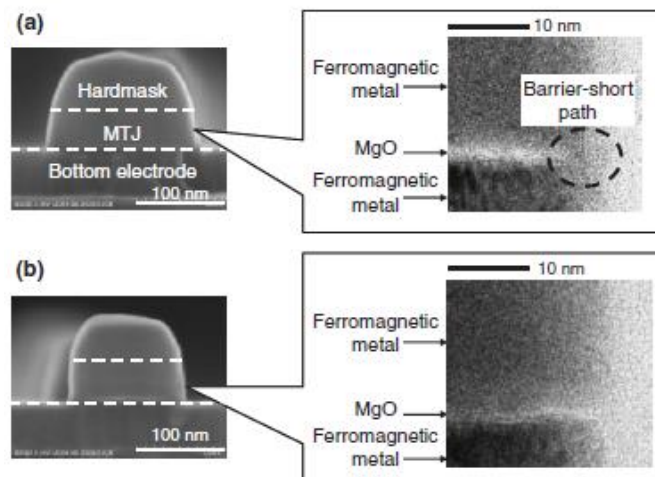


Figure 1-4. Cross sectional SEM and TEM images of ion beam etched MTJ stacks with (a) no wafer tilt—note the rounding of the stack profile—and (b) optimal 45° angle (Sugiura 2009).

There are two general classes of techniques that can be used to etch, wet and dry. Wet etching utilizes a solution-based approach to deliver high concentrations of etchant to the substrate.

This allows for economical usage of high concentrations chemicals to achieve very high etch rates, allowing increase throughput of patterning materials. However, when handling features that exist on a nanometer scale, wet etch cannot be used to pattern complex structures due to the large amount of material removal in all directions, known as isotropic etching. Isotropic etching causes unacceptable degradation to structures with phenomena such as undercut, compromising the overall integrity of the device. The incorporation of increasingly complex device structures and 3-D topology requires strict directionality in material removal.

From a process development standpoint, it is necessary to construct a methodology for choosing appropriate chemistries that can be used to pattern both etch-resistant as well as complex structures. Thermodynamics offers a perspective from which systems can be analyzed based on their initial and final chemical states, narrowing the parameter space in the choice for potential etchant chemistries. The goal of this work is to further develop this methodology so as to enhance understanding of which chemistries excel in patterning one material over others. By implementing strategies such as surface modification and controlling various parameters in the processing window, the advancement toward precise atomic layer etching of metallic films and potentially high aspect ratio structures can be achieved.

1.2 Challenges of Metal Etch

Wet etching of copper was established before the investigation of organic-based etchants. A number of studies were conducted that solidified the usage of inorganic acids as key players in wet etching. Nitric acid (HNO_3), for example was used in the cleaning of single crystal copper specimens for later use in irradiation studies (Magnuson 1963). Additional experimentation found that phosphoric acid (H_3PO_4) was an agreeable method for removing chemical impurities as well as a means of testing for dislocation etch pit density (Young 1962). With the established success

of inorganic acid etchants for copper, these same chemicals were utilized in the context of wet etching of Co and Fe for early studies on process development due to the lack of sufficiently high etch rates seen in plasma processing. Studies on 500 nm Co and Fe films were performed using concentrated nitric, sulfuric, phosphoric, and hydrochloric acids (HNO_3 , H_2SO_4 , H_3PO_4 , and HCl). Etch rates were observed to vary dramatically across the four different solutions. The thickness change for HNO_3 and H_3PO_4 appeared to be linear with respect to time (Figure 1-5a,b). H_2SO_4 , on the other hand, exhibited square root-like behavior, indicating that the etch could be limited by diffusion of the sulfuric acid to the reaction sites on the film surface (Jung 1997).

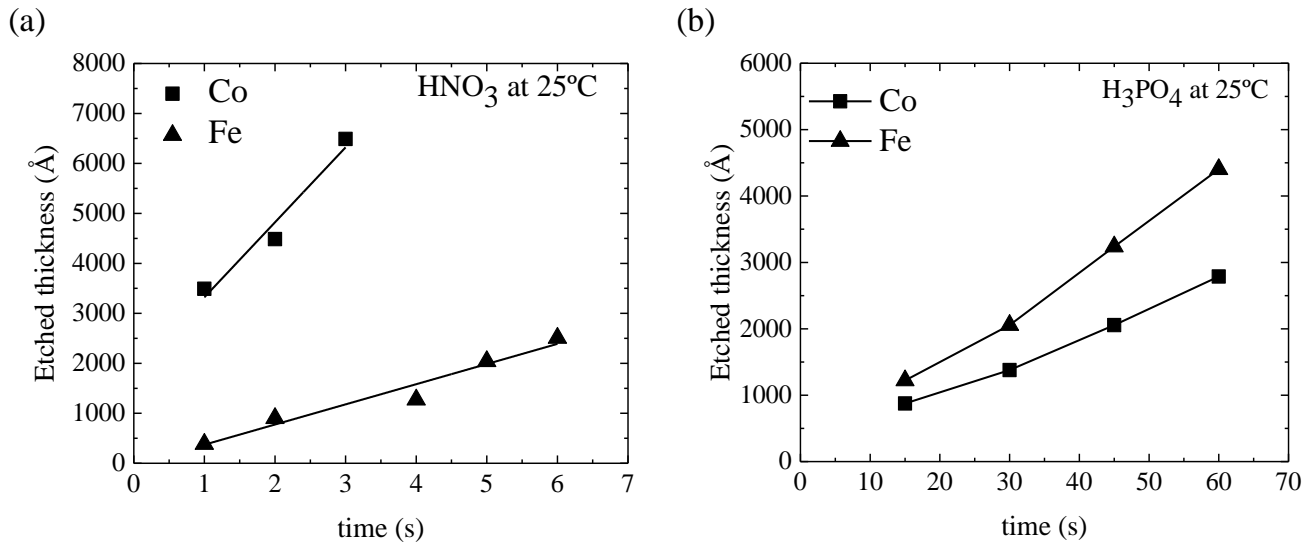


Figure 1-5. Measured thickness changes for Co and Fe films etched in solutions of a) 68% HNO_3 and (b) 85% H_3PO_4 in water at 25°C. Reproduced from (Jung 1997).

Along similar lines, while it is possible to etch magnetic metals such as Co and Fe in these inorganic acids, some of the additional targets to be studied in this work, such as platinum and palladium, are impervious to dissolution by the aforementioned mineral acids. However, by combining two key acids, HNO_3 and HCl , in a fixed ratio, etching is observed. Dilutions of the

aptly named “aqua regia”, Latin for “royal water”, as it is seen to dissolve noble metals, are often used in the solvation of gold, palladium, and platinum. Specifically, etch rates of up to 390 nm/min and 3.6 nm/min are seen for mixtures of 3:1:2 parts HCl:HNO₃:H₂O (Williams 2003).

However, recent discoveries has led to the development of a kind of “organic aqua regia” which uses thionyl chloride (SOCl₂), a powerful chlorinating agent previously used in catalysis research as a means of modifying platinum on alumina supports (Giannetti 1969, McKervey 1971), and pyridine. From the literature, it is reported that palladium and platinum were specifically studied using this SOCl₂/pyridine mixture in 3:1 ratio SOCl₂:pyridine. 250 nm films of palladium and platinum were deposited using electron beam evaporation on 9 cm² silicon substrates using an underlying 20 nm chromium layer to promote adhesion, weighed, and immersed in 20 mL of SOCl₂/pyridine at 25°C for preset time periods. The samples were weighed a second time to record mass loss due to dissolution of the films. A singular 250 nm film of chromium was subjected to this same procedure, showing that it was not soluble in this mixture.

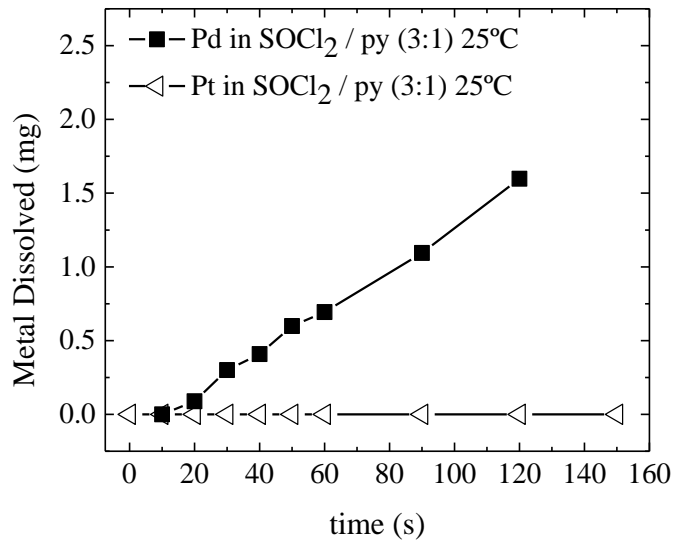


Figure 1-6. Measured dissolved mass of Pd and Pt in SOCl₂/pyridine post-etch solution as a function of etch time. Reproduced from (Lin 2010)

As Figure 1-6 shows above, the organic aqua regia is capable of dissolving a substantial mass of palladium, approximately 1.7 mg over the span of two minutes. Platinum, however, remains impervious to chemical attack from this liquid, resulting in no mass of metal dissolved (Lin 2010).

Despite the efficacy with which solution based etchants can be used for patterning metallic films, the wet etch method has drawbacks. Liquid phase etching is inherently isotropic due to the contact between high concentrations of etchant—compared to vapor phase—and the material(s) of interest. Furthermore, the liquid phase causes difficulties in subsequent processing steps due to surface tension effects. For high aspect ratio features with critical dimensions on the order of tens and hundreds of nanometers, liquid etchant can remain long after a wet processing step and result in over etch and loss of pattern transfer fidelity. Nonetheless, the wet etch step serves of a means

of preliminary experimental screening of etch chemistries that are of interest for transference to the vapor phase.

1.3 Dry etching of metals

1.3.1 Physical sputtering of metals

Dry etching can be used to effectively pattern nanometer scale features due to its anisotropic nature. Sputtering uses an ionized noble gas such as argon to physically bombard the surface. Through the application of an electric bias, the positively charged argon ions are accelerated through the plasma sheath in a direction normal to the substrate surface. Incident ions collide with condensed phase atoms residing at the surface, causing a transfer of energy through their chemical bonds. If a sufficient amount of energy, above a material-specific limit known as the sputtering threshold energy, is transferred through this resulting cascade, the material is desorbed into the gas phase, exposing underlying layers for further bombardment. This method of patterning is seen as reliable and has been used extensively in industrial settings to achieve anisotropic etch of otherwise chemically inert materials. However, as seen in Figure 1-7, the sputter yield for the elements of interest to this study are all centered near unity. This fact has led to issues in the indiscriminate manner in which the constituent stack layers are removed, showing no selectivity between materials. These problems can lead to encounters with mask erosion, reduced etch rates, and redeposition of etch products, making this approach, while reliable, not attractive from the standpoint of selectivity.

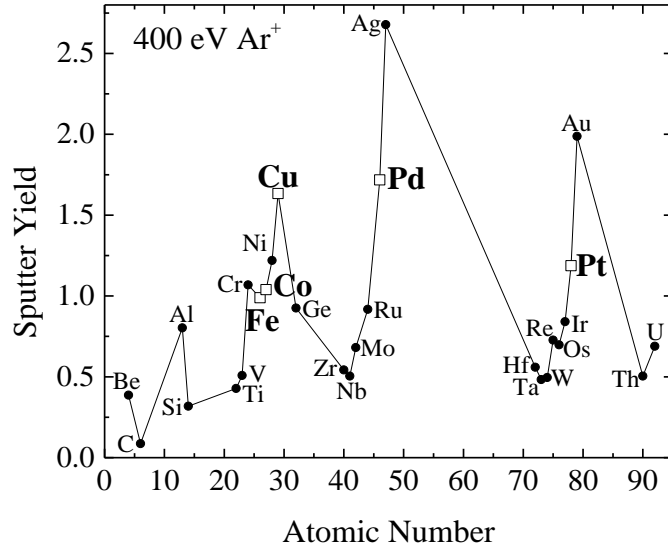


Figure 1-7. Sputter yield of various elements as a function of atomic number for 400 eV Ar⁺ ion beam. Note the bolded elements of interest all having sputtering yields around unity. Adapted from (Laegreid 1961)

1.3.2 Spontaneous etching of metals

With the transition from aluminum to copper interconnects in microprocessors, a number of researchers have investigated potential chemistries for etching using etchants in the vapor phase. The difference between solution phase and vapor phase etch is the substantial difference in concentration. For wet etch, a high concentration of etchant liquid is present at the film surface and solvates the metal ion, surrounding it in a cage of solvent molecules. Vapor phase etching, on the other hand, has substantially lower concentrations of etchant at the surface and requires that the metallic film is in an oxidized form, allowing reaction to occur between the impinging gas phase molecules and the localized metal oxide bond.

Organic chemical reagents for etching metallic species, β -diketonates such as acetylacetonone (acac) (Nigg 1998), trifluoroacetylacetonone (tfac) (Nigg 1998), and hexafluoroacetylacetonone (hfac) (Nigg 1998, Nigg 1999) have been studied as suitable ligands for

creating volatile organometallic complexes and are commonly employed as precursors for chemical vapor and atomic layer deposition. However, due to the metallic nature of copper, for example, use of most of these etchants alone fails to result in net removal of material.

Steger and Masel utilized simultaneous flows of oxygen and hfac to chemically etch bulk copper disks in vacuum. Differences in macroscopic properties of the copper were observed based on the hfac to oxygen ratio. At high values, that is large amounts of hfac with very little O₂, the copper surface retained its metallic luster. However, at lower concentrations the surface changed to a deeper rose color, with a correspondingly strong dependence of etch rate on the hfac concentration.

The observations by Steger and Masel coincided with two distinct regions of reactive behavior for the copper surface. First, in the presence of excess oxygen, the copper surface becomes oxidized, leading to a deep rose color (Steger 1999). As the ratio of hfac to oxygen then increases, past a certain point, the copper retains its metallic surface, while measurements indicate that etching is observed. The visible observation of the lustrous metallic copper surface indicates that the introduction of the hfac ligand is able to remove the surface layers of copper oxide, likely through ligand exchange. Figure 1-8 below shows a schematic of the surface interactions proposed to occur for the copper oxide reacting with hexafluoroacetylacetone. The delocalization of the negative charge through the diketone ring structure allows for the hfac ligand to successfully bond to the electrophilic copper atoms on the surface (Nigg 1999).

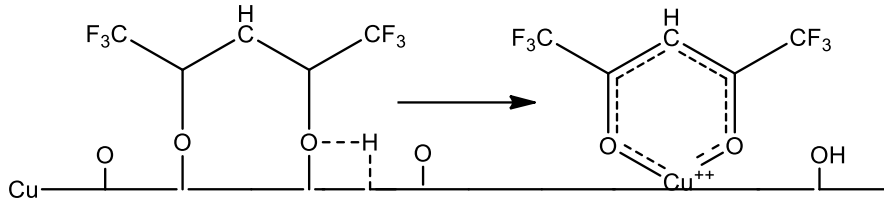


Figure 1-8. Schematic of hfac ligand adsorbed to oxidized copper surface resulting in chelation Adapted from (Nigg and Masel 1999).

As in the case of halogen chemistries, some metallic complexes such as $\text{Cu}(\text{hfac})_2$ require energy to achieve appreciable amounts of desorption. Typically this energy is supplied in the form of heat, with $\text{Cu}(\text{hfac})_2$ requiring temperatures up to 300°C to exhibit noticeable amounts of etching. In the case of complex stack structures, elevated temperatures can cause intermixing between the nanometer thick layers, resulting in the loss of desired properties. However, energy can be applied in more ways than just thermally. Using adsorbed species, it is also possible to surmount this desorption energy barrier through the use of low energy ions colliding with modified surfaces.

One particularly noteworthy chemistry for patterning platinum used a combination of CO and Cl_2 at elevated temperatures as a form of dry etching for 250nm blanket platinum films on 500nm SiO_2/Si . In this study, samples were heated up to temperatures of $200\text{-}230^\circ\text{C}$ in an atmosphere of variable Cl_2 and CO composition. Etch rates, measured by SEM cross sections, were observed to increase with increasing temperature beginning at around 20nm/min at 190°C and monotonically increasing to just below 140 nm/min at 230°C (Figure 1-9 a).

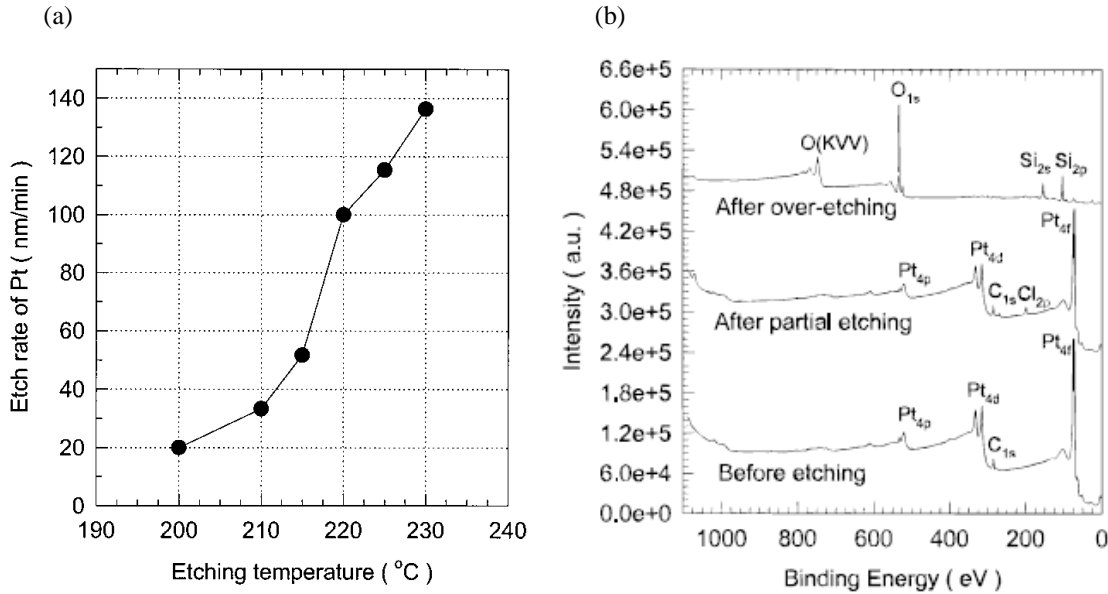


Figure 1-9. (a) Dependence of etch rate of 250 nm Pt films on sample temperature under atmosphere of 22% Cl₂ in CO and (b) XPS survey scan of Pt film surface before and after chemical dry etch at 220 °C with 22% Cl₂. (Kim 1998)

X-ray photoelectron spectroscopy survey scans showed the characteristic Pt 4f metallic peaks of the blank Pt film before etch. Additional scans after a partial etch of 125nm showed the presence of chlorine, as indicated by the Cl 2p peak (Figure 1-9b). A final survey scan after etch denoted the endpoint upon no signal of Pt 4f and emergence of the Si 2p peaks (Kim 1998). Despite showing promising chemical approach, one downside to this method is the high pressure and especially high temperatures necessary to ensure that the CO and Cl₂ react with the platinum. In the case of MTJ stacks in memory applications, and in general for device integration, platinum films are on the order of a few nanometers. Thus, elevated temperatures and low thermal budgets can result in mixing of these very thin layers in an effort to etch, necessitating a low temperature yet effective plasma and/or organic process capable of generating products with substantial volatility.

1.3.3 Reactive ion etching of metals

Likely the most classic study of the synergistic effect between adsorbed species and impinging ions was performed by Coburn and Winters using Ar with Cl_2 to study silicon. The purely physical mechanism of sputtering with a 450 eV argon ion beam alone has very low etch rates on the order of 2 Å/min for silicon surfaces. Upon introduction of a chemical reactive gas ($\text{Cl}_{2(g)}$) that can form volatile products ($\text{SiCl}_{2(g)}$, $\text{SiCl}_{4(g)}$) with the substrate, the etch rate can be enhanced significantly, up to around 10 Å/min (Coburn 1979). Coupling both chemical and physical components of etching led to the development of ion enhanced etch, also known as reactive ion etching (RIE).

Due to the highly energetic nature of a plasma, species generated from the feed gas consist of both neutral radicals and charged ions. These radicals have enhanced chemical reactivity due to the presence of an unpaired electron residing within their valence shells and the energetic favorability of chemical bonding due to formation of electron pairs. Further, due to their uncharged nature, radicals lack any sort of directionality in their travel through the plasma. Ions, on the other hand, retain a charge, and are thus subject to directional travel dictated by the imposition of an electric field. By combining the behavior of both of these particles, the process of reactive ion etching can be harnessed. In general, the process of reactive ion etching can be described as follows. First, reactions occur between the gas and solid phase, most often through chemisorption of neutral species (Winters 1978). Second, the products resulting from these reactions are formed on the surface of the material to be etched. Finally, these products are desorbed, completing a singular local cycle of etching (Coburn 1984). This synergistic approach in coupling adsorbed neutral species with bombardment of energetic ions has been applied to the case of etching metallic and intermetallic films as well. Due to the high boiling points, and thus low volatility of metallic

chlorides, shortcomings of using Cl₂-based plasmas has led to the use of both alternative and sequential chemistries. Table 1-2 summarizes the various etch rates using different plasma chemistries in patterning MTJ materials, specifically CoFeB, Pt, and Pd.

Table 1-2. Summary of plasma etch chemistries reported for CoFeB, Pt, and Pd

Material	Plasma Chemistry	Etch rate (nm/min)	Reference
CoFeB	Cl ₂ /Ar	15 (Cl ₂ : 10%)	(Kinoshita 2010)
	Cl ₂ , H ₂	20 (alternating cycles)	(Kim 2015)
	H ₂ O/Ar	5 (H ₂ O: 20%)	(Lee 2013)
	CO/NH ₃	12 (CO:25%)	(Park 2011)
	CH ₄ /Ar	30 (CH ₄ :20%)	(Kim 2012)
	CH ₃ OH/Ar	10 (CH ₃ OH:15%)	(Xiao 2011)
	CH ₃ OH/H ₂ O	2 (CH ₃ OH:22%)	(Hwang 2014)
	CH ₃ COOH/Ar	15 (CH ₃ COOH:25%)	(Garay 2015)
Pt	SF ₆ /Ar/O ₂	32 (SF ₆ :80%, Ar:16%)	(Yao 2014)
	SF ₆ /C ₄ F ₈	8-10 (SF ₆ :25%)	(Li 2012)
	Cl ₂ /CO	20 (Cl ₂ :20%)	(Kim 1999)
	Cl ₂ /O ₂	60 (Cl ₂ :10%)	(Yokoyama 1995)
	Cl ₂ /C ₂ F ₆	80 (Cl ₂ :20%)	(Chung 1995)
	H ₂ S, HBr	200 (H ₂ S:25%)	(Matsumoto 1996)
	S ₂ Cl ₂ /Cl ₂	180 (S ₂ Cl ₂ :90%)	(Matsumoto 1996)
	CO/NH ₃	5 (CO:15%)	(Abe 2003)
Pd, Pt	SF ₆ /Ar	15 (SF ₆ :90%)	(Kim 2003)
	Cl ₂ /Ar	6 (Cl ₂ :50%)	(Kim 2003)
	CF ₄ /Ar	3 (CF ₄ :80%)	(van Glabbeek 1993)

One such set of experiments utilized a thermodynamic approach similar to that described above for copper wherein Co, Fe, Ni, and CoFe thin films were studied first through the use of volatility diagrams to determine the effect of additional hydrogen (Kim 2014). At temperatures above 600K, 700K, and 500K for Co, Ni, and Fe respectively, the partial pressures of the metallic

halides in each case is calculated to be sufficient to warrant predicting a noticeable etch rate. Due to the elevated temperature, introduction of a secondary chemistry was studied by subsequent reaction of each MCl_x , MBr_x , and MO_x species with the remaining three chemistries. In each case, the metal hydride compound exhibited the highest calculated partial pressure, indicating hydrogen as the best suited secondary chemistry.

To verify the thermodynamic analysis of these perspective etching chemistries, a number of studies using argon, chlorine, and hydrogen plasmas were conducted. Sputtering through exposure to Ar plasma resulted in removal of the CoFe thin film; however, sidewall rounding and significant increase in surface roughness led to an undesirable profile (Figure 1-10a,b). Etching with chlorine plasma exhibited improved sidewall profiles with increased etching of the TiN hardmask (Figure 1-10c,d), but additional material, believed to be metal chlorides were deposited on the sidewall of the mask with additional particulates remaining on the CoFe film. By then exposing the chlorine-etched films shown in Figure 1-10(e,f) to hydrogen plasma for four minutes, the sidewall deposition and residue were visibly removed (Figure 1-10g,h) with little effect to the underlying CoFe film and patterned TiN hardmask.

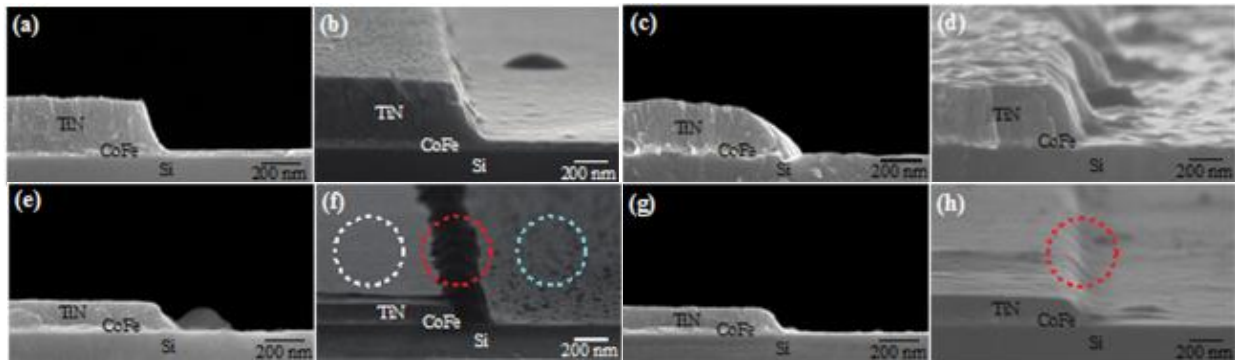


Figure 1-10. Scanning electron micrographs of (a,b) pre-etch patterned CoFe films, (c,d) after 4 min 500W/100W Ar plasma, (e,f) 2 min 500W/50W Cl_2 plasma, and (g,h) subsequent 4 min 500W/50W H_2 plasma exposure (Kim 2015).

To confirm the composition at different locations of the feature, energy dispersive x-ray spectroscopy (EDS) was utilized to target areas of the hardmask, sidewall, and remaining CoFe film. EDS confirmed the presence of metallic chlorides on the mask sidewall, a result of redeposition due to their low volatility. Subsequent use of hydrogen plasma shows that the metallic chloride deposits are then removed from the sidewall, resulting in a reduced metallic surface.

Since the traditionally used halogen chemistries often result in formation of nonvolatile species without the help of secondary chemistries, additional compounds have been studied in an effort to identify not only increases in etch rate, but also improvements upon selectivity seen in common hardmasks such as TiN and curtail the effects of corrosion. Xiao et al introduced methanol (CH_3OH) to an Ar plasma to determine effects on the etch rates of CoFeB using a Ti mask. By increasing the percentage of CH_3OH slightly to just 10%, the etch rate of CoFeB decreased from nearly 45 nm/min to 15nm/min while the rate for Ti decreased from 20nm/min to approximately 3nm/min (Xiao 2011).

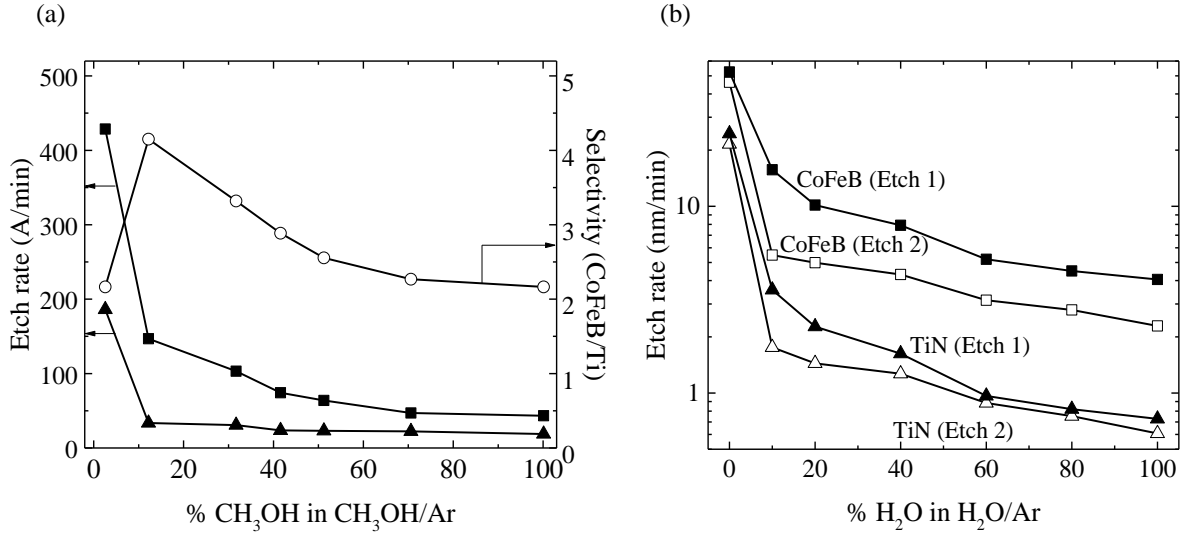


Figure 1-11. (a) Measured etch rates of CoFeB and Ti as well as the calculated selectivity of CoFeB/Ti as a function of methanol concentration in Ar. Films were etched using 800 W source power, 300 V bias, and 5 mTorr. Reproduced from (Xiao 2011). (b) Etch rates of CoFeB and TiN at varying concentrations of H₂O in Ar plasma. Etch 1 was run under 800 W power and 300 V bias at 5 mTorr. Etch 2 was run under 900 W power with 400 V bias at 1 mTorr. Reproduced from (Lee 2013).

Nonetheless, in spite of increasing selectivity, utilization of methanol in the plasma resulting in the formation of additional cobalt and iron oxides on the film surface due to fragmentation of CH₃OH in the plasma. Other chemistries attempted in the search for viable non-halogen candidates include the addition of variable amounts of H₂O to an Ar plasma resulted in decrease in both the etch rate of CoFeB as well as TiN. As shown in Figure 1-11b, a small amount of added water causes nearly an order of magnitude reduction in the etch rate of both materials (Lee 2013). In addition to CoFeB, a number of noble metals are typically employed in the magnetic tunnel junction stack in the form of electrodes or as a replacements for CoFeB in the form of magnetic alloys, generally coupling Pt and Pd with ferromagnetic metals such as Fe and Co and grown on the MgO tunneling barrier (Ohtake 2012). These magnetic-noble metal alloys exist as a multilayered lattice structure that exhibit magnetic anisotropy, the key characteristic sought after

in the development of magnetic materials for spintronic devices such as MRAM (Murdock 1992, Farrow 1996, Chen 2000, Sun 2000, Ohtake 2012).

The patterning of single element noble metal films such as platinum and palladium is difficult due to their inherent chemical inertness. Beyond using just ion milling with noble gases, a number of plasma feed gas mixtures have been investigated to determine optimal conditions and the underlying mechanism for chemical enhancement of the etching of these metals. Halide and noble gas mixtures including Ar/Cl₂ (Nishikawa 1993, Kwon 1998, Shibano 1999), Ar/O₂ (Chou 1990, Shibano 1998, Chiang 2000), Ar/Cl₂/O₂ (Yokoyama 1995, Yoo 1996) have been studied extensively for etching both blanket Pt films as well as features. However, from these studies, platinum displays typical metallic behavior in that its corresponding halides lack volatility. For blanket Pt films, an optimal feed of 90% Ar with 10% Cl₂ exhibits a small etch rate enhancement up to 140nm/min over pure physical sputtering. The authors attribute this phenomenon to the increased concentration of chlorine radicals measured in the plasma as well as creation of high curvature platinum features on the surface due to physical bombardment capable of increased coordination with chemisorbed Cl radicals (Kwon 1998). Three species mixtures have also been studied by combining Ar, Cl₂, and O₂ in hopes of synthesizing PtO₂Cl₂ as an etch product. For patterned features, this chemistry showed improvement in the sidewall, achieving angles up to 70°; however, the etching mechanism was dominated by physical sputtering (Yoo 1996). Additional combinations of Ar/CF₄ and CF₄/Cl₂ were studied on platinum top electrodes for FeRAM applications wherein physical sputtering also played the predominant role in etching; however, at lower bias powers selectivity could be achieved against conventional organic photoresists (van Glabbeek 1993).

1.4 Thermodynamic Approach for Screening Viable Etch Chemistries

Thermodynamics functions as a powerful tool for analyzing chemical reactions within a system. By assessing favorable reactions between an etchant and material from the standpoint of equilibrium, patterning chemistries can be identified without the added capital cost of physically implementing a process for trial and error studies. One way of visualizing thermodynamic equilibrium in solid-vapor systems are introduced to patterning of metallic films by Kulkarni (Kulkarni 2002). With the replacement of aluminum interconnect materials by copper, the semiconductor industry reverted to using chemical mechanical polishing techniques to remove deposited copper and form connections for integrated circuits due to the low volatility of copper halides (Steigerwald 1995, Zantye 2004, Ein-Eli 2007). Construction of the volatility diagram allows for a decoupling of the complicated surface reactions typically seen within plasma patterning into idealized reactions that describe reversible product formation seen at equilibrium between both gas and solid phases.

Examination of these reactions from a thermodynamic standpoint requires thermochemical information such as standard enthalpies, entropies, and Gibbs free energies of formation which are known for a number of common copper and copper halide compounds (HSC 2003, NIST-JANAF 2013). The first step in construction of the volatility diagram is the identification of condensed phase equilibria. This can be first isolated by determination of the reactions occurring within the system between the surface and gas phases. By then calculating the change in Gibbs free energy of reaction from each of the constituent species standard state Gibbs energies, the equilibrium constant can then be calculated by the following simple relationship:

$$\Delta G_{rxn} = -RT \ln(K) \tag{1.5}$$

From the value of K, the activities of each reacting component within the idealized reaction can be related through Eq. 1.6 as follows:

$$\ln(K) = \frac{\prod_{prod} a_i^{n_i}}{\prod_{reac} a_i^{n_i}} \quad (1.6)$$

For all pure solid phase species, the activity is presumed to be unity. However, for gas phases, the activity can be replaced with an effective concentration, this case, in the form of a partial pressure of vapor phase reactants and products. Using this substitution for solid phase equilibria allows for construction of horizontal lines on a log-log plot of partial pressures of reactants as a function of etchant Cl₂ using the list of reactions summarized in Table 1-3.

Table 1-3. Reactions used for creating volatility diagram shown in Figure 1-12 for the Cu-Cl system.

No.	Reaction	Log(K) = -ΔG/RT
(1)	Cu(c) + 1/2 Cl ₂ (g) → CuCl(c)	19.17
(2)	CuCl(c) + 1/2 Cl ₂ (g) → CuCl ₂ (c)	8.34
(3)	Cu(c) → Cu(g)	-47.63
(4)	CuCl(c) → Cu(g) + 1/2 Cl ₂ (g)	-66.80
(5)	CuCl ₂ (c) → Cu(g) + Cl ₂ (g)	-75.13
(6)	Cu(c) + 1/2 Cl ₂ (g) → CuCl(g)	-9.91
(7)	CuCl(c) → CuCl(g)	-29.09
(8)	CuCl ₂ (c) → CuCl(g) + 1/2 Cl ₂ (g)	-37.43
(9)	Cu(c) + Cl ₂ (g) → CuCl ₂ (g)	8.16
(10)	CuCl(c) + 1/2 Cl ₂ (g) → CuCl ₂ (g)	-11.02
(11)	CuCl ₂ (c) → CuCl ₂ (g)	-19.36
(12)	3 Cu(c) + 3/2 Cl ₂ (g) → Cu ₃ Cl ₃ (g)	39.61
(13)	3 CuCl(c) → Cu ₃ Cl ₃ (g)	-17.91
(14)	3 CuCl ₂ (c) → Cu ₃ Cl ₃ (g) + 3/2 Cl ₂ (g)	-42.63

The use of volatility diagrams has allowed for an equilibrium scenario of various gas and condensed phase reactions to allow for insight into the partial pressure dependence of the products seen in cases such as the Cu-Cl₂ system. A partial pressure of ~ 10⁻⁸ atm is calculated as a threshold

for seeing appreciable amounts of etching under these conditions. This pressure is established based on the resolution of thermogravimetric analysis, cited by the authors and reviewed by previous works discussing graphical displays of thermodynamic analysis of metals and metallic oxides, which accounts for the corresponding detectable change in mass that would result in partial pressures of this magnitude (Lou 1985, Kulkarni 2002).

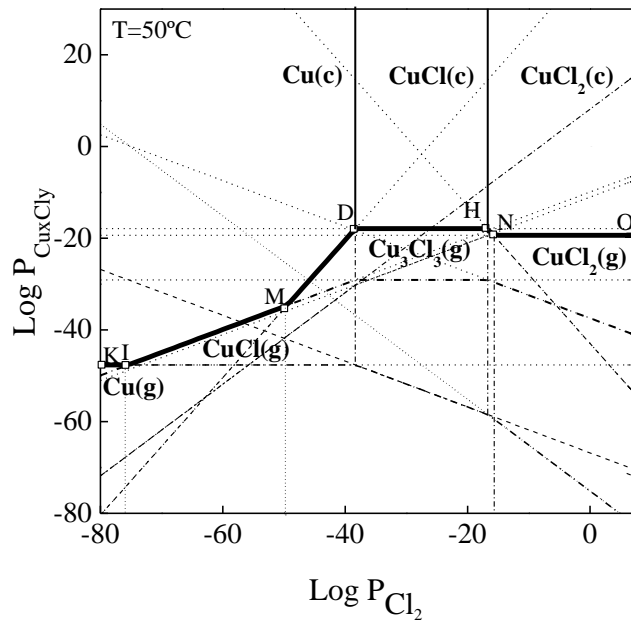


Figure 1-12. Complete volatility diagram of Cu-Cl₂ system at 50°C constructed based on the chemical reactions listed in Table 1-3. Reproduced with slight modifications from (Kulkarni 2002).

The analysis performed by Kulkarni and DeHoff found the Cu-Cl system to lack the necessary volatility for generating substantial pressures of etch product (Cu_xCl_y) at typical operating temperatures. Wafer heating was one approach used as a means of generating volatile copper chlorides, generally requiring temperatures between 100-300°C; however, precisely controlling this temperature was shown to be key in exploiting temperature regimes for reactive

ion etching. By increasing the sample temperature to 150°C, etch rates of up to 400 nm/min were observed under Cl₂ plasma (Hosoi 1993). Additional methods included direct contact heating of the wafer. Etch rates at reduced pressures of 2-10 mTorr were shown to reach a minimum at around 200°C where it was suggested that the dissociative adsorption of Cl₂ at the copper surface is the rate limiting step leading to the formation of Cu₃Cl₃, a trimeric form of copper chloride recognized as the main etch product at reduced temperatures (Winters 1985, Miyazaki 1997).

Following the analysis of Kulkarni and DeHoff, the use of a reductive chemistry to facilitate formation of the gas phase trimer Cu₃Cl₃ was studied by Tamirisa et al. using alternating exposures of Cl₂ and H₂ discharges at temperatures below 25°C. 9nm and 400nm copper films were studied using Cl₂ plasma as a means of generating CuCl₂. A two-step cycle was introduced wherein Cl₂ plasma at 500W source power and 150W bias power was used to chlorinate the copper films for 2 minutes at 1 mTorr while holding the substrate temperature between 12-15°C and immediately followed by either a 2 minute (9nm) or 5 minute (400nm) H₂ plasma exposure at the same temperature and pressure. Both before and after etch cycle surface composition was analyzed using XPS () to determine the chemical bonding states of the Cu film. Strong peaks at 931.9 and 934.5 eV indicated presence of CuCl₂ and CuCl on the film post 2 minutes chlorination (Battistoni 1985). In the case of the thicker 400nm Cu blanket film, after 10 cycles (2min Cl₂, 5min H₂), shown in Figure 1.17a “After etching”, only a residual amount of copper is detected. As can be seen in Figure 1.17b, the thickness of the 400nm Cu film approaches the etch endpoint, further supported by the author’s claims of emergence of Si 2p peak in the XPS spectrum (Tamirisa 2007).

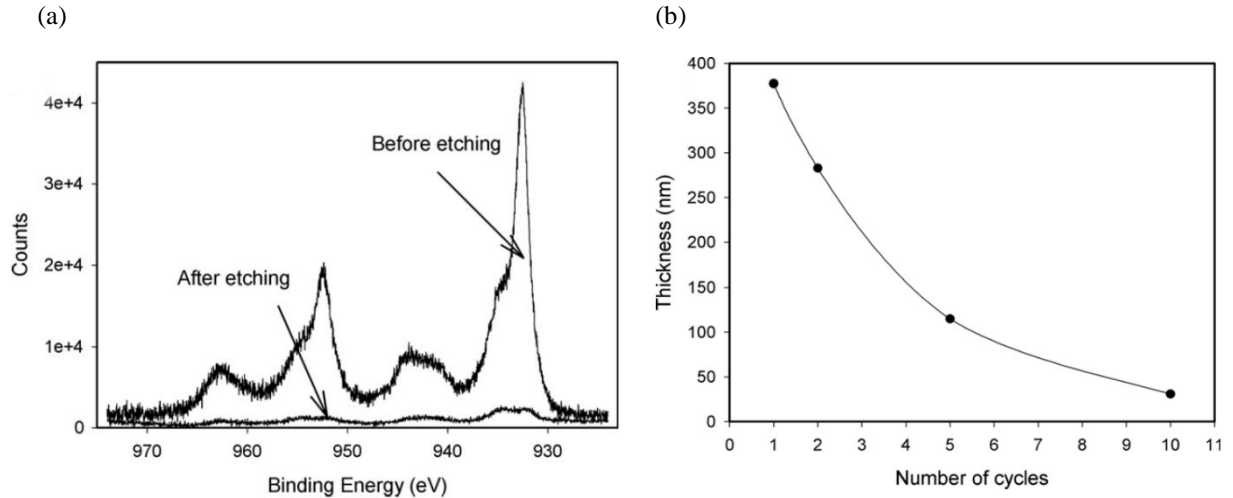


Figure 1-13. (a) XPS spectrum of 400nm Cu film before etching and after etching for 10 cycles of 2 min Cl_2 and 5 min H_2 at 12-15 °C with 500W source power and 150 bias power and (b) thickness measurement of 400nm Cu as a function of number of cycles (Tamirisa 2007)

The XPS characterization performed in this case are paramount in the determination of copper chloride formation for the chlorination step. Peak fitting the CuCl and CuCl_2 characteristic peaks at 934.5 and 931.9 eV result in nearly 2 times the area of CuCl_2 compared to CuCl , showing that a majority of the chlorinated surface exists at CuCl_2 (Tamirisa 2007). This results confirms the thermochemical analysis performed previously showing that CuCl_2 exists as the thermodynamically preferred species upon reaction between Cu(c) and $\text{Cl}_2(\text{g})$ (Kulkarni 2002).

Additional studies have looked into the use of H_2 plasma alone as a means of etching copper (Wu 2010, Wu 2010, Wu 2011). Based on studies using the aforementioned two-step chlorination/reduction process, it was determined that the rate limiting step was the second exposure to hydrogen plasma (Tamirisa 2007). In order to investigate the potential products formed, optical emission spectroscopy studied were carried out for Cu films exposed to H_2 plasma to determine the effects of temperature on the desorption of potential etch products such as CuH and CuH_2 (Wu 2012). It is worth noting that both hydrides are thermally unstable, with CuH

decomposing at temperatures below 100°C (Fitzsimons 1995). This behavior was confirmed by analyzing the etch rate of Cu between substrate temperatures between -150-10°C. Etch rates were observed to increase monotonically as the temperature increased, but subsequently decreased at temperatures above 10°C (Choi 2014).

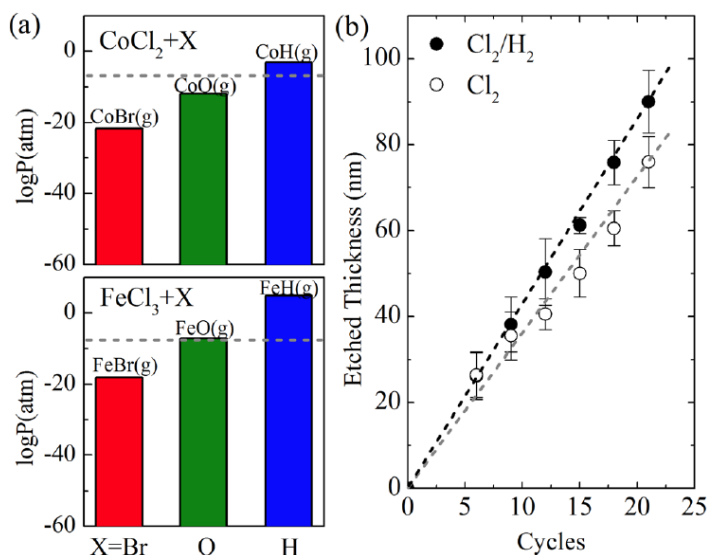


Figure 1-14. (a) Calculated partial pressure of etch products generated from reaction of CoCl_2 and FeCl_3 with atomic Br, O, and H. (b) Etched thickness of CoFe as a function of chlorine and hydrogen plasma cycles. Each cycle consisted of one 20 second half-cycle of Cl_2 and a second 20 second half-cycle of H_2 (Kim 2015).

The thermodynamic assessment introduced by Kulkarni was extended to patterning CoFe thin films. The results are summarized in Figure 1-14a for analysis of CoCl_2 and FeCl_3 to atomic Br, O, and H. Hydrogen exposure is the sole chemistry which, according to the calculations performed, was capable of generating a substantial partial pressure of metal hydride. Subsequent etch experiments confirmed this calculation upon introduction of a cyclical process that used 20 s exposure to chlorine plasma followed by 20 s exposure to hydrogen plasma. A noticeable increase in the etch rate was observed, and XPS analysis confirmed the removal of metallic chlorides surface species (Kim 2015).

1.5 Atomic Layer Etching

The concept of thin film processing with monolayer precision has been a long-standing idea within the semiconductor community. The ability to control the deposition of a wide range of materials at the atomic level has gained prominence over the last three decades due to the advantages it maintains over methods such as chemical vapor and physical vapor deposition. Atomic layer deposition (ALD) namely relies on the ability to engage self-limiting reactions, allowing for delicate handling of many elements. This methodology has been proposed to extend to the approach of atomic layer etching that is utilizing the self-limiting reaction step commonly seen in ALD to allow for modification of the surface of thin films, allowing for formation of localized bonds and thus subsequent targeting through auxiliary chemistry or the introduction of an energy source. The use of a low energy source enables targeting of underlying homogenous layers of material below the modified surface. Thus, it is necessary to incorporate an electronegative aspect to this surface modification step that is both self-limiting and strongly polarizing to first ensure that there is no penetration beyond the first layer of material to be etched and second to guarantee that removal ceases past this first layer.

The use of atomic layer etching would play a crucial role in the patterning of sensitive stack-based structures for emerging memory technologies such as the magnetic tunnel junction described previous in section 1.1. Circular magnetic tunnel junctions with diameters down to 50nm have been fabricated with stack structures consisting of 1.1 and 1.4nm thick layers of CoFeB as the free and fixed magnetic layers as well as 0.25nm Ta (Grezes 2016). Further scaling and successful implantation of these technologies in higher densities rely on the ability to pattern even smaller MTJs by providing monolayer control and enhanced selectivity in removing each material.

A general methodology was first proposed for atomic layer etch (ALE) of silicon which utilized a self-limiting process similar to atomic layer deposition, but in reverse. A silicon surface is first exposed to a sufficiently reactive gas, such as chlorine, and allowed to saturate the surface. After a sufficient period of time, the silicon surface is fully covered with adsorbed chlorine, preventing further mixing into the subsurface layers of silicon. The chemisorbed Cl atoms are able to weaken the underlying Si-Si by reducing their bond energy through the electronegative interaction of Si bonding with Cl. The chlorine source is removed, and the chamber is purged for a fixed amount of time. Positively charged ions are then introduced and gently accelerated through a bias towards the silicon surface. Upon striking the surface, the positively charged ions allow for transference of energy which cascades through to the underlying weakened Si-Si bonds causing them to break and freeing the SiCl (Figure 1-15a). The ion beam is then shut off, and the volatilized SiCl products are removed through evacuation of the chamber (Athavale 1995). By tuning the energy of the ions striking the surface to be below the sputtering threshold energy of Si, controlled removal of only the modified top atomic layer can be achieved, resulting in a limited etch per global cycle of exposure and subsequent ion irradiation (Figure 1-15b).

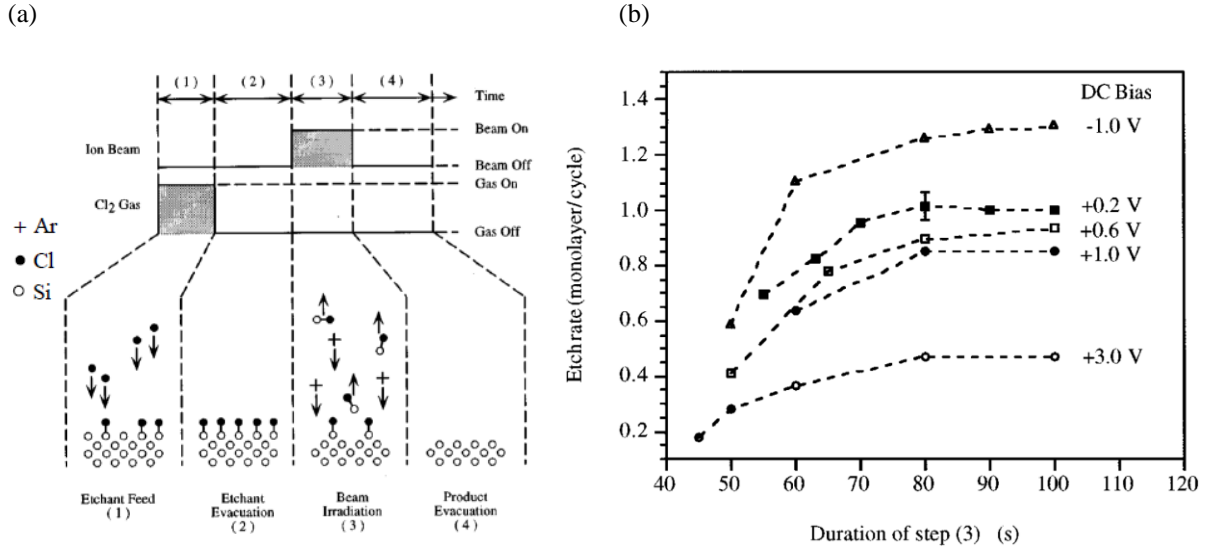


Figure 1-15. (a) Schematic of discretized atomic layer etching steps (Athavale 1995), and (b) atomic layer etch rate as a function of chlorine adsorption step at different applied bias conditions for 140W Ar plasma with 15 mTorr Ar pressure and chlorine partial pressure of 2.4 mTorr (Athavale 1996).

Extension of this concept to a more complicated material such as silicon dioxide was not achieved until 2009. Using a particle-in-cell method, the etching of SiO₂ across numerous cycles of a process similar to that described by Economou was simulated using common C_xF_y etchants in place of chlorine (Agarwal 2009). An additional step that complicated matters further was the formation of polymer upon exposure to fluorocarbon discharge which was commonly seen in etching experiments using C_xF_y etchants on SiO₂ (Bell 1994). Figure 1-16a details the delicate balance of reactive polymer formation on the silica surface, resulting in anisotropic etch through protection of the feature sidewall and layer-by-layer removal of SiO₂ through mixed layer reaction.

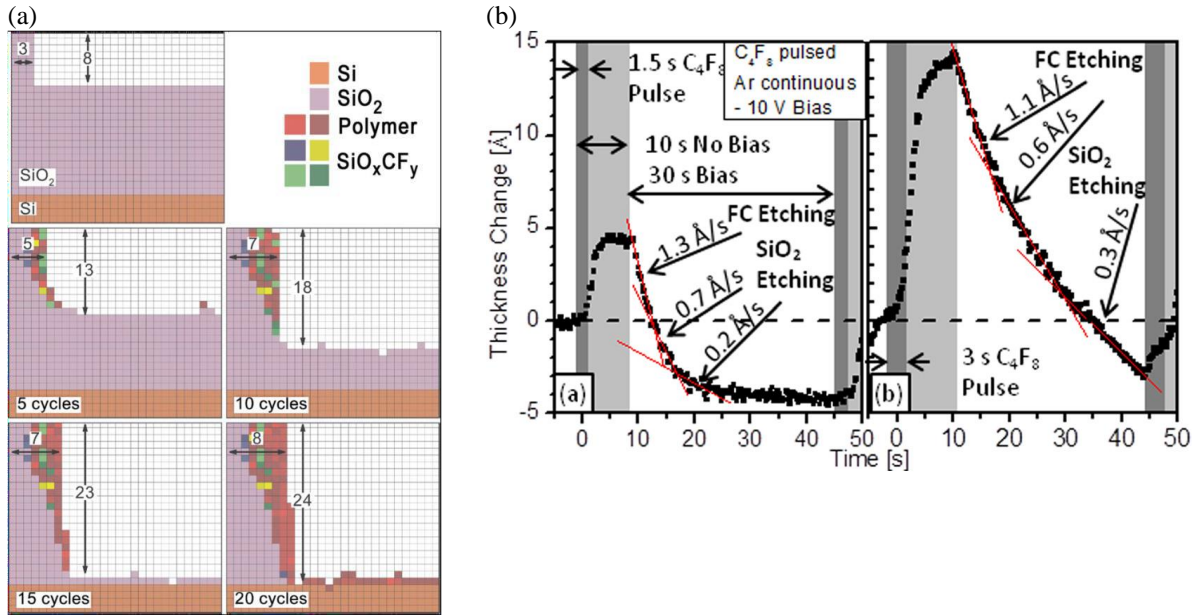


Figure 1-16. (a) Particle-in-cell simulation of atomic layer etching of SiO₂ with Ar and C₄F₈ (Agarwal 2009), and (b) in-situ ellipsometry measurements of SiO₂ thickness over time in continuous Ar plasma with pulsed C₄F₈ (Metzler 2014).

Experimental confirmation of simulated atomic layer etching would require ten years. The reported success of ALE for silicon dioxide was accomplished through the use of argon ion bombardment and pulsed C₄F₈, utilizing a strategy similar to the steps proposed for silicon. In this case, the silicon dioxide surface was exposed to argon ions under no bias continuously (Metzler 2014). Without an applied bias, the mean ion energy was significantly lower than the sputtering threshold energy of SiO₂. C₄F₈ was injected into the reaction chamber in 1.5 s pulses, allowing for surface reaction to occur, resulting a polymer formation and thickness increase over the remaining 8.5 s of no applied bias. After this point, a 10V bias was applied to accelerate the argon ions toward the surface, breaking through the reactive polymer layer and volatilizing SiF_x species through ionic bombardment. Metzler et al. reported an instantaneous etch rate of 1.3 Å/s for removal of the fluorocarbon polymer layer, decreasing to 0.7 and 0.2 Å/s for subsequent removal of silica. From

Figure 1-16b, one observes that the thickness change ceases after the initial 10-15 seconds of ion bombardment upon exposure of an unmodified silicon dioxide surface.

More recent studies have looked further into the process of atomic layer etching of common metallic oxides. By applying a reversal to the logic of thermal ALD, Al_2O_3 was reported to be etched at rates of 0.14 \AA/cycle up to 0.61 \AA/cycle (Lee 2015). The reported two-step process utilized surface modification by donation of the acac ligand from $\text{Sn}(\text{acac})_2$ to produce $\text{Al}(\text{acac})_3$. Introduction of HF-pyridine allows for $\text{SnF}(\text{acac})$ and water to leave as byproducts, while the volatile $\text{Al}(\text{acac})_3$ is evaporated off by increasing the substrate temperature to (Figure 1-17a). The reactive fluorinated aluminum surface is regenerated by exposure to hydrogen fluoride (Figure 1-17b).

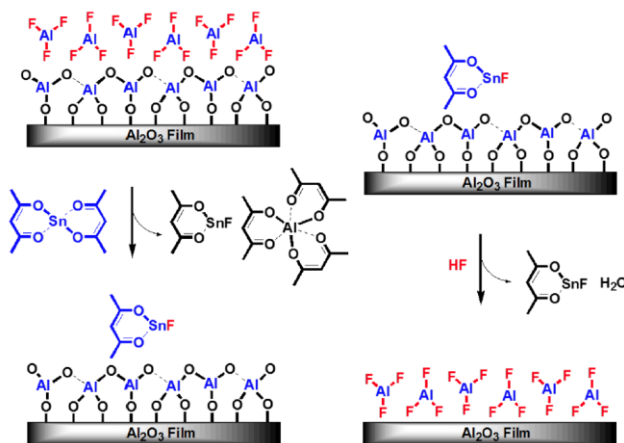


Figure 1-17. Reaction of fluorinated aluminum surface through donation of acac ligand from $\text{Sn}(\text{acac})_2$ to form $\text{Al}(\text{acac})_3$ and subsequent introduction of HF from HF-pyridine facilitates removal of $\text{SnF}(\text{acac})$ and water to regenerate AlF_3 surface (Lee 2015).

The industrial driving force behind the implementation and scaling of atomic layer etching has been strong over the last three years. Kanarik et al. recently summarized the theoretical obstacles to achieving atomic layer etch by noting three specific criteria (Kanakrik 2015). First is

the synergy test wherein the amount of material removed in each cycle is measured and compared that which is removed at each individual step.

It is necessary that the amount removed at each of these steps corresponds to a small amount in the saturation step while a majority of the material is ablated by the exposure to the ion source. Figure 1-18a details the saturation curve that should appear for the usage of successful atomic layer etching.

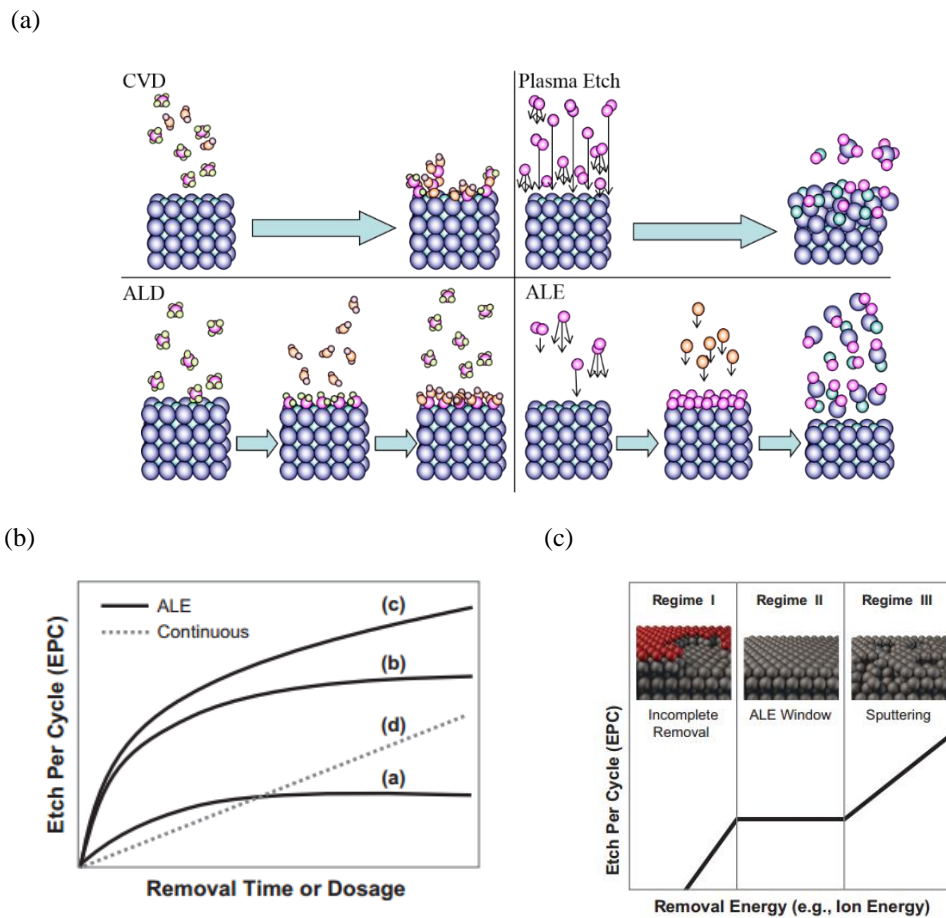


Figure 1-18. (a) Comparison of chemical vapor deposition (CVD) to plasma etching and the corresponding analogy of atomic layer etch (ALE) as reversing the ALD process (Marchack 2011) (b) Saturation curves detailing the self-limiting (a, b) nature of first step adsorption. (c) Energy regimes for etching, removal energy remains constant in ALE window due to threshold energy required to removed modified surface without damaging underlying layers (Kanarik 2015).

Corresponding to this saturation step, there exists a resulting energy window wherein the removal energy necessary (e.g. sputtering threshold) exists for the removal of the modified surface while retaining the virgin film re-exposed underneath. Figure 1-18b shows the energy diagram wherein there should exist a window, similar to that seen in atomic layer deposition, where the removal of approximately monolayers of modified material occurs.

These three tests detailed for achieving the criteria of atomic layer etching are intimately entwined. It is necessary to use methods such as thermal or plasma processes to effectively modify the surface of the material to be etched by introducing a reactive gas such as chlorine that can modify the surface bonds and then irradiating through the use of an argon ion beam. By measuring the thickness change at each separate step, one can quantify the exact change which occurs in the plasma and ideally achieve a veritable removal of material at the atomic level (Kanarik 2015).

In spite of the advancements made in the last two decades in realizing atomic layer etch of various materials, one subset of those widely used in the semiconductor industry has not been studied to as great of an extent as oxides or nitrides. Metallic thin films have been recognized as generally difficult to etch due to the lack of directional bonding present within the material due to the nature of delocalized electrons within metallic bonds. As with most single element and binary compounds that have been shown to etch at the atomic scale, a modification chemistry and etch energy source is required. Table 1-4 summarizes the wide range of materials, which can be split into semiconductors and oxides, along with their respective modification chemistries and energy sources. Work by Chen et al. has shown that ion beam modification can be utilized to roughness and active surface sites which allow for a subsequent exposure of organic vapor to adsorb to the metal atoms and create volatile metalorganic etch products for materials such as Co (Chen 2017).

The ion beam exposure, which irradiated the sample with 500 eV Ar⁺ was capable of an etch rate up to 0.7 nm/min. In contrast, a direct dosing of the sample with acetylacetone vapor alone resulted in no etch. However, when the ion beam was alternated in sequential exposures with the acac vapor, a chemically enhanced sputtering effect occurred, resulting in an etch rate up to 1.3 nm/min. The authors attribute this enhancement to an increase in reactive surface sites caused by disruption of the sample surface by the Ar⁺, allowing acac molecules to chemisorb to the Co, resulting in formation of volatile Co(acac)₂ etch products. Subsequent ion exposure assisted in desorption as well as further modification of the Co surface. (Chen 2017) Introduction of a chemical contrast was achieved to cyclically etch Co, Fe, Cu, Pd, and Pt using a similar approach. However, through exposure to oxygen plasma, modification of up to approximately five nanometers of material was transformed into a metal oxide. This stable oxide was shown to be reactive towards formic acid vapor, creating a chemical contrast and enable high selectivity in the etching process. (Chen 2017, Chen 2017) The ultimate goal of this work is to identify additional effective modification chemistries that can be used in their ionic forms as a means of controlling the directional modification down to an atomic thickness. Additionally, use of these modification chemistries have enabled the generation of contrasted modified layer which can be subsequently removed using organic vapor. Coupling this anisotropic modification, generation of volatile etch products through either introduction of select organic vapor phase chemistries or subsequent noble ion beam exposure to remove the modified layer or less volatile etch product enables development of a process by which metals can be patterned. Scaling this process to the atomic level requires investigation into the effects of parameters such as the ion energy used in the modification step and noble ion irradiation as well as the influence of dosage used for the modification chemistry.

Table 1-4. Summary of reported atomic layer etching of materials

Material	Chemistry	Energy source	E _{ion} (eV)	Etch rate (Å/cyc)	Directional	Ref.
Semiconductor						
AlN	Sn(acac) ₂ /HF	Thermal	-	0.36-1.96	No	(Johnson 2016)
GaAs	Cl ₂	Ar ⁺	22	~14	-	(Meguro 1990)
	Cl/Cl ₂		20	~3	-	(Aoyagi 1992)
GaN	Cl ₂	Ar plasma	16	2.87	-	(Kauppinen 2017)
		Ar ⁺	70	3.3	-	(Kanarik 2017)
Ge	Cl ₂	Ar ⁺	~13	1.5	-	(Sugiyama 1997)
			25	8.0	-	(Kanarik 2017)
Si	CF ₄ /O ₂ , NF ₃ /N ₂ , F ₂ /He plasmas	Ar ⁺	~20	3.0	Yes	(Horiike 1990),
			10	0.5-2.5	-	(Matsuura 1993),
			20	1 ML/cyc	-	(Athavale 1996)
			20-30	2.6-7.0	-	(Metzler 2017)
MoS ₂	Cl ₂	Ar ⁺	50	7.0	-	(Kanarik 2017)
			<20	1 ML/cyc	-	(Lin 2015)
C	O ₂ plasma	Thermal	-	1 ML/cyc	-	(Zhu 2016)
			Ar	~30	1 ML/cyc	-
Oxide						
Al ₂ O ₃	Sn(acac) ₂ , HF	Thermal	-	0.14-0.61	No	(Lee 2015)
	Al(CH ₃) ₃ , HF	Thermal	-	0.14-0.75	No	(Lee 2016)
HfO ₂	Sn(acac) ₂ , HF	Thermal	-	0.07-0.12	No	(Lee 2015)
	CHF ₃ /C ₄ F ₈	Ar plasma	20-30	~1-4	-	(Metzler 2016)
SiO ₂	Al(CH ₃) ₃ , HF	Thermal	-	0.03-0.31	No	(DuMont 2017)
	CHF ₃	Ar ⁺	50	5.0	-	(Kanarik 2017)
TiO ₂	WF ₆ , BCl ₃	Thermal	-	0.6	No	(Lemaire 2017)
WO ₃	BCl ₃ , HF	Thermal	-	0.55-4.19	No	(Johnson 2017)
ZnO	HF, Al(CH ₃) ₃	Thermal	-	2.19	No	(Zywotko 2017)
Nitride						
Si ₃ N ₄	H ₂ plasma	Ar ⁺ /H ₂	100	~20-60	-	(Posseme 2014)
	CHF ₃ , C ₄ F ₈	Ar plasma	20-35	4-12	-	(Metzler 2016)
	CH ₃ F	Ar plasma	150	6	-	(Kim 2018)
TaN	Cl ₂ /He	H ₂ /He	-	35-70	Yes	(Marchack 2017)
TiN	Cl ₂ /He	H ₂ /He	-	50-73	Yes	(Marchack 2017)
	O ₃ /H ₂ O ₂ , HF	Thermal	-	0.06-0.25	No	(Lee 2017)
Metal						
W	Cl ₂	Ar ⁺	60	2.1	-	(Kanarik 2017)
	O ₂ /O ₃ , BCl ₃ , HF	Thermal	-	2.5	No	(Johnson 2017)
	O ₂ , WF ₆	Thermal	-	0.34-6.3	No	(Xie 2018)
Co	Acac	Ar ⁺	500	12.9	Yes	(Chen 2017)
	Formic acid	O ₂ plasma	200	28.0	Yes	(Chen 2017)
Fe				42.0		
Cu				37.0		
Pd	Formic acid	O ₂ plasma	200	12.0	Yes	(Chen 2017)
Pt				5.0		

1.6 Scope and Organization

The scope of this research encompasses development of a methodology for the screening, identification, and implementation of plasma and organic chemistries for use in patterning etch-resistant metallic and intermetallic-based thin films, such as Co, Fe, Cu, Pt, and CoFeB with the ultimate goal of achieving atomic level precision. Current processes employ ion milling techniques to remove material commonly found in the MRAM stack structure resulting in redeposition on feature sidewalls and ultimately device degradation. To narrow the parameter space in selecting viable etchants, equilibrium conditions are first simulated by minimizing the total Gibbs free energy to identify favorable etch products at thermodynamic equilibrium. These products are then used in the construction of condensed and gas phase reactions, used to graphically express equilibrium through volatility diagrams, rendering etch product pressure—and thus amount of material to be removed—as functionally dependent on etchant pressure, with a minimum partial pressure of etch product above 10^{-8} atm is necessary to observe a measurable etch. Doing so allows for gauging the feasibility of using the selected chemistries in the gas phase. Additionally, the reactivity between plasma and vapor etch chemistries and modified surfaces layers was assessed while ensuring temperatures did not exceed 300 °C to keep the process well within a reasonable thermal budget.

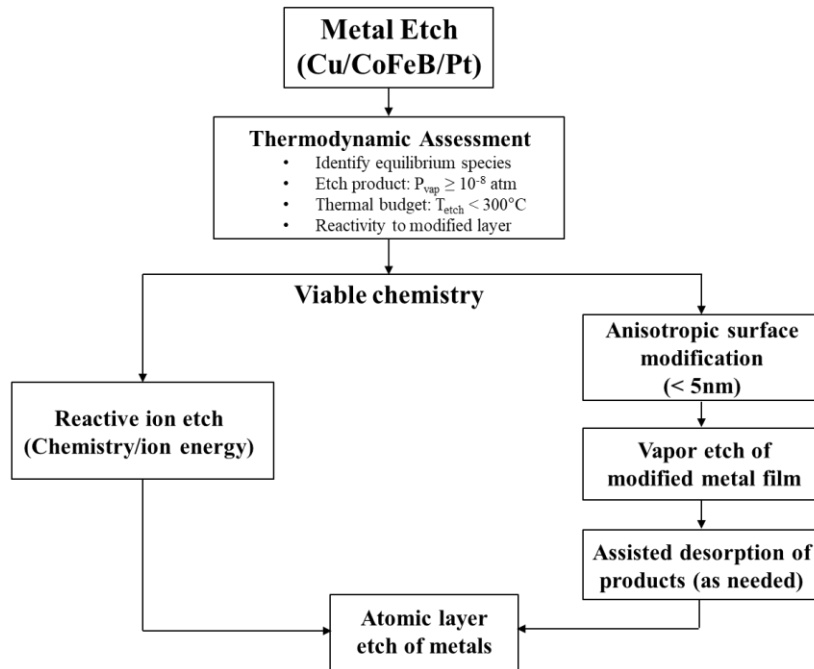


Figure 1-19. Flowchart summarizing the key objectives presented in this work for studying reactive ion etch and atomic layer etch for patterning metallic and intermetallic thin films.

For experimental validation aforementioned thermodynamic analyses, reactive ion and atomic layer etch processes were pursued in parallel in this work utilizing an inductively coupled plasma reactor and ion beam chamber as means for delivering reactive plasma species through O_2 , Cl_2 , and H_2 feed gases. Liquid and vapor phase organics were studied for chemical etching using a solution-based etch as well as a commercial vaporizer setup capable of delivering high pressures of organics at temperatures up to 80°C .

The use of alternating Cl_2/H_2 based on initial volatility analysis has shown that dry etch of Cu could be realized using cyclical plasma etch in a reductive environment. (Tamirisa 2007) However, up until this point, limited there have been limited reports of developing a successful self-limiting etch process for Cu using surface modification. Chapter 3 of this work focuses on

organic etch of Cu, first using solution phase processing of metallic Cu and CuO in acetylacetone, hexafluoroacetylacetone, acetic acid, and formic acid to determine the etch rate selectivity of these two materials. From this, formic acid was tested in the gas phase. An alternating inductively coupled plasma oxidation with subsequent formic acid vapor exposure was found to directionally etch both blanket and patterned Cu lines and square pads at dimensions down to 70 nm using an applied bias during the plasma modification step.

In chapters 4 and 5, reactive ion etch studies were investigated through use of Cl_2 for etching CoFeB and Pt. However, due to corrosion and loss of magnetic properties, an alternative approach was explored through subsequent exposure to H_2 plasma. Previously published cyclical Cl_2/H_2 plasma was predicted through volatility analysis and subsequently confirmed through experiment to result in an enhanced etch rate for Cu, Co, and Fe. (Tamirisa 2007, Kim 2014, Kim 2015) The observed etch rate enhancement and H_2 plasma removal of the modified metallic chloride layer on both CoFeB and Pt indicated that this process was viable for a bulk reactive ion etch. Additionally, restoration of static magnetic properties for CoFeB was observed hydrogen exposure.

In the development of an organic chemical etch, use of vapor etching techniques is necessary since liquid phase etchants cannot be used for the processing of increasingly small feature sizes with aspect ratios greater than 5:1. Due to the effect of surface tension, solution phase etchants used in this manner would remain trapped in areas of high curvature within the feature, causing continued etching, device degradation, and potential issues with short-circuiting. Chemical solution and vapor etching using single components such as acetylacetone, hexafluoroacetylacetone, formic acid, and acetic acid were investigated through the introduction

of a commercially available vaporizer system, capable of delivering high fluxes of organic etchant to the sample surface.

Ultimately, the goal of this work was to achieve self-limited etch through the implementation of surface modification, wherein the metallic surface was made to react with an electronegative species to transform the network of delocalized metallic bonds into highly polarized metal-halide or metal-chalcogenide bonds. Both an oxygen plasma and ion beam were demonstrated to be effective routes. Through tuning of the incident ion energy to below the sputtering threshold energy for each material, no unwanted removal was observed, and directional modification was achieved. Second, formic acid was vaporized and delivered directly to the surface where the modified metal sites underwent reaction, replacing the oxygen with a deprotonated organic ligand, forming volatile metalorganic complexes leaving behind the metallic surface.

Chapter 2 : Experimental Setup

The interaction of several hard-to-etch materials, such as CoFeB and Pt, with modification and etch chemistries were explored through two parallel approaches, reactive ion etch and modified vapor etch. Each route was initiated using a dual-step thermochemical assessment which allowed for identification of species using minimization of Gibbs free energy and subsequent volatility analysis of the etch product pressures through construction of idealized surface-gas reactions within a specified etchant pressure regime to screen potential etch chemistries. Experimental validation was conducted for both reactive ion and vapor etch cases.

First, an alternative reactive ion etch process based on sequential halogenation (Cl_2) and reduction (H_2) was explored with the goal of enhanced etch rates measured by film thickness changes and identification of etch products measured through spectroscopic ellipsometry and quadrupole mass spectrometry, thus verifying the initial thermodynamic calculations. Application of this process to ferromagnetic materials necessitated the removal of surface-bonded species which negatively affect the static magnetic properties to ensure proper memory device performance.

Second, a pathway to atomic layer etching was investigated using solution and vapor phase processing. Both solution and vapor were critical to confirming the thermodynamic predictions through the aforementioned measured thickness changes and presence of metalorganic etch products using electrospray ionization mass spectrometry. However, a chemical contrast was necessary to enable a selective vapor etch process and was established by calculations for the change in Gibbs free energy of reaction. This contrast was a result of a plasma-based modification step which was incorporated into a cyclical etch process, allowing the etch rate to be tuned through

the controlled growth of the modified layer. The thickness and chemical composition of the modified layer was elucidated using surface characterization techniques such as x-ray photoelectron spectroscopy (XPS), allowing for sub-nanometer resolution and compositional analysis to a few atomic percent. The second goal of the atomic layer etch process necessitated the use of directional ionic species from the plasma to enable an anisotropic modification process and create chemical contrast in the preferred vertical direction. Characterization of discharge used in the modification process was achieved using Langmuir probe to calculate the electron temperature and optical emission spectroscopy to identify active discharge species. Subsequent use of isotropic etch chemistries, such as the organic vapor, removed the directionally modified layer and resulted in the evolution of an anisotropic feature profile which was measured through cross-section scanning electron microscopy.

2.1 Ultra-High Vacuum Transfer Tube and Load Lock

To prevent sample exposure to atmosphere, a transfer tube held under ultra-high vacuum (UHV), with a base pressure of 2×10^{-9} Torr, is utilized. Figure 2-1 below illustrates the constructed UHV transfer tube used in transporting samples from a centralized load lock chamber to the inductively coupled plasma (ICP) etcher and XPS.

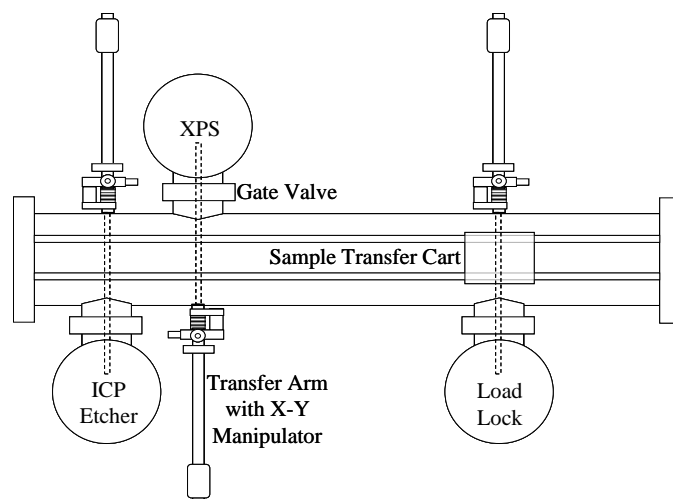


Figure 2-1. Schematic of ultra-high vacuum transfer tube.

Three pumps are connected to the UHV transfer tube, serving to evacuate the system to achieve different pressure ranges. First, an Edwards E2M-18 dual stage rotary vane mechanical pump is used as a roughing pump capable of evacuating the system to 1×10^{-3} Torr. A Leybold 360 turbomolecular pump with a corresponding pump speed of 360 l/s is then able to evacuate the transfer tube to pressures around $\sim 10^{-6}$ Torr. Finally, for higher vacuum applications, a CTI CT-8 cryogenic pump capable of speeds up to 4000 l/s and is utilized to obtain ultimate pressures of 2×10^{-9} Torr. Pressure is monitored by a hot-filament ionization gauge. A centralized load lock is used to introduce samples to the UHV system. This portion of the transfer tube is evacuated first through the same Edward E2M-18 and a Leybold 361 turbomolecular pump with pumping speeds identical to the Leybold 360 mentioned above.

A magnetically coupled transfer arm located opposite the load lock can be manipulated from across the transfer tube to secure samples placed on stages in the loading platform carousel. The transfer arm contains a small fork which can be inserted into the sample stage, lifted up to remove the stage from a small post on the loading platform carousel, and the arm retracted to allow

for transference to the sample cart located in the center of the main transfer tube. Through manipulation of the arm height, the sample stage can be lowered onto small posts protruding from the cart surface and held in place.

Both the loading platform carousel and the sample cart contains six posts. The sample cart can be moved along a track spanning the entire length of the transfer tube. Movement is achieved by operating a wire-pulley system attached to the cart and secured to a knob on the outside of the tube, allowing atmosphere-side operation of the cart. An electric motor is coupled to the wire-pulley knob which enables electronic control over both the speed and direction from various remote locations along the transfer tube.

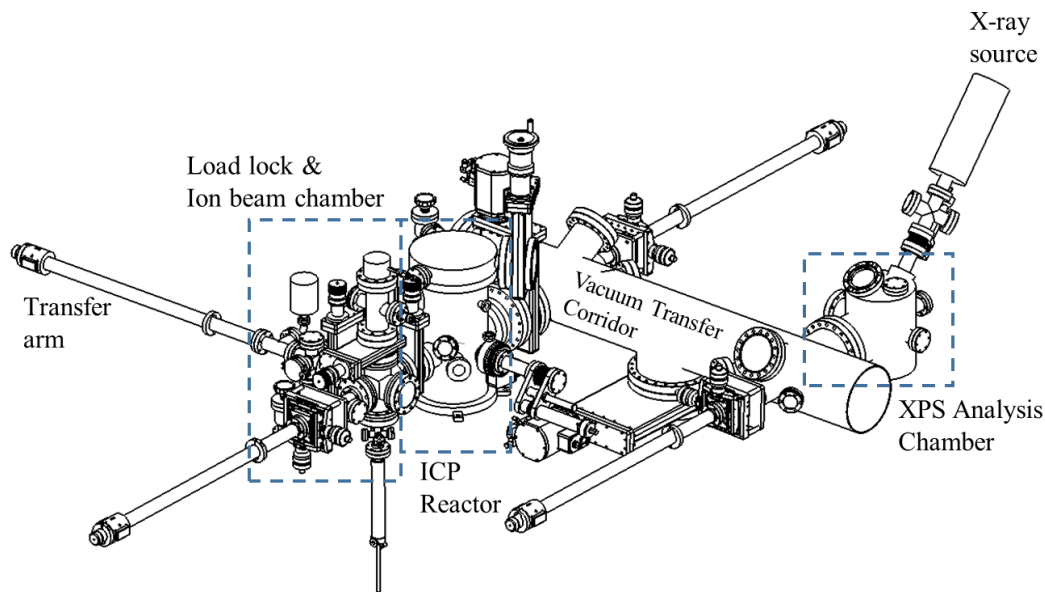


Figure 2-2. Schematic of integrated ion beam chamber, inductively coupled plasma reactor, and UHV transfer tube with *in situ* XPS.

2.2 Inductively Coupled Plasma Reactor

The system used predominantly in these studies is a custom constructed inductively coupled plasma etcher. Plasma is ignited and sustained through the use of a radio frequency (RF) power source which allows for electromagnetic induction. The reactor chamber is constructed of stainless steel and partitioned, through the use of an orifice plate which spans the diameter of the chamber and separates it into two sections. The upper chamber is lined with a quartz bell jar and ring. Plasma is generated in the upper portion of chamber which is capped by a custom-made quartz dielectric window. On top of this window rests a three turn copper coil seated within a grounded cage. The coil is connected to an auto-tuned matching network and subsequently the RF power supply operating at 13.56 MHz, which was previously discussed.

The inside of the top half of the chamber is lined with a custom dielectric liner in the shape of an inverted bell jar, constructed entirely of quartz. This liner acts as an insulating layer to separate the plasma generated within the chamber from the stainless steel chamber wall. A separate electrode is present at the bottom of the upper chamber section, connected to a Kepco BOP 500M power supply capable of applying bias voltages up to 500 V. Figure 2-3 displays a schematic representation of the entire ICP plasma chamber with the attached vapor etch chamber. These two chambers were separated through the use of a 2.75" CF gate valve.

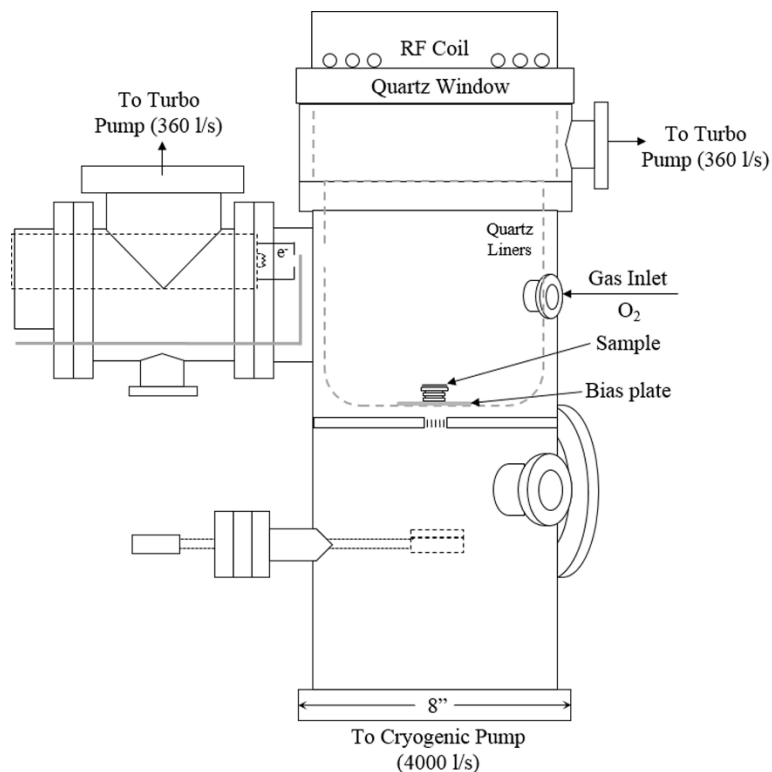


Figure 2-3. Schematic of inductively coupled plasma (ICP) etcher showing division between upper and lower sections.

The ICP chamber is evacuated through a Leybold D25 rotary vane mechanical pump, capable of achieving pressures of 5×10^{-3} Torr. This upper section also contains the gas inlets through which argon (99.999% pure), nitrogen (99.999%), oxygen (99.993%), chlorine (99.999%), boron trichloride (99.995%), sulfur hexafluoride (99.996%), hydrogen (99.999%), and methane (99.97%) can all be supplied. Flow rates are controlled by MKS mass flow controllers with standard maximal flow rates of 20-100 sccm (Table 2-1).

Table 2-1. Process gases available for use in inductively coupled plasma reactor with their corresponding purities and maximal flow rates.

Gas	Ar	N ₂	O ₂	Cl ₂	BCl ₃	SF ₆	H ₂	CH ₄
Purity (%)	99.999	99.999	99.993	99.999	99.995	99.996	99.999	99.97
Max. flow rate (sccm)	50	100	50	50	50	50	20	36

A UTI 100C quadrupole mass spectrometer is attached to the upper portion for analysis of gas phase species and is capable of detecting masses up to 200 amu. The lower boundary of this section is the stainless steel partition plate containing a 0.7 inch diameter orifice. This orifice contains a grounded grid and allows for extraction of a beam of collimated plasma from the upper section to the lower area. The mean free path of particles is given by the equation:

$$\lambda = \frac{KT}{\sqrt{2}p\pi d_o^2} \quad (2.1)$$

where p is the pressure, and d_o is the collision diameter of the gas molecule. For diatomic Cl₂ with collision diameter of 4.11 Å (Ono 1997), the mean free path in the upper chamber operating pressure of 5 mTorr and a neutral gas temperature of 590 K (Donnelly 2000) is estimated as 1.6 cm. In the lower chamber, where the operating pressure is 5×10⁻⁵ Torr, the mean free path is substantially higher at 107 cm for the extracted Cl₂ plasma. In comparison, for diatomic O₂ with a collision diameter of 3.46 Å (Ismail 2015), the mean free path in the upper chamber at an operating pressure of 5 mTorr and neutral gas temperature of 590 K is estimated to be 2.3 cm, while in the lower chamber, where the operating pressure is 5×10⁻⁵ Torr, the mean free path is 114 cm for extracted O₂ plasma.

The lower area of this system is connected to a CTI CT-8 cryogenic pump with a pumping speed of 4000 l/s and capable of maintaining a base pressure of 2×10^{-8} Torr. The inclusion of a cryogenic pump is necessary for evacuation of the bottom portion of the reactor due to the severely limited conductance through the dividing orifice plate.

2.3 Vapor Etch Chamber Coupled with ICP Reactor

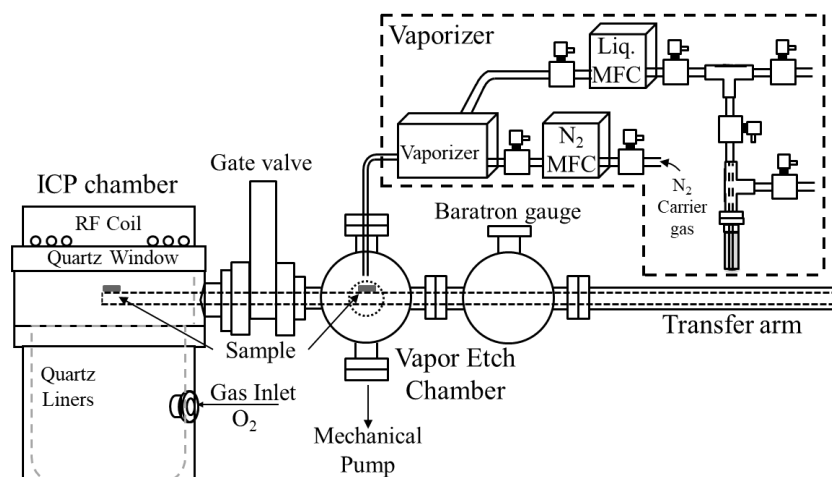


Figure 2-4. Schematic of inductively coupled plasma (ICP) etcher with attached gate valve and vapor etch chamber and commercial vaporizer.

After assessing the etching efficacy of materials in organic chemical solutions, studies of the same organics is necessary in the vapor phase for integration with a vacuum-compatible process. Previous results using organic solution-based etch have indicated that, in general, metal oxides etch more quickly than their metallic counterparts.(Altieri 2017) This observation suggests that plasma oxidation is effective in enabling etch and high selectivity to the underlying metallic thin film. A vapor etch chamber was constructed and coupled to the inductively coupled plasma reactor discussed above. A schematic of these two interfaced chambers is shown above in Figure

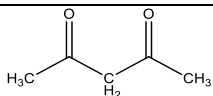
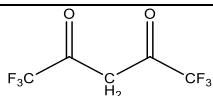
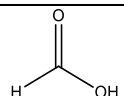
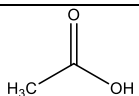
2-4. The vapor etch chamber is connected to a 2.75" CF port using a 2.75" gate valve (for isolation from the ICP) and 2.75" to 1.33" conflate zero-length adapter. To this zero-length adapter is attached a 1.33" six-way-cross, which serves as the body of the vapor etch chamber, due to the ease of temperature control and reducing the required volume of organic solution necessary to generate a substantial pressure (greater than 50 Torr) of organic vapor. Use of too large of a chamber results in temperature fluctuations and subsequent condensation. Use of a smaller chamber allows for generation of higher densities of organics in the vapor phase. The chamber was heated to 80 °C to prevent condensation of the organic vapor through the use of several resistive heating wires wrapped uniformly around the external chamber wall. The chamber is connected to an Edward E2M-18 mechanical pump, and the pressure is monitored using an MKS 627B Baratron capacitance manometer gauge, with an operational range from 1 to 1000 Torr. A precision magnetically coupled transporter arm was utilized to move the sample between the ICP reactor and vapor etch chamber while also allowing for alignment of the sample respective to the organic vapor doser. This doser is constructed from 1/8" stainless steel tubing and is connected to a commercially available vaporizer system.

Delivery of organic chemicals in the vapor phase to the sample surface was enabled by the use of a M1-1141-PN liquid vaporizer system manufactured by Horiba™ and allows for fine-tuned control over vapor flow and temperature. The vaporizer setup is comprised of three elements: a liquid mass flow controller, carrier gas mass flow controller, and heater. Liquid supply to the heater is regulated by the LF-F20M-A liquid mass flow controller which is capable of delivering between 0.02 to 0.1 g/min of liquid chemical. The organic liquid was heated to 80 °C using a ceramic resistive heating element housed in the M1-1000 vaporizer unit. Finally, nitrogen was used as a

carrier gas and controlled by the SEC-E40 mass flow controller to provide a backpressure and facilitate organic vapor delivery.

Liquid vaporization can be accomplished in two ways. First, the temperature can be increased while holding pressure constant, resulting in boiling of the liquid. Alternatively, the vaporizer described above utilizes a change in both temperature and pressure. The liquid feed is initially heated to the preset vaporizer temperature, in these studies chosen to be 80 °C, while subsequently decreasing the pressure, resulting in generation of gas phase organics. Introduction of N₂ carrier gas into the vaporizer unit facilitates organic vapor delivery into the processing chamber through the mixed gas outlet. The organic chemistries studied in this work were chosen for their substantial volatility, exemplified by their vapor pressure (P_{vap}) at ambient conditions (25 °C) and elevated processing temperature (80 °C). These organic chemistries are summarized with their corresponding vapor pressures boiling points in Table 2-2.

Table 2-2. Organic etchants chosen for testing in the vapor phase with their corresponding molecular structures, purities, vapor pressures, and boiling points.

Chemical name	Acetylacetone (acac)	Hexafluoroacetylacetone (hfac)	Formic acid (FA)	Acetic acid (AA)
Molecular structure				
Purity	>99%	98%	>95%	99.5%
P_{vap} (Torr)	7	90	40	16
Boiling point (°C)	140	70	101	118

2.4 Ion Beam Etch Reactor

Ion beams are commonly utilized in industrial settings for physical etching of hard-to-etch materials such as metal and intermetallic thin films. Additionally, ion beams are useful tools for enabling low energy sputter cleaning of samples before processing in order to eliminate native oxidation or carbon contamination from previous atmospheric exposure. A modification was made to the ICP reactor described in section 2.2 in order to integrate a 3 cm ion beam source for both the physical sputtering etch rate studies and sputter cleaning of samples before exposure to reactive plasmas.

Ion beam etch studies were performed using a 3 cm Commonwealth Scientific Kaufman ion source. This source generates a DC discharge by creating a difference in potential between the anode and cathode. A 0.25 mm tungsten wire serve as the cathode filament inside the discharge chamber and ignites and sustains the discharge through thermionic emission of electrons into rarefied Ar feed, supplied to the chamber via a 1/8" diameter stainless steel tube. A permanent magnet is positioned beneath the anode, generating a magnetic field parallel to the source axis to confine the energetic electrons emitted by the cathode. The potential of the anode determines the energy of ions extracted from the discharge with respect to the grounded sample. A set of two interspaced graphite grids serve as electrostatic optics to facilitate ion beam extraction from the discharge. The primary grid serves to confine the plasma and possesses a potential similar to that of the cathode. The secondary grid has an applied negative bias which serves to extract the Ar^+ from the discharge chamber to impinge upon the sample surface. Graphite was chosen in this case due to its low sputtering yield, thus extending the lifetime of this dual grid configuration. A second 0.25 mm tungsten wire serves as an external neutralizer and provides low energy electron emission to prevent charging of the sample surface and reduce positive-positive repulsion of Ar^+ and

minimize the resulting beam spreading. The chamber configuration of the Kauffman ion source is summarized in Figure 2-5.

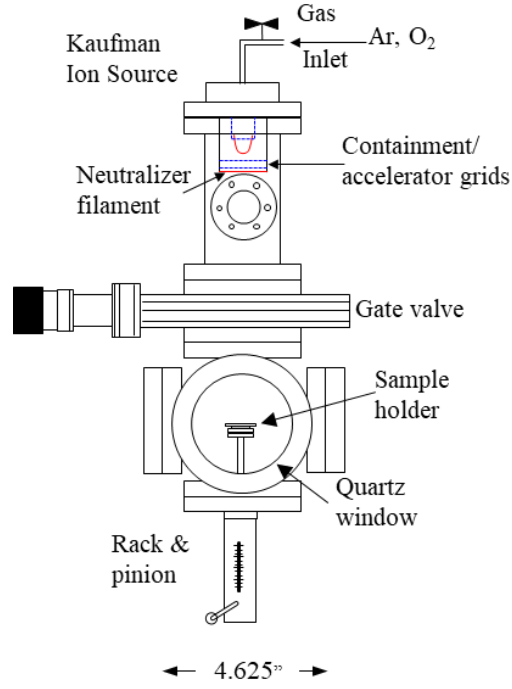


Figure 2-5. Schematic of ion beam chamber.

The resulting current density, j , of the extracted ion beam can be calculated using Child's law as follows,

$$j = \frac{4\epsilon_0}{9} \left(\frac{2q}{m} \right)^{1/2} \frac{V^{3/2}}{l^2} \quad (2.2)$$

where ϵ_0 is the permittivity of free space, q/m is the ratio of charge to mass of the extracted ions, and V and l are the differences in potential and spacing between the primary and secondary grids.

A feed of 5 sccm of Ar is streamed into the discharge chamber to sustain a sufficient ion flux while maintaining a lower background pressure of approximately 2×10^{-4} Torr. A maximum current density of $50 \mu\text{A}/\text{cm}^2$ can be achieved using 1 keV Ar^+ .

The ion source was housed in a 4.625 inch CF reducing tee and mounted to the top of a 4.625 inch CF six way cross, which served as the ion beam chamber. This chamber was subsequently joined with a 4.625 inch CF manual gate valve and connected to the 4.625 CF port on the bottom partition of the ICP reactor. A magnetically coupled transfer arm was installed on the opposite side of the ion beam chamber to enable sample transfer from the ion beam chamber into the bottom half of the ICP reactor. A 1.33 inch CF rack and pinion was installed on the bottom of the 4.625 six way cross and served as the sample stage for ion beam experiments. A 2.75 inch CF six-way cross was connected perpendicular to the ion beam chamber-gate valve-ICP passage and outfitted with a 2.75 inch CF quick access door and magnetically coupled transfer arm. A manually 2.75 inch CF manual gate valve was used in conjunction with a 2.75 inch to 4.625 inch CF zero length adapter to interface the load lock with the ion beam chamber while allowing for the two chambers to be separated. The load lock was connected to an Edward E2M-18 mechanical pump, and the pressure was monitored using an MKS 627B Baratron capacitance manometer gauge, with an operational range from 1 to 1000 Torr. The load lock was capable of achieving a base pressure of 30 mTorr.

2.5 Organic Solution Etching

The etching studied in this work relies on the utilization of organic chemistries as a means for removing solid state material through formation of metalorganic complexes exhibiting increased volatility. The chosen etchants were investigated in solution form first to assess the chemical reactivity and generation of etch products upon reaction with metallic thin films. Chemistries studied in this work include multiple beta-diketonate molecules such as acetylacetonone (acac, >99% pure), hexafluoroacetylacetonone (hfac, 98%), and tetramethylheptanedione (tmhd, 98%), as well as organic acids such as formic acid (>95%) and acetic acid (99.5%). A summary

of these etchants as well as their purities and corresponding physical properties are summarized in Table 2-2.

Blanket thin films of hard-to-etch materials such as Co, Cu, Pt, and CoFeB were used in these studies to assess the etch feasibility of wet chemistries. For each experiment, the organic chemicals were loaded into 1 dram glass vials. A water bath, heated using an electric hot plate, was chosen to ensure uniform heating of the vial to 80°C, measured using a type K thermocouple. Samples were immersed in the heated solutions for predetermined etch times ranging from 1-10 minutes. Post-etch solutions were collected and analyzed using inductively coupled mass spectrometry to determine the concentration of metal after etch as well as electrospray ionization mass spectrometry to identify the etch product present in solution phase. Additionally, surface composition and changes in the surface chemical bonding states were analyzed using EDS and XPS.

2.6 Sample Preparation

Samples used in this work were synthesized using physical vapor deposition (PVD) techniques, namely electron-beam and sputter deposition. Both approaches rely on bombardment of the target material to be deposited and thus require evacuation of the process chamber to a minimum pressure of 10^{-6} Torr. Electron-beam, or e-beam, deposition uses an electron beam generated through emission from a tungsten filament and focused through an applied magnetic field to bombard and heat an ingot of material to be deposited. At low pressures, the metal atoms evaporate from the ingot and deposit on wafers suspended above the crucible. E-beam deposition is useful for single element metallic thin film deposition and can achieve rates as high as 3 Å/s with good adhesion. A CHA Mark 40 was used for deposition of up to 100 nm thick films of Co,

Fe, Cu, Pd, and Pt on Si substrates for studies done in this work. Sources used consisted of 99.95% and 99.99% pure pellets 0.25” in diameter and 0.25” long.

Table 2-3. Thin film sample materials, source purities, deposited film thicknesses, and patterned feature sizes.

<i>Material</i>	<i>Purity (%)</i>	<i>Deposition method</i>	<i>Deposited film thickness (nm)</i>	<i>Patterned</i>	<i>Feature size</i>
Co	99.95	Sputter, E-beam evaporation		Yes (30 nm)	70 nm × 10 μm lines
Fe	99.95	E-beam evaporation		No	N/A
Cu	99.99	Sputter, E-beam evaporation	20-100	Yes (35 nm)	70 nm × 10 μm lines 1 μm × 1 μm squares
Pd	99.95	E-beam evaporation		No	N/A
Pt	99.99	E-beam evaporation		No	N/A
Co ₃₀ Fe ₄₅ B ₂₅	99.95	Sputter	30-50	No	N/A

Additional materials, such as CoFeB, were deposited using sputter deposition. Sputtering employs a noble gas discharge at low pressure. To ensure efficient deposition, the noble gas is chosen to be similar in atomic weight to the material sputtered. A negative bias is applied to the material target, thus accelerating ions within the plasma towards the target. These ions bombard the surface and eject particles from the source. The ejected particles are directed toward a substrate, resulting in thin film growth. In general, sputter target materials are required to have a high purity of at least 99.9%. CoFeB was deposited from a single target with 99.95% purity and a stoichiometry of Co₃₀Fe₄₅B₂₅ under 40 sccm Ar gas flow at a power of 120 W and 1 mTorr pressure. A summary of the thin film samples, source purities, deposition methods, deposited thicknesses, and patterned sample features have been summarized in Table 2-3.

2.7 Etch Rate Quantification

2.7.1 Scanning electron microscopy

In this work, a scanning electron microscope (SEM) was used for top down and cross-section measurements of etched blanket and patterned thin films. This technique enables observation of surfaces at significantly higher resolutions than that of an optical microscope, with a depth of field that is orders of magnitude larger. In an SEM, electrons are accelerated toward the anode with energies ranging from, in this case 200 V to 30 kV and subsequently pass through two lenses which serve to reduce the image of the electron source to a nanometer scale as it impinges upon the sample surface. The electron beam is deflected by a scan generator. Secondary electrons are generated during the interaction between the electron beam and sample surface and are subsequently collected to construct the image. Physical dimensions of the pre- and post-etched samples can be measured and used to calculate the etched thickness, and thus etch rate, of a material as well as the sidewall angle and etch profile of patterned features. The microscope primarily used for this work is an FEI Nova 600 NanoLab DualBeam SEM that is capable of resolution down to ~2 nm at an accelerating voltage of 15 kV. The chamber is backed by a PVP variable volume piston pump and 240 l/s turbomolecular pump with pressures below 10^{-4} Torr while the electron beam column is maintained under high vacuum through three ion getter pumps.

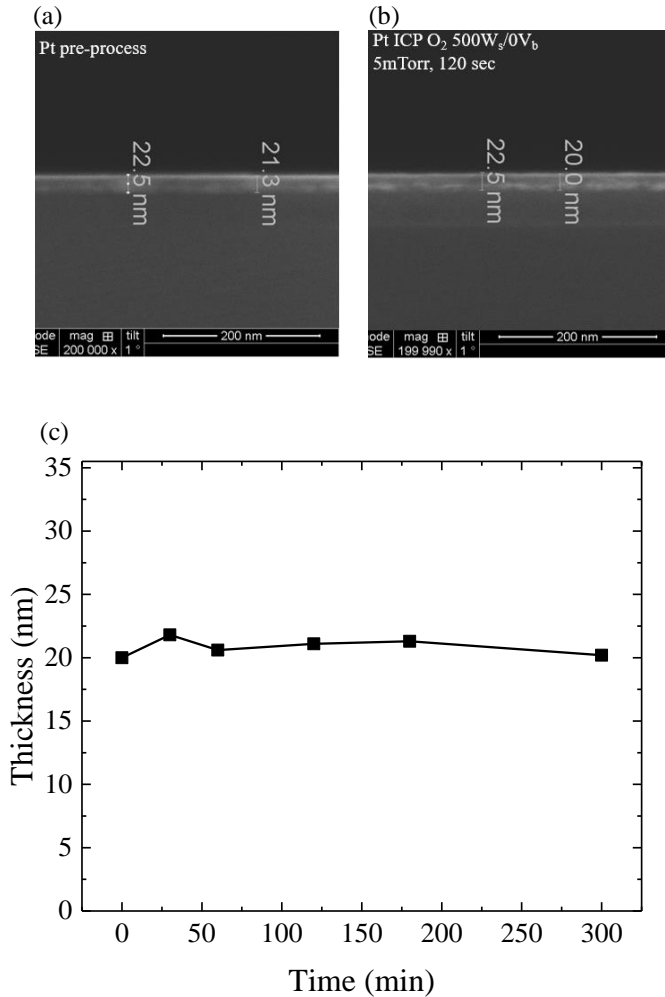


Figure 2-6. Scanning electron micrographs of 20 nm platinum film (a) pre-processing and (b) after exposure to inductively coupled O₂ plasma with 500 W source power, no applied bias, 5 mTorr, and 120 seconds. (c) Summary of measured thicknesses of 20 nm films post time-dependent exposure to 5 mTorr O₂ plasma at 500 W source power and 0 W bias power.

In Figure 2-6a above is shown a cross section scanning electron micrograph of a 20 nm platinum film used to study the effects of oxidation on thickness change over time alongside a summary of the obtained thickness measurements for oxidized Pt films as a function of plasma exposure time (Figure 2-6b). Scanning electron microscopy offers a secondary method for using visual measurement in verification of other thickness measurement techniques such as spectroscopic ellipsometry and profilometry, which is discussed later in this section. As can be

seen from the data reported below, thickness changes on the order of 1-2 nm can generally be measured; however, it is generally advised that for very thin samples and small thickness changes, SEM measurements are not to be taken as absolute.

2.7.2 Inelastic mean free path thickness calculation

In addition to elucidating the chemical bonding states present on the surface of samples analyzed by XPS, spectra can also enable measurement of material thicknesses through the use of a simple bilayer model. Films must be less than 10 nm thick for the overlayer method to be applicable due to the limited sampling depth of the XPS, ensuring that photoelectrons from the underlayer as detectable by the energy analyzer portion of the instrument. An example of the metal-oxide bilayer model for cobalt pre and post-processing in oxygen plasma is shown in Figure 2-7.

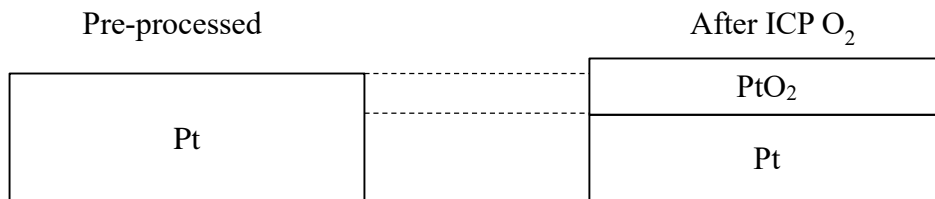


Figure 2-7. Overlayer model for the formation of cobalt oxide on metallic platinum after inductively coupled O₂ plasma exposure. As the oxide is generated, the total thickness of metallic Pt decreases while the growth of less dense PtO₂ results in an overall thickness greater than that of the initial pre-processed Pt. Adapted from (Blackstock 2003).

For each of the metals studied in this work, their densities are substantially higher than the densities of their corresponding oxides. Platinum, as an example, has a density of 21.5 g/cm³ while PtO and PtO₂ have densities of 14.1 and 10.2 g/cm³, respectively. Substantial differences in the

metal and oxide densities suggest that volumetric expansion occurred during the conversion of platinum to platinum oxide.

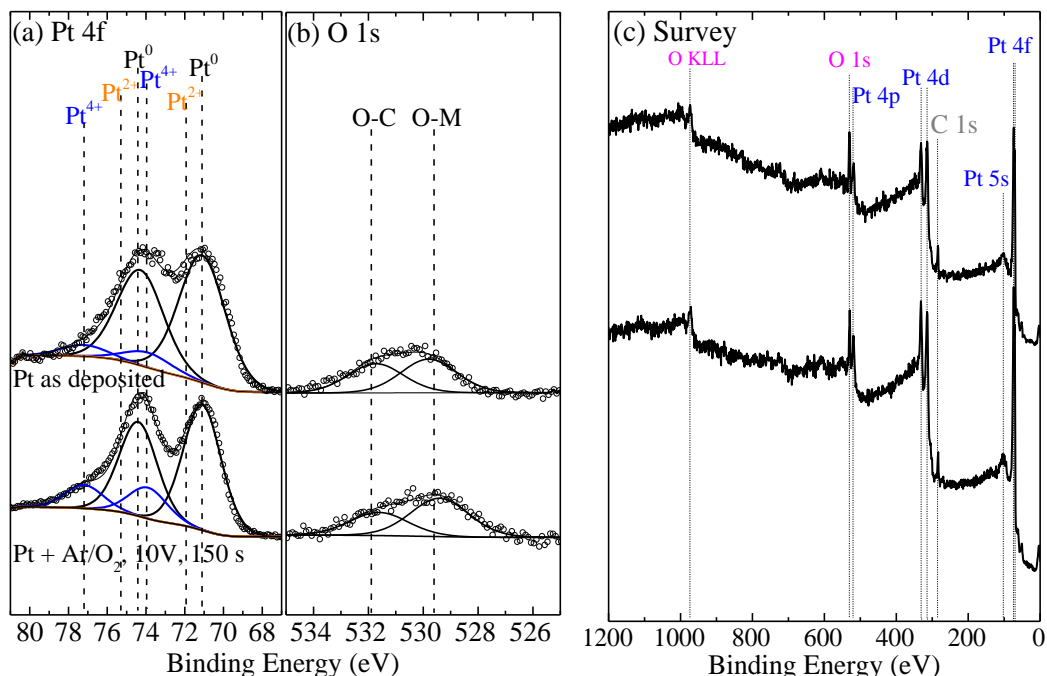


Figure 2-8. High resolution x-ray photoelectron spectra of (a) Pt 4f, (b) O 1s regions and (c) survey scan of elements on the sample surface for as deposited 30 nm Pt before and after 150s exposure to Ar/O₂ plasma at an applied bias of 10V.

The model shown in Figure 2-7 was used to measure the thickness of oxide layers generated during plasma exposure. High resolution x-ray photoelectron spectra of both the Pt 4f and O 1s regions were used to deconvolute the contributions of the Pt⁰, Pt²⁺, and Pt⁴⁺ bonding states using modified Gaussian-Lorentzian lineshapes for the Pt 4f doublet while constraining the oxidized Pt²⁺ and Pt⁴⁺ contributions by the normalized area of the O 1s spectra for O-Pt bonding measured at a binding energy of 529.7 eV (Figure 2-8a,b). A survey scan of the surface indicates that Pt, C, and O are the only three elements present on the sample (Figure 2-8c), confirming that the Pt is sufficiently thick to guarantee no Si substrate is seen. According to the overlayer model, the

intensity of the Pt 4f metallic peaks (Pt⁰), with binding energies of 71.1 and 74.4 eV, are attenuated by a factor of $e^{\frac{-d}{\lambda \cos \theta}}$, where d is the thickness of platinum oxide on platinum, λ is the inelastic mean free path of the photoelectron associated with the Pt⁰ peak through the PtO₂, and θ is the photoelectron take-off angle—set in these measurements to 0° by fixing the electron analyzer normal to the sample surface. The ratio of the Pt⁰ peaks for samples before and after ICP O₂ exposure is directly related to this exponential decay in signal intensity, resulting in the expression for the oxide thickness:

$$d = -\lambda \cdot \ln \left(\frac{Pt_{after\ ICP\ O_2}^0}{Pt_{before\ ICP\ O_2}^0} \right) \quad (2.21)$$

Calculation of the inelastic mean free path can be achieved using predictive formulae such as the approximation published by Tanuma et al. which provides an empirical relation for estimating λ as a function of the photoelectron kinetic energy through a specified material. (Tanuma 1994, Tanuma 2011) The parameters necessary for obtaining mean free path data using this TPP-2M equation are tabulated below in Table 2-4 and include E_k, the photoelectron kinetic energy of the M⁰ metallic bonding state; E_g, the band gap energy for each given oxide; N_v, the number of valence electrons; and λ , the inelastic mean free path of the photoelectron of each metal in its corresponding oxide.

Table 2-4. Parameters necessary for calculation of the photoelectron inelastic mean free path (λ) in metal oxides (Tanuma 2011).

Metal	Pt		Pd		Co		Fe			Cu	
Compound	PtO	PtO ₂	PdO	PdO ₂	CoO	Co ₃ O ₄	FeO	Fe ₂ O ₃	Fe ₃ O ₄	Cu ₂ O	CuO
E _k (eV)	1415.5		1152.0		708.4		779.9			553.6	
E _g (eV)	1.40	1.25	4.50	2.00	2.40	1.96	2.40	2.20	0.10	2.17	1.55
N _v (#)	16	22	16	22	15	51	14	34	48	28	17
Density(g/cm ³)	14.10	10.20	8.30	4.23	6.44	6.11	5.7	5.2	5.0	6.0	6.3
λ (nm)	1.74	1.96	1.82	2.40	1.43	1.47	1.59	1.67	1.67	1.23	1.22

Using the parameters above in conjunction with equation 2.21, the Pt processed in Ar/O₂ discharge shown in Figure 2-8 is measured to generate an oxide layer thickness of approximately 0.6 nm.

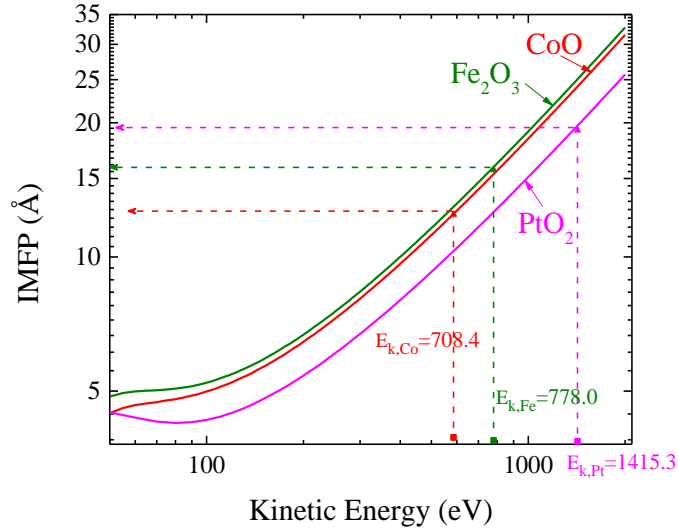


Figure 2-9. Inelastic mean free path for PtO₂, FeO, and CoO as a function of the photoelectron kinetic energy. The kinetic energies of photoelectrons for each of the corresponding metallic bonding states are also shown.

2.7.3 Spectroscopic ellipsometry

Due to the electromagnetic nature of light, it can be described by its electric field behavior in space and time, or polarization. This polarization can change upon interaction between the light and a solid surface or interface. The change caused by this interaction can then be measured and modeled by monitoring both the amplitude (Ψ) and phase (Δ) after the subsequent reflection off of the sample to be studied. Optical constants provide information about the response of the studied material to changes in response to electromagnetic radiation, e.g. incident light, and give details regarding characteristics such as absorptive, reflective, and dispersive nature of the material. These

optical constants can be expressed as either the complex dielectric function shown in equation 2.22 or the complex refractive index shown in equation 2.23.

$$\tilde{\epsilon} = \epsilon_1 + i\epsilon_2 \quad (2.22)$$

$$\tilde{n} = n + ik = \sqrt{\tilde{\epsilon}} \quad (2.23)$$

Through measurement by SEM to confirm the thickness of various thin films of CoFeB, it is possible to develop a unique model capable of fitting a variety of thicknesses below 100nm using a Bruggeman Effective Medium Approximation (EMA). This type of model weights the constituent elements in accordance with their respective volume fractions and dielectric functions. For a three part model, such as the one developed for CoFeB thin films, the model can be expressed mathematically as seen in equation 2.24.

$$f_{Co} \frac{\tilde{\epsilon}_{Co} - \tilde{\epsilon}}{\tilde{\epsilon}_{Co} + 2\tilde{\epsilon}} + f_{Fe} \frac{\tilde{\epsilon}_{Fe} - \tilde{\epsilon}}{\tilde{\epsilon}_{Fe} + 2\tilde{\epsilon}} + f_B \frac{\tilde{\epsilon}_B - \tilde{\epsilon}}{\tilde{\epsilon}_B + 2\tilde{\epsilon}} = 0 \quad (2.24)$$

Further extending this model incorporates a depolarization factor, DF, which is capable of accounting for changes in geometry that could affect the polarization of incident light. By assuming a factor of 0.333, the distinct shape of the film material is assumed to be spherical. In general, it is useful to use the Bruggeman EMA for measuring films greater than 3 nm as it captures some of the roughness effects as well as intermixing between layers (Nguyen 1993, Cheng 2008). The model used for characterizing these films is a JA Woollam M88 Spectroscopic Ellipsometer capable of measuring a spectral range between 280 and 760 nm. Figure 2-10a details the dependence of the refractive index (n) and extinction coefficient (k) at the corresponding wavelengths of 280 through 760 nm.

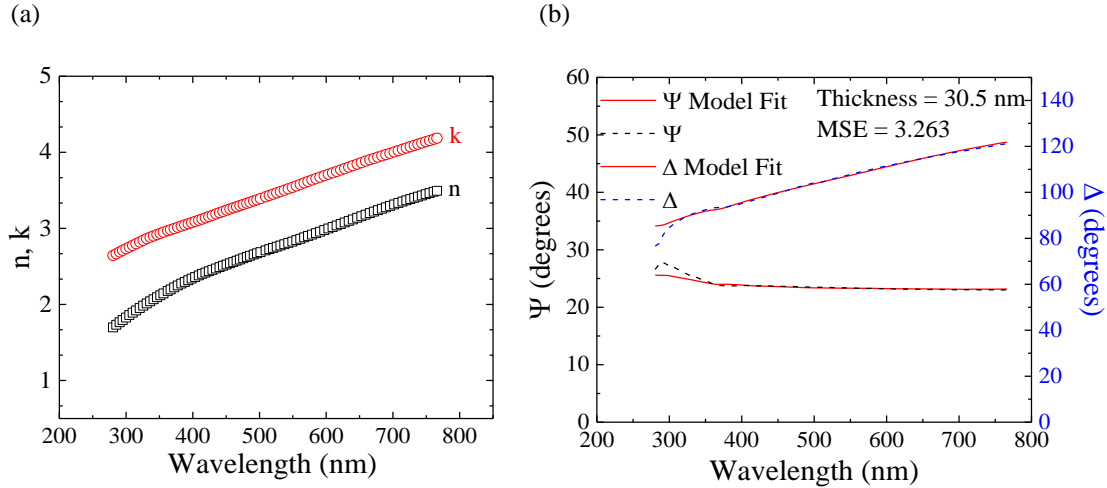


Figure 2-10. (a) Extinction coefficient (k) and refractive index (n) as a function of wavelength for CoFeB using Bruggeman Effective Medium Approximation and (b) measured amplitude (Ψ) and phase (Δ) data for a 30nm CoFeB film with corresponding Ψ and Δ model fitting.

Figure 2-10b shows the model fit developed using thin films of CoFeB between 10 and 30 nm for use in etching experiments. It is worth noting that the drawbacks typically suffered by ellipsometry include distinct susceptibility to surface roughness as well as composition. Due to the nature of the dielectric function of the material depending strongly on the variation in composition across nominal films such as CoFeB, one model may fit a film which contains specific ratios of each of the three elements. Additionally, at greater thicknesses, metallic and intermetallic films can, at times, become too reflective to secure an accurate measurement using this technique. Thus it is essential that measurements be occasionally double checked using secondary methods such as SEM to ensure the consistent validity of the developed model. For the metallic films in general, the lower reported MSE, or mean squared error, reported by the fitting describes the “goodness of fit” of the constructed model and can be calculated by using equation 2.25.

$$MSE = \sqrt{\frac{1}{2n - m - 1} \sum_{i=1}^n [(\Psi_i^{cal} - \Psi_i^{mea})^2 + (\Delta_i^{cal} - \Delta_i^{mea})^2]} \quad (2.25)$$

where Ψ_i^{cal} , Ψ_i^{mea} , Δ_i^{cal} , and Δ_i^{mea} are the calculated and measured amplitudes and phases, respectively, and n and m are the number of data points and analytical parameters. Maximum values of the MSE are limited to around 10 to substantiate a well-fit model and provide good empirical thickness measurements. Single element thin films of Co, Fe, Pd, Pt, and Cu have been measured at thicknesses up to and including 50 nm with mean squared error values below 5. The constructed model shown for CoFeB in Figure 2-10b has a calculated MSE of 3.263 and was corroborated at a thickness of 32 nm through cross sectional SEM measurements.

2.7.4 Contact profilometry

Contact profilometry is a thickness measurement method with the ability to measure features with sizes between a few nanometers to 1 millimeter using a stylus which is dragged across the sample surface at a fixed rate and force. The resolution of the measurement is directly affected by the amount of force and speed with which the stylus moves across the surface. Changes in the height of the stylus are measured by a transducer, converting the physical output of the stylus arm into an electrical signal to be read by the computer interfaced with the profilometer. For these studies, a VeecoTM Dektak 6M Surface Profilometer was used with a 12.5 μm diamond stylus, capable of measurements of aspect ratios up to 1:1. The scan length may be set from 3 to 100 seconds, with horizontal resolution of 0.07 to 2.22 μm , respectively. In general, the scan length is set between 30 and 45 seconds, yielding a resolution of 0.18 to 0.15 μm .

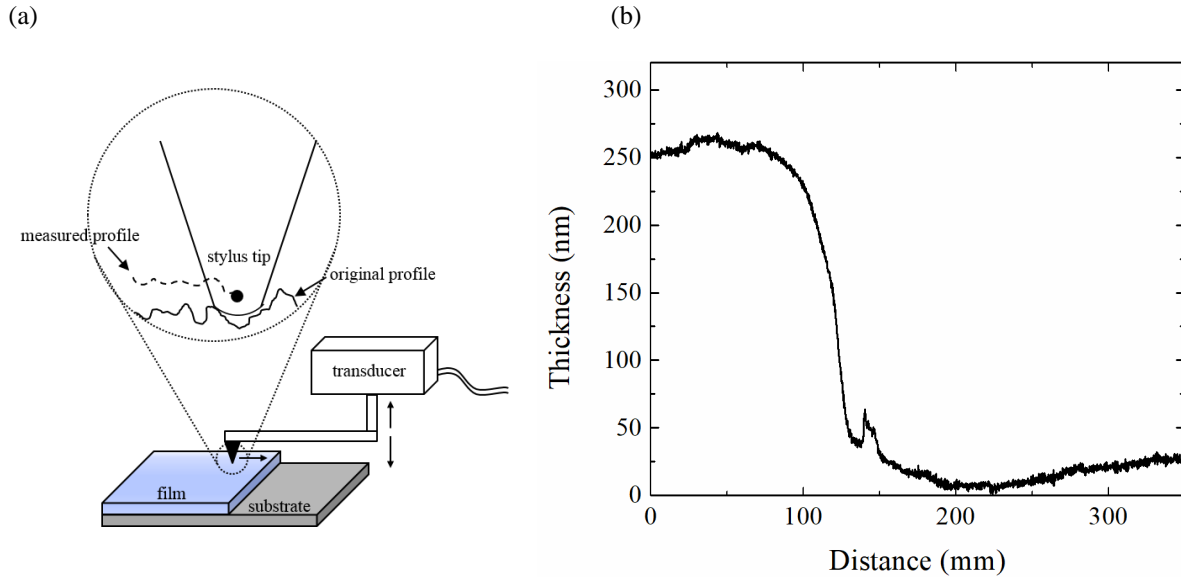


Figure 2-11. (a) Schematic of contact profilometer with an enlarged portion detailing the contact of the stylus tip with the original sample surface, and (b) raw data of a profilometry scan performed on 250 nm CoFeB after etching in 500 W Ar plasma with 50 W bias power for 1 minute.

Masking one portion of the sample and etching the unexposed portion results in the creation of a vertical step measurable using the profilometer. Masking tape is removed from the sample, leaving a much thicker unetched portion next to the etched film. As can be seen from the data for 250 nm CoFeB in Figure 2-11b, the decrease in thickness is not instantaneous over a large distance likely due to the act of peeling off the Kapton[®] tape and causing a small amount of film delamination or adhesive residue. The small peak seen between 140-150 mm is likely residue from the Kapton[®] or small particulates lying at the interface between the etched and unetched films. Contact profilometry provides a means of performing a direct physical measurement of an etched film by monitoring the height change as the stylus is moved over the film surface.

2.8 Etch Product Identification

Characterization of the post-etch solution can yield important information regarding which chemistries are effective at removing material. Additionally, through further analysis data can be quantified to determine the effective concentration of materials of interest. The subsequent section serves as a description of both the operating principle behind, and subsequent analysis of post-etch solutions using mass spectrometry to characterize the amount of etched material present within solution collected after solution phase etch experiments.

2.8.1 Inductively coupled plasma mass spectrometry (ICP-MS)

ICP-MS is a mass spectrometry technique which utilizes a high temperature inductively coupled plasma and is capable of breaking up complex molecules into their constituent atomic species. Argon is often chosen as the carrier gas for introduction of a liquid sample via generation of an aerosol. Once the plasma has been ignited, the argon is ionized, resulting in Ar^+ , which can subsequently ionize the neutral species. These ionized species are then fed in the form of an ionized beam from the ICP torch, through a lens with a shadow stop which functions to block photon emission from the plasma. The species pass through a small orifice known as a skimmer cone, ultimately through a secondary sampler cone. These passes result in pressure reduction of the sample stream to 10^{-5} Torr. To ensure no clogging of the skimmer cone occurs, dilution of the sample solution is required. The final stream of ions is focused by an electrostatic lens into the aperture of the quadrupole mass spectrometer, allowing for only species with specific mass-to-charge ratio to pass through the rods and reach the detector. This process is summarized in Figure 2-12a.

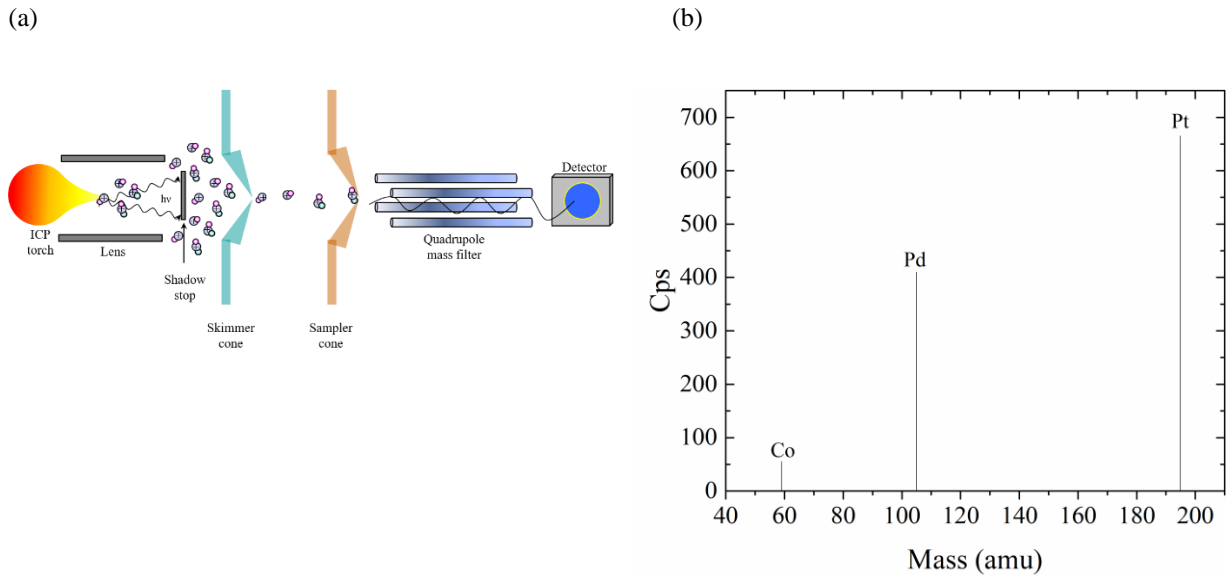


Figure 2-12. (a) Schematic of ICP-MS operation, and (b) raw data from characterized post-etch solution of 95% formic acid used in 10 min liquid phase etching of chlorinated Pd, CoPd, and CoPt thin films.

The resulting data are comprised of the masses of ions striking the detector located at the final portion of the spectrometer. These typically appear in the form of counts per second located at various ion masses tuned to by the resulting potential applied to the quadrupole filter. The ICP-MS used in this study was a PerkinElmerSCIEX™ Elan DRC II. Argon was used as the carrier gas with a 20 l/min flow rate and 175 μ l/min sample solution uptake rate.

Sample preparation is critical for proper characterization of post-etch solutions through ICP-MS. At excessively high concentrations, excess sample species may block the skimmer cone orifice and potentially contaminate the ICP-MS. On the other hand, too low of a concentration may result in the inability of the detector to distinguish dissolved species from background noise. The instrumental detection limit, or IDL, is the lower limit of detection for specific elements in an ICP-MS (Figure 2-13). In these studies, a standardized sample size of 7 cm \times 10 cm and 10 ml solution volume were used. Pt (30 nm), CoPd (30 nm), and Pt (20 nm) films were first exposed for five

minutes to Cl₂ plasma at 200W source power and 10W bias power. The samples were then submerged in 95% formic acid for 10 minutes at 80 °C. Post-etch solutions were then stored in metal-free polyethylene 50 ml vials with a 1:10 dilution ratio to ensure no contamination from the container during storage.



Figure 2-13. Periodic table of elements measured by ICP-MS along with their corresponding detection limit ranges for ELAN series mass spectrometers. All of the elements studied in this work have limit ranges between 0.1-10 parts per trillion. (Image courtesy of PerkinElmer, Inc.)

ICP-MS was used to determine whether the modified metal and intermetallic thin films, such as Pd, CoPd, and Pt surfaces, once chlorinated or oxidized, could be solvated and removed in the formic acid environment at increased temperatures. By comparison to the detection limits for the three elements—0.03 µg/l for Co, 0.39 µg/l for Pd, and 0.14 µg/l for Pt—it was determined that the resulting data showed a substantial amount of all three metals compared to a standard

formic acid blank taken from the stock solution. The post etch solution was determined to have concentrations of the following: 2.61 $\mu\text{g/l}$ Co, 2.72 $\mu\text{g/l}$ Pd, and 2.76 $\mu\text{g/l}$ Pt while the formic acid stock solution used as the control contained 0.08 $\mu\text{g/l}$ Co, 0.39 $\mu\text{g/l}$ Pt, and Pd concentrations below the limit of quantification (0.39 $\mu\text{g/l}$).

2.8.2 Electrospray ionization mass spectrometry (ESI-MS)

Identification and measurement of etch products is key to validating the thermodynamic assessment developed in this work as well as fully understanding the reaction mechanism and determining which chemistries are most effective in material removal. Compared to the previously discussed ICP-MS, which is effective at determining concentrations of atomic species such as metals through the use of “hard” ionization techniques such as an inductively coupled plasma, ESI-MS is generally seen as a “soft” ionization and mitigates fragmentation commonly seen in other mass spectrometry techniques resulting in the ability to measure larger complexes.

The solution phase sample is contained within a capillary tube resulting in a meniscus at the open end. Application of a high voltage results in a Taylor cone which emits a jet of liquid droplets, from which excess solvent evaporates, forming a charged aerosol. As the evaporation process continues, the droplets become increasingly unstable due to charge-charge repulsion, ultimately deforming and exploding into smaller droplets with greater stability. This process repeats until only ions remain, which subsequently travel into a mass spectrometer for analysis. The formation of this Taylor cone, jet, and subsequent plume has been captured using high speed photography. ESI-MS is useful for determining the solution phase etch products of metalorganic etch products such as those seen in solution phase etch of metallic thin films. ESI-MS was used for detection and confirmation of the efficacy and selectivity of etching iron in hexafluoroacetylacetone (hfac) solution heated to 80 °C over cobalt films at the same condition.

The sample spectra shown in Figure 2-14b summarizes the characterization hfac solutions after immersion of Co and Fe films with a scanning range of 674-684 amu. The $\text{Co}(\text{hfac})_3$ complex, with a mass of 683 amu is not detected; however, $\text{Fe}(\text{hfac})_3$ with a mass of 680 amu is measured with a high normalized intensity. The isotope distribution corroborates the presence of a small amount of ^{54}Fe and ^{57}Fe in addition to the abundant ^{56}Fe . In each case, mass spectrometry relies on the ability to ionize the complexes in solution and subsequently detect these ions using, in many cases, a quadrupole mass spectrometer to achieve high resolution in filtering ions of different mass-to-charge ratios.

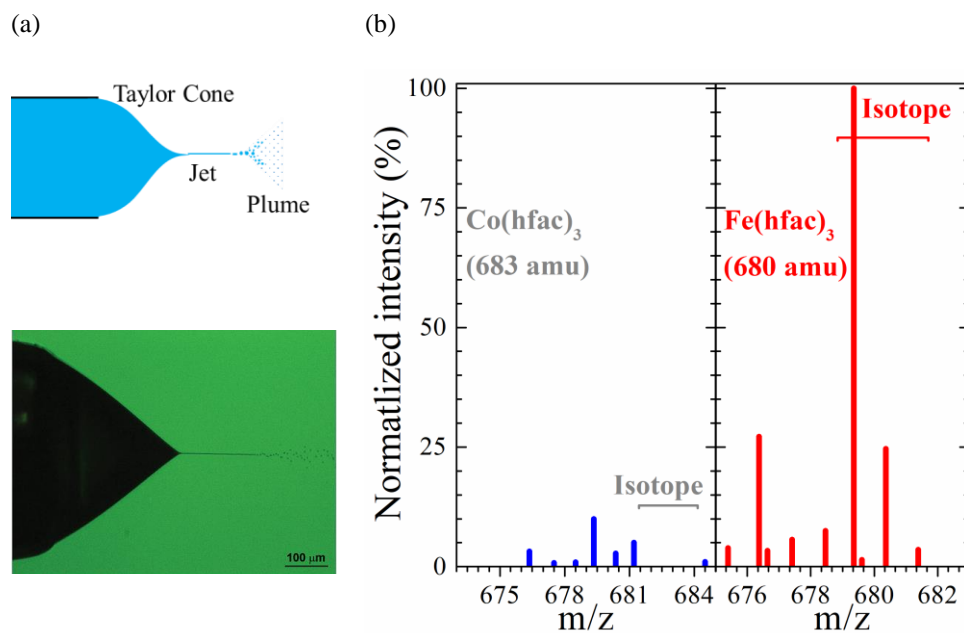


Figure 2-14. (a) Schematic and high speed photograph of Taylor cone, jet, and plume formation for ESI-MS sample introduction (Nemes 2007) and (b) sample spectra of hexafluoroacetylacetonate solution after etch of Co and Fe thin films, indicating substantial amount of $\text{Fe}(\text{hfac})_3$ complex in solution with the corresponding isotope pattern. (Chen 2017)

2.8.3 Quadrupole mass spectrometry

Within the studies presented in this work, mass spectrometry serves as an important tool for analyzing the composition of species within a plasma. Whereas OES served to identify specific electronics transitions, QMS is capable of measuring detailed compositional analysis of larger and more complex molecular species with a range of masses. The operating principle of mass spectrometry relies on the ability to filter charged species using a variable magnetic field, allowing species with a fixed mass to charge ratio (m/z) to be focused into a collector, resulting in spectra dependent only on mass.

The mass spectrometer utilized in these studies was a UTI 100C line-of-sight quadrupole mass spectrometer connected to a 4.625" CF port on the inductively coupled plasma reactor and evacuated by a Leybold 361C turbomolecular pump. A 0.065 inch diameter orifice allows for ions to pass from the discharge in the upper ICP chamber to the QMS. Neutral species from the discharge are ionized via thermionic emitted electrons sourced from a filament with a -70 V potential and 1.0 mA current. The quadrupole consists of a square array of four parallel metal rods. A maintained RF/DC field acts as a mass filter while simultaneously increasing collector sensitivity and analysis speed.

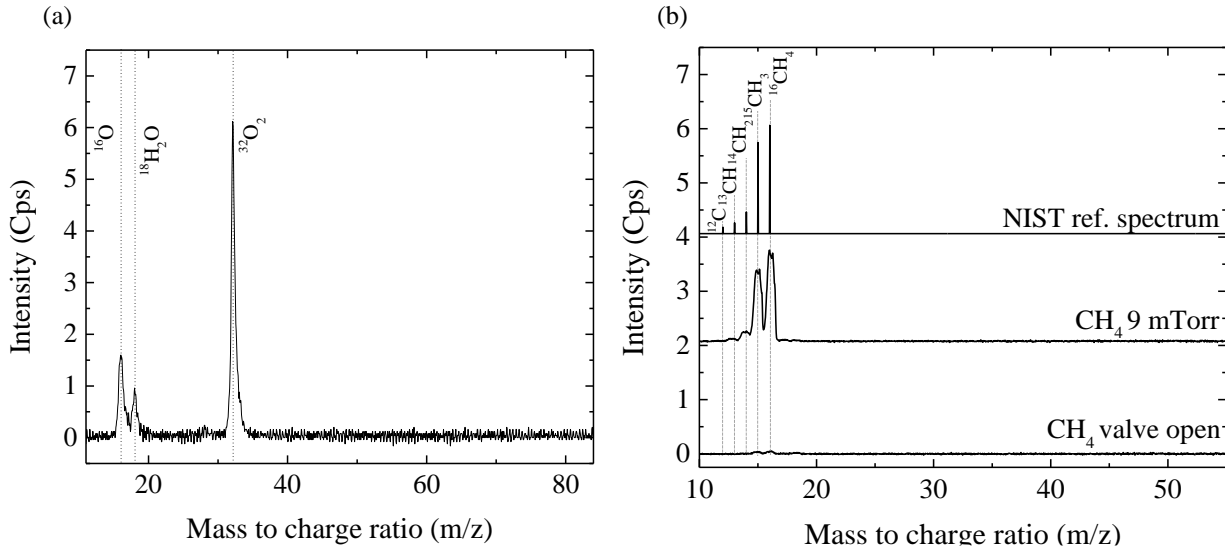


Figure 2-15. Mass spectra of (a) inductively coupled O₂ plasma at 500 W source power, 0 V applied bias, and 16 mTorr indicating presence of main ¹⁶O and ³²O₂ species as well as residual water (¹⁸H₂O) and (b) CH₄ after opening the gas line valve and in an inductively coupled CH₄ plasma at 500 W source power, 0 V applied bias and 9 mTorr indicating characteristic cracking pattern. All sets of data are collected with the ionization filament current (I_{fil}) of 1.0 mA and a 70 V potential.

QMS systems are sensitive to detection of naturally occurring isotopes, such as processing gases like O₂. Oxygen exists mainly as diatomic ³²O₂, comprised of two ¹⁶O atoms (Figure 2-15a). Furthermore, mass spectrometry can detect small amounts of water (¹⁸H₂O), generally due to the exposure of a chamber to atmosphere. Furthermore, for hydrocarbons such as CH₄, mass spectrometry can resolve the cracking patterns characteristic of these molecules through deprotonation and subsequent formation of CH₃, CH₂, and CH species in the gas phase (Figure 2-15b). Additionally, there exists an inverse relationship between the mass to charge ratio of species detected using QMS and the sensitivity of the spectrometer. For quantitative analysis of mass spectrometry data to be accurate, the sensitivity change in relation to mass to charge ratio must be determined. The following relationship has been obtained for this instrument as follows:

$$I \propto \frac{1}{m_c^k} \quad (2.16)$$

where I is the signal intensity, m_c is the mass to charge ratio (m/z), and k is a constant which varies between 1.0 and 1.2. (Chae 2003)

2.9 Plasma Diagnostics

Discharges used for plasma processing of materials can be characterized using a number of different methods. These methods operate using a variety of principals and have specific aims. The analytical techniques mainly used for plasma diagnostics in this work include the Langmuir probe, optical emission spectroscopy (OES), and quadrupole mass spectrometry (QMS) which allow for measurement of the electron temperature, plasma potential, and species present within the discharge.

2.9.1 Langmuir probe

The Langmuir probe was developed by Irving Langmuir in 1924 and was utilized for measuring electron density (n_e), space potential (V_s), and electron temperature (T_{eV}). Probes are metallic and typically made in spherical, cylindrical, or planar geometries, and immersed in the discharge. An external power supply is used to apply a potential (V_p) to the probe. The current measured on the probe (I_p) is a result of the difference between the plasma potential (V_{sp}) and V_p . V_p can be varied across a range of voltages to generate a characteristic current-voltage, or I-V, curve. This I-V curve can be further analyzed to extract plasma parameters such as those mentioned above. An ESPIon Langmuir probe manufactured by Hiden Inc. was used for these studies, and consists of a 3 mm long and 0.075 mm radius cylindrical tungsten tip biased from -200 V to +100 V in steps of 0.1 V, resulting in a current between -100 mA to 1000 mA.

The assumption of an idealized non-equilibrium plasma with a collisionless sheath and Maxwellian electron energy distribution is invoked. Additionally, it is assumed that the mean free path of all particles within the discharge are greater than the radius of the Langmuir probe and Debye length, and that the electron temperature is substantially higher than the ion and neutral temperatures. The electric potential of the point locally within the discharge is given by V_{sp} and results in a probe current of I_p , which is the sum of both the ion current (I_i) and electron current (I_e), expressed as $I_p = I_i + I_e$.

When a large negative bias is applied, namely that $V_p \ll V_{sp}$, electrons are repelled from the probe, ions are attracted, and the dominance of the ion current in the value of I_p is observed. At this bias value, the ion saturation current, or I_{is} , is measured. In contrast, when a large positive bias is applied, such that $V_p \gg V_{sp}$, ions are repelled, electrons are attracted to the probe, and the electron saturation current, I_{es} , is measured. When the applied potential is equal to the plasma potential, or $V_p = V_{sp}$, no current is measured through the probe, and the floating potential is obtained wherein the ion current and electron current contributions are equal. These regimes are summarized in the sample I-V curve shown in Figure 2-16. Mathematically, one can determine the space potential more accurately through differentiation of the I-V curve at the point where the electron current begins to deviate from exponential growth, namely where dI_e/dV is at a maximum and d^2I_e/dV^2 is equal to zero. (Chen 2012)

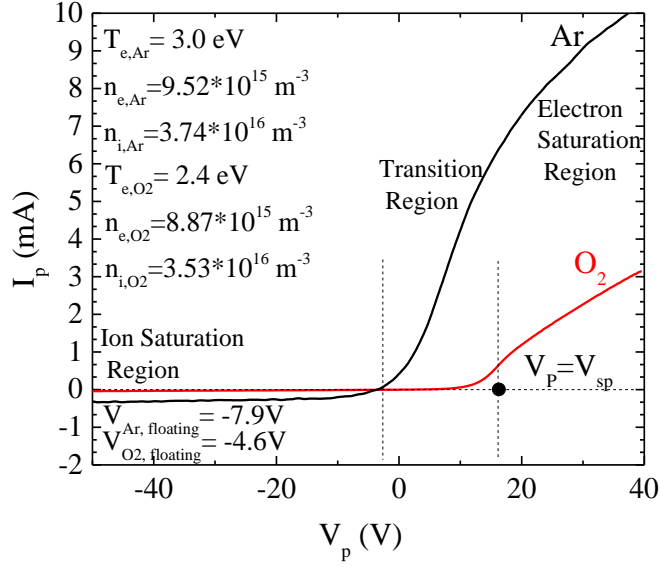


Figure 2-16. Sample I-V curves for inductively coupled Ar (black) and O₂ (red) plasmas taken from ICP reactor described previously at 500 W source power, 0 V bias voltage, and 10 mTorr pressure.

When the electron temperature is higher than that of the ions ($T_{eV} > T_i$), the ion saturation current can be calculated from T_{eV} using the equation,

$$I_{is} = I_{Bohm} = 0.6en_i \sqrt{T_{eV} / m_i} A_{probe} \quad (2.3)$$

When the probe has a different potential compared to the local plasma potential, electrons and ions distribute spatially around the probe to shield this potential from the bulk plasma. Electron shielding would surround the positively biased probe, while positive space charge would surround a negatively biased probe. The characteristic shielding distance for a negatively biased probe can be captured by the Debye length λ_D , expressed as,

$$\lambda_D = \sqrt{\left(\frac{\epsilon_0 T_{eV}}{e^2 n_e} \right)} \quad (2.4)$$

Positive space charge only forms when the density of ions is greater than that of the electrons at the sheath edge, where the ion velocity is greater than the Bohm velocity, $u_B = \sqrt{T_{eV} / m_i}$. In order for the ions to achieve this velocity, they must overcome a potential decrease equivalent to $0.5(kT_e / e)$.

On the other hand, the electron current (I_e) can be expressed as a function of the applied voltage (V_p) in two different scenarios,

$$I_e(V_p) = I_{es} \exp[-e(V_{sp} - V_p) / kT_e], \text{ when } V_p \leq V_{sp}, \quad (2.5)$$

and

$$I_e(V_p) = I_{es}, \text{ when } V_p > V_{sp}, \quad (2.6)$$

The electron saturation current is given by,

$$I_{es} = \frac{1}{4} en_e v_{e,th} A_{probe} \quad (2.7)$$

where n_e is the electron density, $v_{e,th} = \sqrt{8kT_e / \pi m_e}$ is the thermal velocity of the electron, m_e is the electron mass, k is the Boltzmann constant, and T_e is the electron temperature. Since the discharge is assumed to be quasineutral, the electron and ion densities are similar. Additionally, since the ion mass (m_i) is substantially greater than the electron mass (m_e), the resulting electron saturation current is greater than the ion saturation current. Using the sample I-V curves shown in Figure 2-16, T_{eV} , n_e , and n_i were calculated to be 2.4 eV, $8.9 \times 10^{15} \text{ m}^{-3}$, and $3.5 \times 10^{16} \text{ m}^{-3}$, respectively for inductively coupled O_2 plasma and 3.0 eV, $9.5 \times 10^{15} \text{ m}^{-3}$, and $3.7 \times 10^{16} \text{ m}^{-3}$ for inductively coupled Ar.

2.9.2 Optical emission spectroscopy

The presence and interaction of plasma species such as electrons, ions, and neutrals results in the creation of particles with a number of excited electronic states. Photon emission from these particles occurs upon relaxation and are characteristic of specific transitions in the discharge species, related to the change in quantum energy states of the electron. This measured energy can be used to identify species within the plasma through translation into a wavelength of emitted light. Optical emission spectroscopy is advantageous due to its non-intrusive nature and has been used to monitor plasma etching endpoints, quantify relative species concentrations, calculate the reaction kinetics through a method known as actinometry, and obtain information on plasma parameters such as electron temperature, electron density, and the electron energy distribution. (Flamm 1981, Donnelly 2000, Donnelly 2013)

An Ocean Optics S2000 was used in these studies to measure emission intensities across a wavelength range of 200-1000 nm. The system is comprised of five fiber optic cables, labeled Master and Slaves 1-4, which are connected to an analyzer which interfaces with a personal computer through a universal serial bus connection. The fiber optic cables are attached to the opening in the RF coil cage through a machine Teflon cover. Optical emission spectra are gathered over the experiment time. Use of OES as an endpoint detector can be leveraged by measuring observed emissions, such as those from the substrate in the form of atomic Si. Actinometry can also be used to quantify species concentrations as follows. The measured emission intensity (I_λ) is related to the radical concentration (n_A) in electron impact excitation as,

$$I_\lambda = \alpha_{\lambda A} n_A \quad (2.8)$$

where $\alpha_{\lambda A}$ is defined as,

$$\alpha_{\lambda A} = k_D(\lambda) \int_0^{\infty} 4\pi v^2 dv Q_{A^*}(p, n_e) \sigma_{\lambda A}(v) v f_e(v) \quad (2.9)$$

where $\sigma_{\lambda A}$ is the cross section for the emission of a photon having wavelength λ due to electron impact excitation of A to A^* , k_D is the detector response constant, Q_{A^*} is the quantum yield for photon emission from the excited state, and f_e is the electron energy distribution function. It is impossible to solve directly for n_A due to the inability to measure these values.

To remedy this issue, a trace amount—generally less than 5% of total gas flow—of a known concentration of inert gas actinometer, T, is fed into the discharge. An excited state with a similar excitation threshold energy and emission line close to that of the radical, A, is chosen. The intensity of the emission line from the actinometer is analogous to the first set of equations for radical A:

$$I_{\lambda'} = \alpha_{\lambda T} n_T \quad (2.10)$$

where,

$$\alpha_{\lambda T} = k_D(\lambda') \int_0^{\infty} 4\pi v^2 dv Q_{T^*}(p, n_e) \sigma_{\lambda T}(v) v f_e(v) \quad (2.11)$$

Since only the energetic tail of the electron energy distribution is above the threshold energy for photon emission cross sections, the cross sections near the threshold energy can be approximate as linear functions of electron velocity:

$$\sigma_{\lambda A} \approx C_{\lambda A} (v - v_{thr}) \quad (2.12)$$

and,

$$\sigma_{\lambda T} \approx C_{\lambda T} (\nu - \nu_{thr}) \quad (2.13)$$

where $C_{\lambda A}$ and $C_{\lambda T}$ are proportionality constants. The radical density can then be expressed using the ratio of the two emission line intensities as,

$$n_{\lambda} = C_{AT} n_T \frac{I_{\lambda}}{I_{\lambda'}} \quad (2.14)$$

where,

$$C_{AT} = \frac{k_D(\lambda) Q_{A^*} C_{\lambda A}}{k_D(\lambda') Q_{T^*} C_{\lambda T}} \quad (2.15)$$

If the chosen emission wavelengths are similar to each other, i.e. $\lambda' \sim \lambda$ and $Q_{A^*} \sim Q_{T^*}$, then $C_{AT} \sim C_{\lambda A}/C_{\lambda T}$ can be determined and an absolute value of the radical density n_A can be calculated.

(Coburn 1980)

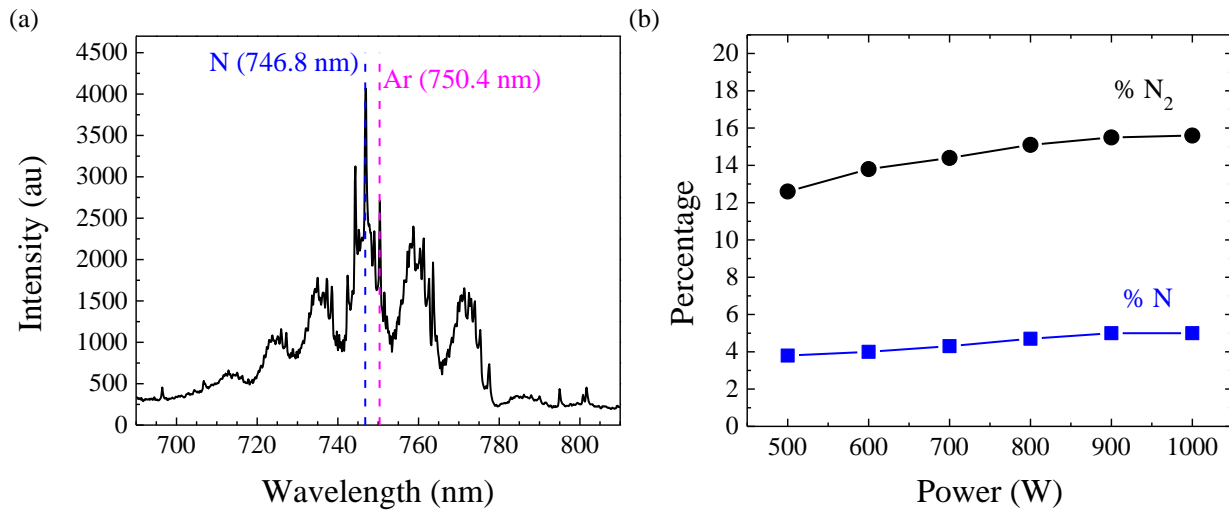


Figure 2-17. (a) Optical emission spectrum for inductively coupled N₂ plasma at 500 W source power, 0 V applied bias, 6 mTorr, and 5% Ar actinometer feed and (b) calculated percentage of excited molecular N₂ and atomic N increasing as a function of increasing source power.

In this work the actinometer used is 5% argon in the inlet gas feed. An example of an inductively coupled N₂ discharge with a 5% argon actinometer feed is shown in Figure 2-17a. The emission line for atomic N was chosen at 746.8 nm due to its proximity to Ar at 750.4 nm. Molecular N₂ and atomic N concentrations were calculated and shown to increase upon increasing source power from 500 W to 1000 W (Figure 2-17b).

2.10 Thin Film Analysis

For the studies done in this work, it is necessary to understand the state in which the chosen materials, in this case a range of metallic and intermetallic compounds used in the fabrication of MRAM, are modified. This section serves as an introduction to the techniques employed for determining the chemical composition, magnetic properties, morphology, and thickness of these films. In addition, the purpose, underlying operation, and examples of data analysis for each technique has been provided.

2.10.1 X-Ray photoelectron spectroscopy

X-Ray Photoelectron Spectroscopy (XPS) is a surface analysis technique that is used to determine the chemical composition and bonding states of atoms in a thin surface layer (7-10 nm thick). Samples are bombarded with x-rays, causing core shell electron emission. By measuring the kinetic energy of these electrons, the ionization potential or binding energy can be derived using the following equation:

$$E_k = h\nu - E_b - \Phi \quad (2.17)$$

where E_k is the kinetic energy of the electron, $h\nu$ is the energy of the incident radiation, E_b is the characteristic binding energy of the electron, and Φ is the work function of the spectrometer (Hagström 1964). XPS can also be used to obtain information about the local structure of solid

surfaces. The immediate environment, charge and oxidation state of a particular atom can all have effects on the binding energies of its electrons. By comparing the shift in energy of an atom relative to a standard value, specific details about the aforementioned parameters can be deduced. The integrated intensity of a specific peak is proportional to the number of photoelectrons per second from that peak, given by the following equation:

$$I = nf\sigma\theta y\lambda AT \quad (2.18)$$

where n is the number density of atoms of that element in the sample, f is the x-ray flux, σ is the photoelectric cross-section for the atomic orbital of interest, θ is the angular efficiency factor for the instrumental arrangement, y is the efficiency of the photoelectric process for formation of photoelectrons with the normal photoelectron energy, λ is the mean free path of the photoelectrons in the sample, A is the area of the sample from which photoelectrons are detected, and T is the detection efficiency. If rearranged in terms of the density:

$$n = \frac{I}{f\sigma\theta y\lambda T} = \frac{1}{S} \quad (2.19)$$

where the denominator is defined as the atomic sensitivity factor S and used only in calculations involving a ratio of sensitivity factors. S can vary from film to film but the ratio is unaffected. The atomic fraction of an element in the film can then be determined from the fraction of corrected integrated intensity of one peak from the element of interest over the summed corrected integrated intensities of each peak from all of the elements in the film as shown in the following equation:

$$C_x = \frac{n_x}{\sum_i n_i} = \frac{I_x / S_x}{\sum_i I_i / S_i} \quad (2.20)$$

Atomic sensitivity factors are XPS equipment-dependent, however, the elements encountered in this study are tabulated along with their corresponding reference binding energies

in Figure 2-18b. As the XPS sample is bombarded with x-rays, the overhead analyzer collects a spectrum based on the number of counts detected at a specific binding energy. Using these counts, a spectrum is constructed either for a survey scan, which generally captures a rough spectrum of the entire range of binding energies, typically from 1200 eV to 0 eV, or a detailed elemental scan with a much narrow window generally on the order of 40-50 eV.

Detailed XPS spectra for the Co 2p, Fe 2p, Cl 2p, and B 1s can be found below in Figure 2-18a for CoFeB thin films etched via Cl₂ and sequential Cl₂/H₂ plasma exposure. Since the main goal of this work is to understand the different metallic and oxidized bonding states of thin films, one can qualitatively characterize the emergence and disappearance of oxidized metallic species in the form of, for example, metal or boron chlorides. Furthermore, by utilizing equation 3.19, and performing a Gaussian-Lorentzian fit to the peaks present within the spectrum, the film can be decomposed into the corresponding bonding states of each scanned element.

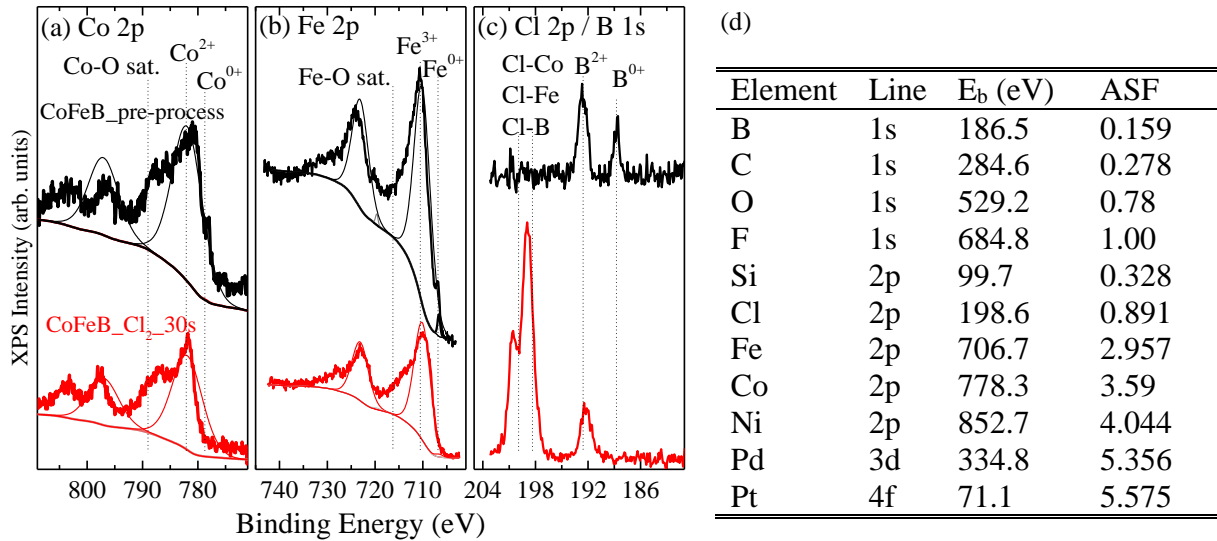


Figure 2-18. High resolution x-ray photoelectron spectra of (a) Co 2p, (b) Fe 2p, and (c) Cl 2p and B 1s for 30 nm CoFeB before processing (black), after 30 second exposure to Cl₂ plasma (red) as well as (d) binding energies of interest for constituent elements studied in this work.

2.10.2 Superconducting quantum interference device (SQUID)

In order to characterize the magnetic property of thin films, one can utilize a superconducting quantum interference device (SQUID) as an extremely sensitive magnetometer capable of measuring ultra-small magnetization signals. The enabling phenomenon behind SQUID operation is the Josephson junction, which is comprised of a superconducting loop separated by two thin parallel pieces of non-superconducting material through which electrons tunnel in the form of Cooper pairs. These Cooper pairs are a single pair of electrons that are bound together in a very low energy state that allows for long range interaction on the order of hundreds of nanometers (Allender 1973). The low energy state which these pairs occupy is energetically favorable; however, due to the interaction remaining very weak, i.e. ~ 0.001 eV, even small amounts of thermal energy can break it. A current, I , is applied to the loop, which is split equally across the two parallel branches. If a subtle magnetic field is applied, a resulting screening current I_s is generated to cancel it. This is due to expulsion of the magnetic field by the superconductor due to the Meissner effect (Bardeen 1957). This induced current travels in the same direction as current in one branch, and opposite in the other, causing the total current to become

$$I_1 = \frac{I}{2} + I_s \quad (2.26)$$

and

$$I_2 = \frac{I}{2} - I_s \quad (2.25)$$

Once a critical current is reached, a voltage then appears across the junction that can be measured. If the magnetic flux exceeds $\phi_0/2$, or half of the magnetic flux quantum, the system energetically favors an increase in this value to an integer of ϕ_0 , resulting in the current flipping

direction again. This phenomenon causes the current to oscillate as a function of the applied magnetic flux. Equation 2.27 represents the magnetic flux quantum, where h is Planck's constant and e is the elementary charge.

$$\varphi_0 = \frac{h}{2e} = 2.067833 \times 10^{-15} \text{ tesla-m}^2 \quad (2.27)$$

By maintaining a constant current within the SQUID, the measurable voltage fluctuates at each of the two Josephson junctions, allowing for the oscillation to be correlated to the amount of magnetic flux through the sample. The resultant voltage change is dependent on the resistance, R , and the loop's inductance, L , as well as the change in the magnetic flux quantum, $\Delta\varphi$.

$$\Delta V = \frac{R}{L} \Delta\varphi \quad (2.28)$$

To measure the magnetic responses via SQUID, the sample is first moved up and down between two electromagnets that change the applied field. A pair of sensory coils around the sample then measure the voltage. For these measurements, a Quantum Design Magnetic Property Measurement System (MPMS) XL was used. A single scan begins at large, positive applied field values, which are then decreased to small, negative values and once again increased to the initial applied field value. Upon closure of this loop the film is saturated, and the dependence of magnetization on applied field becomes linear. A positive linear response indicates paramagnetic behavior, while a negative linear response indicates diamagnetic behavior. Due to the paramagnetic nature of air, the raw SQUID scan exhibits a positive linear response with regards to the applied field after the loop is closed and just before the film reaches saturation magnetization. A linear fit of the three values in the positive linear regime is first performed to obtain a slope detailing the dependence of magnetization on applied field. This slope is multiplied by the difference between the raw moment and each field value, leaving only the ferromagnetic

response of the characterized film. Material volume is calculated from thickness and area measurements and used to normalize the magnetization. The resulting figure from these measurements produces a hysteresis loop showing magnetization (\mathbf{M}) as a function of the applied field (\mathbf{H}). From this hysteresis loop, static magnetic properties such as the coercivity (H_c) and the saturation magnetization (M_s) can be extracted. Coercivity indicates the stability of the magnetization in the chosen direction of the measurement by determining the effective field necessary to change the magnetization direction of domains within the material. Saturation magnetization represents the maximal field strength necessary to completely change the magnetization direction of all domains present in the sample, resulting in no additional measurable magnetic response from the material past a specific field strength. The value of the H_c is quantified by determining the intersection of the hysteresis curve with the x-axis intercept at $M/M_s=0$. The value of the applied field, represented as the x value for this intersection, is the value of the H_c . For the ferromagnetic materials studied in this work, the coercivity was measured using the x-axis intercept methodology described above using the left half of the hysteresis loop. The M_s is determined mathematically by calculating the magnetization value where the instantaneous rate of change of the magnetization with respect to the applied field is equal to zero, or $dM/dH=0$,

indicating that no further applied field can cause a measurable change in the material magnetization.

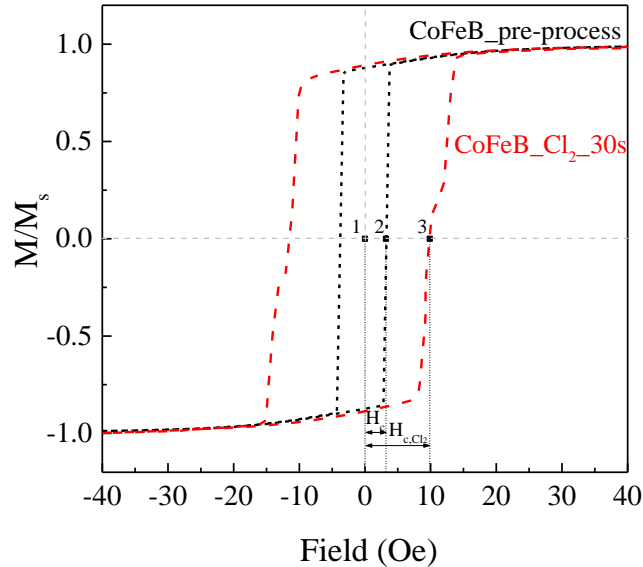


Figure 2-19. SQUID magnetometer hysteresis loop measurement of 30 nm CoFeB before plasma treatment (black, dotted) and post 30 s exposure to 500 W_s Cl₂ plasma (red, dashed). The total magnetization measured by the SQUID magnetometer is normalized by the saturation magnetization (M_s) and shown on the y-axis with the applied field shown on the x-axis. The coercivity, H_c, is measured as the absolute value difference between 0 Oe field value (point 1) to the intersection of the sample hysteresis with M/M_s=0 value (point 2), and indicates the field necessary to change the magnetization direction. The measurement has been repeated and shown for the coercivity (H_{c,Cl₂}) of the sample exposed to 30 s Cl₂ plasma as the absolute value difference between points 1 and 3.

From Figure 2-19, which represents the magnetization of a CoFeB film normalized by the saturation magnetization, the change in static magnetic properties upon exposure of the CoFeB film to a 300W_s Cl₂ plasma can be quantified. With the blank CoFeB film, a H_c of 4 Oe is measured to be necessary to change the direction of the magnetically polarized domains. After a 30 second exposure to chlorine discharge, a change in the magnetic properties is observed with the H_c increasing to 10 Oe due to the formation of metallic chlorides on the surface of the film, making

the material magnetically “hard” relative to the pre-processed sample. By measuring the H_c both before and after modification chemistries, SQUID data can be correlated to surface modification chemistries employed in atomic layer etching.

Chapter 3 : Organic Chemical Etch of Cu and CuO

In this chapter, etching of copper was investigated first using a thermodynamic analysis framework previously validated in literature using Cl_2 and H_2 chemistries. Organic solution phase etch of metallic copper films was observed to occur due to the thermodynamic favorability of the formation of $\text{Cu}(\text{acac})_2$ and $\text{Cu}(\text{COOH})_2$ at etch rates between 1-4 nm/min at 80 °C. A chemical contrast was enabled through the oxidation of copper thin films upon exposure to thermal annealing as well as inductively coupled O_2 plasma, resulting in solution phase etch rates of CuO films at rates between 100-550 nm/min for acac, hfac, acetic acid, and formic acid at 80 °C. This large difference in etch rate was exploited to enable an entirely gas phase processing scheme using formic acid vapor at 80 °C. CuO films were measured to etch at a rate of 19 nm/min while no etch was observed for metallic films processed under identical conditions, suggesting a near infinite vapor phase etch selectivity between removing CuO over Cu. By combining plasma oxidation and formic acid vapor exposure, formic acid and acac were measured to have etch rates of 3.7 and 1.3 nm/cycle, respectively. Energy dispersive x-ray spectroscopy was utilized to confirm the chemical removal of the 35 nm Cu layer post-processing. Application of a -100 V bias resulted in directional formation of the modified CuO layer which was subsequently removed during the isotropic etch step, resulting in successful patterning of 70 nm wide Cu lines using this cyclical oxidation and chemical vapor etch process in conjunction with a Ta hard mask.

3.1 Beyond the Damascene Process

Copper was introduced into the semiconductor industry as the chosen material for replacing aluminum interconnects in 1997. (Bourhila 1997, Markert 1997) This radical change, necessitated by the need for a more effective conductor material which could scale to smaller dimensions, ultimately enabled the creation of smaller metal components and higher performing devices.

However, due to the perceived inability to etch copper using plasma-based processes at the time of introduction, a change was undertaken to introduce a completely new means for patterning copper. The damascene process, as it came to be known, consisted of first depositing a Cu seed layer over the patterned insulator layer using CVD. Subsequent electroplating enabled Cu growth to occur only in areas where the seed layer was present. Chemical mechanical planarization (CMP), which combined the chemical etch aspect of solution phase processing and physical removal through mechanical abrasion, was then used to remove the excess surface layer of Cu, leaving a surface of Si-based insulator as well as a Cu-inlaid trench which would serve as the interconnect. (Andriacos 1998)

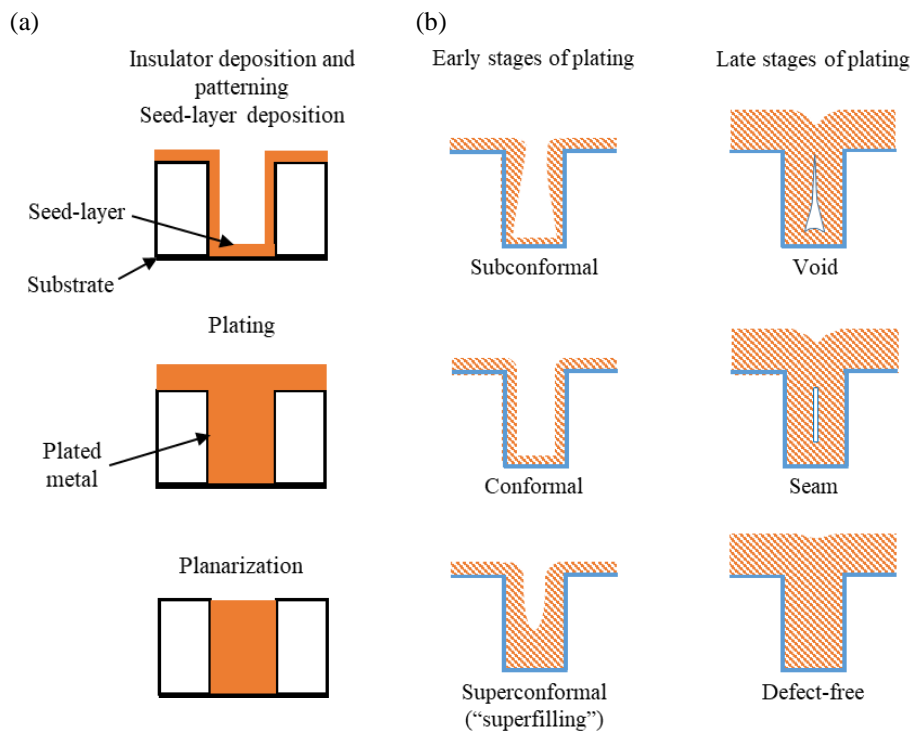


Figure 3-1. (a) Process steps for integration of damascene plating process, and (b) typical evolution profiles observed in damascene plating.

The damascene process was not without flaw; however, and numerous plating issues arose. For example, if the Cu^{2+} concentration in the plating solution within the pattern feature was depleted, a significant overpotential would result, causing current to flow preferentially to more easily accessed areas of the feature, such as the outer trench corners. As a result, in early stages of the plating process, subconformality would develop and ultimately lead to void formations due to increased growth rate at the high curvature portions of the feature. In order to address this issue and successfully fill a trench, it was necessary to have increased deposition rates at the bottom of the feature, resulting in superfilling and ultimately leading to a defect free inlay (Figure 3-1b). (Andriacos 1998)

From the perspective of interconnects, two important aspects must be taken into consideration when trying to pattern increasingly small features, especially for Cu. First, the resistance of Cu has been shown to increase by orders of magnitude as the dimensions of interconnects shrink to the 10 nm or sub-10 nm regime due to the width of the interconnect line being less than the intrinsic electron mean free path of ~39 nm in Cu. This size effect of Cu wiring significantly increases the resistivity in these dimensions compared to bulk Cu. (Liang 2012, Li 2015) Additionally, the process by which smaller metallization layers must be capable of patterning such small features. For wet etch, of which chemical mechanical planarization makes abundant use, use of liquid, especially at smaller feature sizes, can result in detrimental pattern collapse due to increased surface tension as well as the inability for etchants to reach high curvature areas within the pattern, necessitating the need for dry etch processing. (Yang 2012)

Cu was been shown to be etchable at lower temperatures. (Kuo 2001, Kuo 2004) In retrospect, this could have been realized earlier, building upon previous work investigating Cu- Cl_2 surface interactions and the measurement of gas phase etch products. (Winters 1985, Winters

1985) In an effort to find a gas-phase chemistry capable of patterning copper for interconnect applications using Cl₂ chemistry, Kulkarni and DeHoff pioneered the use of volatility diagrams as a means to assess viable processing conditions. (Kulkarni 2002) In the case of copper etching in chlorine (Cl₂(g)), the volatility diagram discussed in Chapter 1 of this work was able to show that the trimeric Cu₃Cl₃(g) has the highest vapor pressure of all Cu-Cl etch products, consistent with previous experimental findings. (Winters 1985) However, this vapor pressure at the equilibrium condition was deemed too low to be considered viable in etching copper in Cl₂ at temperatures below 200°C. (Kulkarni 2002) To enhance the etching rate of copper, the utilization of atomic hydrogen was found to be most effective, through its reaction with CuCl₂ (i.e. 3 CuCl₂(c) + 3 H(g) ↔ Cu₃Cl₃(g) + 3 HCl(g)).

The prediction from these thermodynamic calculations was experimentally verified using cycles comprised of sequential steps of Cl₂ (2 min) and H₂ (5 min) plasma exposure. (Tamirisa 2007, Wu 2010) Hydrogen plasma was demonstrated to also be effective at temperatures below 20°C in removing the copper chloride layer generated upon Cl₂ plasma exposure, as confirmed by XPS analysis, resulting in etch rates up to 100 nm/cycle.

Literature reported reactive ion etch chemistries are summarized in Table 3-1 for patterning Cu, including etch rates, hard mask materials used, and etch selectivity to hard mask materials, where available. In addition to the commonly encountered halogen-based etch chemistries, use of CO and CH₄ as primary etchants has also been reported. (Abe 2003, Choi 2013, Choi 2014)

Table 3-1 Reactive ion etch chemistries reported for copper and the corresponding etch rates, temperatures, masks used, and selectivity, where reported.

Plasma Chemistry	Etch rate (nm/min)	T (°C)	Mask	Selectivity	Ref.
Cl ₂	120	> 200	SiO ₂	2.0	(Miyazaki 1997)
Cl ₂ (80%)/Ar	500	200	PR	-	(Lee 1998)
H ₂	13	10	SiO ₂	-	(Wu 2010, Wu 2010, Wu 2011, Wu 2012)
Cl ₂ /H ₂	50 (nm/cycle)	15	-	-	(Tamirisa 2007)
CCl ₄ (50%)/Ar	500	225	PR	-	(Schwartz 1983)
SiCl ₄ (20%)/Ar	25	220	Polyimide PR	-	(Howard 1991)
SiCl ₄ (20%)/N ₂	70				
BCl ₃ (50%)/Ar	53	225	Spin-on glass	-	(Howard 1994)
BCl ₃ (50%)/N ₂	5				
CO(12.5%)/NH ₃	20	20	Ti	8.0	(Abe 2003)
CH ₄ , CH ₄ (50%)/H ₂	17, 20	10	SiO ₂ , PR	-	(Choi 2013, Choi 2014)

While halogen-based chemistries have been shown to be effective in etching copper, the associated corrosion issue is a concern to materials and device reliability. Utilization of organics in the gas-phase to pattern copper could potentially alleviate the corrosion issue related to the use of halogen chemistries. A thermodynamic assessment has been used to evaluate viable solution and gas phase organic chemistries that can be used to etch copper through the formation of volatile metalorganic compounds. Leveraging knowledge available for the synthesis of metalorganic deposition precursors such as copper acetylacetonate (Cu(acac)₂) and copper hexafluoroacetylacetonate (Cu(hfac)₂) that have substantial vapor pressures and have been used in chemical vapor deposition (CVD) and atomic layer deposition (ALD) processes, this work examined first the changes in Gibbs free energy of reaction for Cu-acac and Cu-hfac systems.

3.2 Thermodynamic analysis of organic etchants for Cu and CuO

At ambient temperature and pressure conditions (300 K and 1 atm), the changes in Gibbs free energy listed in Table 3-2 indicate that reactions of liquid phase acetylacetone and hexafluoroacetylacetone with solid metallic copper are spontaneous due to the negative value of their corresponding ΔG_{rxn} . Contrary to this, reaction between copper and gas phase acac or hfac were calculated to have positive ΔG_{rxn} values, indicating that these reactions would not be spontaneous. There are no available thermochemical data to support the calculations at higher temperatures; however, it should become feasible to etch Cu in both solution as well as in the gas phase using acac and hfac as temperature increases and the processing pressure decreases.

Table 3-2. Gibbs free energies for reaction of metallic copper with liquid and gas phases of acetylacetone and hexafluoroacetylacetone at 300 K and 1 atm.*

Reaction	ΔG_{rxn} (kJ/mol)
$\text{Cu(c)} + 2 \text{ acac(l)} \rightarrow \text{Cu(acac)}_2\text{(l)} + \text{H}_2\text{(g)}$	-39.2
$\text{Cu(c)} + 2 \text{ hfac(l)} \rightarrow \text{Cu(hfac)}_2\text{(l)} + \text{H}_2\text{(g)}$	-57.6
$\text{Cu(c)} + 2 \text{ acac(g)} \rightarrow \text{Cu(acac)}_2\text{(g)} + \text{H}_2\text{(g)}$	508.4
$\text{Cu(c)} + 2 \text{ hfac(g)} \rightarrow \text{Cu(hfac)}_2\text{(g)} + \text{H}_2\text{(g)}$	946.6

*Data only available at 300 K and 1 atm. Please note that etch Experiments conducted in the gas phase was carried out at elevated temperatures and reduced pressures.

Since patterning of copper is desirable to be achieved in the gas phase for device integration, an alternative route must be considered to enable the reaction as the thermodynamics suggest unfavorable reactions for gas phase acac and hfac. Interestingly, copper oxides have been shown to dissolve through complexation in β -diketones and other organic acids in the solution phase. (Rousseau 1992, Chavez 2001) Similar reports exists as well for vapor phase cleaning of copper, wherein the hfac chemistry has been used to remove oxidized copper with a rate of up to 150 nm/min at temperatures as high as 350°C. (Nigg 1998, Steger 1999) Cupric oxide (CuO) was

reported to have been removed through the production of volatile $\text{Cu}(\text{hfac})_2$ gas phase product. However, at elevated temperatures, the reduction of Cu(II) to Cu(I) directly competes with the aforementioned chelation reaction. (George 1995) Nonetheless, the reaction of Cu_2O with hfac remains important as a means for etching through disproportionation. Removal of Cu(I) and Cu(II) oxides was observed to terminate upon reaching the Cu^0 surface, due to the reduced reactivity between metallic Cu and hfac, consistent with the thermodynamic analysis shown above. (George 1995) This spontaneous termination implies that a very high selectivity between etching copper and copper oxide can be achieved and an effective route to removing of copper by tailoring its oxidation states.

Using the same calculation shown above, the thermodynamic assessment was applied to investigate the spontaneity of the CuO-acac and CuO-hfac systems by calculating the changes in Gibbs free energy in both liquid and gas phase reactions (Table 3-3). The negative values reported for CuO reacting with acac and hfac in the liquid phase suggest that $\text{Cu}(\text{acac})_2$ and $\text{Cu}(\text{hfac})_2$ can be effectively generated through the reaction since it is spontaneous. Though reactions between CuO and acac/hfac remained unfavorable in the gas phase, they are more likely than Cu reacting with acac and hfac. It has been shown that copper complexation with acac and hfac occurs with the organic molecule in the “standing up” mode, with C=O group pointing downward to the surface. (Steger 1999) Similar mechanisms have been reported for carboxylic acids, (Panias 1996) prompting the evaluation of additional organics in this study, namely formic and acetic acid. Due to the lack of thermodynamic data for the formation of these chemicals, no thermodynamic calculations have been shown. However, while there are no available thermochemical data to support the calculations at higher temperatures, it should become feasible to etch CuO in both

solution and gas phase as temperature increases and the processing pressure decreases, a process which was verified for CuO and hfac. (Nigg 1998)

Table 3-3. Gibbs free energies for reaction of copper oxide with liquid and gas phases of acetylacetone and hexafluoroacetylacetone at 300 K and 1 atm.*

Reaction	ΔG_{rxn} (kJ/mol)
$\text{CuO(c)} + 2 \text{ acac(l)} \rightarrow \text{Cu(acac)}_2\text{(l)} + \text{H}_2\text{O(l)}$	-119.1
$\text{CuO(c)} + 2 \text{ hfac(l)} \rightarrow \text{Cu(hfac)}_2\text{(l)} + \text{H}_2\text{O(l)}$	-428.7
$\text{CuO(c)} + 2 \text{ acac(g)} \rightarrow \text{Cu(acac)}_2\text{(g)} + \text{H}_2\text{O(g)}$	409.2
$\text{CuO(c)} + 2 \text{ hfac(g)} \rightarrow \text{Cu(hfac)}_2\text{(g)} + \text{H}_2\text{O(g)}$	847.4

*Data only available at 300 K and 1 atm. Please note that etch Experiments conducted in the gas phase was carried out at elevated temperatures and reduced pressures.

Etching of copper and copper oxide in both liquid and gas phases of selected organic chemistries were conducted in this study to corroborate the thermodynamic calculations. Cu films (50 nm) were deposited by electron-beam evaporation on a p-type silicon wafer. Thick CuO films were generated through rapid thermal annealing of copper thin films in an AccuThermo AW 610 RTP furnace with a flow of 3000 sccm of O₂ at 200°C. Organics, including acac, hfac, acetic acid, and formic acid of 99% purity (Sigma-Aldrich) were used, with the exception of hfac (98% purity) and utilized in both solution and vapor phase etch studies. Etching efficacy was first tested in high purity solutions (no dilution) in a vial in a water bath at 80°C. Changes in thickness of the films were measured by cleaving samples after processing and imaged by examining each cross section in an FEI Nova 600 scanning electron microscope (SEM) (1.4 nm resolution at 1kV).

3.3 Solution and Vapor Phase Etch of Cu and CuO

For etching elemental copper thin films, as shown in Figure 3-2a, both acac and hfac solutions were able to etch copper at a very small rate of 0.9 nm/min. Slightly higher etch rates of copper were observed in acetic acid (1.4 nm/min) and formic acid (2.2 nm/min) solutions. These

etch rates, while measurable, indicate that the corresponding etch rates in the gas phase would be negligible due to substantially lower concentrations of the organic etchants. Indeed, all four organic chemistries were used in the vaporizer system described in Chapter 2, and no measurable etch rates were found for these organic vapors reacting with metallic copper at 80 °C. From literature, measurable etch rates of CuO_x have been reported for acetic acid(g) and hfac(g), but at much higher temperatures of 200-350 °C. (Steger 1999, Suda 2012)

For etching CuO_x thin films, much higher etch rates were observed at 80°C, with etch rates of 110, 150, 540, and 338 nm/min in acac, hfac, acetic acid and formic acid solutions, respectively (Figure 3-2a). The observed high etch rate of CuO_x is consistent with literature reports using similar organics and other chemistries (aqua regia, CuCl_2 , FeCl_3 , and $(\text{NH}_4)_2\text{S}_2\text{O}_8$). (Chavez 2001, Çakır 2005, Çakır 2006)

These observations suggest that an organic chemistry based vapor phase etching process may be feasible if copper is first oxidized. To verify this point, formic acid was selected and used in the vaporizer to etch both Cu and CuO_x films. No measurable etch rate was observed for etching Cu in the gas phase under all experimental conditions explored in this study. At reduced pressures and elevated temperatures of 10 Torr and 150 °C for 5 min as well as 540 Torr, 80 °C for 10 min, etch rates of CuO_x at 19 nm/min and 5 nm/min were obtained, respectively. The etch rate as well as the cross-sectional SEM image of CuO_x etched in formic acid vapor at 10 Torr, 150 °C for 5 min are shown in Figure 3-2(a-c).

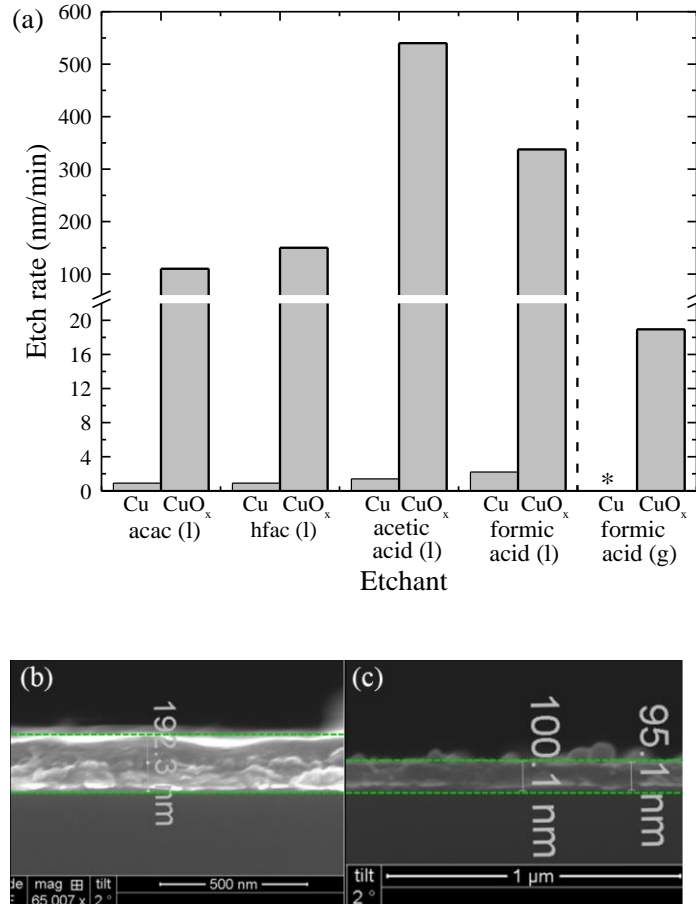


Figure 3-2. (a) Etch rates of Cu and CuO_x in liquid phase acac, hfac, acetic acid and formic acid are shown as measured at 80°C. Shown in comparison are results from etching Cu and CuO_x thin films in formic acid vapor at 150 °C and 10 Torr for 5 min. SEM cross-sections (b) before and (c) after etching CuO_x thin films in formic acid vapor. The asterisk (*) denotes a zero etch rate as measured in this work.

3.4 Plasma Modification for Enabling Selectivity in Cu Etch

The substantially higher etch rate of oxidized copper over metallic copper suggests that a viable dual step process could be developed to etch metallic Cu by first converting it to copper oxide then exposing it to the organic vapor. Thus in this work, an O₂ plasma was used (500 W source power, -100 V bias) to oxidize the copper surface and generate a thin layer of copper oxide, a thin layer (~3nm) of copper oxide can be formed after the plasma oxidation for 2 min. Next, acac or formic acid vapor was delivered at flow rates up to 3 cm³/min to achieve pressures of 85

and 148 Torr, respectively. A cyclic processing alternating between oxidation and organic vapor exposure was used to etch the copper. Both chemicals achieved measurable etch rates of CuO_x , as shown in Figure 3-3. It was clear that these organic vapors are much more effective in removing CuO_x than Cu. In addition, since this etch rate is reported in nm/cycle, the etching process can reach precise etch depths through the careful control of the oxide formation and the etching efficacy of the organic vapor.

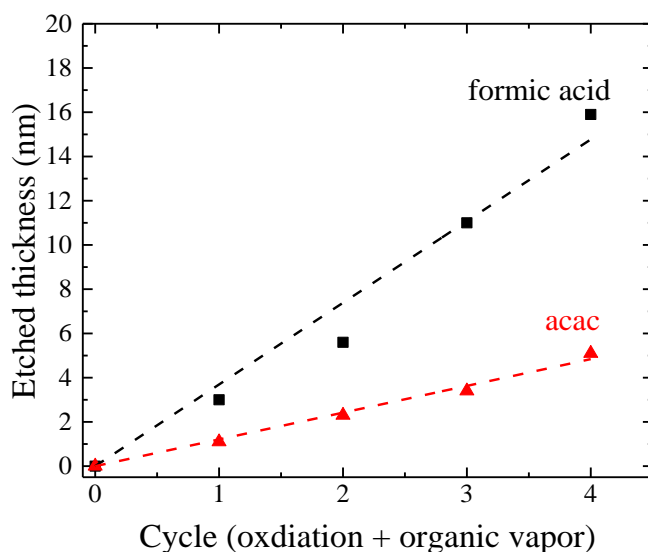


Figure 3-3. Measured etched thickness per cycle for copper as a function of a cyclic process alternating between O_2 plasma and organic vapor exposure (the dotted lines are linear regressions with R^2 values >0.98).

An etch rate of 1.3 nm/cycle was determined for a cyclic process with acac vapor (85 Torr), while a rate of 3.7 nm/cycle was measured for a cyclic process with formic acid vapor (148 Torr). High resolution XPS characterization of thin film Cu after exposure to oxygen plasma indicated that the sample surface was comprised mainly of CuO formed through reaction with energetic oxygen species present in the discharge. The Cu 2p doublet showed strong Cu^{2+} signal

centered at binding energy values of 934.0 and 953.8 eV as well as the presence of CuO satellite peaks at 941.6 and 962.4 eV. After subsequent formic acid vapor exposure for 50 s at 80 °C, the CuO is removed, evidenced by the elimination of Cu²⁺ signal at the aforementioned binding energies, substantial increase in metallic Cu⁰ signal at 933.0 and 952.8 eV, and substantial reduction in CuO satellite peaks. Deconvolution of the Cu 2p spectra into corresponding chemical bonding states after formic acid vapor etch indicates a small percentage (<10%) of Cu exists as Cu²⁺, attributed to re-oxidation during transport under atmosphere after processing.

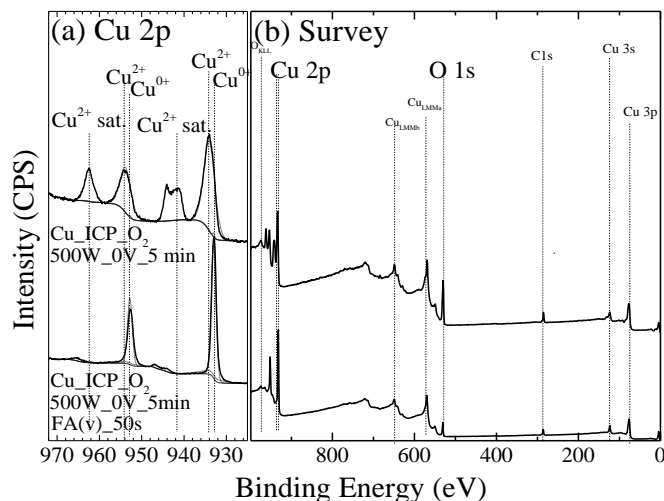


Figure 3-4. X-ray photoelectron spectra of (a) high resolution Cu 2p region and (b) survey of all elements present on the surface of Cu film after exposure to ICP O₂ surface modification and subsequent formic acid vapor etch.

Based on the results shown in Figure 3-3 and Figure 3-4, formic acid was chosen for subsequent experimental study due to its substantial gas phase etch rate of copper oxide at a lower temperature and its high vapor pressure (50 Torr at 25°C). Blanket Cu (35 nm) films were etched using alternating cycles of plasma oxidation and formic acid vapor exposure described above, using a custom-built inductively coupled plasma reactor with integrated vapor etch chamber

described previously in Chapter 2. SEM cross-section measurement indicated that the 35 nm Cu film was completely removed after 15 cycles (Figure 3-5a).

Energy dispersive x-ray spectroscopy was used to chemically verify the removal of Cu from the sample surface. Pre-processed samples show strong signatures of O L α (0.52 keV), Cu L α (0.93 keV) and Si K α (1.73 keV) emission from the 35 nm Cu film and underlying Si substrate. A small peak attributed to C L α at 0.27 keV was observed as well due to atmospheric exposure and resulting adventitious carbon contamination. Upon processing by 15 cycles of alternating O₂ plasma oxidation and formic acid vapor exposure with a terminal oxidation step, the Cu L α signature was almost entirely removed, confirming the etch of the Cu film (Figure 3-5b).

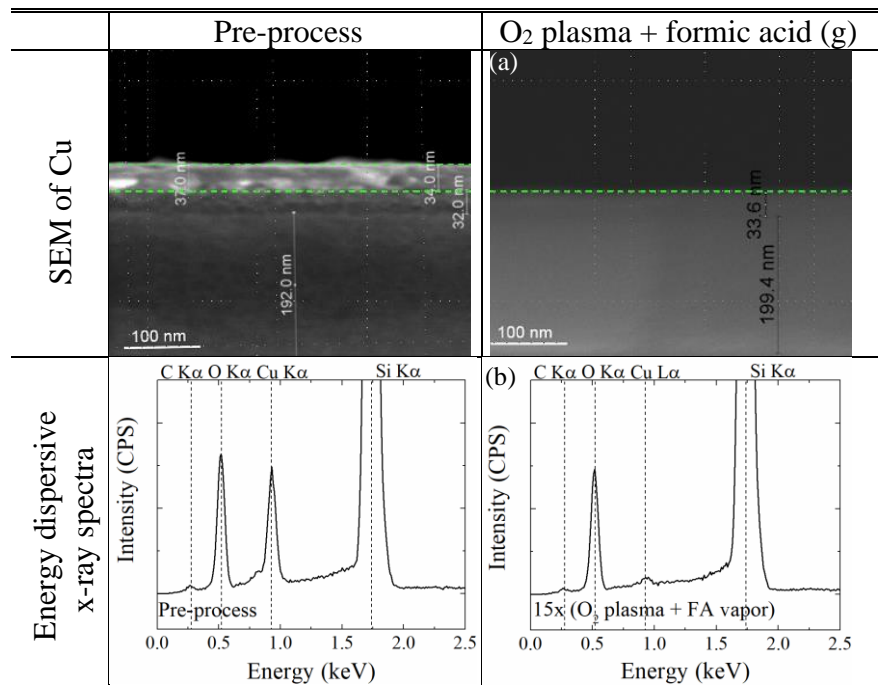


Figure 3-5. (First column) SEM cross-section and EDS spectrum of pre-process Cu (35 nm) on 35 nm of low-k material and 200 nm of SiO₂. (a) SEM cross-section of 35 nm Cu etched under 15 cycles consisting of alternating plasma oxidation (500 W, -100 V, 2 min) and formic acid vapor etch (50 s). (b) Energy dispersive x-ray spectrum (EDS) of sample surface after exposure to 15 cycles. The interface between the mask and copper is outlined with a dashed line to help guide the eyes for comparison.

While etch rate measurements with blanket films are useful to confirm the disparity in etching metallic and oxidized copper, a direct comparison between solution- and gas-phase formic acid etching processes was made in this work utilizing pre-patterned copper films. Specifically, a 35 nm Cu thin film was patterned by a 40 nm Ta hard mask to form 70 nm \times 10 μ m lines and 1 μ m \times 1 μ m pads, as shown in Figure 3-6 and Figure 3-7.

3.5 Cyclical Oxidation and Organic Vapor Etch for Patterning Cu Thin Films

Studies conducted on blanket Cu films were useful for determination of etch rates as well as confirming that the cyclical oxidation and chemical vapor etch process was capable of removing CuO. However, the value of this process lies in its ability to not just etch Cu but also pattern it into various smaller shapes through the use of a hard mask material such as Ta. This process was studied in parallel with formic acid solution phase patterning, allowing for comparison of the isotropic and anisotropic etch profiles that evolved, delineating the influence and ability to manipulate etch directionality through anisotropic surface modification using oxygen plasma in conjunction with a biased sample.

In formic acid solution, a 500 s exposure at 80 °C resulted in removal of a substantial amount of metallic copper at a rate consistent with the reported value in the earlier section, and as shown in Figure 3-7 (a-b) a significant amount of undercutting (more than 200 nm in the lateral direction) under the 1 μ m \times 1 μ m hard mask and a complete suspension of the 70 nm lines were observed.

Vapor dosing time was found to be critical during the alternating oxidation and formic acid vapor etch process. Mask adhesion was found to be affected by the duration of formic acid exposure to patterned features. Most notably, 60 nm \times 10 μ m lines with reduced spacing of pitch

distances from 70-120 nm were showed to have no etch with 15 s formic acid vapor exposure (Figure 3-6a). Increasing the vapor exposure time to 50 s, etch of copper in the unmasked regions was observed (Figure 3-6b); however, further increases up to 90 s of formic acid vapor exposure caused detrimental effects to the line hard mask, resulting in complete undercut and loss of mask adhesion (Figure 3-6c).

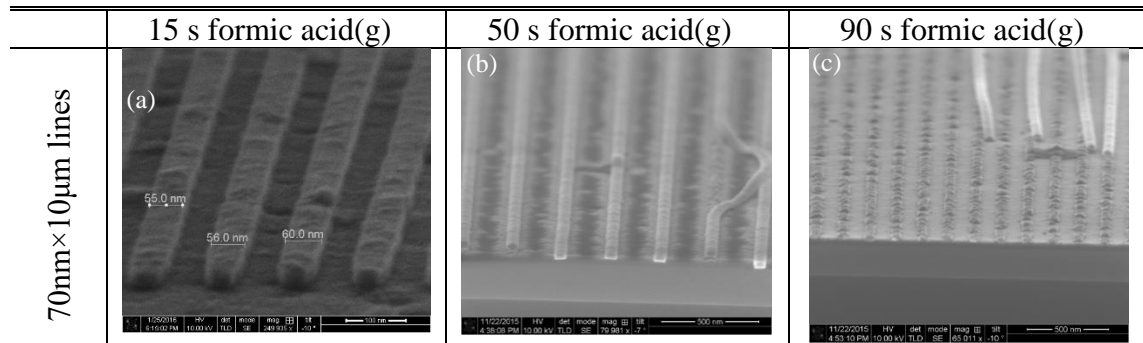


Figure 3-6. Bird eye view scanning electron micrographs of patterned (a) 60 nm × 10 µm lines with 70 nm pitch, (b) 60 nm × 10 µm lines with 120 nm pitch, and (c) 60 nm × 10 µm lines with 100 nm pitch after exposure to 4 cycles of alternating O₂ plasma (500W, -200 V bias, 2 min) and formic acid vapor (15, 50, and 90 s, respectively).

By reducing the exposure of formic acid (148 Torr, 50 s, 80 °C) and applying a -100 V bias, an anisotropic etch profile after 10 such cycles with a terminal oxidation step for both 1 µm×1 µm pads (Figure 3-7c) and 70 nm×10 µm lines (Figure 3-7d) was achieved.

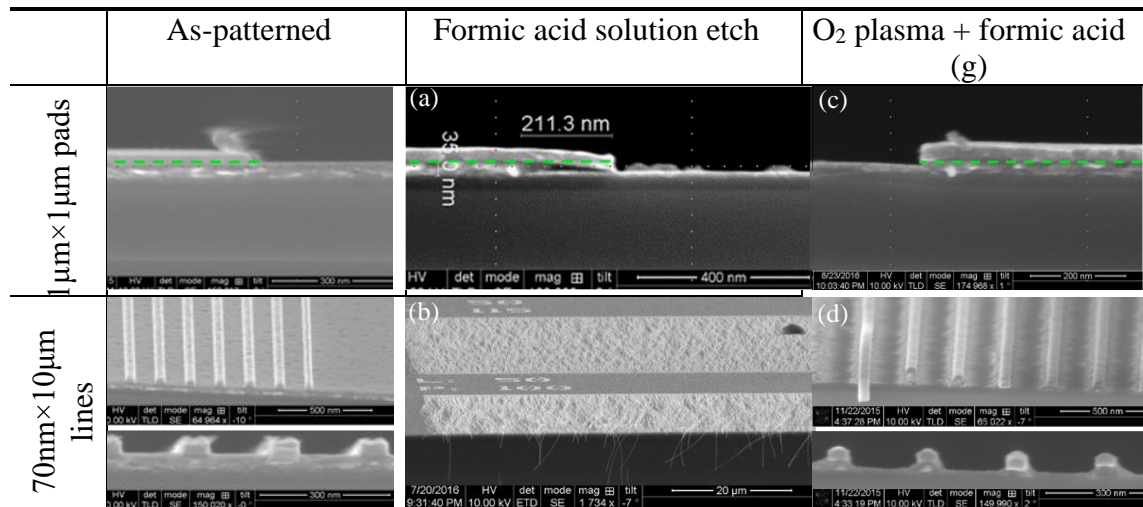


Figure 3-7. (First column) As-patterned 1 $\mu\text{m} \times 1 \mu\text{m}$ pads and 70 nm \times 10 μm lines of 40 nm Ta hard mask (HM) patterned 35 nm Cu films, in cross-sectional and birds-eye views. The interface between the mask and copper is outlined with a dashed line to help guide the eyes for comparison. (a-b) SEM images of patterned copper etched in formic acid (500 s) in solution (no oxidation). (c-d) SEM images of patterned copper etched by 10 cycles of alternating O₂ plasma (500 W, -100 V bias, 2 min) and formic acid vapor (50 s), terminating with a final exposure to O₂ plasma.

Use of EDS afforded spatial resolution when measuring which elements were present on the patterned Cu sample in areas covered with the Ta hard mask as well as areas of exposed Cu. Spectra for the masked regions were taken by collecting the stimulated x-ray emission from a region where the SEM electron beam was aimed at a chosen point on the line patterned with Ta hard mask. This process was repeated for the exposed region by collecting spectra from areas of exposed Cu between the patterned lines. As shown in Figure 3-8, before processing both the masked (solid) and exposed (dashed) portions of the sample area have nearly identical spectra, with both indicating a strong signal emitted from the Cu L α transition at 0.93 keV and indicating that the amount of Cu in each area was effectively the same. After the initial two cycles of oxidation and formic acid vapor etch, spectra for the masked region indicates a Cu L α signal intensity comparable to the pre-processing masked region. In contrast, the exposed Cu region shows a

substantial decrease in Cu L α intensity due to etch. After six cycles, the masked region maintains strong Cu L α signal intensity while the measured exposed region between the patterned hard mask lines continues to decrease, corroborating the effective removal of Cu.

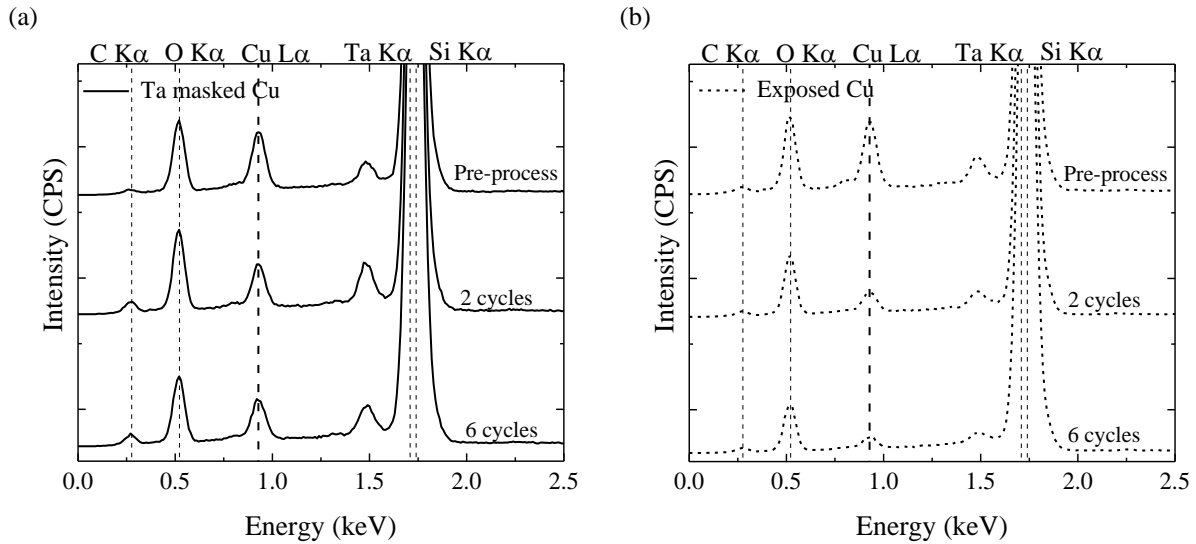


Figure 3-8. Energy dispersive x-ray spectra for (a) Ta hard masked and (b) exposed regions of Cu patterned by 70 nm \times 10 μ m lines pre-processing, after 2 cycles of plasma oxidation and formic acid vapor etch, and after 6 cycles of plasma oxidation and vapor etch.

Although the delivery of the formic acid vapor to the surface and its subsequent reaction is isotropic, the removal of a directionally oxidized CuO $_x$ under a patterned feature results in high selectivity to metallic copper and an anisotropic etch profile because the oxidation step is a directional one, involving the use of an oxygen plasma and a substrate bias. The alternating oxidation and formic acid vapor etch process provides a number of benefits for furthering the patterning of copper films. First, the high selectivity with which formic acid vapor removes copper oxide over metallic copper indicates that this cyclic approach can be utilized for pursuing etch at the atomic scale by controlling the etched thickness through the modified layer thickness. Second,

directionality of etch can be induced by applying a bias voltage to the sample during plasma oxidation. Finally, this dual step approach is functional at temperatures substantially lower than those used for halogen-based plasma etch

Chapter 4 : Reactive Ion Etch and Atomic Layer Etch of Co, Fe, and CoFeB

The experimental studies discussed herein verified the thermodynamic analysis performed for Co, Fe, and B as well as process chemistries such as Cl_2 , H_2 as well as subsequent use of surface modification and organic chemistries. An enhanced etch rate of 5.4 nm/cycle was observed upon use of cyclical Cl_2/H_2 plasma exposure for CoFeB over continuous Cl_2 , which resulted in an equivalent etch rate of 3.4 nm/cycle. Surface characterization confirmed that this enhancement was the result of removal of a chlorinated surface layer and was corroborated by an observed partial restoration in the static magnetic coercivity of the CoFeB films to near pre-process value of 6 Oe (cf. 4 Oe pre-process). Subsequent examination of single element Co and Fe organic etch showed enhanced selectivity in choosing acac and hfac solution etch chemistries, leading to confirmed efficacy of acac/hfac mixtures in etching CoFeB.

Oxidation was shown to provide an effective route for self-limiting cyclical etch in combination with organic vapor exposure, confirming additional thermodynamic analysis and enabled a process whereby metal oxide surface modification layers could be grown to within sub-nanometer thicknesses with subsequent removal at rates up to 2.8 and 4.2 nm/cycle for Co and Fe in conjunction with a 5 min exposure to O_2 plasma. Reducing this oxidation time while holding the etch time constant resulted in an etch rate of 1.8 nm/cycle for CoFeB. Directional etch was also demonstrated, as well as simulated using a Monte Carlo profile modeling setup, in using a -200 V bias during oxidation, allowing for patterning of 35 nm thick Co thin films into $70 \text{ nm} \times 10 \text{ }\mu\text{m}$ lines.

4.1 Thermodynamic assessment of Co, Fe, and B in Cl₂

Identification of a reactive ion etch (RIE) process is a critical step for patterning non-volatile materials such as metallic and intermetallic thin films. RIE is capable of providing a bulk etch which can also be studied to identify the influence of parameters such as chemistry, pressure, and ion energy to determine the surface effects as well as additional potential for scaling down to an atomic layer etch process. Studies using Cl₂/H₂ chemistry were shown in literature to be capable of etching Co, Fe, and pattern CoFe using TiN hard mask. (Kim 2014, Kim 2015)

In these investigations, thermodynamics was utilized to screen the chemistries in two sequential steps. First, a minimization of Gibbs free energy scheme was used to determine the temperature-dependent distribution of which species were thermodynamically favorable during the interaction between solid phase Co, Fe, and B with gaseous Cl₂. These calculations were effective for determining which binary chloride species formed as a starting point for the subsequent analysis. Second, a collection of gas and condensed phase reactions were constructed to model the surface reactions occurring during the etch process and facilitate calculation of the partial pressure of etch product as a function of etchant pressure.

The algorithm previously described in Chapter 1 known as minimization of Gibbs free energy was utilized for the cases of Co and Fe condensed phase system in the presence of chlorine. Through the process of Gibbs minimization, the distribution of constituent molecules present within the system can be calculated at a given pressure and temperature. These absolute amounts, in kmol of each compound, were calculated as a function of temperature for Co-Cl₂, Fe-Cl₂, and B-Cl₂ systems.

Figure 4-1 shows a side-by-side comparison of these three systems wherein 1 kmol of Co(c), Fe(c), and B(c) was modeled to equilibrate with 200 kmol Cl₂ and 50 kmol Ar. Due to its nonreactive nature, the calculated amount of Ar remains constant due to the lack compounds capable of forming. However, the calculated evolution of products distributed across a wide range of temperatures allows for the identification of CoCl_x, FeCl_x, and BCl_x compounds.

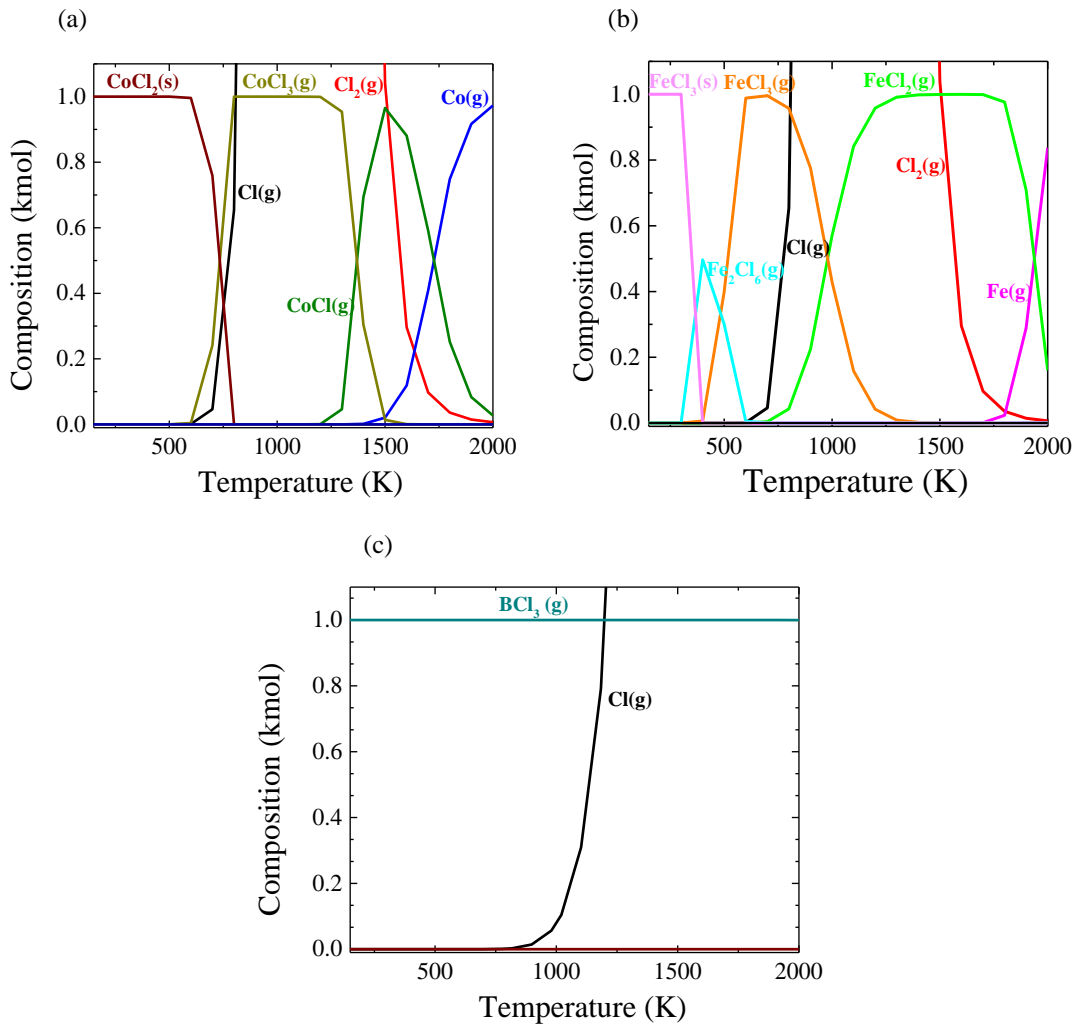


Figure 4-1. Product distribution of (a) Co-Cl, (b) Fe-Cl, and (c) B-Cl systems simulated through minimization of Gibbs free energy scheme to determine gaseous and condensed phase species present at thermodynamic equilibrium as a function of temperature (K).

For the Co-Cl₂ system, the minimization of Gibbs free energy indicates that the formation of CoCl₂(c) is thermodynamically favorable at reduced temperatures and suggests that chlorination results in a cobalt(II) chloride surface layer. Formation of CoCl₃(g) was calculated to occur at temperatures above 600 K (327 °C), with subsequent CoCl(g) calculated to be produced at even higher temperatures above 1200 K (927 °C). In comparison, for the Fe-Cl₂ system, FeCl₃(c) formation is achievable at temperatures up to 405 K (132 °C), suggesting chlorination of Fe is easily achievable by plasma exposure. The gas phase dimer Fe₂Cl₆(g) is predicted to occur in a temperature range of 300-600 K (27-327 °C) and is in equilibrium with FeCl₃(g), which becomes the dominant species at 485 K (212 °C). In addition to FeCl₃, FeCl₂ was predicted to form in the gas phase, albeit at temperatures above 710 K (437 °C). The predicted behavior of boron is substantially different than both Co and Fe. While these transition metals are not predicted to favorably form a stable gas phase chloride at typical operating temperatures, the formation of BCl₃(g) was shown to be thermodynamically favorable even at reduced temperatures and was expected to be the dominant volatile product upon reaction of boron in the ferromagnetic CoFeB with Cl₂ plasma.

By taking the results of the single element analysis from the Gibbs minimization, the predicted formation of CoCl_x and FeCl_x condensed phases as well as the corresponding gas phase metal chlorides and BCl₃ etch products can then be used as starting points for the second step in the thermodynamic analysis, construction of volatility diagrams. By functionalizing the partial pressure of FeCl₃(g), for example, to be dependent on the partial pressure of Cl₂(g), the feasibility of calculating any noticeable amount of etch can be determined by investigating the position of equilibrium lines for the coexistence of condensed and vapor phases.

To calculate the vapor pressure of the etch products formed upon reaction of Co, Fe, and B with gaseous Cl_2 , the same tool in the investigation of Cu- Cl_2 systems summarized in Chapter 1 was utilized. Table 4-1 and Figure 4-2 summarizes the gas-surface reactions and corresponding equilibrium for the three elements present within one of the materials of interest in this work, CoFeB, and their corresponding condensed and vapor phase chlorides. A horizontal dotted line at 10^{-8} atm represents the threshold, below which was deemed to predict no significant or noticeable amount of net material removal through the reaction between Co, Fe, or B and $\text{Cl}_2(\text{g})$. As can be seen below, the formation of metal chlorides and the resulting equilibrium between their corresponding gas and condensed phases predicts that no noticeable amount of etch would occur for the Co- Cl_2 system, since none of the equilibrium line crosses or lies above the $\log(\text{P}) = -8$ threshold. For Fe, the same is true, as equilibria between condensed phases and $\text{FeCl}_2(\text{g})$ and $\text{FeCl}_3(\text{g})$ provide insufficient partial pressure. At an increased temperature of 500 K (227 °C), the phase equilibrium between condensed and gas phase FeCl_3 is sufficient to pass this threshold; however, this increased temperatures is unfavorable from a materials processing standpoint. In particular, these elevated temperatures would not be advantageous for processing multilayered stacks of materials, such as those encountered in the MTJ, due to interdiffusion of constituent compounds between layers which would be detrimental to device operation.

Table 4-1. Reactions used for creating volatility diagram shown in Figure 4-1 for Co-Cl, Fe-Cl, and B-Cl systems.

	Reaction	ΔG (kJ/mol)
(1)	$\text{Co(c)} \rightarrow \text{Co(g)}$	379.8
(2)	$\text{Co(c)} + \text{Cl}_2(\text{g}) \rightarrow \text{CoCl}_2(\text{c})$	-269.3
(3)	$\text{Co(c)} + \text{Cl}_2(\text{g}) \rightarrow \text{CoCl}_2(\text{g})$	-107.2
(4)	$\text{CoCl}_2(\text{c}) \rightarrow \text{CoCl}_2(\text{g})$	162.1
(5)	$\text{CoCl}_2(\text{c}) \rightarrow \text{Co(g)} + \text{Cl}_2(\text{g})$	593.8
(6)	$\text{Co(c)} + 1/2 \text{Cl}_2(\text{g}) \rightarrow \text{CoCl(g)}$	141.3
(7)	$\text{CoCl}_2(\text{c}) \rightarrow \text{CoCl(g)} + 1/2 \text{Cl}_2$	382.9
(8)	$\text{Co(c)} + 3/2 \text{Cl}_2(\text{g}) \rightarrow \text{CoCl}_3(\text{g})$	-148.4
(9)	$2 \text{Co(c)} + 2 \text{Cl}_2(\text{g}) \rightarrow \text{Co}_2\text{Cl}_4(\text{g})$	-323.1
(10)	$2 \text{CoCl}_2(\text{c}) \rightarrow \text{Co}_2\text{Cl}_4(\text{g})$	160.3
(11)	$\text{Fe(c)} \rightarrow \text{Fe(g)}$	369.4
(12)	$\text{Fe(c)} + \text{Cl}_2(\text{g}) \rightarrow \text{FeCl}_2(\text{c})$	-301.6
(13)	$\text{FeCl}_2(\text{c}) + 1/2 \text{Cl}_2(\text{g}) \rightarrow \text{FeCl}_3(\text{c})$	-32.0
(14)	$\text{Fe(c)} + \text{Cl}_2(\text{g}) \rightarrow \text{FeCl}_2(\text{g})$	-155.7
(15)	$\text{FeCl}_2(\text{c}) \rightarrow \text{FeCl}_2(\text{g})$	145.9
(16)	$\text{FeCl}_2(\text{c}) \rightarrow \text{Fe(g)} + \text{Cl}_2(\text{g})$	671.6
(17)	$\text{FeCl}_3(\text{c}) \rightarrow \text{Fe(g)} + 3/2 \text{Cl}_2(\text{g})$	703.0
(18)	$\text{Fe(c)} + 1/2 \text{Cl}_2(\text{g}) \rightarrow \text{FeCl(g)}$	215.4
(19)	$\text{FeCl}_2(\text{c}) \rightarrow \text{FeCl(g)} + 1/2 \text{Cl}_2(\text{g})$	517.5
(20)	$\text{FeCl}_3(\text{c}) \rightarrow \text{FeCl(g)} + \text{Cl}_2(\text{g})$	548.9
(21)	$\text{FeCl}_3(\text{c}) \rightarrow \text{FeCl}_2(\text{g}) + 1/2 \text{Cl}_2(\text{g})$	177.8
(22)	$\text{Fe(c)} + 3/2 \text{Cl}_2(\text{g}) \rightarrow \text{FeCl}_3(\text{g})$	-247.8
(23)	$\text{FeCl}_2(\text{c}) + 1/2 \text{Cl}_2(\text{g}) \rightarrow \text{FeCl}_3(\text{g})$	54.2
(24)	$\text{FeCl}_3(\text{c}) + \text{FeCl}_3(\text{g})$	85.7
(25)	$2 \text{Fe(c)} + 3 \text{Cl}_2(\text{g}) \rightarrow \text{Fe}_2\text{Cl}_6(\text{g})$	-598.3
(26)	$2 \text{FeCl}_2(\text{c}) + \text{Cl}_2(\text{g}) \rightarrow \text{Fe}_2\text{Cl}_6(\text{g})$	5.8
(27)	$2 \text{FeCl}_3(\text{c}) \rightarrow \text{Fe}_2\text{Cl}_6(\text{g})$	68.7
(28)	$\text{B(c)} \rightarrow \text{B(g)}$	520.9
(29)	$\text{B(c)} + 1/2 \text{Cl}_2(\text{g}) \rightarrow \text{BCl(g)}$	120.8
(30)	$\text{B(c)} + \text{Cl}_2(\text{g}) \rightarrow \text{BCl}_2(\text{g})$	92.6
(31)	$\text{B(c)} + 3/2 \text{Cl}_2(\text{g}) \rightarrow \text{BCl}_3(\text{g})$	-387.9

Compared to the transition metals, boron has a substantially lower mass than both Co and Fe and reacts readily with Cl_2 to form volatile halide species, most noticeably $\text{BCl}_3(\text{g})$. The reaction between B(c) and $\text{Cl}_2(\text{g})$ to generate $\text{BCl}_3(\text{g})$ has a substantial negative change in Gibbs free energy

of reaction of -387.9 kJ/mol at 300 K. The equilibrium displayed at typical operating partial pressure Cl_2 (10^{-3} - 10^{-7} atm) shows that the equilibrium between B(c) and $\text{BCl}_3(\text{g})$ is quite high, even at reduced Cl_2 partial pressures and operating temperatures as low as 300 K. From this volatility analysis, these calculations suggest that the etch of boron should be easily accomplished due to the high pressures of $\text{BCl}_3(\text{g})$ formed in this surface-gas reaction.

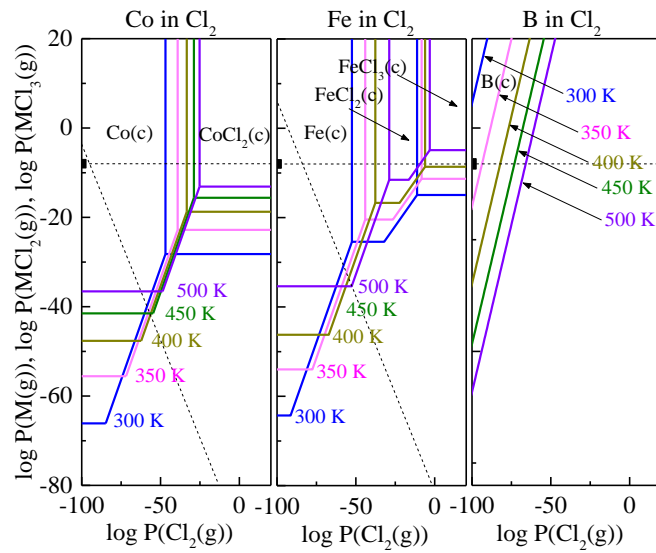


Figure 4-2. Volatility diagrams for Co, Fe, and B in Cl_2 at 300 , 350 , 400 , 450 , and 500 K

By exposing the formed metal chloride condensed phase species to hydrogen gas—or in this case, plasma—at a fixed partial pressure of hydrogen, there is indication that the metal can be volatilized and removed. Analysis of the inclusion of auxiliary hydrogen in this process is characterized by fixing the partial pressure of hydrogen introduced into the system and subsequently analyzing reactions for the formation of volatile $\text{CoH}(\text{g})$ and $\text{FeH}(\text{g})$. From a graphical standpoint used in the volatility diagrams, this hydrogen isobar is characterized by a negatively sloped dotted line present in the analysis of Co-Cl_2 and Fe-Cl_2 systems. The reaction between $\text{CoCl}_2(\text{c})$ and atomic $\text{H}(\text{g})$ generated in the inductively coupled hydrogen plasma results

in formation of CoH(g) and HCl(g). This specific reaction at 300K was calculated to have a change in Gibbs free energy of reaction of -121.7 kJ/mol, indicating that the reaction is spontaneous and elucidates a reaction pathway suitable for the removal of nonvolatile CoCl₂(c) under H₂ discharge. The analogous reactions for surfaces of FeCl₂ and FeCl₃, that is FeCl₂(c) + 3H(g) → FeH(g) + 2HCl(g) and FeCl₃(c) + 4H(g) → FeH(g) + 3HCl(g) were calculated to also be spontaneous at 300 K, with a ΔG_{rxn} values of -84.9 and -351.4 kJ/mol, respectively. It is worth comparing these reactions, which indicate the thermodynamically favorable formation of volatile metal hydrides, to the direct reaction of each metal with atomic hydrogen (i.e. Co(c) + H(g) → CoH(g) and Fe(c) + H(g) → FeH(g)), which have ΔG_{rxn} values of 206.0 and 210.4 kJ/mol for Co and Fe, indicating that these reactions are nonspontaneous.

4.2 Experimental validation of thermodynamic assessment

The power of the thermodynamic assessment lies in its ability to provide a means for identifying and analyzing candidate chemistries for further investigation. The factor which determines the occurrence of a specific reaction lies in the thermodynamic favorability of that reaction, as expressed through the aforementioned change in Gibbs free energy. However, in order to ensure that the thermodynamic analysis detailed above is effective, it must be confirmed and substantiated through experimental validation.

4.2.1 ICP Reactive ion etching of CoFeB

The surface chemical bonding state and composition of films before and after processing were characterized using X-ray photoelectron spectroscopy (Kratos XPS Axis Ultra DLD with monochromatic Al Kα source and a fixed electron analyzer energy of 20 eV for high resolution scans). Co₃₀Fe₄₅B₂₅ stoichiometry was confirmed using depth profiling XPS with multiple 100 s exposures of 1keV Ar⁺ beam milling to an etch depth of 25 nm (Figure 4-3)

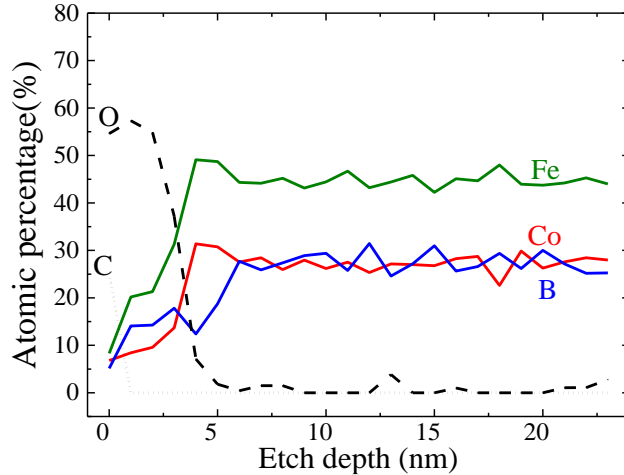


Figure 4-3. Atomic percentage of Co, Fe, B, O, and C measured in 30 nm $\text{Co}_{30}\text{Fe}_{45}\text{B}_{25}$ as a function of etch depth for XPS depth profile using 1 keV Ar^+ .

In order to assess the effect of Cl_2 plasma modification with H_2 etch, CoFeB was exposed to 30 s alternating cycles of sequential Cl_2 and H_2 plasmas (800 W_s source power, 50 W_b bias power) to determine the etch rate, change in surface composition, as well as effect on static magnetic properties. Figure 4-4 represents the etched thickness of CoFeB as a function of etch cycle for alternating Cl_2 and H_2 plasma etch as well as, for comparison, previously measured etched thicknesses of 800 nm Co and Fe films processed under 20 s alternating Cl_2 and H_2 plasma (800 W_s source power, 100 W_b bias power). CoFeB was observed to etch at an average rate of 10.9 nm/min under alternating 30 s Cl_2 and H_2 plasmas. This average rate was found to agree well when compared to the measured etch rates for Co and Fe thin films, 13.8 and 25.5 nm/min respectively. The small decrease in etch rate of CoFeB compared to Co and Fe was attributed to the reduced physical sputtering component caused by reduction in the bias power from 100 W_b for etching Co and Fe to 50 W_b for etching CoFeB. Limited etch of CoFeB was observed under H_2 plasma alone, exhibiting an average etch rate of approximately 0.9 nm/min in the initial 30 s etch time, while CoFeB exposure to Cl_2 plasma alone was observed to cause a limited amount of chemical etch,

resulting in an average etch rate of approximately 6.5 nm/min (not shown). The substantial 68% enhancement in the cyclical etch rate observed for alternating sequential 30 s cycles of Cl₂ and H₂ plasma was attributed to the chemical removal of the chlorinated surface layer through formation of metallic hydrides. Removal of the metallic chlorides was observed to occur through formation of volatile metal hydrides, as shown in previous work. Analysis of the corresponding reactions between the CoCl₂ and FeCl₃ condensed phases and atomic H generated in the process plasma indicate that the formation CoH(g) and FeH(g) are thermodynamically favorable and spontaneous, with ΔG_{rxn} values of -150.3 and -391.3 kJ, respectively. Analysis of the B-Cl reaction system indicated that the formation of BCl₃(g) was the dominant etch product for removal from the surface, as this species exhibits a substantially higher partial pressure than either of its metallic chloride counterparts under standard conditions.

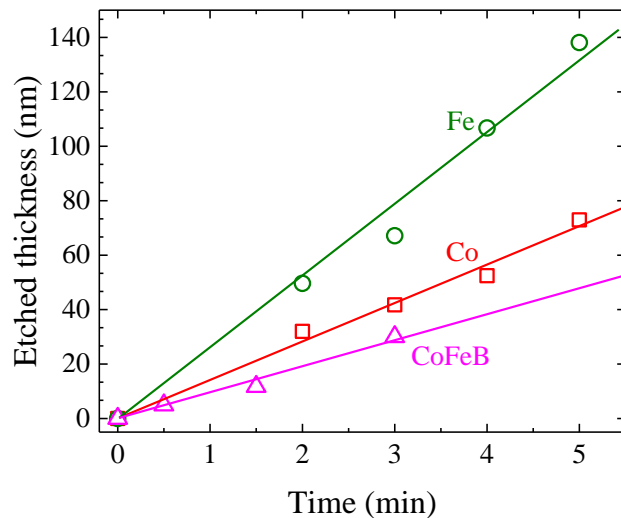


Figure 4-4. Etched thickness as a function of time for 30 nm CoFeB and 800 nm Co and Fe films etched in alternating exposures of Cl₂ and H₂ plasmas. Co (□) and Fe (○) were etched under sequential 20 s exposures to Cl₂ and H₂ plasma (800 W source power, 100 W bias power). CoFeB (Δ) was etched under sequential 30 s exposures to Cl₂ and H₂ plasma (800 W source power, 50 W bias power). Dashed lines have been added to guide the eye.

Presence of halides on the surface can lead to corrosion as well as degradation of magnetic properties. Surface characterization methods and magnetic measurements using XPS and SQUID were performed to investigate the pre- and post-processing surface chemical bonding states and static coercivity of the CoFeB films. High resolution x-ray photoelectron spectra for Co 2p, Fe 2p, Cl 2p and B 1s, O 1s, and a survey of elements present on the sample surface are shown in Figure 4-5 and Figure 4-6.

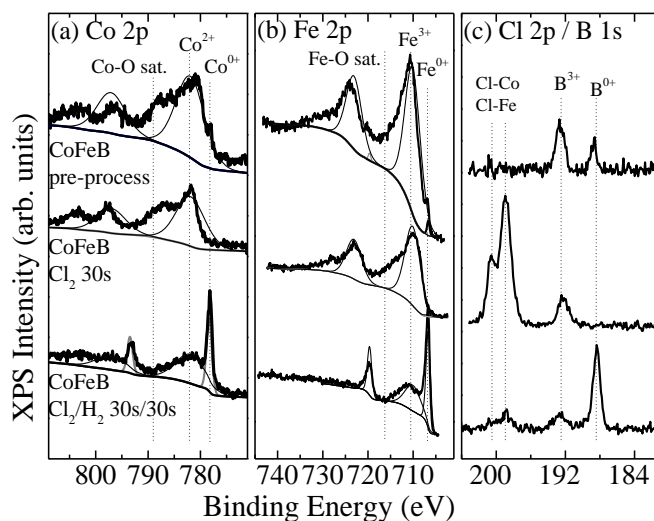


Figure 4-5. High resolution x-ray photoelectron spectra of (a) Co 2p, (b) Fe 2p, (c) Cl 2p and B 1s of pre-process CoFeB, CoFeB after 30 s of Cl₂ plasma, and CoFeB after a single cycle of alternating Cl₂ and H₂ plasma, each for 30 s.

Before exposure to the inductively coupled Cl₂ plasma Co, Fe, and B exhibit signs of oxidation from atmospheric exposure due to the presence of Co²⁺, Fe³⁺, and B²⁺ oxidation states present at binding energies of 782.0, 710.4, and 192.4 eV. A small amount of metallic Co⁰ and Fe⁰ and elemental B was measured at 778.2, 706.8 eV, and 188.5 eV, suggesting that the native oxidation is only a few nanometers thick.

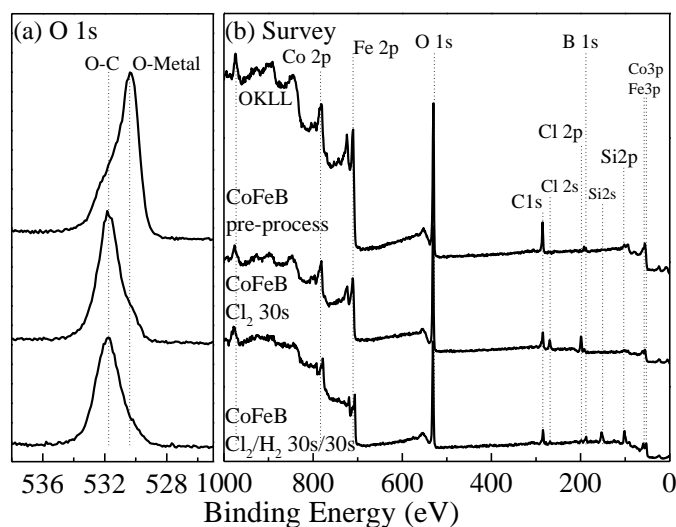


Figure 4-6. High resolution x-ray photoelectron spectra of (a) O 1s and (b) a survey scan of all elements present on the surface of pre-process CoFeB, CoFeB after 30s of Cl₂ plasma, and CoFeB after a single cycle of alternating Cl₂ and H₂ plasma.

After exposure to Cl₂ plasma, no elemental Co, Fe, or B was observed, with only Co²⁺, Fe³⁺ and B²⁺ peaks remaining. The emergence of the Cl 2p doublet present at 198.9 and 200.4 eV indicates surface presence of chlorine, corroborating the presence of surface metal chlorides as well as subchlorinated boron compounds. Subsequent exposure to H₂ plasma results in the emergence of strong elemental Co⁰, Fe⁰ and B⁰ signals as well as a substantial reduction in the Cl 2p peak, suggesting that the H₂ cycle was able to remove nearly all of the surface chlorides.

4.2.2 Effect of plasma etch on static magnetic properties of CoFeB

To determine the effect of this cyclical approach on static magnetic properties such as the coercivity, samples of pre-process CoFeB as well as after continuous Cl₂ and a single cycle of Cl₂/H₂ exposure were characterized via SQUID magnetometry. Before processing, the 30 nm CoFeB film was measured to have a coercivity of approximately 4 Oe. Following a 30s etch using Cl₂ plasma described above, the coercivity increased by 367% to 11 Oe. This increase is coercivity

is attributed to the formation of magnetically hard metallic chlorides. Subsequent exposure to reductive H₂ plasma partially restored the measured CoFeB coercivity value to 6 Oe (Figure 4-7).

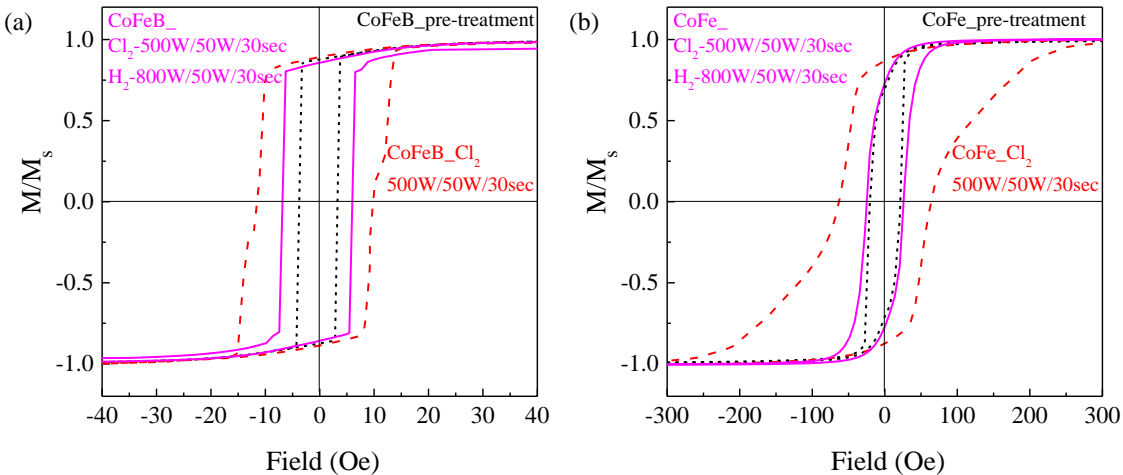


Figure 4-7. Magnetic measurement of (a) 30 nm CoFeB blank film (black), following 30s of Cl₂ plasma (red), and following single cycle of sequential Cl₂ and H₂ plasma (magenta) and (b) 50 nm CoFe blank blank film (black), following 30s of Cl₂ plasma (red), and following single cycle of sequential Cl₂ and H₂ plasma (magenta). Note the order of magnitude change in x-axis due to increasing magnetic hardness of CoFe compared to CoFeB due to high concentration of boron.

This partial restoration was due to the two phenomena. During the chlorination step, the preferential removal of B through formation of BCl₃ adversely affects the static magnetic properties of CoFeB, effectively resulting in a B-depleted surface layer of CoFe, which exhibits an increased coercivity relative to the underlying pristine CoFeB. Inclusion of boron in ferromagnetic alloys such as CoFe has been shown to increase the material's magnetic softness, resulting in a decreased coercivity. (Ikeda 2012, Kodzuka 2012, Sharif 2008) This effect can also be seen when comparing pre- and post-processed CoFeB to pre-process CoFe, which has an increased coercivity of 21 Oe (Figure 4-7b). Second, from the surface characterization shown Figure 4-5, a small concentration of metallic chloride species remains on the surface after exposure

to H₂ plasma, contributing to the increase in coercivity which can be remedied through further optimization of the H₂ etch time.

4.3 Organic chemical etch of Co, Fe, and CoFeB

Halogen-based chemistries are essential to enable a reactive ion etch process for non-volatile transition metals such as Co and Fe. However, as was shown in the previous sections, the effects of these halogen chemistries on the magnetic properties of single element and ferromagnetic alloys has to be mitigated through the introduction of a reductive chemistry like H₂. Additionally, the reactive ion etch process tends to have very little chemical selectivity when it comes to removing specific layers of material from the stack in a well-controlled fashion. Although this chemistry is capable of sustaining an enhanced etch rate, the problems of corrosion, degradation of magnetic properties, and lack of selectivity suggested that additional routes for patterning these thin films with atomic scale fidelity be explored.

4.3.1 Thermodynamic assessment of organic etch of Co and Fe

The initial step in finding additional, non-corrosive chemistries that were capable of forming volatile etch products was inspired by the use of chemical vapor deposition precursors. These compounds contain bulky organic ligands which surround the transition metal atom core, creating metalorganic molecules with substantial volatility. Beta diketonate complexes, for example, are sufficiently stable to be synthesized and transported for CVD and ALD of metals such as Co and Fe. Study of chemical interactions between these two metals as well as two organic compounds, acetylacetonate (acac) and hexafluoroacetylacetonate (hfac), were undertaken by first delineating the idealized gas-surface reactions (Table 4-2) and subsequently constructing the volatility diagrams for the corresponding equilibria (Figure 4-8).

Table 4-2. Reactions used for creating volatility diagram shown in for Co-acac/hfac and Fe-acac/hfac systems.

	Reaction	ΔG (kJ/mol)
(1)	$\text{Co(c)} \rightarrow \text{Co(g)}$	379.8
(2)	$\text{Co(c)} + 2 \text{ acac(g)} \rightarrow \text{Co(acac)}_2\text{(g)}$	1053.0
(3)	$\text{Co(acac)}_2\text{(c)} + \text{ acac(g)} \rightarrow \text{Co(acac)}_3\text{(g)}$	551.8
(4)	$\text{Co(acac)}_2\text{(c)} \rightarrow \text{Co(acac)}_2\text{(g)}$	50.6
(5)	$\text{Co(acac)}_3\text{(c)} \rightarrow \text{Co(acac)}_3\text{(g)}$	44.7
(6)	$\text{Co(c)} + 3 \text{ hfac(g)} \rightarrow \text{Co(hfac)}_3\text{(g)}$	885.3
(7)	$\text{Co(hfac)}_3\text{(c)} \rightarrow \text{Co(hfac)}_3\text{(g)}$	13.0
(8)	$\text{Fe(c)} \rightarrow \text{Fe(g)}$	369.4
(9)	$\text{Fe(c)} + 3 \text{ acac (g)} \rightarrow \text{Fe(acac)}_3\text{(g)}$	1537.9
(10)	$\text{Fe(acac)}_3\text{(c)} \rightarrow \text{Fe(acac)}_3\text{(g)}$	34.3
(11)	$\text{Fe(c)} + 3 \text{ hfac(g)} \rightarrow \text{Fe(hfac)}_3\text{(g)}$	881.6
(12)	$\text{Fe(hfac)}_3\text{(c)} \rightarrow \text{Fe(hfac)}_3\text{(g)}$	9.3

In this volatility analysis, the threshold for achieving a substantial etch rate is fixed by the partial pressure of etch products at a value of 10^{-8} atm. From the volatility diagrams for Co reacting with acac and hfac in Figure 4-8, the calculated pressure of gas phase Co(acac)_2 was predicted to occur at pressure slightly less than the 10^{-8} atm threshold within the etchant operating pressure regime of 10^{-5} to 10^{-2} atm of acac(g). On the other hand, the volatility analysis of Co in hfac suggests that substantially higher pressures of hfac(g) would be necessary to achieve any substantial pressure of $\text{Co(hfac)}_3\text{(g)}$. From this analysis, the acac chemistry was predicted to be more effective at etching Co than hfac.

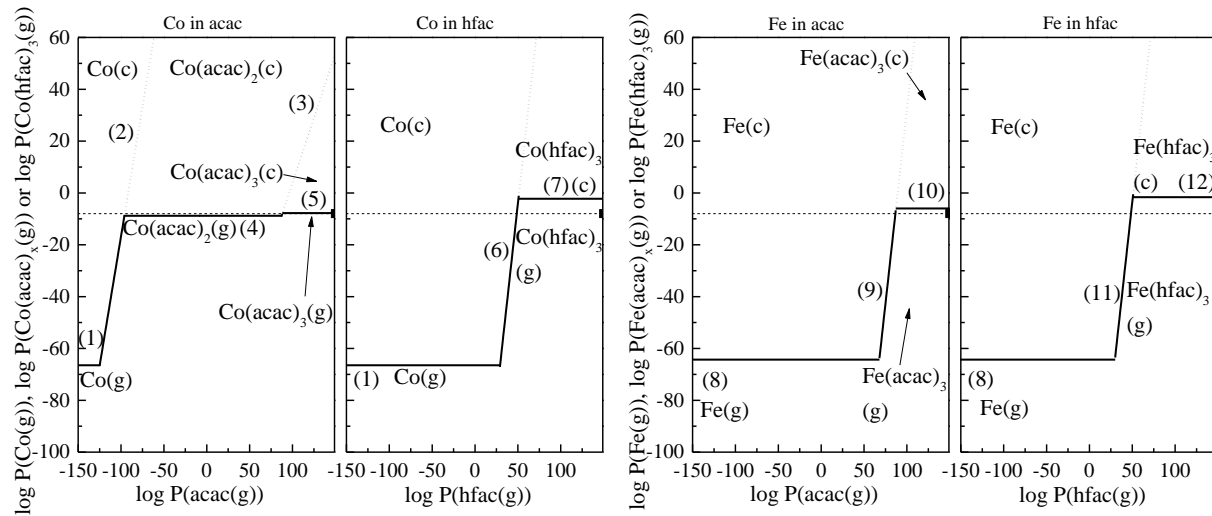


Figure 4-8. Volatility diagrams for Co-acac, Co-hfac, Fe-acac, and Fe-hfac systems at 300 K with the corresponding dashed line at 10^{-8} atm as the threshold for observable etch.

Analysis of Fe in the same acac and hfac systems led to a substantially different result. The pressures necessary to generate $\text{Fe}(\text{acac})_3$ in the gas phase were significantly higher than those predicted for $\text{Fe}(\text{hfac})_3$, which although still requiring a high pressure of hfac, was achievable by manipulating the equilibrium line through increasing the temperature beyond the initially assessed 300 K. The results from these volatility assessments suggested that selectivity may exist between Co and Fe depending on the form of chemistry used to etch them. In the case of Co, acac would be the more effective etchant, while hfac would be more effective at etching Fe.

4.3.2 Organic chemical etch of Co, Fe, and CoFeB

Etch of Co and Fe was investigated using solution phase processing at increased temperatures of $80\text{ }^\circ\text{C}$ with high concentrations of acac (>99 %) and hfac (97 %). Ten milliliters of each solution were pipetted into 10 dram glass vials and heated to $80\text{ }^\circ\text{C}$ in a mineral oil bath using a temperature-controlled hotplate to ensure uniform heating of the etch solution. Square ($1\text{ cm} \times 1\text{ cm}$) coupons of 500 nm Co and Fe deposited on p-type Si using a 10 nm Ti adhesion layer

were each immersed in 10 mL of acac or hfac for etch times up to 120 min, with the exception of Fe, due to the etch endpoint being reached after forty minutes. After etching, samples were cleaved and their cross-sections were measured to determine the change in thickness using SEM. This etched thickness was then plotted as a function of etch time (Figure 4-9). The resulting etch rate of Co in acac (3.3 nm/min) was significantly higher than in hfac (0.3 nm/min). Additionally, Fe was measured to etch much more quickly in hfac (12.1 nm/min) than in acac (0.9 nm/min).

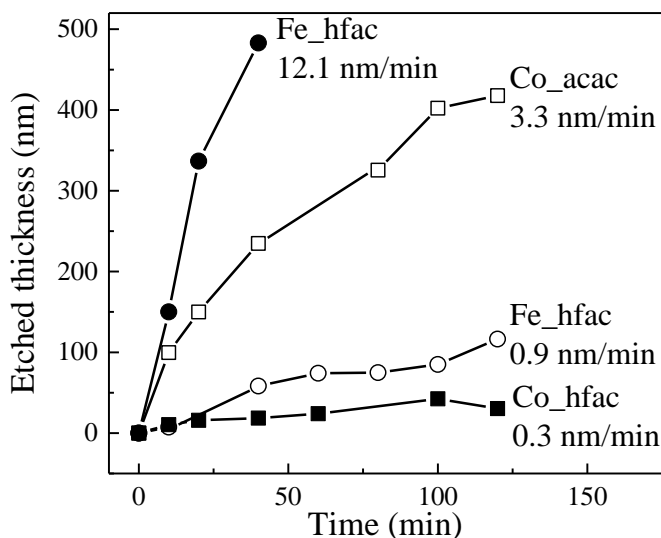


Figure 4-9. Etched thickness of Co and Fe etched in pure acac and hfac solutions at 80 °C as a function of time.

This large difference in each metal etch rate confirms the thermodynamic assessment discussed before. Nonetheless, characterization of etch products was necessary to verify the idealized reactions listed in Table 4-2. Post-etch solutions of Co-acac, Co-hfac, Fe-acac, and Fe-hfac were examined using electrospray ionization mass spectrometry in order to identify etch products existing in the solution phase. ESI-MS indicates that Co and Fe form different etch products. As shown in Figure 4-10a, $\text{Co}(\text{acac})_2$, with a mass-to-charge ratio value of 257 amu was measured to form upon Co etching in acac solution with an isotope distribution pattern for m/z

values of 257 (87.6%) and 258 (11.2%), 259 (1.3%), and 260 m/z (0.1%). In the measured spectra, 257 and 258 m/z were observed; however, both 259 and 260 m/z values were below the limits of detection. As suggested by the very small etch rate of Co in hfac (0.3 nm/min), the corresponding ESI mass spectra shown in Figure 4-10b indicates no detectable amount of $\text{Co}(\text{hfac})_3$ which is expected to have a dominant peak at mass-to-charge values of 680.

On the other hand, for Fe etched in acac, the very slow etch rate was experimentally corroborated by no detectable concentration of $\text{Fe}(\text{acac})_3$ etch product, generally observed at m/z values of 353 amu. However, for hfac, a prominent peak was measured at 677 amu and corresponds well to the calculated isotopic pattern of 677 (77.7%), 678 (18.9%), and 679 (3.1%) (Figure 4-10c,d).

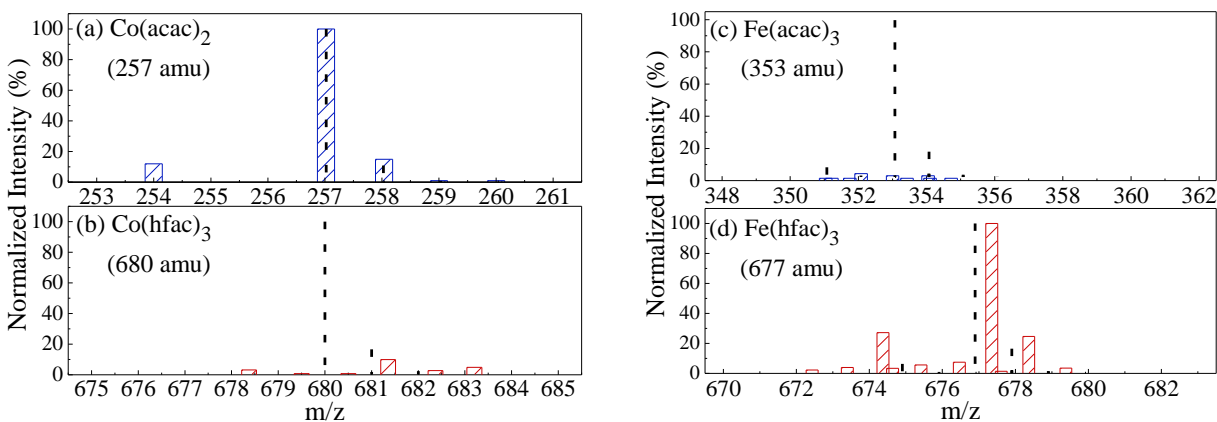


Figure 4-10. Electrospray ionization mass spectra for post etch solutions of Co etched in solutions of (a) acac and (b) hfac as well as Fe etched in solutions of (c) acac and (d) hfac at 80 °C. Vertical dashed lines indicate the typical isotope distribution for $\text{Co}(\text{acac})_2$, $\text{Co}(\text{hfac})_3$, $\text{Fe}(\text{acac})_3$, and $\text{Fe}(\text{hfac})_3$.

Identification of the $\text{Co}(\text{acac})_2$ and $\text{Fe}(\text{hfac})_3$ etch products as well as the measured selectivity of Co in acac and Fe in hfac were critical as these observations confirm the hypothesized

etch products used in the original volatility diagram construction. Additionally, use of acac and hfac as effective etchants for Co and Fe, respectively, gave rise to subsequent etch experiments for assessing their efficacy in solution phase etch of CoFeB.

Using an identical experimental setup as that described above, square (1 cm × 1 cm) coupons of 30 nm CoFeB were etched first in concentrated solutions of acac (>99%) and hfac (97%) at 80 °C for times up to 120 seconds. SEM cross-section measurements indicated the initial removal of 3 and 4 nm in the first thirty seconds of solution etch for acac and hfac, respectively. The etched thickness was observed to saturate at etch times past this initial thirty second period, suggesting that the thickness change resulted from selective removal of oxidized CoFeB generated by exposure to atmosphere. Additionally, since acac and hfac were observed in previous elemental Co and Fe etch studies to selectively etch these materials, the saturation of etch for CoFeB was also due to possible selective removal of Co in acac chemistry, forming an Fe-rich etch stop layer, while the opposite occurred for hfac through selective removal of Fe and formation of an Co-rich etch stop layer. (Chen 2017)

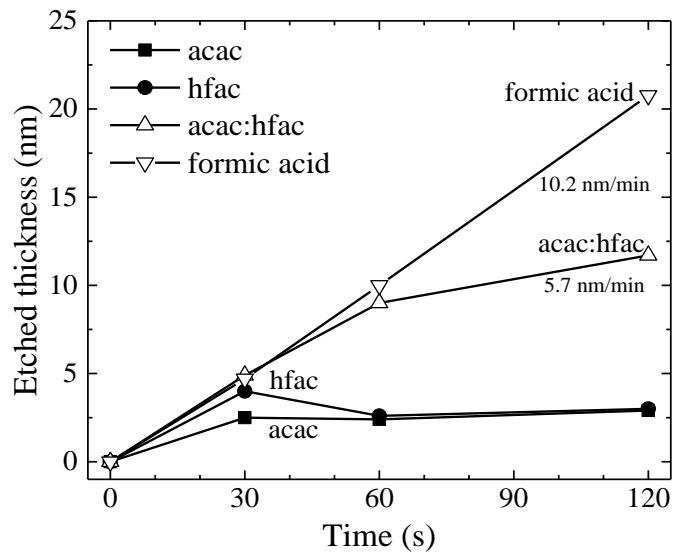


Figure 4-11. Etched thickness of 30 nm CoFeB in acac, hfac, formic acid, and mixtures of acac/hfac for etch times up to 120 s.

Based on previous experimental results, the efficacy of acac and hfac in etching Co and Fe separately suggested that both solution phase etchants together could be effective for removal of CoFeB. An equal volume mixture of acac and hfac solutions was studied at 80 °C for CoFeB etch, resulting in an average etch rate of 5.7 nm/min. This increased etch rate was attributed to the ability of acac and hfac to separately etch Co and Fe, which, when combined in the solution phase enabled etch of CoFeB alloy. In addition to beta-diketonate chemistries, formic acid was also studied as a candidate etchant for metal, yielding a substantial increase in etch rate to 10.2 nm/min. Nonetheless, translation of these chemistries into the gas phase results in a substantial reduction in concentration of the organic vapor, hindering the chemical etch process.

4.4 Cyclical oxidation and chemical vapor etch of Co, Fe, and CoFeB

In order to achieve etch in the gas phase using organics, formic acid was chosen as the candidate chemistry due to its high etch rate compared to acac, hfac, and the acac/hfac mixture. However, in order to achieve an atomic layer etch process, it was necessary to, instead of a continuous etch process, create a chemical contrast that allowed for selective removal of atomically thin layers of material with each etch cycle. This contrast was achieved using plasma oxidation which generated energetic oxygen neutrals and ions capable of reacting with the surface and forming a metal oxide layer.

The goal was to determine how the oxidation depth could be controlled first using oxidation time, which allowed for the elucidation of which mechanism was responsible for Fe₂O₃ and CoO formation. Additionally, the effect of ion energy was also explored, as the use of oxygen ions enables directional surface modification. Directionality could be exploited to pattern metallic thin films, resulting in the anisotropic etch profile necessary for implementation as a device patterning process.

4.4.1 Enabling chemical contrast for selective etch of metal oxide

From thermodynamic calculations done previously, the change in Gibbs free energy of reaction indicated that selectivity was achievable depending on the chemistry for etching Co and Fe. However, in subsequent cases, as with vapor phase etch of CoFeB, the aim was for selective etching of a surface modified layer using a cyclical process such as that applied to etch copper in the previous chapter.

In order to determine the feasibility of selective vapor phase etch using plasma oxidation to modify the thin film surface, ΔG_{rxn} values between condensed phase Co, CoO, Fe, and Fe₂O₃

and gaseous formic acid were performed at 300 K to determine the spontaneity of these reactions. The corresponding reactions and free energy values are summarized in Table 4-3. From these calculations, it can be seen that for both Co and Fe, upon transitioning to their corresponding oxides, a change in sign (from positive to negative) of the value of ΔG_{rxn} was observed. These negative values indicated that the vapor phase reactions with CoO and Fe₂O₃ were indeed spontaneous while direct reaction of formic acid with the metal surface was not.

Table 4-3. Reactions and corresponding ΔG_{rxn} values for Co, CoO, Fe, and Fe₂O₃ reacting with vapor phase formic acid (HCOOH) at 300 K.

	Reaction	ΔG (kJ/mol)
(1)	$\text{Co(c)} + 2 \text{HCOOH(g)} \rightarrow \text{Co(HCOO)}_2\text{(g)} + \text{H}_2\text{(g)}$	177.1
(2)	$\text{CoO(c)} + 2 \text{HCOOH(g)} \rightarrow \text{Co(HCOO)}_2\text{(g)} + \text{H}_2\text{O(g)}$	-132.3
(3)	$\text{Fe(c)} + 3 \text{HCOOH(g)} \rightarrow \text{Fe(HCOO)}_3\text{(g)} + 3/2 \text{H}_2\text{(g)}$	26.5
(4)	$\text{Fe}_2\text{O}_3\text{(c)} + 6 \text{HCOOH(g)} \rightarrow 2 \text{Fe(HCOO)}_3\text{(g)} + 3 \text{H}_2\text{O(g)}$	-48.5

Harnessing this selectivity first required studying the extent to which the surface of single element Co and Fe thin films could be oxidized. For these cases, the most effective means for measuring not just the chemical bonding states present on the surface, but also the thickness was x-ray photoelectron spectroscopy. Using this technique, the first 10 nm of each film were probed to determine the predominant oxidation states as well as to calculate the thickness of oxide using the attenuation of the Co⁰ or Fe⁰ signal at binding energies of 778.2 and 706.8 eV through the metal oxide overlayer. Initial studies focused on investigating the thickness change upon oxidation as well as time dependence. Further experiments were conducted to assess the ability to oxidize by manipulating the applied bias voltage and thus the ion energy.

4.4.2 Controlling oxide growth through plasma oxidation

Controlling the thickness of generated oxide during the surface modification step was crucial to controlling the etch rate. One means of achieving this control is through limiting the time to which thin films are subjected to the plasma modification step. For both Co and Fe, the thickness of CoO and Fe₂O₃ formed were measured using an overlayer model based on post-processing XPS characterization. Upon chemisorption of the initial monolayer of oxygen to the surface during plasma exposure, oxidation occurs through diffusion of atomic oxygen to the metal interface or metal cations to the oxide interface. The observed increase in Fe₂O₃ thickness as a function of oxidation time compared to CoO is attributed to the difference in diffusivity of each of these metals in their corresponding oxides (Figure 4-12). Both metals oxidize very quickly up to approximately 2 and 3 nm of oxide for Co and Fe, respectively, in the initial minute of plasma exposure and subsequently proceed to saturate in oxide thickness with increasing time to values of around 3.5 nm and 4.4 nm after 5 min exposure.

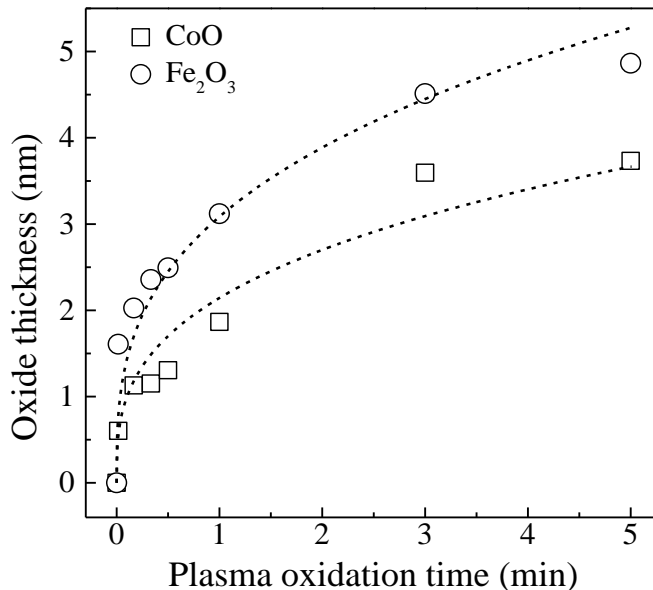


Figure 4-12. Thicknesses of CoO and Fe₂O₃ as a function of plasma oxidation time for O₂ plasma at 500 W source power and -100 V applied bias.

For Fe, the diffusion coefficient of $4.4 \times 10^{-2} \text{ cm}^2/\text{s}$ is greater than that of Co, $1.2 \times 10^{-1} \text{ cm}^2/\text{s}$. In addition, as transition metals, Fe and Co have the propensity to adopt multiple valence states, namely in the form of Co^{2+} , Co^{3+} , Fe^{2+} and Fe^{3+} , during oxidation with preferential diffusion along grain boundaries and defects within the film as a result of the reduced activation energy at these locations. (Duffy 1983) Multiple empirical kinetic models have been proposed; however, the most effective fitting was observed to be in the form of an inverse logarithmic rate law:

$$\frac{1}{d} = A - B \log(t) \quad (4.1)$$

where d is the oxide thickness, t is oxidation time, and A and B are constants. Fitting the iron oxide thickness using this model resulted in values of 0.06 and 0.01 for A and B with a corresponding correlation value (r) of 98%. CoO thickness was fit similarly, yielding A and B values of 0.16 and 0.02 with a corresponding r -value of 97%. The efficacy of this model fit suggests that oxidation of both Fe and Co proceed predominantly through diffusion of metal cations.

Studies on the effect of low energy ion bombardment during the modification step focused mainly on single element Co, as this material was found to be more difficult to oxidize than Fe. From literature, processing took place in a custom built plasma reactor which utilizes an electron beam to drive ionization and generate a discharge with an electron temperature (T_e) from 0.3-1.0 eV, substantially lower than conventional RF or microwave plasma sources. (Walton 2015) Subunity values of T_e can be achieved through the introduction of reactive gas mixtures into the plasma feed—such as the Ar/O₂ mixture used in these experiments—creating additional pathways for electron cooling through vibrational and rotational excitation. (Boris 2013, Petrov 2013)

Decreased electron temperature results in a subsequent reduction in the plasma potential to a range of 3-6 eV. Elevation of this ion energy can be achieved by applying a negative DC voltage to the sample itself, which is the method commonly found in conventional plasma reactors. Alternatively, a positive voltage can be applied to the electron beam termination anode in contact with the plasma, resulting in an increased plasma potential and uniformly increased ion energies across the entire sample geometry. (Walton 2004)

Leveraging this method of biasing the electron beam terminal anode, or beam dump, the oxidation of Co was studied in a mixture of Ar/O₂ at a fixed time of 600 s and increasing bias voltages of 0, 10, 30, and 50 V. Characterization of these samples before and after processing in Ar/O₂ as well as after subsequent exposure to formic acid solution was performed using XPS. Surface analysis of these samples before processing indicated the presence of mixed Co⁰ and Co²⁺ bonding states on the surface due to storage of the as-deposited material under atmosphere and resulting formation of a native oxide layer. For each subsequently plasma oxidized sample, XPS indicates the formation of an oxide layer that is equivalent or thicker than the 7-10 nm penetration depth accessible by the XPS. Samples were then subjected to short and long etch times in concentrated formic acid solutions at 80 °C for 5 seconds and 15 minutes. After five second exposure, a majority of the CoO was removed, leaving again a mixture of Co⁰ and Co²⁺ surface bonding states; however, compared to pre-processed Co, the amount of Co²⁺ was substantially reduced, confirmed by a decrease in O 1s signal as well. After the long 15 min etch time in solution, the film was completely removed, evidenced by no signal in the high resolution Co 2p binding energy regime and the presence of O-Si bonding. Additionally, a survey scan of all elements present on the sample surface after this formic acid exposure shows strong Si 2p and Si 2s peaks from the detection of the underlying Si substrate.

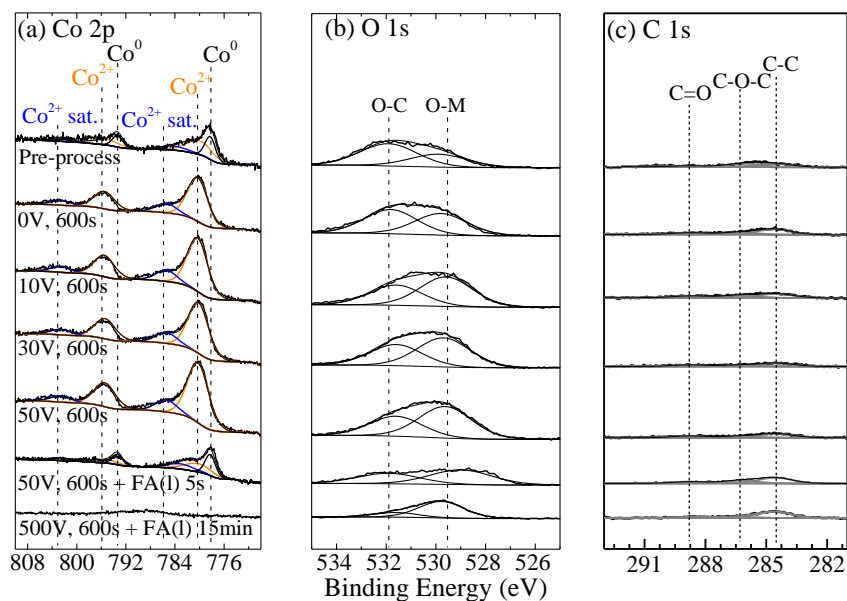


Figure 4-13. High resolution x-ray photoelectron spectra of (a) Co 2p, (b) O 1s, and (c) C 1s binding energy regions for 30 nm Co samples pre-processing, after exposure to electron beam driven O₂ plasmas with increasing applied bias voltages of 0, 10, 30, and 50 V for 600 s, and after plasma oxidation at 50 V bias with separate subsequent exposure to concentrated formic acid solutions (>97%) at 80 °C for 5 s and 15 min.

Oxidation of Co using longer exposure times at reduced ion energies show comparable thicknesses of oxide generation compared to inductively coupled plasma oxidation. Complete removal of the 30 nm Co after the prolonged etch rate of 15 min was observed to be within agreement considering the modification depth achieved under ion energies up to 200 eV. Due to the prolonged plasma exposure time, even at low ion energy values, the oxidation of Co was measured to increase beyond the initial modification observed under ICP conditions as expected. Additionally, at reduced solution phase etch times down to 5 s, the observed removal of oxidized Co and subsequent emergence of metallic Co in Figure 4-13 confirms that CoO etches rapidly in solution phase, exhibiting a high selectivity over the remaining Co.

4.4.3 Chemical vapor etch of oxidized Co, Fe, and CoFeB

Based upon the success of selectively removing oxidized Co in solution phase formic acid, this chemistry was transferred to the gas phase through the use of the vaporizer setup described previously in Chapter 3. The vapor chamber, which was heated in conjunction with the formic acid vapor to 80 °C was capable of achieving formic acid pressures up to 148 Torr through isolation of the chamber from the mechanical pump. The accumulation of the formic acid vapor to a high pressure was responsible for the chemical removal of oxidized Co and Fe. To ensure a measurable etch of both materials, a cyclical process was implemented consisting of 5 min of O₂ plasma oxidation at 500 W source power and -100 V applied bias followed by exposure to formic acid vapor at 80 °C and 148 Torr for 50 s.

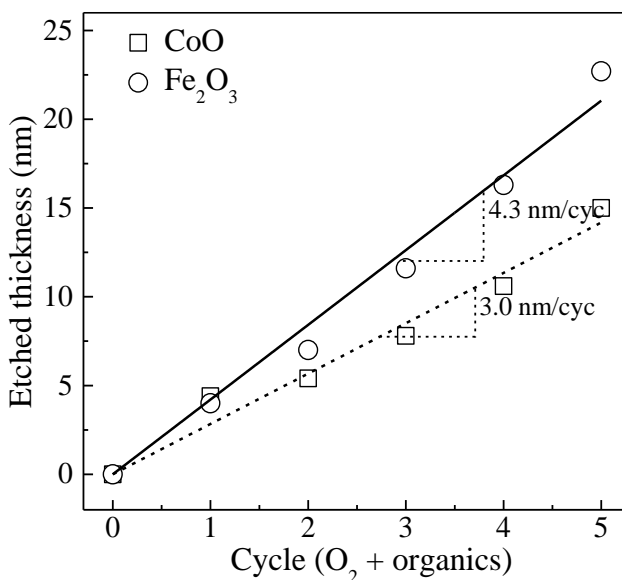


Figure 4-14. Etched thickness of CoO and Fe₂O₃ as a function of oxidation and formic acid vapor etch cycles. Cycles consisted of O₂ plasma at 500 W source power and -100 V applied bias for 5 min followed by formic acid vapor at 80 °C, 148 Torr for 50 s.

For both Fe and Co, cyclical etch rates using this approach resulted in etch rates of 4.3 and 3.0 nm/cyc, respectively. When compared to the grown thicknesses of Fe_2O_3 and CoO , one can see that these etch per cycle rates closely tracked the thickness of oxide generated in the measured films. With this knowledge, it can be concluded that controlling the oxide thickness of single element thin films provides a route for effectively controlling the thickness of material removed during the chemical etch portion of the cycle. However, in the context of etching ferromagnetic thin films for the MTJ stack, CoFeB remains as the main material of interest. In general, thicknesses of CoFeB used in the free and fixed layers which must be patterned are generally less than 3 nm. In order to scale down the etch rate of CoFeB to conform to these thickness requirements, the effect of reducing the oxidation time was explored in parallel with studying the effects of exposure to plasma oxidation and formic acid vapor alone. Plasma oxidation time was reduced to 2 min while formic acid vapor exposure conditions were kept the same as those implemented for Co and Fe. Figure 4-15 summarizes the measured etched thickness using SEM cross-sections of CoFeB samples after numerous cycles of oxidation and formic acid, oxidation alone, and formic acid vapor alone.

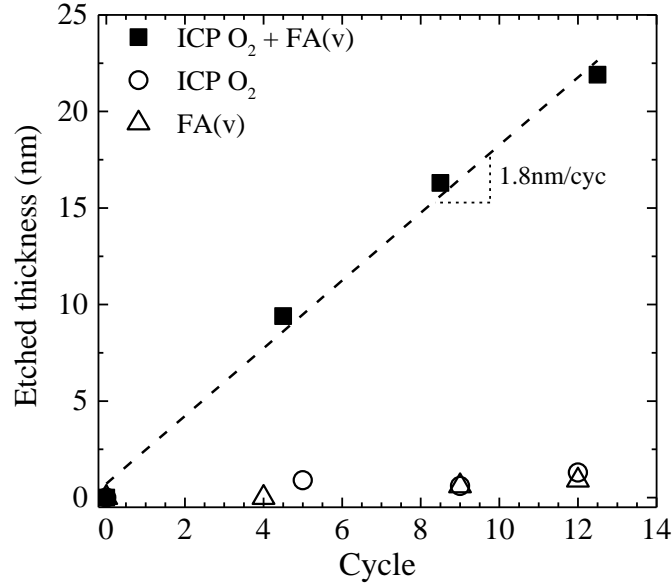


Figure 4-15. Etched thickness of CoFeB as a function of oxidation and formic acid vapor etch cycles as well as equivalent time exposures of only plasma oxidation and only formic acid vapor. Each cycle consisted of O₂ plasma at 500 W source power and -100 V applied bias for 2 min followed by formic acid vapor at 80 °C and 148 Torr for 50 s.

For both plasma oxidation and formic acid vapor exposure alone at time-equivalent cycles, no significant etch was observed. However, when used in conjunction, oxidation for only 2 min followed formic acid vapor etch resulted in a linear etch rate of approximately 1.8 nm/cycle. Comparing this etch rate to one calculated by calculating the weighted average etch rates for Co and Fe alone under 5 min oxidation indicates that the reduction in plasma exposure time was effective in reducing the attained etched thickness per cycle.

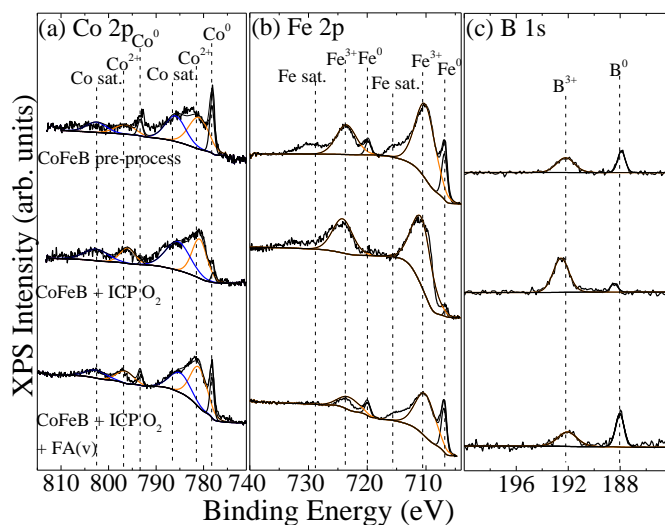


Figure 4-16. High resolution x-ray photoelectron spectra of (a) Co 2p, (b) Fe 2p, (c) B 1s binding energy regimes for pre-process CoFeB, CoFeB after oxidation in 500 W_s, -100 V_b O₂ plasma for 2 min, and oxidation with subsequent formic acid vapor at 80 °C and 148 Torr for 50 s.

Confirmation of the changing chemical bonding states before and after processing under oxygen plasma and subsequent formic acid vapor exposure were characterized using high resolution x-ray photoelectron spectroscopy (Figure 4-16). Pre-process CoFeB exhibits a mixture of both metallic and oxidized Co and Fe bonding states as well as oxidized B³⁺ and elemental B⁰. Following a 2 min exposure to 500 W_s O₂ plasma with an applied -100 V_b DC bias, the concentration of metallic Co⁰ and Fe⁰ decreased significantly, as seen in the decrease in relative area of their corresponding peaks alongside the oxidation of elemental B to B₂O₃. This oxidized surface layer was then removed after 50 s exposure to 148 Torr formic acid vapor at 80 °C, evidenced by the reduction in Co²⁺, Fe³⁺ and B³⁺ oxidation states and corresponding emergence of signatures of the metallic Co⁰ and Fe⁰ and elemental B⁰.

4.4.4 Directional etch of patterned metallic thin films

To confirm that the directional surface modification can lead to an anisotropic profile with high selectivity, a vapor phase etch of patterned Co films was demonstrated through sequential exposure O₂ plasma oxidation (500 W, 5 min, 0 V and -200 V bias) and formic acid vapor etch (148 Torr, 50 s). The as-patterned Co film stack was comprised of a 40 nm TiN hard mask/10 nm SiN/ 30 nm Co/ 10 nm barrier layer/ Si substrate and patterned into 70 nm × 10 μm lines. The etch profile of the patterned Co films was characterized by cross-sectional SEM. For comparison, as-patterned Co is shown in the first image column of Figure 4-17. The cross-section of the as-prepared patterned Co shows a line width of 70 nm, slight undercut into the SiN layer, and 30 nm Co. After the sample was subjected to six alternating cycles of O₂ plasma oxidation with no applied bias and formic acid vapor etch, after which, a significant undercut below the hard mask into Co was observed (Figure 4-17a). This undercut is attributed to isotropic oxidation and subsequent formic acid vapor etch completely removing the oxide layer. The hard mask remained intact, confirming the high selectivity of Co to TiN in formic acid vapor. Directional modification of the Co was explored using an applied -200 V substrate bias during oxidation step. An optimized cyclical process comprised of an O₂ plasma (-200 V, 500 W, 5 min) followed by formic acid vapor (50 s) was developed for anisotropic etch. The anisotropic etch profile was observed with the optimized process, with a 5 nm recess in the TiN hard mask, demonstrating the viability of a cyclic oxidation and organic chemical vapor etch process for achieving anisotropic etch profiles (Figure 4-17b).

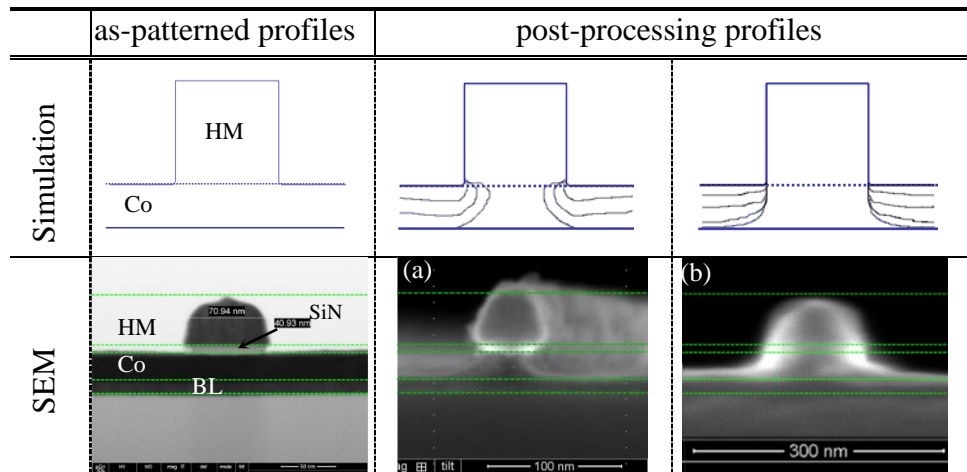


Figure 4-17. Simulated etch profiles and corresponding SEM images of 40 nm TiN hard mask (HM) and 10 nm SiN, patterned on 30 nm Co, with a 10 nm barrier layer (BL) on Si before and after processing. The boundary between each layer is outlined with a thin dashed line. The cyclical etch process was comprised of exposure to an O₂ plasma (500 W, 5 min) and formic acid vapor (50 s). Etch profiles of patterned Co after (a) 6 cycles of oxidation (0 V bias) and formic acid vapor exposure, and (b) 4 alternating cycles of oxidation (-200 V bias) and formic acid vapor exposure.

Subsequent studies utilized direct simulation Monte Carlo modeling previously developed by Hoang et al. for simulating profile evolution of shallow trench isolation etch. (Hoang 2008, Hsu 2008) This methodology, which uses particle-in-cell methods to track the trajectory of species fluxing towards and away from the simulated sample geometry, was able to capture the feature profile for patterning lines of Co with a simple rectangular hard mask in two dimensions. Plasma oxidation conditions followed those presented in the experimental work in Figure 4-17. For isotropic oxidation and etch (Figure 4-17a), an average ion energy of 10 eV as well as a neutral to ion ratio of 0.5 were used. For anisotropic modification and etch, an ion energy of 200 eV was utilized (due to the application of a -200 V bias during the processing step) in conjunction with the same neutral to ion ratio of 0.5. In both cases, simulated profiles are in good agreement with the

experimental results, capturing the substantial mask undercut with no applied bias (10 eV ion energy) as well as the directional etch profile achieved during the application of -200 V bias.

Chapter 5 : Controlled Pt Etch through Tunable Surface Modification

Cl_2 and O_2 -based plasmas were both shown to be effective for generating measurable PtCl_2 and PtO_2 modified surface layers up to thicknesses of 0.5 nm. Removal of PtCl_2 was shown to be effective in subsequent H_2 plasma exposure and resulted in an enhanced etch rate of up to 8.7 nm/cycle compared to 6.4 nm/cycle for equivalent exposures to continuous Cl_2 discharge. This 36% enhancement was attributed to the removal of the chloride layer and confirmed from x-ray photoelectron spectra obtained at each step within the cyclic etch process. Subsequent studies focused on controlling the oxide growth of Pt, which was found to proceed by a starkly different mechanism than most other transition metals, due to the limited valency which Pt adopts upon oxidation (Pt^{4+}). Use of both low energy ions as well as manipulation of the oxidation time gave rise to fine-tuned control over growth of sub-nanometer oxide layers between 0.1-0.5 nm thick. Removal of this modified surface oxide layer was achieved using a chemical etch in concentrated formic acid solution at 80 °C. Leveraging this in the gas phase required generating high pressures of formic acid up to about 150 Torr at 80 °C. The observed etch rate for cyclical plasma oxidation and chemical etch of Pt in formic acid solution and vapor. Etching stopped upon removal of the oxide and reaching the metallic Pt surface, indicating high selectivity. With additional optimization, the etch rate of platinum was confirmed to track closely the thickness of generated oxide layer thickness, indicating that the etch process itself was self-limiting and an atomic scale processing technique.

5.1 Controlled modification of metallic Pt surfaces

As a noble metal, platinum is one of the least reactive elements on the periodic table. It is additionally one of the rarest elements. The nonreactive nature of Pt makes it an attractive choice for applications such as jewelry, but also useful for memory applications through the creation of

the synthetic antiferromagnetic layer present at the bottom of the magnetic tunnel junction where it serves in combination with Mn or magnetic transition metals such as Co and Fe to pin the magnetization direction of the fixed ferromagnetic layer. (Chen 2000, Ohtake 2012)

Platinum's chemical inertness makes it an extremely difficult material to etch. Since its use in DRAM capacitors, etching of thicker platinum electrodes have utilized multiple different chemistries; however, in general these have relied up the reactive nature of Cl_2 and O_2 to enable removal during the plasma etch process. (Kwon 1998, Kim 1999, Kim 2003, Li 2012, Yao 2014) The work presented herein has focused on first examining how platinum thin film surfaces can be precisely modified through exposure to inductively coupled plasmas, ion beams, as well as electron beam generated discharges.

Enhancing the reactivity of metallic Pt can be approached in a fashion similar to chemical synthesis. In this case, elevating the oxidation state of Pt is necessary to achieve reaction with organic ligands, reminiscent of deposition precursor synthesis for creation of volatile metalorganic compounds. From literature, this form of synthesis requires Pt in either to 2+ or 4+ oxidation state. Generally, this has been achieved through chlorination, to change Pt^0 to Pt^{2+} , or oxidation, to change Pt^0 to Pt^{4+} .(Kumar 1989) Alternatively, substitution of PtCl_2 can be achieved as well with subsequent oxidation, providing for a more facile synthesis route with higher yield. (Thurier 2008) In subsequent studies discussed here, an approach similar that which is shown in Figure 5-1 has been utilized with plasma exposure to Cl_2 and O_2 in order to facilitate subsequent reaction with organic ligands and create volatile platinum etch products towards creating an atomic layer etch process (Figure 5-1).

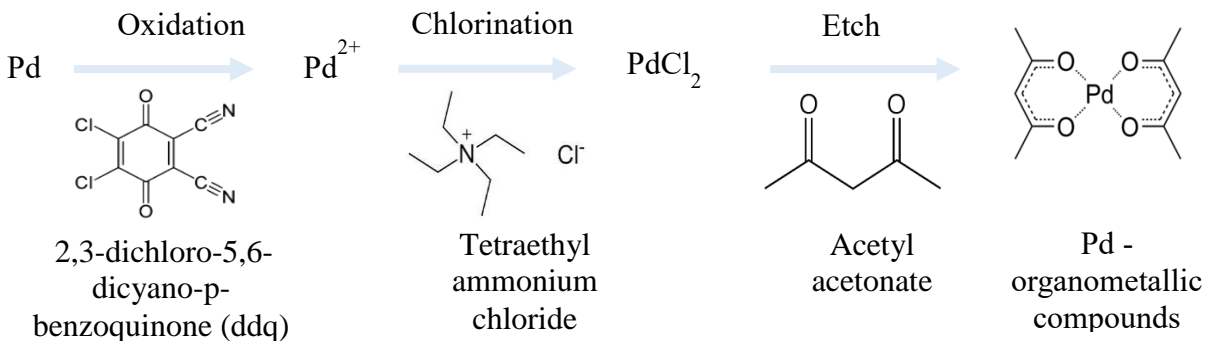


Figure 5-1. Example synthesis route for Pd(acac)₂ using sequential oxidation, chlorination, and reaction with acetylacetone (acac). A similar approach was taken for surface modification and organic chemical etch of Pt.

As was seen before in Chapters 3 and 4, the modification of metallic and intermetallic thin films was a crucial step for controlling the amount of etched material for an atomic layer etch process. Controlled surface modification of platinum has been achieved through manipulation of parameters such as the process chemistry, ion energy—either through use of an inductively coupled plasma or ion beam—as well as oxidation time. Process chemistries explored include the use of Ar, Cl₂, and O₂ which were studied in the form of plasma feed mixtures or sequential steps.

Thermodynamic assessment using minimization of Gibbs free energy as well as volatility analysis indicated that O₂ plasma was a viable surface modification in conjunction with acetylacetone and formic acid. The distribution of favorable species shown in Figure 5-2 indicates that volatile Pt(acac)₂ forms, with increasing concentration at increasing temperature, existing in equilibrium with oxidized Pt.

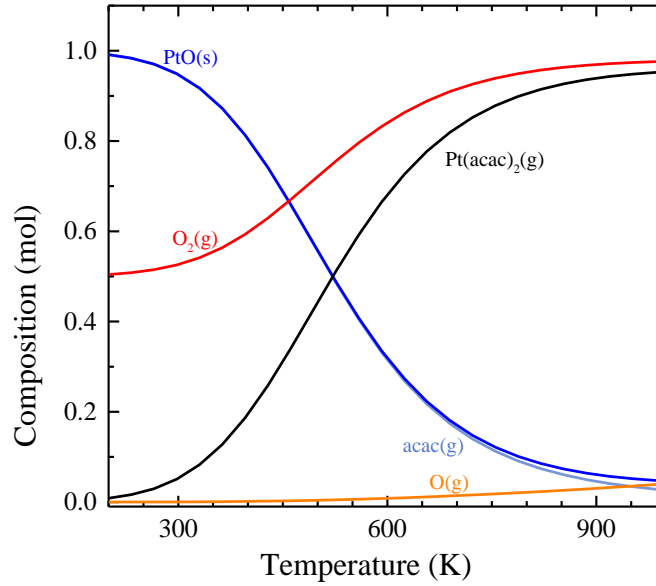


Figure 5-2. Product distribution of Pt-O-acac system simulated through minimization of Gibbs free energy scheme to determine gaseous and condensed phase species present at thermodynamic equilibrium as a function of temperature (K).

Using the results obtained from the minimization of Gibbs free energy, a volatility analysis was undertaken for assessing gas and condensed phase reactions for the Pt-O-organic systems using acac and formic acid vapor as chemical etchants. The calculated equilibrium partial pressure of etch product was determined to be highest for reaction between oxidized Pt and formic acid vapor, suggesting a two-step approach consisting of plasma oxidation and formic acid vapor exposure would be effective for etching Pt thin films (Figure 5-3).

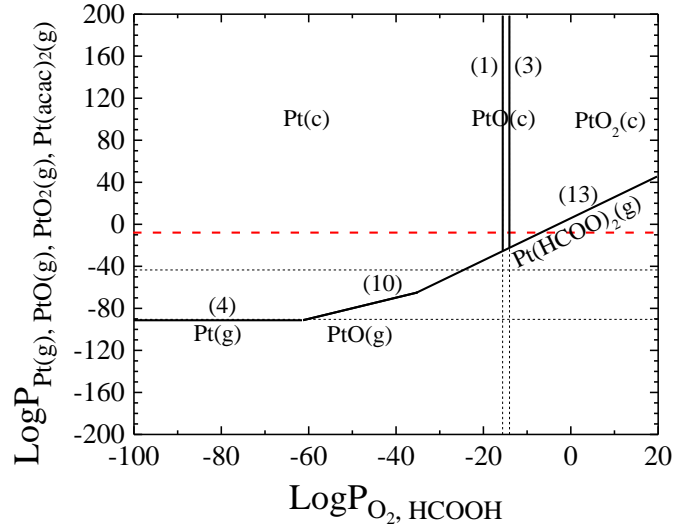


Figure 5-3. Volatility diagrams for Pt-O-formic acid (HCOOH) system at 300 K with the corresponding dashed line at 10^{-8} atm as the threshold for observable etch.

Nonetheless, due to its substantial lack in reactivity compared to the previously studied materials in this work, plasma chlorination and oxidation were both explored as potential routes for enabling surface modification of Pt.

5.1.1 Plasma chlorination and oxidation of Pt

For noble metals such as Pt, these metallic surfaces are especially resistant to changes from a metallic to an oxidized state. Studies were conducted to determine the level to which the platinum films could be chlorinated directly using inductively coupled plasma. Inductively coupled Cl_2 plasma at 200 W and 800 W source powers as well as 10 W and 30 W bias powers were chosen in an effort to reduce potential effects of physical sputtering. Table 5-1 details the conditions investigated first for a pure chlorine plasma, continuing on to then determine the effects of using additional Ar in the discharge.

Table 5-1. Summary of experimental conditions and XPS analysis of chlorinated 30 nm Pt thin films under Cl₂ and Cl₂ with varying amounts of Ar.

Material	Chemistry	Power (W)	Bias (W)	Time (s)
Pt	Cl ₂	200	10	60
		200	30	
	800	10		
	800	30		
	Cl ₂ +Ar (9:1)	800	10	
	Cl ₂ +Ar (5:5)	800	10	
	Cl ₂ +Ar (1:9)	800	10	

Direct exposure to Cl₂ discharge at both source power and bias conditions were shown to result in a small conversion of the metallic Pt surface to an elevated valence state, namely through the formation of PtCl₂, evidenced in the raw XPS spectra through detection of a Pt²⁺ peak. However, across all four combinations of source and bias power conditions for 60 s, no percentage of chlorinated Pt exceeded 15% (Figure 5-4).

Introduction of Ar into the plasma gas has been shown previously to enhance the etch rate of Pt thin films in reactive ion etch processes, suggesting that further surface chlorination may be achievable.(Shibano 1999) The addition of Ar had little effect 10% and 50%, however, use of 90% Ar resulted in a nearly threefold increase in the ratio of the Pt^{X+} oxidation state to metallic platinum as measured by XPS to a value of 29.6%. By using a surplus of Ar, the observable increase in platinum chlorination is likely due in part to the increased dissociation and ionization of Cl₂ as well as increased roughness from Ar⁺ bombardment to the surface. This bombardment resulted in the creation of additional reactive surface sites, and allowed for reactive Cl species to then bond to exposed Pt with increased coordination numbers.

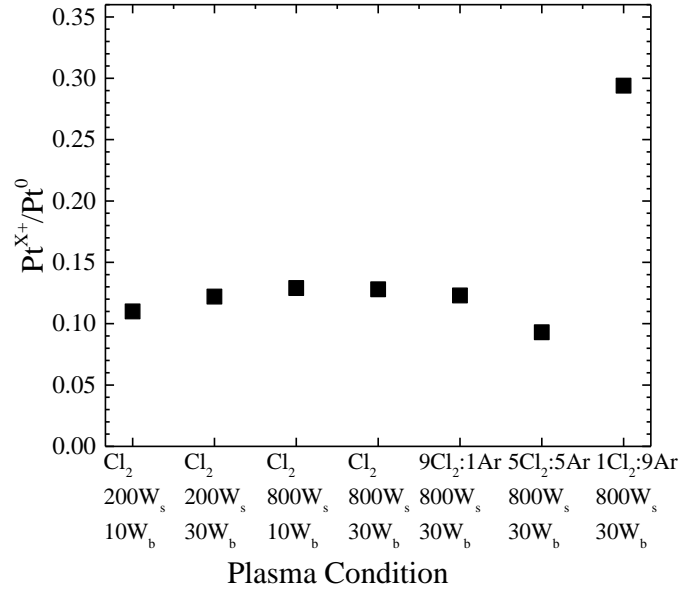


Figure 5-4. Summary of Pt^{X+}/Pt^0 ratio for 60 nm Pt films processed under inductively coupled Cl_2 and Cl_2+Ar plasmas at 200 and 800 W source powers and 10 and 30 W bias powers.

Use of oxygen for chemical modification of Pt was also explored. Formation of PtO_2 is thermodynamically favorable and exists as a stable oxide phase for Pt. In this case, Pt adopts a 4+ oxidation state which has, as expected, a signature binding energy in x-ray photoelectron spectra substantially higher than both Pt^0 and Pt^{2+} . Table 5-2 outlines the experimental conditions used to study O_2 plasma chemistries with added Ar as well as subsequent exposure to Cl_2 discharge.

Table 5-2 Summary of experimental conditions and XPS quantification of oxidized 30 nm Pt thin films. Additional experiments investigated oxidation as a primary step to ultimately achieve chlorination.

Material	Chemistry	Power (W)	Bias (W)	Time (s)
Pt	O ₂ +Ar(9:1)	800	10	
	O ₂ +Ar(5:5)	800	10	60
	O ₂ +Ar(1:9)	800	10	
	O ₂ /Cl ₂	200	30	
	O ₂ /Cl ₂	200	100	60/60
	O ₂ /Cl ₂	800	30	

Starting with an O₂ to Ar ratio of 9:1 at 800 W source power and 10 W bias, a Pt⁴⁺/Pt⁰ ratio of 0.761 is observed, showing a substantial increase compared to the results previously discussed for a similar mixture of Cl₂:Ar. However, compared to previous Ar:Cl₂ mixtures, further increasing the amount of Ar in the plasma led to a decrease in the ratio of oxidized to metallic platinum to 0.66 and 0.48 at 5:5 and 1:9 O₂:Ar ratio, respectively. In both cases, these ratios remain higher than the corresponding ratios observed in Cl₂:Ar and attributed to be likely due to a dilution effect.

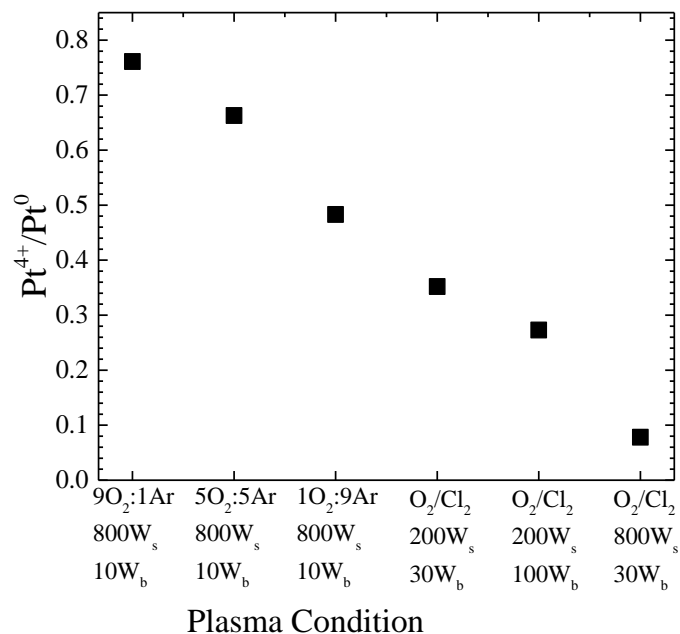


Figure 5-5. Summary of Pt⁴⁺/Pt⁰ ratio for 60 nm Pt processed under inductively coupled plasma mixtures of O₂ and Ar as well as O₂ with subsequent Cl₂ exposure.

Due to the large difference in direct chlorination and oxidation of the platinum films observed using solely chlorine/argon and oxygen/argon mixtures, Pt films were further studied using cyclical exposures of O₂/Cl₂. Pt films were processed under identical conditions for O₂ and Cl₂ plasma, namely 200 W source power with 30 and 100 W bias power as well as 800 W source power and 30 W bias power with the objective of synthesizing a chlorinated Pt surface through displacement of oxygen.

As summarized in Figure 5-5, the decrease in Pt⁴⁺ oxidation state shows little improvement when compared to the use of direct exposure to chlorine plasma. However, when examining the Cl 2p XPS spectrum, a shift is observed from the metal oxide to metal chloride as shown in Figure 5-6a. From this Pt 4f spectra, the three distinct peaks indicating mixed valence of Pt were not

observed indicating lack of Pt⁴⁺; however, Pt²⁺ is observed, suggesting the formation of PtCl₂ on the surface.

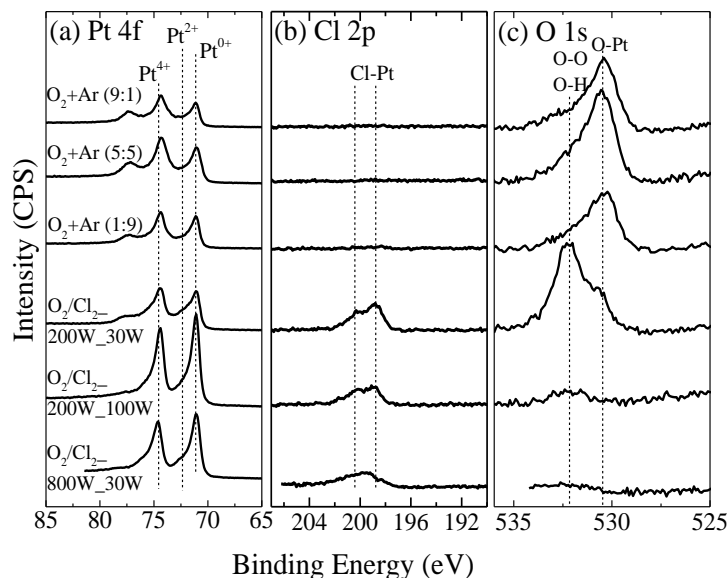


Figure 5-6. High resolution x-ray photoelectron spectra of (a) Pt 4f, (b) Cl 2p, and (c) O 1s binding energy regimes for Pt films processed under mixtures of O₂:Ar as well as sequential exposure to O₂/Cl₂.

In addition, a substantial amount of chlorine was measured on the surface following Cl₂ plasma exposure across all three conditions, with the greatest percentage occurring at the 200 W source power and 30 W bias condition. Furthermore, Figure 5-6c shows a substantial amount of O-Pt bonding on the surface after O₂:Ar exposure. However, after a single cycle of O₂ followed by Cl₂ no O-Pt signature was observed on the surface, suggesting reaction of PtO₂ with excited chlorine species to create PtCl₂.

5.1.2 Oxygen ion beam modification of Pt

Ion beams have been utilized in the semiconductor industry mainly for the purpose of ion beam milling, a process which relies on the ability of large charge particle, namely noble gas ions,

to physically sputter material in order to achieve etch. (Kamata 2004, McMorran 2010, Read 2014) This form of processing can be used when materials have low volatility, such as with patterning transition and noble metal thin films. In the case of ion beam milling, a nonreactive gas, such as Ar, is used, resulting in a coherent beam of Ar^+ which can be directed at the sample surface. One drawback of this method is the lack of selectivity in sputtering various materials. Use of ion beam milling has been wide spread in patterning memory devices; however, due to the nonvolatile nature of sputter etch products—as these are predominantly gas phase metal atoms—unwanted redeposition can also occur for high aspect ratio features, causing detrimental effects to devices. In these studies, a 3 cm Kaufman ion beam source was used to generate directional oxygen ions with tunable ion energies as an alternative to employing inductively coupled plasmas for studying surface modification. This beam was explored to determine the efficacy of using excited oxygen ions to modify the surface at energies of 50, 100, 200, and 500 eV.

For the following studies, 30 nm Pt films were exposed to ion beam energies of 50 to 500 eV for 300 seconds. Surface characterizations of these samples were undertaken using XPS to determine the overall chemical bonding states and surface composition for each film. As shown in Figure 5-7a, deconvolution of high resolution Pt 4f x-ray photoelectron spectra into corresponding chemical bonding states indicates a substantial increase in the fitted peak area of the Pt^{4+} oxidation state, confirming the formation of PtO_2 occurs as a result of samples exposed to beams with oxygen ions at energies of 50 and 100eV. This elevated valence state was mainly observed at these two lower ion energy conditions. Increasing the ion energy to 200 eV and 500 eV indicated that the PtO_2 was no longer present on the surface in the substantial amount observed at 50 and 100 eV.

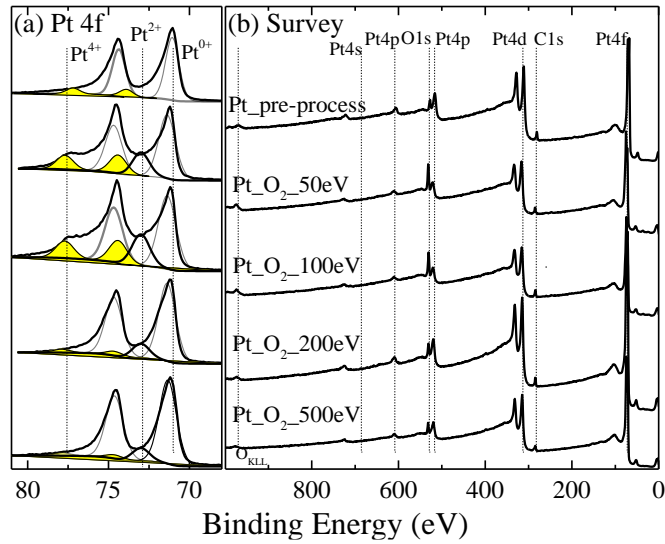


Figure 5-7 XPS spectrum of Pt films before processing and after exposure to oxygen ion beams with ion energies of 50, 100, 200, and 500 eV for 300 seconds.

Integration of the spectral area of each of these Pt bonding states allowed for quantification of these spectra. Both 50 eV and 100 eV oxygen ions were shown to be quite effective at modifying the metallic pre-processing Pt sample and generating a surface layer of PtO₂, resulting in 53% and 49% of total measured platinum on the surface existing in the Pt⁴⁺ valence state. This percentage of Pt⁴⁺ was shown to decrease substantially as the ion energy was increased to 200 and 500 eV. From the raw spectra in Figure 5-7, the Pt⁴⁺ peak was observed to be substantially smaller, decreasing to result 20% and 16% of the platinum on the surface existing in the form of PtO₂.

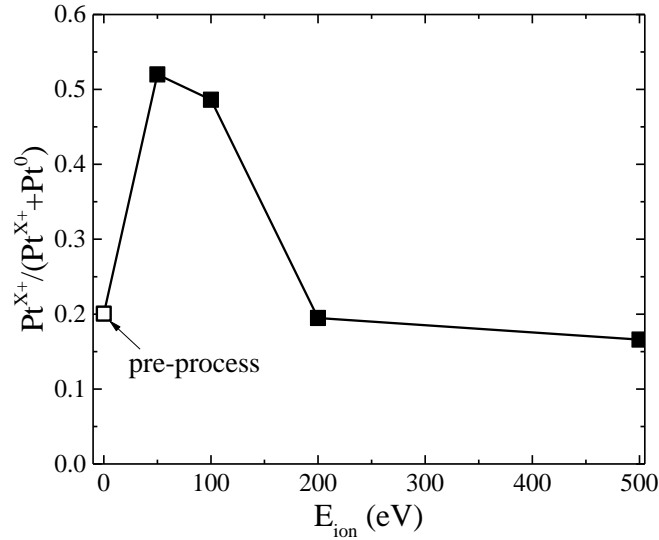


Figure 5-8. Fraction of oxidized Pt as a function of ion energy for 30 nm Pt films exposed to 50, 100, 200, and 500 eV oxygen ion beam for 10 min.

The dependence of the fraction of the oxidized Pt state was summarized as a function of the ion energy (E_{ion}) in Figure 5-8. These reduced percentages of Pt^{4+} observed at higher ion energies was an indication of the physical sputtering effect. Ions bombarding the surface at reduced energies, such as those at or below 100 eV resulted in chemical modification, transforming the Pt^0 bonding state into Pt^{4+} through the formation of PtO_2 . However, upon increasing this energy to 200 eV and beyond, etching supplanted chemical modification as the dominant phenomenon. This sputter etching from excited oxygen ions resulted in not just chemical modification of Pt^0 to Pt^{4+} , but also a small amount of material removal which limited the measured formation of oxidized platinum.

Confirmation of this physical sputtering effect was obtained through etch rate measurements performed on the same 30 nm Pt exposed to the same ion energies. At 50 eV, no etch was observed for Pt. However, as expected, the sputter etch rate increases with increasing ion

energy, resulting in rates of 0.3, 0.4, and 1.0 nm/min at 100, 200, and 500 eV respectively (Figure 5-9).

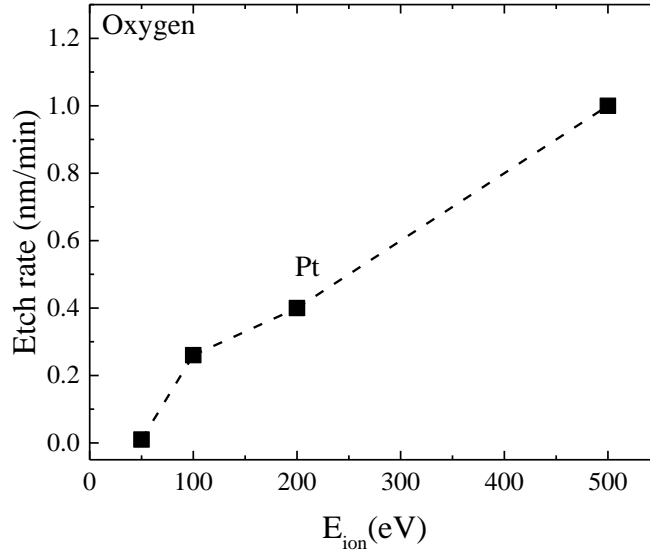


Figure 5-9. Etch rate of 30 nm Pt films as a function of ion energy for samples processed at 50, 100, 200, and 500 eV under oxygen ion beam.

The strong dependence of oxidation fraction for platinum observed at reduced ion energies was a promising indication that low energy ion bombardment could be utilized to accomplish the surface modification scheme. This approach was further examined using inductively coupled and electron generated discharges in conjunction with ion energies below 200 eV to realize surface modification and create a chemical contrast which was subsequently exploited in combination with subsequent etching.

5.1.3 Influence of plasma oxidation time on Pt modification

In addition to controlling the ion energy for use in surface modification, one can also manipulate the oxidation time. The corresponding measurement of oxide thickness can provide as a function of time provides further insight into elucidating the underlying oxidation mechanism. In the case of the conventional inductively coupled plasma used predominantly in this work, the

application of a -100 V bias to samples exposed to O₂ plasma for up to 5 minutes was studied. Oxide thicknesses were obtained through inelastic mean free path calculations for photoelectrons emitted from the metallic Pt underlayer and attenuated through the PtO₂ surface measured using high resolution XPS for the Pt 4f binding energy regime.

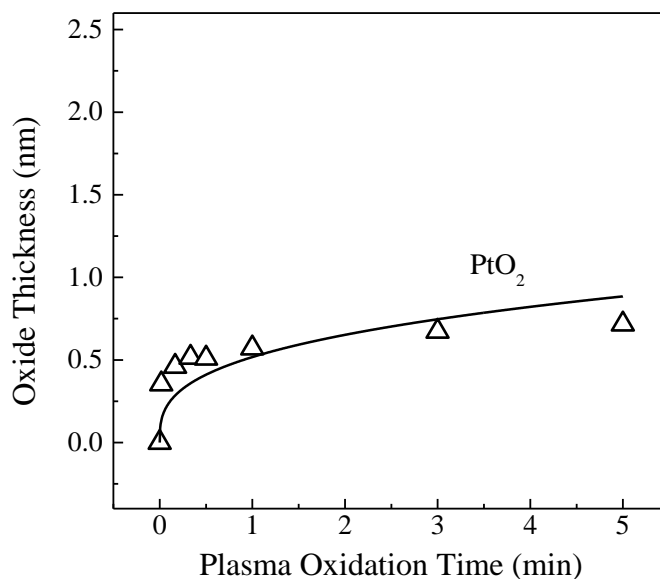


Figure 5-10. Oxide thickness as a function of plasma oxidation time for Pt thin films exposed to O₂ plasma with 500 W source power and -100 V applied bias. The curve corresponds to the inverse log model used to fit the oxide thickness.

A number of different empirical kinetics have been proposed for low-temperature oxidation of metals and include linear, parabolic, and logarithmic models. The use of regression curve fitting was helpful in determining the mechanism by which PtO₂ formed. (Evans 1960) From the measured oxide thickness, PtO₂ formation saturates relatively quickly compared to other previously studied metals, forming up to approximately 0.5 nm in the initial 30 seconds. This rapid oxidation was best described using a parabolic model, wherein the squared thickness, d^2 , can best

be expressed as the product between a constant, A, and time, t. Recasting this model to solve for the thickness results in:

$$d = \sqrt{At} \quad (5.1)$$

which, when used for fitting the time-dependent PtO₂ thickness shown in Figure 5-10, results in a value of 0.55 for A and corresponding statistical correlation factor of 95%. In accordance with this model, as well as the limited number of valence states that Pt can adopt when oxidized (i.e. predominantly Pt⁴⁺) suggest that the oxidation of Pt likely proceeds through the Cabrera-Mott model wherein a large potential is established after the adsorption of the first oxygen monolayer on the Pt surface. This potential drives the transport of metal cations and oxygen anions, as well as electron transport through tunneling until reaching a thickness whereby tunneling can no longer occur. (Cabrera 1949). Subsequent oxidation is then limited by reactive oxygen diffusion to the metal-oxide interface. (Blackstock 2005, Wang 2007)

5.2 Etch of metallic and modified Pt

Etching Pt and enacting a process whereby removal was controlled towards the atomic level was the ultimate goal for this portion of work. However, this level of control required the use of reactive plasma or ion beam species to first create a chemically contrasting modification layer which could be removed through subsequent reactions. Controlling the thickness of that modified layer was the first step in understanding how it could be used to control the overall etch process. Validation of the surface modification scheme with subsequent chemical reactions was first examined using a process comprised of alternating plasma exposure. Based on the success of previous studies in using alternating Cl₂/H₂ etch, this process was compared first to continuous Cl₂

plasma exposure on Pt. Analogous to the previously discussed enablement of vapor phase etching through surface modification, the reactive ion etch of Pt in Cl_2 and H_2 served as a starting point for confirming the etch enhancement effect caused by formation of the modification layer. Further studies have focused on the efficacy of using formic acid solution and vapor phase etch in conjunction with plasma oxidation to enable sub-nanometer etch rates.

5.2.1 Enhanced plasma etch of chlorinated Pt

Platinum thin films (60 nm) were deposited via electron beam evaporation and subsequently studied using continuous Cl_2 and sequential Cl_2/H_2 chemistries for plasma etch. The etch rates for both processes were quantified using spectroscopic ellipsometry and confirmed with SEM measurements. Figure 5-11 summarizes the etched thickness as a function of time for continuous chlorine exposure compared to chlorine exposure followed by hydrogen. Both Cl_2 and H_2 plasma conditions were fixed at 800 W source power and 50 W bias power for 30 seconds. Through linear interpolation of the measured thicknesses at each time step, the average etch rate of platinum in Cl_2 plasma was 6.4 nm/cycle. For the sequential Cl_2/H_2 exposure, the etch rate was calculated to be 8.7 nm/cycle. While small, this 36% increase in the etch rate shows that sequential chemical exposures can be utilized in an inductively coupled plasma to enhance the removal rate of platinum.

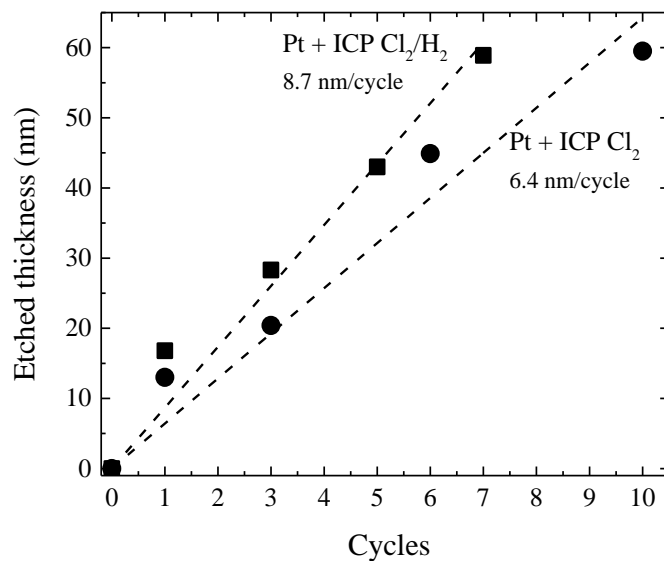


Figure 5-11. Etched thickness of 60 nm Pt films as a function of etch cycle under Cl₂ and Cl₂/H₂ alternating chemistry. Both Cl₂ and H₂ plasmas were held at 800 W source power and 50 W bias power.

Sample surfaces were then analyzed to determine the bonding states of the platinum and chlorine present (Figure 5-12). Samples of Pt before processing, after Cl₂ plasma exposure for 30 seconds, and after sequential Cl₂/H₂ for 30 seconds each are shown. Pre-processing, Pt samples were observed to contain mainly metallic Pt⁰. Additionally, no chlorine was observed as confirmed from the Cl 2p high resolution spectrum. Continuing to the Cl₂ plasma etch step, a significant increase in the Pt²⁺ bonding state is observed and is shown in the shaded region at a binding energy of 72.1 eV. Additionally, on the Cl 2p high resolution spectra, a noticeable peak was observed at 196 eV, indicating the presence Cl-Pt bonds on the surface of the film. Subsequent exposure to H₂ plasma for an additional 30 seconds results in the reduction of Pt²⁺ to completely reduced metallic platinum shown. Furthermore, the chlorine doublet measured previously after Cl₂ plasma exposure was no longer observed.

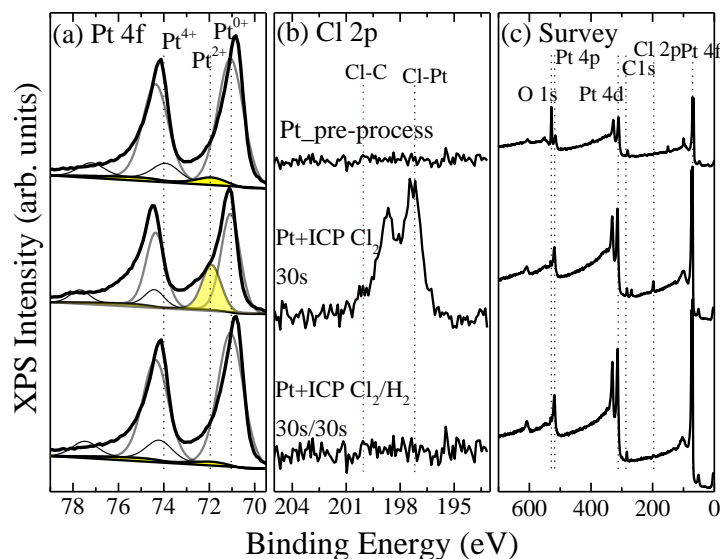


Figure 5-12. High resolution x-ray photoelectron spectra of (a) Pt 4f and (b) Cl 2p binding energy regimes as well as (c) survey scan of all elements present on the surface pre-processing, after exposure to 800 W source power Cl₂ plasma with 50 W bias power for 30 s, and after subsequent exposure to 800 W source power H₂ plasma with 50 W bias for 30 s.

5.2.2 Organic chemical etch of Pt and PtO₂

In addition to plasma-based processing, organic chemical removal of Pt and modified PtO₂ were explored as avenues for atomic layer etching. This approach took inspiration from the synthesis of metalorganic precursors similar to those discussed in the chemical vapor deposition processes for depositing metal thin films. In many cases, these precursors contain a central metal atom surrounded by organic ligands. In many cases, these organic ligands contain acidic functional groups, which, when deprotonated, allow for bonding to the metal through a terminal oxygen atom.

These studies have focused on the use of formic acid, both in concentrated solution and in the vapor phase to enable a well-controlled etch process capable of exploiting the chemical contrast between metal and metal oxide explored in detail in the previous sections. Due to the

aforementioned concerns about sputtering at higher ion energies, the following work focused on low energy modification in conjunction with solution and vapor etch at elevated temperatures of 80 °C.

An electron beam driven discharge consisting of a mixture of Ar (60%) and O₂ (40%) was used to study the effect of oxidation at increasing ion energies of 0, 10, 30, and 50 eV through application of a DC bias to the electron beam terminal anode, or beam dump. An increased exposure time of 600 s (10 min) was used. Additional conditions for these oxidation processes are summarized in Table 5-3.

Table 5-3. Conditions for 30 nm Pt samples processed under electron beam generated Ar/O₂ discharge with increasing terminal anode bias voltages.

Material	Feed Gas	Pressure (mTorr)	Terminal Anode Bias (V)	Time (s)	I _{cathode} (mA)	V _{cathode} (kV)
Pt	Ar (60%) O ₂ (40%)	62	0, 10, 30, 50	600	12	2.5

Samples were characterized after processing through the use of XPS, allowing for determination and quantification of individual chemical bonding states of Pt as well as the calculation of PtO₂ thickness at each condition. Fitted XPS data for high resolution Pt 4f, O 1s, and C 1s binding energy regimes are shown in Figure 5-13 for 30 nm Pt before processing, after each increasing bias (ion energy) condition, as well as after exposure to concentrated formic acid solution at 80 °C.

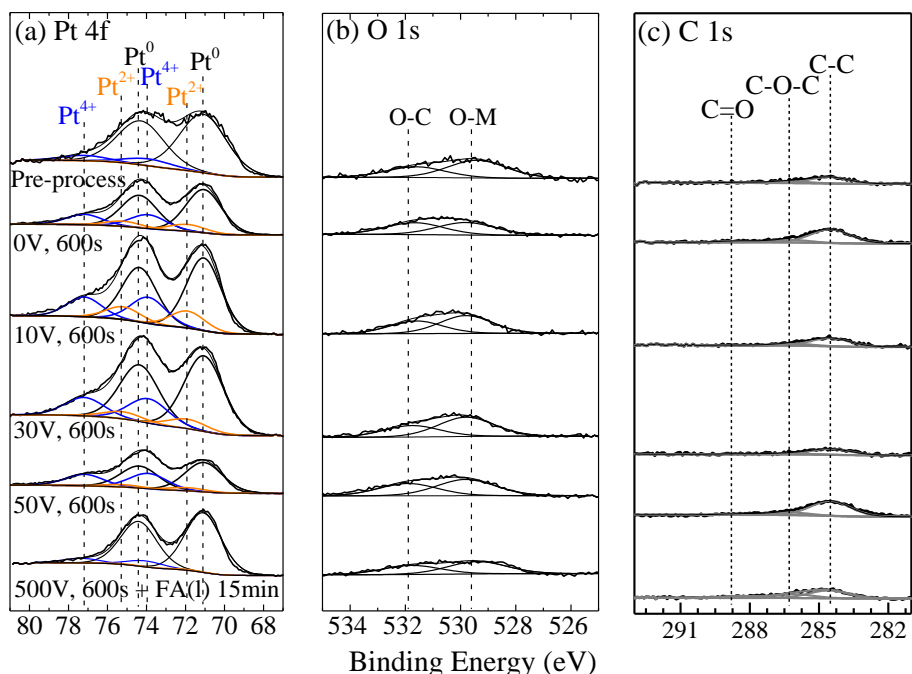


Figure 5-13. High resolution x-ray photoelectron spectra of (a) Pt 4f, (b) O 1s, and (c) C 1s binding energy regions for 30 nm Pt samples with 5 nm Ti adhesion layer pre-processing, after exposure to electron beam driven O₂ plasma with increasing applied bias voltages of 0, 10, 30, and 50 V for 600 s, and after plasma oxidation at 50 V bias with separate subsequent exposure to concentrated formic acid solutions (>97%) at 80 °C for 5 s and 15 min.

The quantified percentages of chemical bonding states of Pt into Pt⁰, Pt²⁺, and Pt⁴⁺ for each condition are summarized in Figure 5-14. Across all conditions, the presence of Pt⁰ dominates with the highest percentage. Pre-processing, this value is approximately 91% with the remainder existing at Pt⁴⁺ and attributed to the native oxide formed upon exposure to atmosphere. After the exposure to 600 second plasma oxidation with no applied bias (0 V), the percentage of Pt⁰ decreases substantially to 72% while Pt⁴⁺ and Pt²⁺ increase to 21% and 7%, respectively. Across the remaining bias voltage conditions, the percentage of Pt²⁺ was measured to remain relatively constant at values between 7-10%. Pt⁴⁺, on the other hand, exhibits a dependence on the ion energy,

increasing from 21% at 0 V to 33% at 50 V. A corresponding decrease in metallic Pt⁰ was also observed, decreasing to 62% at 50 V.

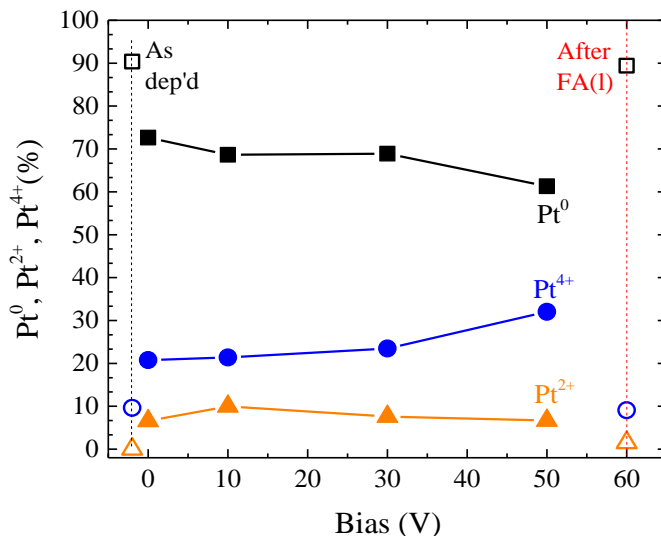


Figure 5-14. Percentage of Pt in metallic Pt⁰ and oxidized Pt²⁺ and Pt⁴⁺ oxidation states for as deposited, oxidized, and after formic acid (FA) solution etch as a function of applied bias during plasma oxidation.

The 50 V bias condition was selected for subsequent chemical etch treatment due to the largest fraction of PtO₂ present on the surface. Exposure for 900 sec in concentrated formic acid solution (97%) at 80 °C resulted in the removal of the generated modification layer. The fraction of Pt⁰ was found to be nearly identical to the pre-processing value, while Pt⁴⁺ decreased slightly to 9% and an increase of 2% was observed in Pt²⁺. This small change was attributed to the unavoidable exposure to atmosphere after formic acid solution etch and before transferring the sample to high vacuum for characterization. The corresponding oxide thickness calculation was performed using the aforementioned bilayer approximation in conjunction with the Pt/PtO₂ inelastic mean free path (Figure 5-15).

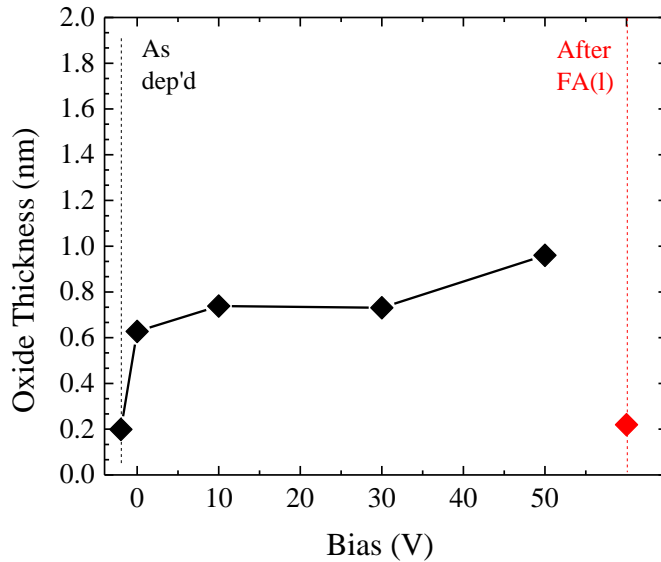


Figure 5-15. Measured thickness of oxide for as-deposited, oxidized, and formic acid (FA) etched Pt as a function of applied bias during plasma oxidation.

The thickness of generated oxide under low ion energies was observed to maintain a weak dependence on the bias voltage. With no applied bias (0 V), the oxide thickness was calculated to be 0.63 nm. This thickness increases to similar values of approximately 0.75 nm at 10 and 30 V. At 50 V, the modification layer was calculated to be 0.95 nm. This substantial increase in oxide thickness was likely a result of the increased bias, which resulted in increased ion energies and allowed an increased penetration depth of oxygen ions bombarding the surface. Additionally, at these ion energies the sputtering effect during modification is likely minimized, allowing for a majority of oxygen ions to contribute to the growth of PtO₂. For comparison, Pt films modified by the oxygen ion beam in section 5.1.2 indicated no measurable etch from physical sputtering after 300 seconds of exposure at 50 eV.

Translation of the organic solution phase etch to the vapor phase required similarly high temperatures and increased pressures of formic acid vapor combined with plasma oxidation to

overcome large changes in chemical etchant concentration. Cyclic exposure to alternating steps of oxidation followed by formic acid vapor exposure were studied to determine the change in oxidation states of Pt on the sample surface as well as measure the etched thickness of 20 nm Pt films after each cycle. Studies were conducted using the inductively coupled plasma reactor and organic chemical vaporizer setup described previously in Chapter 2 to compare the effect of cyclical oxidation and vapor etch to oxidation alone.

As with previous studies, XPS was used to measure the change in chemical bonding states pre-processing as well after each individual step in the etch cycle. Before processing, XPS of Pt indicates a small amount of oxidation (~10%) due to storage in atmosphere. After exposure to 60 seconds of O₂ plasma at 500 W source power and no applied bias, formation of PtO₂ was observed. A subsequent formic acid vapor exposure step at 148 Torr, 80 °C for 50 s showed complete removal of the oxide layer, returning the Pt to oxidation composition similar to the pre-process condition. Spectroscopic ellipsometry was used to measure the change in thickness as a function of etch cycles for plasma oxidation and formic acid vapor etch as well as equivalent cycles of oxidation alone at the same 500 W oxidation and 148 Torr formic acid vapor condition described above. As seen in Figure 5-16b, an initial large change in thickness was observed for the first cycle. This was attributed to removal of contaminants present on the sample surface.

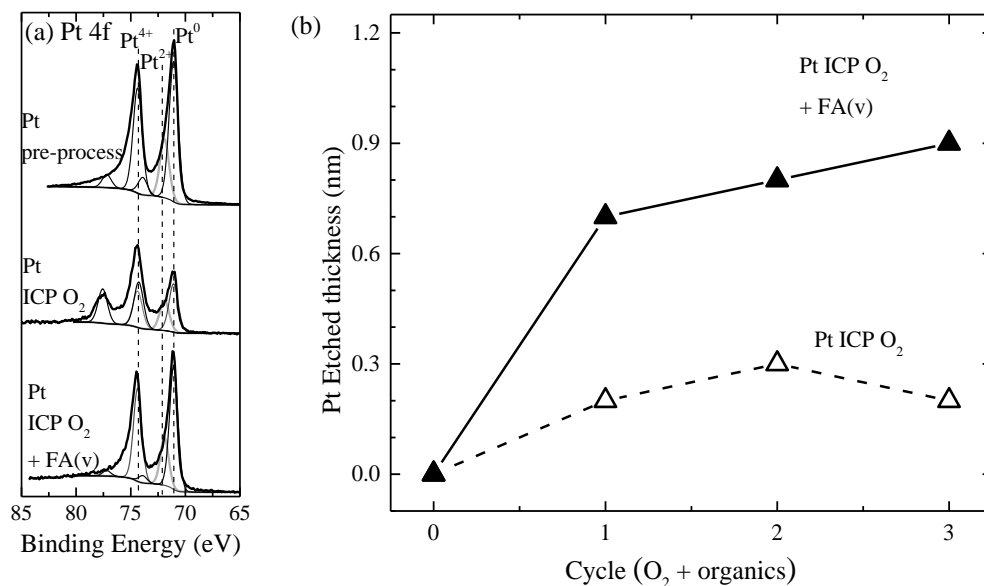


Figure 5-16. (a) High resolution x-ray photoelectron spectra of 20 nm Pt pre-processing, after exposure to plasma oxidation, and after subsequent exposure to formic acid vapor. (b) Etched thickness of Pt as a function of cycle for alternating plasma oxidation and formic acid vapor etch and equivalent cycles of plasma oxidation alone.

After the initial cycle of oxidation and vapor etch, an etch rate of approximately 0.1 nm/cycle was observed for 60 s oxidation with 50 s formic acid vapor etch. In contrast, the etched thickness of Pt saturated at approximately 0.2 nm over an equivalent three cycles of plasma oxidation alone. This small change in thickness was attributed to a small physical component as a result of the plasma potential or removal of some adventitious carbon layer on the surface of the film.

Tuning the etch rate of the combined surface modification and organic vapor etch process required optimization of the oxidation step. As was shown in preceding sections, the modification depth can be controlled using plasma oxidation time as well as ion energy to generate a substantial thickness of PtO₂ on the surface. This etch rate dependency was explored by increasing the oxidation time to 300 s as well as increasing the applied bias to -100 V while holding the formic

acid exposure cycle constant at 148 Torr, 80 °C, and 50 s. The resulting etched thickness of the same 20 nm thickness of Pt is summarized in Figure 5-17

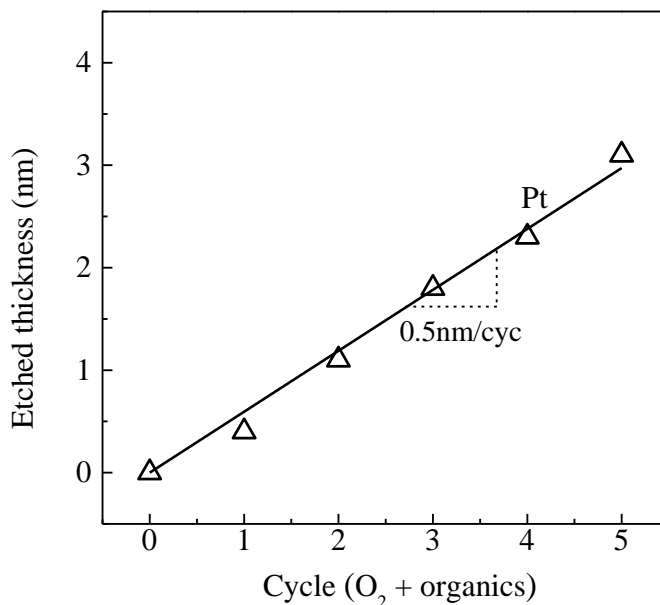


Figure 5-17. Etched thickness as a function of cycles consisting of plasma oxidation and formic acid vapor etch.

A linear dependence of the Pt etched thickness is again observed, similar the previous 1 min oxidation condition with no applied bias. However, in contrast to the previous study, the etch rate increased substantially to an average value of 0.5 nm/cycle. The organic vapor etch step can be characterized as a self-limiting reaction due to its ability to be controlled through tuning of the surface modification layer thickness. This selectivity is necessary in order to ultimately realize an atomic layer etching process for platinum.

The formation of a modification layer in platinum was found to be largely dependent on both exposure time as well as the energy of impinging ions in both plasma and ion beam-based modification. Exercising precise control over both exposure and ion energy enables fine tuning of

the modification depth and directionality while minimizing sputter etch effects. Chemical removal of chlorinated platinum surfaces was shown to be effective in enhancing the etch rate; however, in order to scale down this rate, it was necessary to transition to the use of organic chemistries such as formic acid. In doing so, nearly infinite selectivity in removing PtO₂ over the underlying metallic Pt was achieved. This removal can also be controlled through the manipulation of time for plasma exposure in conventional ICP systems to limit to removal down to sub-nanometer thicknesses.

Chapter 6 : Summary

The ability to control removal of material with atomic scale fidelity is necessary to further shrink the size of electronic devices. Whether it be for the etching of interconnect materials such as Cu, ferromagnetic metals such as Co and Fe, or noble metals such as Pt, atomic layer etch is necessary for patterning increasingly high aspect ratios and small critical dimensions beyond what is currently achievable.

Dry etch of copper was originally thought to be an impossible task when the semiconductor industry transitioned to using this metal as an interconnect material. As a result, the damascene process was developed, requiring the implementation of CMP and solution-based etch processing. However, less than a decade after this change, the dry etch of Cu was explored first through thermodynamic means, identifying a route for plasma etching using Cl_2 chemistry alongside H_2 to enhance the volatility of the trimeric Cu_3Cl_3 etch product. (Kulkarni 2002) This predicted enhancement was confirmed when the enhancement of Cu etch rates was confirmed using a cyclical process of alternating Cl_2/H_2 plasma exposure and subsequent confirmation that the auxiliary reductive hydrogen chemistry was capable of removing nonvolatile copper chlorides remaining on the surface even at reduced temperatures. (Tamirisa 2007)

By utilizing thermodynamics, a cyclical etch process of Cu using, instead of halogen-based plasma chemistries, an organic chemical vapor etch approach was developed. In spite of measurable etch of metallic Cu thin films in organic solutions such as acac, acetic acid, and formic acid, translation of an etch process wherein organic vapor would directly etch Cu was shown to be unfeasible, as these reactions were nonspontaneous. To overcome the lack of reactivity of Cu, an inductively coupled O_2 plasma was used to modify the surface of Cu films through transformation

into CuO. When reaction between CuO and organic solutions were studied, a substantial increase in the etch rate was observed, suggesting that selectivity to metallic Cu could be achieved. Subsequent etch studied using vapor phase organics at increased temperatures showed substantial etch rates for thermally oxidized CuO blanket films. A cyclical process, involving exposure of Cu to O₂ plasma and subsequent organic vapor such as formic acid and acac was shown to etch Cu in a cyclical fashion with extremely high selectivity.

Complete removal of Cu blanket films was observed using this cyclical oxidation and organic vapor etch process. This process was then applied to etch Ta-masked Cu features. When compared to an isotropic formic acid solution etch process, substantial undercut was observed. However, alternating oxidation and chemical vapor etch was observed to etch through the Cu with no observable loss of hard mask adhesion or suspension. Through application of a DC bias to the sample during the O₂ plasma modification step, oxygen ions with increased ion energies were made to bombard the sample surface, causing directional modification of the Cu which was removed during the isotropic etch enabling patterning down to 70 nm wide lines.

Enabling etch processes of Co-based ferromagnetic thin films, on the other hand, was crucial to the implementation of MRAM devices. Further scaling of these devices requires development of both reactive ion and atomic layer etching chemistries that are capable of producing not just reasonably high etch rates but also ensuring preservation of the metallic surface bonding states. The development of bulk RIE chemistry was important for patterning MRAM devices; however, the possibility of enabling atomic layer etch using a well-controlled modification process was paramount to ensuring the continued scaling of MRAM, more specifically, the magnetic tunnel junction. Using the same thermodynamic assessment, Co and Fe were shown to be more reactive to organic chemistries, such as acac and hfac. In fact, Co was

calculated and confirmed to etch more quickly in acac, producing $\text{Co}(\text{acac})_2$ as the dominant etch product; while Fe etched more quickly in hfac, resulting in the formation of $\text{Fe}(\text{hfac})_3$. The combination of these two chemistries together was found to also be capable of etching the ferromagnetic alloy CoFeB. However, due to slow solution phase etch rates, and the corresponding issues this would result in upon transitioning to a gas phase process led to the exploration of formic acid as the chosen chemical etchant.

Achieving a highly selective process required the implementation of surface modification. Plasma oxidation was studied as the main driver for this process, as it allowed for the creation of a thin modified layer on top of the metallic substrate. Oxide layer thickness was strongly dependent on plasma oxidation time, with both Co and Fe following a similar mechanism. This mechanism was elucidated using an inverse logarithmic kinetic model, which sufficiently described the time-dependent oxide film growth, indicating that the predominant mechanism consisted of metal cation diffusion to the oxide interface.

With the knowledge that oxide thickness was able to be controlled by plasma oxidation time, a chemical vapor etch process was explored. Surface modification enabled the creation of a thin surface film of metal oxide which reacted quite differently than the underlying metal. Specifically, formic acid vapor was observed to etch metal oxide at significant rates while not etching metal. This observed chemical contrast and selectivity between surface oxide and underlying metal led to a cyclical process of separate plasma oxidation followed by chemical vapor etch. As was expected, since Fe oxidized to greater thicknesses than Co for identical plasma exposure times, the corresponding Fe etch rate was greater than Co. By reducing the oxidation time and thus the oxide thickness, the etch rate could also be decreased (Figure 6-1).

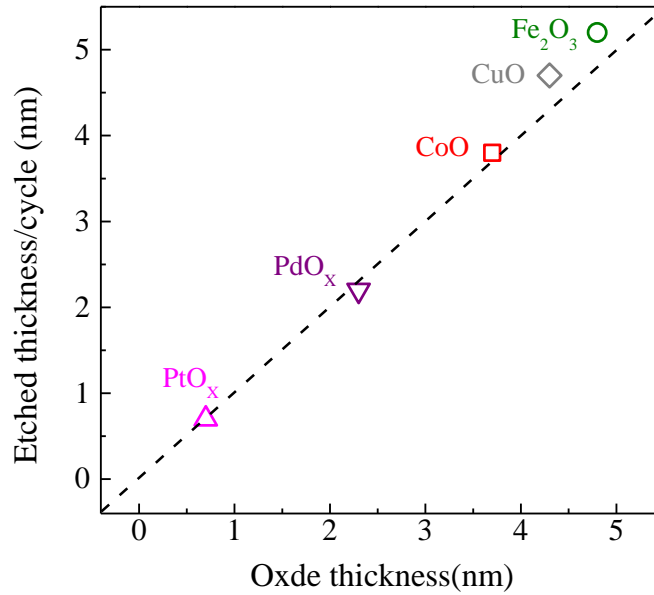


Figure 6-1. Etched thickness per cycle as a function of oxide thickness for plasma oxidized and formic acid vapor etched Pt, Pd, Co, Cu, and Fe. Each material falls on or close to the dashed line with a slope of 1, indicating that alternating oxidation and formic acid vapor etch exhibits selective removal of the metal oxide as well as the ability to control the etch thickness by controlling the modified layer thickness.

This same two-step approach was applied to etch CoFeB, the ferromagnetic alloy commonly used in MTJ stacks. Although a mixture of three separate elements, CoFeB was found to etch at well-controlled rates through manipulation of the plasma oxidation time. This same process was further used to pattern Co films using a TiN hard mask down to 70 nm wide lines. Without the application of a bias voltage, the plasma modification step was observed to form an isotropic modification layer which was subsequently etched away, resulting in substantial mask undercut after multiple cycles. As with Cu, the introduction of an applied DC bias enabled the modification step to proceed in a directional fashion due to oxygen ion bombardment, creating a directionally formed oxide layer. Subsequent formic acid vapor etch removed this layer, resulting in the evolution of an anisotropic etch profile, giving rise to the ability to pattern magnetic metals similarly to Cu, and allowing for directional atomic layer etch.

Finally, Pt, which was seen as the most difficult material to etch due to its chemically resistant nature, was found to etch after using H₂ as well as organic vapor exposure after oxidation or other plasma modification chemistries. Prior to achieving a successful etch process, it was necessary to first investigate the modification process to elucidate the mechanism by which modification, such as oxidation, occurred on the Pt surface.

Both time and ion energy were found to play crucial roles in the growth of a PtO₂ modified surface. Increasing oxidation time led to investigation of the kinetics surrounding plasma oxidation resulting in a mechanism confirmed to proceed via parabolic growth rate and indicating that oxidation for platinum is quite different than magnetic metals or Cu and proceeds via a Cabrera-Mott mechanism, explaining the initial rapid oxide formation.

Subsequent studies focused on confirming the effect of both chlorination and oxidation modified layers. Alternating Cl₂/H₂ reactive ion etch indicated an enhancement in the etch rate of Pt over equivalent cycles of Cl₂ plasma in conjunction with surface chemical bonding state characterization, which indicated the removal of PtCl_x species after exposure to subsequent H₂ plasma. Although not an atomic layer etch process, this approach suggested that oxidation and organic vapor etch could be. Formic acid, based on its efficacy with previous studied materials, was chosen as the chemical etchant.

Oxidation studies combined with solution etch at an increased temperature of 80 °C showed complete removal of PtO₂. Transferring this process to the vapor phase required, as before, increased partial pressures of formic acid vapor up to 148 Torr and the same 80 °C operating temperature. Utilizing an inductively coupled O₂ plasma for 60 s exposure at 500 W source power and no applied bias in combination with organic vapor etch for only 50 s resulted in observable Pt

etch at rates down to 0.1 nm/cycle. The etch of Pt was found to be dependent on the oxidation step and was measured to increase to an etch rate of 0.5 nm/cycle after 300 s oxidation at 500 W source power and -100 V bias with formic acid vapor conditions identical to the previous process (Table 6-1).

Table 6-1. Summary of etch rate, selectivity (for metal oxide to metal as well as to hard mask materials), and directionality for etching Cu, Co, and Pt by an oxidation process followed by formic acid etch. Cu and Co thin films were patterned using Ta and TiN hard masks; however, Pt patterned samples were unavailable.

	<i>Cu</i>	<i>Co</i>	<i>Pt</i>
<i>Etch rate (nm/cycle)</i> <i>(O₂ + formic acid (g))</i>	4.4	2.8	0.5
<i>MO_x to M Selectivity*</i> <i>(formic acid (g))</i>	>> 100	>> 100	>> 100
<i>M to Hard mask Selectivity</i> <i>(O₂ + formic acid (g))</i>	Cu:Ta > 100:1	Co:TiN > 100:1	N/A
<i>Directionality</i>	Yes 70 nm	Yes 70 nm	(Yes) **

*M signifies the metals summarized in this table, namely Cu, Co, and Pt

**Although patterned samples were not available, cyclical oxidation and formic acid vapor etch are expected to achieve directional etch for Pt

Along with Cu, Co, and Fe, the etching process developed for Pt has been shown to be capable of controlling etch rates of each of these metallic films down to nanometer, and in some cases, sub-nanometer thicknesses. Direct dependence of the etch rate per cycle on the modification depth, which was in turn controlled by plasma exposure time, indicated that the chemical vapor etch process achieved selectivity values of greater than 100 in removing metal oxides over underlying metal thin films and confirmed self-limited removal of the modified surface layer. Corresponding manipulation in the directionality of modification, and thus directionality of etch, was achieved with similarly high selectivity to Ta and TiN hard masks through manipulation of ion energy during the application of a DC bias, substantiating the processing capability of cyclical

O₂ plasma oxidation and formic acid vapor etch as an effective chemistry for patterning metallic nanostructures.

Moving forward, this etch chemistry selection approach of assessing the thermodynamic favorability to identify potential etch chemistries could be applied to materials beyond just single element metals and intermetallic compounds, such as those commonly encountered as binary or ternary mixtures in other forms of memory. Phase change materials, such as GeTe, SbTe, and GeSbTe are complex materials. However, applying the same thermodynamic assessment and verifying through experimental studies can open new routes for developing successful patterning chemistries in the future.

Appendices

A. Integrated Inductively Coupled Plasma Reactor and Ion Beam

PLEASE SEE ATTACHED DIAGRAM AT THE END OF THE EMERERGENCY SHUT DOWN FOR LOCATION OF VALVES, GAS AND PUMPS, IF PICTURE IS NOT PROVIDED!

A.1. Emergency Shutdown Procedures

Inductively Coupled Plasma Reactor

I. In case of Cl₂ is smelled

1. Close tank valve.
2. Close others valve if possible. The diaphragm valve D4, located directly behind chamber, and the regulator R1 on Cl₂ cylinder located in gas cabinet to the right of the MFC cabinet.

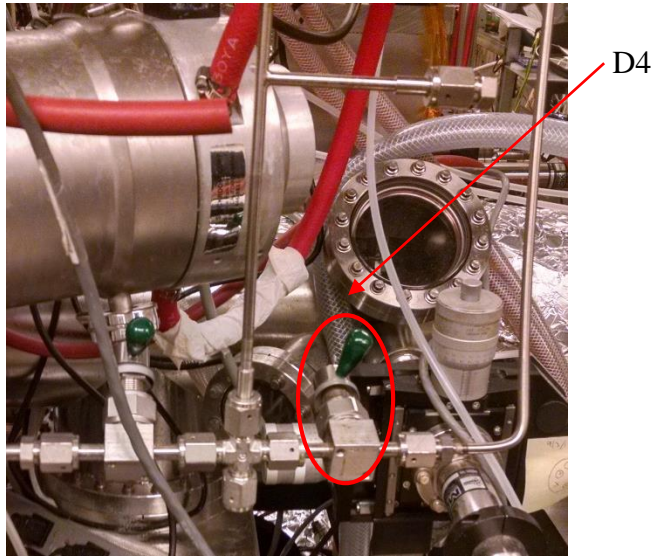


Figure A-0-1 D4 valve directly behind chamber.

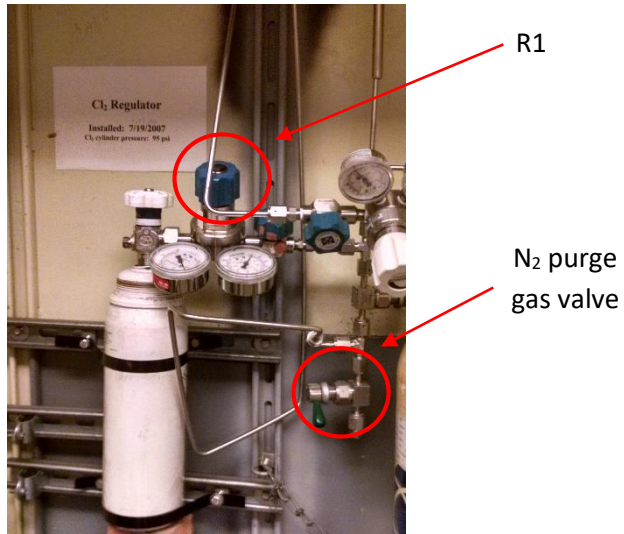


Figure A-0-2 R1 regulator located in chlorine gas cabinet.

3. Evacuate.
4. Contact EH&S as needed.

II. In case a noise is heard from turbo molecular pump on Main Chamber

1. Close manual gate valve between turbo pump and chamber.

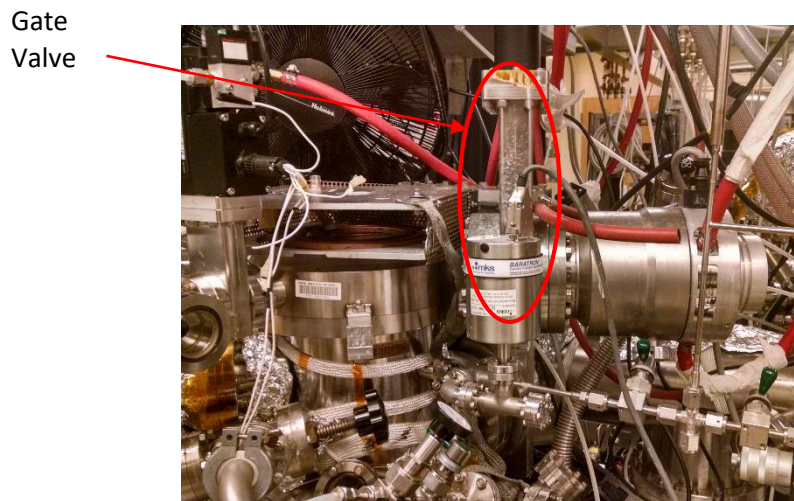


Figure A-0-3 Gate Valve for Main Chamber Turbo Pump.

2. Turn off the turbo molecular pump by pushing the “stop” button on the controller.



Stop button
(read label to
confirm)

Figure A-0-4. Turbo Pump Controller for Chamber.

3. Isolate mechanical pump by closing manual valve between turbo and MP.

III. In case a noise is heard from mechanical pump on Chamber

1. Close manual gate valve between turbo pump and chamber. (See Figure 3)
2. Turn off the turbo molecular pump by pushing the “stop” button on the controller. (See Figure 4) And close the roughing from turbo pump to mechanical pump.
3. Switch off the mechanical pump by turning off the breaker.
- 4.

IV. In case a ratcheting is heard from Cryopump on Chamber

1. Close the pneumatic gate valve between ICP and Cryopump by pressing the corresponding switch on the control box (trace the cable if unsure). (See Figure 5)

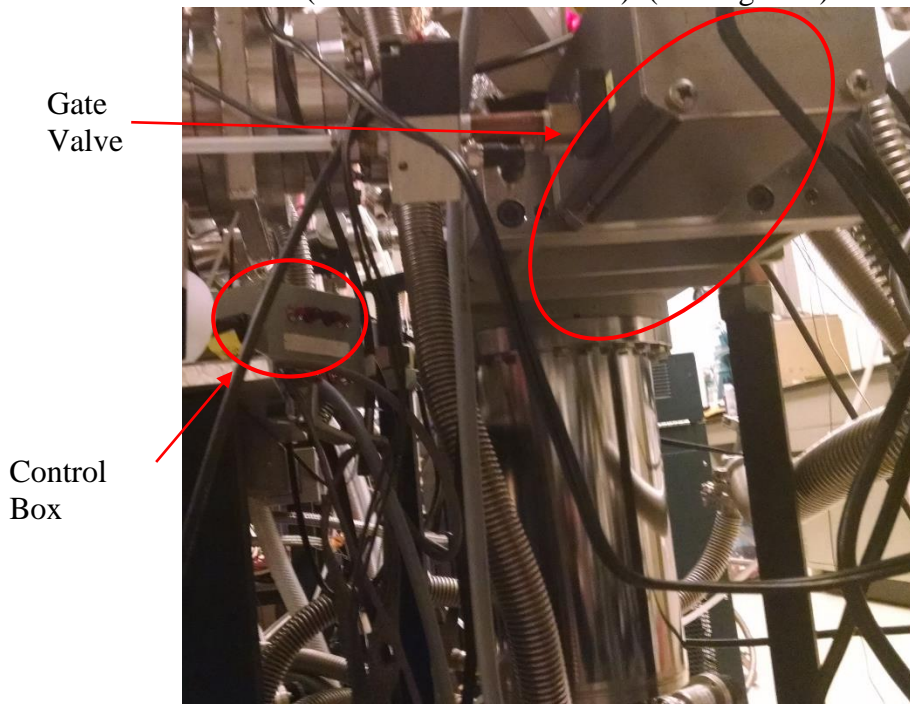


Figure A-0-5 Gate Valve between Cryopump and ICP.

2. Ensure that the roughing valve between the cryopump and the chamber mechanical pump is closed.

3. Turn off the cryopump by flipping the white circuit breaker on the compressor (See Figure 6 - in the event of pump failure this may turn off automatically – check to see if the unit is operating).

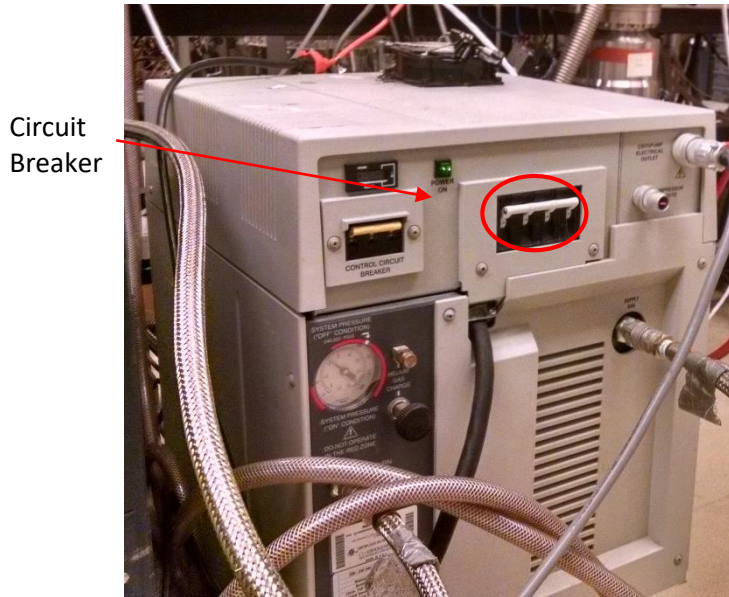


Figure A-0-6 Compressor and Circuit Breaker Switch.

V. In case noises are heard from any of the electronics

1. If units have power switches, turn them off and unplug all units (see pictures below).

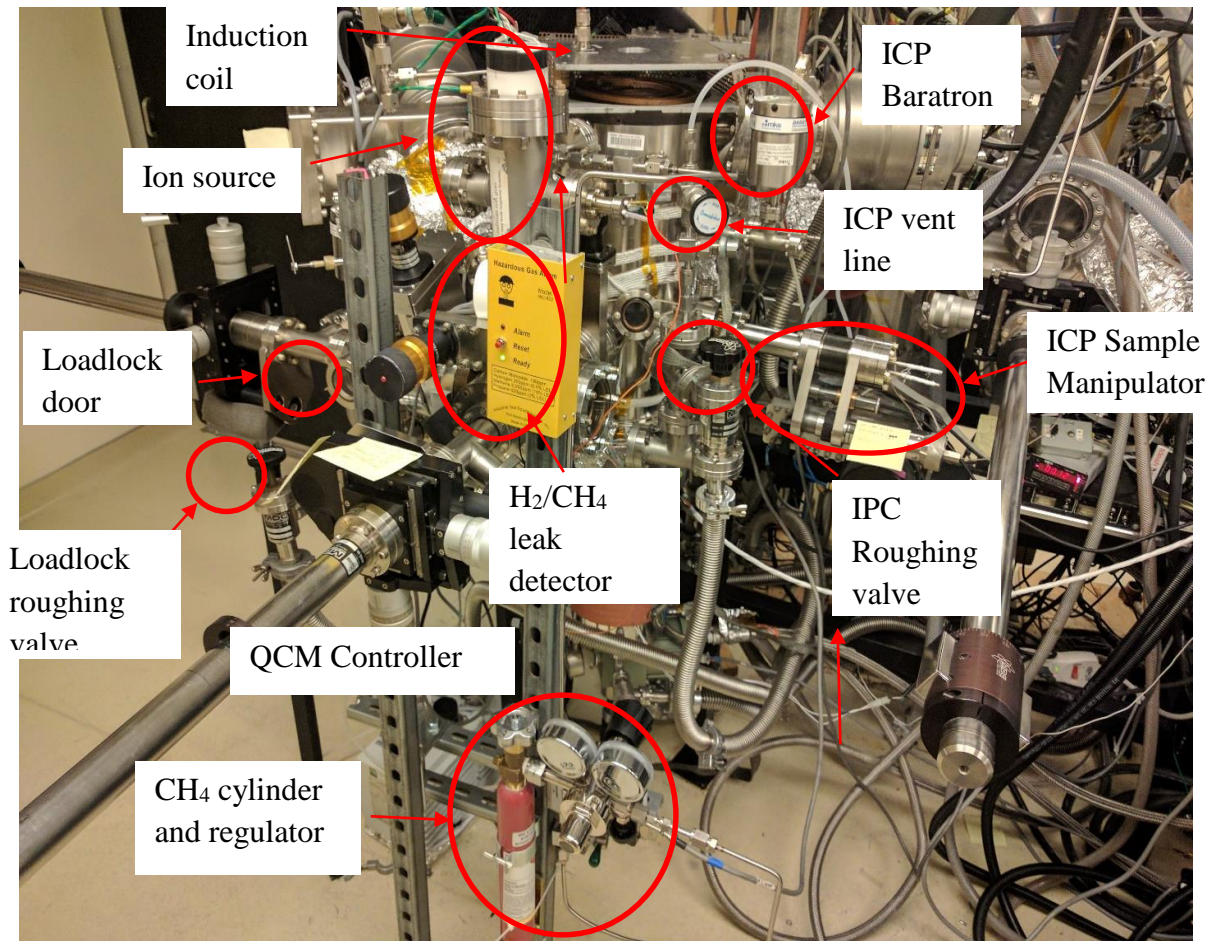


Figure A-0-7 The components of ICP system.

Ion Source Chamber

I. In case there is issue with discharge or beam electronics

1. Turn off the right “Beam” switch located on the left-hand side of the panel, next to the “Source” switch
2. Turn the “Neutralizer”, “Cathode”, and “Discharge” dials counter-clockwise until they stop.
3. Turn off the Source switch.
4. Turn off the “Power” switch.
5. Turn off Ar gas switch on MFC.

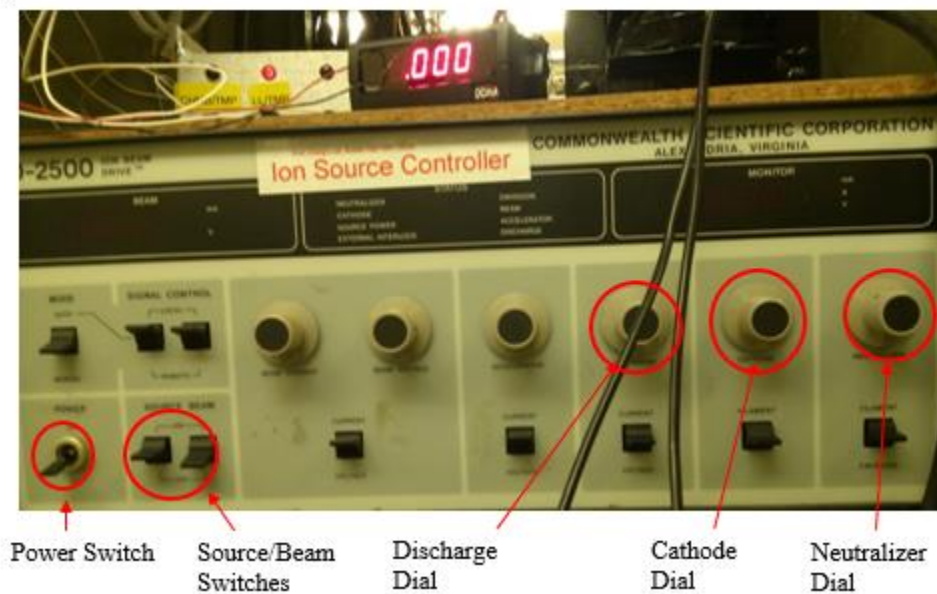


Figure A-0-8 Ion source controller

A.2. Operating Procedures

Inductively Coupled Plasma Reactor

Pump down the main chamber (Note: The chamber's default state should be pumped down, check the pressure reading on the ion gauge to verify. The following steps should only be taken if you are aware that the chamber has been vented and not pumped back down).

- a. THE FOLLOWING INTERLOCKS FOR THE PUMP DOWN PROCEDURE MUST BE MET TO BEGIN PUMPING: COOLING WATER FOR MAIN CHAMBER TURBO PUMP MUST BE ON, COOLING WATER FLOW TO COMPRESSOR SHOULD BE BETWEEN 2.3 AND 3.5 GPM).
 - a. Check that all the flanges are tightened and all the valves are in the closed position.
 - b. Check all the cables are correctly connected.
 - c. Check the oil level in the mechanical pump, which should be 2/3 full in view window.
 - d. Check MP and its exhaust for liquid leaks. (oil, condensation, exhaust fluid)
 - e. Turn on MP by turning on the switch. The thermocouple gauge reading should start going down within 20 seconds. If not, turn off the pump and check connections to chamber, turbopump and cryopump for vacuum leaks.
 - f. Wait until MP reaches the base pressure ~60 mTorr. This process may take several minutes if system was shut down for some time.
 - g. If the Baratron gauge on the chamber is blinking (indicating pressure >300 mTorr) or appears to be rising over 50 mTorr, gradually open the roughing valve on the upper body of the chamber to pump down using the MP. If the gas lines have been exposed to ambient conditions, diaphragm valve D3 and D4 should be open so that the gas lines could be pumped down as well. Rough pump the chamber using MP until a base pressure of ~75-85 mTorr is achieved.
 - h. After the TC gauge reaches the base pressure, close roughing valve between chamber and MP and gradually open roughing valve between TMP and MP.

Before TMP is turned on, check:

1. The cooling water is running
2. **The roughing valve between the chamber and MP should be always CLOSED while the TMP is on.**
3. If TMP is running, the base pressure should be achieved right away. (This would occur only if MP was turned off for less than approximately 10 minutes and TMP was isolated prior to shut off of MP)
4. If pumping down after TMP has been off for a few hours it may be safer to purge TMP1 with N₂ using the N₂ MFC for 30 seconds. Then gradually open the roughing valve and wait until base pressure is reached in MP1.
- i. Open the gate valve between TMP and chamber. At this stage, the TC gauge readout should **NOT** vary at all.

- j. Turn on TMP by pushing the start button on the Leybold controller, unless already on. The green acceleration indicator should turn on. The chamber pressure from Baratron gauge readout should start decreasing in 20 seconds.
- k. Within 5 minutes, the turbo molecular pump should reach full speed and the yellow indicator should be on normal.
 - If any strange noise is heard from TMP, turn it off right away by pushing the off button on the controller.
 - If corrosive gas is anticipated to be used, 36 sccm industrial level nitrogen (corresponding to ~50 mTorr rise in TC pressure) should be provided through the purging port on the bottom of the pump by opening valve D5 and switching on the MFC “N₂ ind.” on the control panel once the pump has reached full rotation, which is indicated by the normal light being lit on the TMP1 controller. (Refer to Leybold 361C Turbo Molecular Pump manual.)
- l. After the Baratron gauge readout reaches 0.1 mTorr or lower, turn on the ion gauge by pushing the “ON” button on the ion gauge controller for IG1.
- m. Wait until the chamber reaches the base pressure 2.0×10^{-8} . This process may take up to couple of days depending on how long the chamber has been under atmosphere.
 - If the chamber has been exposed to ambient or pumping system has been off for more than a day, baking the chamber is necessary to achieve base pressure and remove any build up on the sidewalls of the chamber. Two heating tapes are used to bake the chamber. **Do NOT** turn on the power over 20% of the full range on the variable transformer to prevent over-heating. At this point the chamber pump down procedure is complete. If no processing is to be performed system should be left in this idle state.

After base pressure in the chamber is achieved, plasma processing can begin using the following procedure. If a sample is to be processed the following procedure must be followed to load the sample in to the chamber. However, it is better to warm up the plasma before processing a sample, in which case skip to steps 3-6, and then return to step 2 and repeat the following steps.

2. Transfer the sample from transfer tube to the chamber:

- a. See instructions for loading a sample from the loadlock in the Transfer Tube SOP.
- b. Move the cart into position for transfer to the ICP.
- c. Before opening the gate valve between the ICP and the TT check that their pressures are roughly equivalent. If the ICP pressure is too high the gate valve between the TT and its cryopump/turbo pump can be closed briefly. Ensure that no gas is flowing into the ICP.
- d. Open the gate valve (G4) using the controller box (trace the cable to ensure). Check the ion gauge controllers on both the ICP and TT to ensure that the pressure has not changed significantly.
- e. Secure the sample by sliding the holding fork attached to the end of the transfer arm around the upper groove of the sample holder.
- f. Using the manipulator, lift the sample off the cart. Verify that the arm has cleared the cart (a setting of about 5.5 on the Y-axis manipulator is sufficient).
- g. Slowly slide the transfer arm forward to move the sample into the ICP chamber.
- h. Visually confirm the location of the sample in relation to the sample stage pin by checking through the viewport on the lower section of the ICP chamber.
- i. Lower the sample holder onto the protruding pin. Visually confirm.

- j. Slowly begin sliding the transfer arm out. The holder should stay on the stage.
- k. When re-entering the transfer tube ensure the height of the transfer arm is readjusted so as not to hit the cart or holding pin in front of the ICP chamber.
- l. Fully withdraw the transfer arm into the tube so that it has cleared the gate valve.
- m. Close the gate valve (G4) between the ICP and TT.

With the sample loaded, if necessary, plasma processing can begin. Processing gases must be introduced into the reactor prior to striking plasma by performing the following procedure. Proceed to step 3, 4, or 5 depending on plasma chemistry.

3. Feed in process gas for plasma for inert gas only:

- n. Check that the chamber is at the base pressure of 2×10^{-8} .
- o. Check regulators for all the desired gases (N_2 , Ar, O_2) by opening the gas tank.
- p. Check the cylinders are filled with enough gas to obtain required flow rate.
- q. **Turn off the ion gauge**, which cannot go above 1×10^{-3} .
- r. Open the pneumatic valves for gases to be used before the Mass Flow Controller (MFC), which are V1, V3, and V5.
- s. Gradually open the corresponding valve after the MFC, which are V2, V4, and V6, to prevent a large pressure difference to the MFCs.
- t. Adjust the set point on the MFC control unit to desired flow rate for each gas.
- u. Open Diaphragm valve D3 and then gradually open D4. The chamber pressure should go slightly higher; wait until it goes back to the base pressure. This will pump down the gases which have been sitting in the line.
- v. Zero the Baratron gauge so as to accurately measure chamber pressure once gases begin to flow in.
- w. Turn on the MFCs for the gases to be used. Wait until a steady flow is achieved. Do fine adjustments if needed.
- x. Record pressure achieved in chamber after steady flow is reached

4. Feed in flammable process gas (CH_4) only:

THE FOLLOWING INTERLOCK FOR CORROSIVE GAS USE MUST BE MET TO BEGIN: N_2 PURGE TO MAIN CHAMBER AND QMS TURBO PUMPS MUST BE ON.

- a. Check that the chamber is at the base pressure of 1.0×10^{-7} .
- b. Check that the flammable gas detector is showing a green “Ready” light and no alarm is detected, indicating by a flashing red light and beeping noise.
- c. Check there is enough CH_4 gas in the cylinder and the regulator is CLOSED. (This regulator should always be closed while CH_4 gas is not in use.)
- d. **Turn off the ion gauge.**
- e. Gradually open Diaphragm valve D9. The chamber pressure should go slightly higher; wait until it goes back to the base pressure.
- f. Adjust the set point on MFC control unit, which is channel 1, to desired flow rate for CH_4 gas.

- g. Open the valve on CH₄ cylinder and the isolation valve after the regulator. Adjust the regulator to get 12 Torr outlet pressure
- h. Gradually open the Diaphragm valve D8 and then D9 for.
- i. Zero the Baratron gauge, so as to accurately measure pressure of the chamber.
- j. Turn on the MFC. Wait until the steady flow is achieved. Do fine adjustments if needed.
- k. Record pressure in chamber once steady flow is achieved.

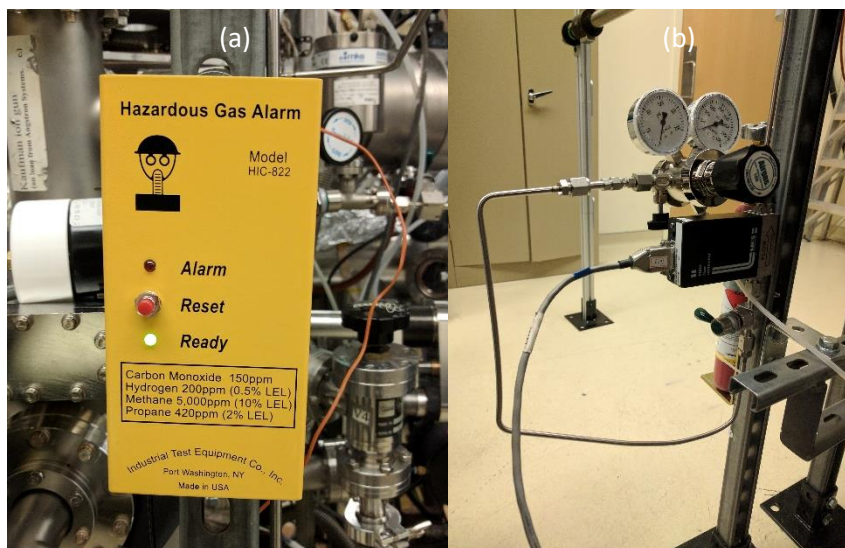


Figure A-0-9 (a) Hazardous gas alarm during normal operation. The “Alarm” red light will be illuminated and an alarm will sound upon detection of lower limits of explosive gases. (b) Methane lecture bottle, regulator, and post-regulator valve.

5. Feed in corrosive process gas (Cl₂ and/or BCl₃) only:

THE FOLLOWING INTERLOCK FOR CORROSIVE GAS USE MUST BE MET TO BEGIN: N₂ PURGE TO MAIN CHAMBER AND QMS TURBO PUMPS MUST BE ON.

- l. Check that the chamber is at the base pressure of 1.0×10^{-7} .
- m. Check there is enough Cl₂ gas in the cylinder and the regulator is CLOSED. (This regulator should always be closed while Cl₂ gas is not in use.)
- n. Check that 36 SCCM nitrogen is supplied to the purging ports of Turbopumps 1 and 2.
- o. **Turn off the ion gauge.**
- p. Gradually open Diaphragm valve D4. The chamber pressure should go slightly higher; wait until it goes back to the base pressure.
- q. Adjust the set point on MFC control unit, which is channel 1, to desired flow rate for Cl₂ gas.
- r. Open the valve on Cl₂ cylinder and the isolation valve after the regulator. Adjust the regulator to get 12 Torr outlet pressure. Then close gas cabinet door.
- s. Gradually open the Diaphragm valve D1 and then D2 for Cl₂ and/or D6 and D7 for BCl₃. Close the gas cabinet door.
- t. Zero the Baratron gauge, so as to accurately measure pressure of the chamber.
- u. Turn on the MFC. Wait until the steady flow is achieved. Do fine adjustments if needed.
- v. Record pressure in chamber once steady flow is achieved.

6. For corrosive gas and inert gas mixture (Cl₂, BCl₃, Ar, O₂, N₂):

THE FOLLOWING INTERLOCK FOR CORROSIVE GAS USE MUST BE MET TO BEGIN: N₂ PURGE TO MAIN CHAMBER AND QMS TURBO PUMPS MUST BE ON.

- a. Check that the chamber is at the base pressure of 9.0×10^{-8} .
- b. Check there is enough Cl₂ and or BCl₃ gas in the cylinder.
- c. The regulators should be CLOSED. (This regulator should always be closed while Cl₂ gas is not in use.)
- d. Check 36 SCCM nitrogen is supplied to the purging ports of Turbopumps 1 and 2.
- e. **Turn off the ion gauge.**
- f. Gradually open Diaphragm valve D3 and D4. The chamber pressure should go slightly higher; wait until it goes back to the base pressure.
- g. Adjust the set points on MFC control unit to desired flow rates for gases.
- h. Open the regulator on Cl₂ cylinder/ and or BCl₃ at their respective gas tanks.
- i. Open the pneumatic valves, for the inert gas, before the MFC (V1, V3, and V5) first, and then open the corresponding valve after the MFC (V2, V4, and V6).
- j. Turn on the MFCs for the inert gases.
- k. Gradually open the Diaphragm valve D1 and then D2 for Cl₂ and/or D6 and D7 BCl₃.
- l. Close the gas cabinet doors.
- m. Turn on the Cl₂ and/or the BCl₃ MFC. Wait until the steady flow is achieved. Do the fine adjustment if needed.
- n. Record chamber pressure once flows have stabilized.

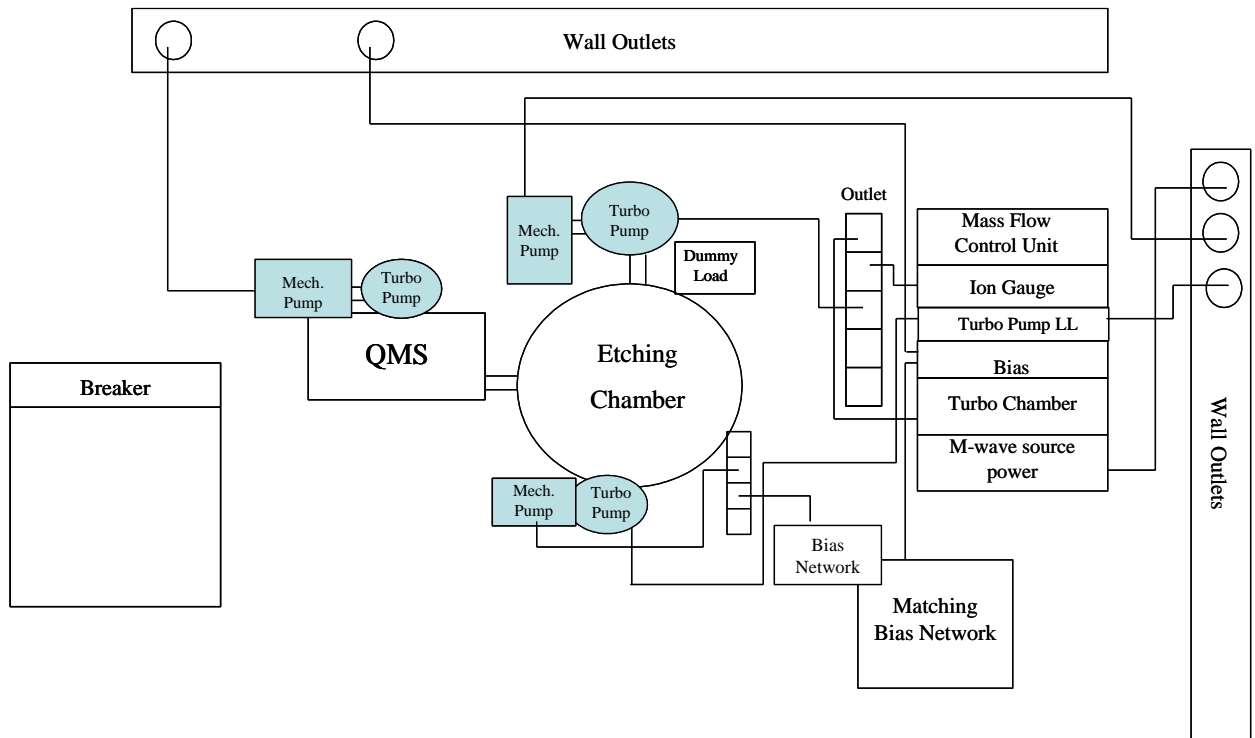
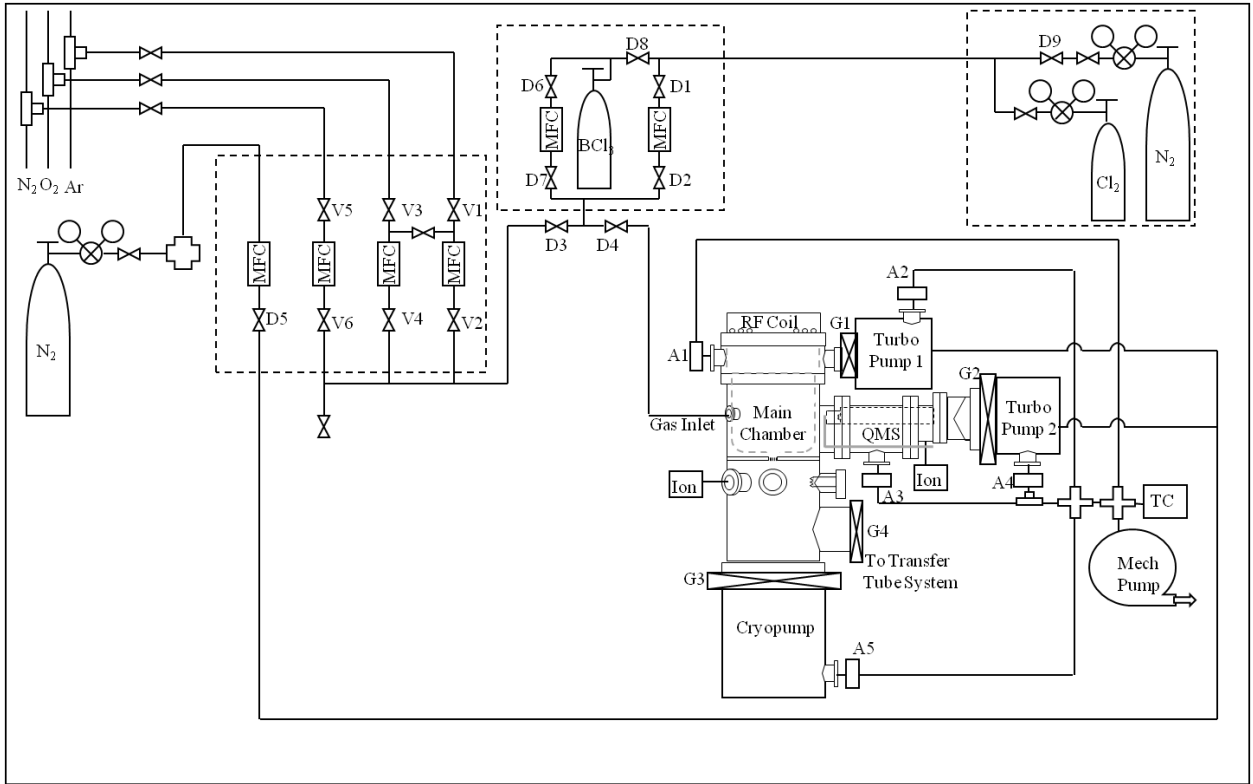
7. Turning on the plasma

THE FOLLOWING INTERLOCK FOR PLASMA GENERATION MUST BE MET TO BEGIN: 1. INDUCTION COIL FAN ON.

- a. Ensure the fan on the induction coil is plugged in and operating.
- b. Turn on the main power of the RF generator (Seren R1000) by flipping the main power switch.
- c. Turn on the main power of the matching network tuning controller (RFPP 761 Unit) and ensure its operation mode is set to "Auto".
- d. If bias is desired, turn on the main power and bipolar voltage control of the DC bias controller (Kepco BOP 500M).
- e. If etching in the lower chamber is desired, turn on the filament power supply (Harrison Labs 6263A). Let all the electronics units warm up for 30 - 45 minutes.
- f. Flow the process gases (pressures should be adjusted in steps 2-4).
- g. Set the RF generator to the desired source power (500W) and press the "RF on" button. A red light should indicate RF power is being supplied.
- h. If plasma does not strike, check that the reflected power as indicated on the generator display is not higher than 70 W, or that no warnings are displayed. If the reflected power is low, consider increasing the gas flow using the appropriate MFC. If the power is high or if

warnings are displayed, turn off the RF supply by pressing the "RF on" button again and check the connections between the generator, matching network and source coil.

- i. If bias is desired, set the DC bias to the appropriate voltage.
- j. If etching in the lower chamber is desired, set the filament power supply to ~2 Amps. Usually this should be done a minute or two before the experiment to ensure the filament is receiving current (indicated by a reddish glow).
- k. After the process is finished, turn off the RF power by pushing the "RF on" button on the front panel of the Seren R1000. Processes should not exceed 15 minutes so as to not over heat system.
- l. Turn off the corrosive process gases first on the MFC.
- m. Leave the inert gases running for about 5 minutes.
- n. Turn off the MFCs, close the corresponding pneumatic valves and the Diaphragm valve D4 and D3 for Cl_2 and/or D6 and D7. BCl_3 .
- o. After the Baratron gauge readout reaches 0.1 mTorr or below, turn on the ion gauge by pushing the "1/T set" button on the ion gauge controller and push channel 1.
- p. Turn off TMP1 purging nitrogen.



8. Troubleshooting

This section details major problems occurring on ICP chamber and the steps taken to fix them.

3/2012:

Problem: Unable to strike the plasma such as $O_{2(g)}$ and $N_{2(g)}$.

Solution:

1. Check the connection of cable on the top of chamber.
2. Shine the light into chamber while turning on the RF generator.
3. Flow the Ar gas with O_2 or N_2 to strike the plasma, once the plasma been ignited then Ar could be slowly decreased to 0.

7/2012:

Problem: The wire connected from voltage supplier to bias ring was burn out.

Solution:

1. Order stainless steel wire from McMaster Carr.
2. Clean up the stainless steel wire by IPA and alcohol, cut into a suitable length and then replace old one.
3. Check by the multimeter for connection between voltage supplier and bias ring.

8/2012:

Problem: The turbo pump started making a high pitch noise.

Solution:

1. Check the turbo pump controller is in normal condition.
2. Isolated the turbo pump. First, close gate valve to chamber, and then switch off the turbo pump by controller. Wait 20 mins to pump out the turbo pump by mechanical pump, and close the roughing valve to mechanical pump.

8/2012:

Problem: The bias beam couldn't be observed during the plasma etching process.

Solution:

1. Check the mesh at the center of upper chamber is clean and grounded.
2. If mesh is covered by green species or other contamination, the mesh need to be cleaned.
 - a. Flip up the plate in the upper chamber, undo the filament connection carefully.

- b. Take out the plate and undo the screws at the center mesh. Be careful that there are three small of stainless steel piece between the plate and mesh which can make the mesh grounded.
- c. Sonicate the mesh with IPA for 10 mins two times.
- d. Reinstall the mesh and plate into the chamber, and connect the filament wire.
- e. Use multimeter to check the mesh is grounded.

4/2018:

Problem: Ran Te sputter target (3" diameter) in ICP under Ar (500W/900W) and H₂ (500W/900W) for etch product identification with QMS. Observed substantial chamber contamination, namely deposition of Te-based compounds (silvery grey metallic color) on inside of quartz bell jar

Solution:

1. Ran 900W Cl₂ plasma at low pressure (~10-20 mTorr) for 3-4 times for 5 min each.
2. Once done processing, let cool for 30 minutes and performed three pump-purge cycles using high vacuum pumps
3. Carefully vented and unload quartz liner assembly (bell jar, ring, top window)
4. Wiped quartz pieces with acetone and IPA using clean room wipe
5. Submitted bell jar for hydrofluoric acid clean as flame polishing (Sci-Tech Glassblowing in Moorpark, CA. Vendor contact information listed in Section M.1)
6. Upon receipt from Sci-Tech, wiped down quartz pieces with acetone followed by IPA and dried using N₂
7. Replaced quartz components in ICP chamber and pumped down
8. Ran 3 cycles of O₂ plasma clean (900 W at 10 mTorr for 5 min increments)
9. Labeled previously Te-contaminated bell jar for use in subsequent etch product identification experiments to ensure contamination doesn't spread to two other cleaned bell jars.

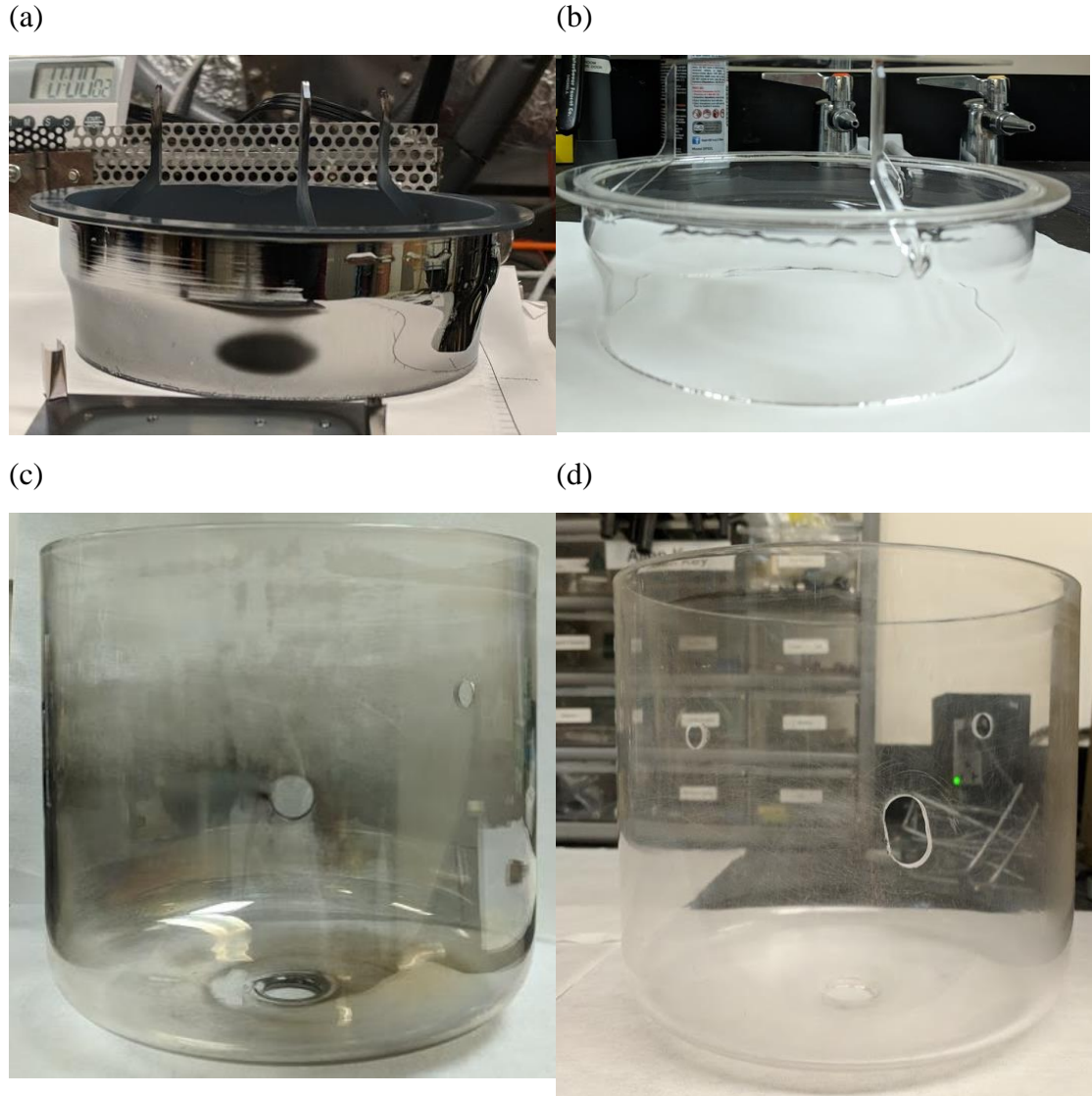


Figure A-0-10 ICP (a) Quartz pedestal and (c) ICP bell jar liner after Te contamination, note the presence of silvery grey metallic color due to deposition. (b) Quartz pedestal and (d) ICP bell jar liner after multiple cycles of ICP Cl_2 clean at 900W source power and subsequent HF acid clean and flame polishing at Sci-Tech Glassblowing.

9. Cryopump Regeneration

- a. Isolate cryopump by closing gate valve and closing backing valve.
- b. Turn off compressor. Leave cryopump for 2-3 hours, expect to see condensation.
- c. After condensation evaporates, apply heating jacket and plug it in.
- d. Let the cryopump heat for 8 hours.
- e. Close backing of transfer tube (TT) and load lock (LL) turbo pumps, set timer to 5 min.

- f. Look at TT mechanical pump thermocouple (TC) gauge, slowly open cryopump backing. You should see a pressure spike.
- g. Let cryopump pump out until timer runs out, then close cryopump backing. Let TC gauge bottom out, then reopen TT and LL backing.
- h. Repeat steps e-g until TC gauge no longer spikes when cryopump backing is opened. Close cryo backing.
- i. Unplug heating jacket, let it cool then remove it.

Ion Beam Chamber

1. **Pumping down the entire system (Note: The chamber's default state should be pumped down; ensure that the gate valve located between the ion beam chamber and ICP chamber is open and check the pressure reading on the ICP chamber ion gauge to verify. If the gate valve is closed, turn off the ion gauge controller for the ICP chamber. Verify that all gas lines to the ICP and ion beam chamber are closed. Close the ICP cryo pump gate valve, and leave the two gate valves to the TMPs on the ICP chamber open. Monitor the Baratron gauge on the ICP, and slowly open the gate valve between Ion Beam and ICP chamber, ensuring that the Baratron readout does not go above 50 on the pressure readout. Once completely open, and the Baratron reads single digits or zero, open the gate valve to the cryo pump. The following steps should only be taken if you aware that the chamber has been vented and not pumped back down).**
 - a. THE FOLLOWING INTERLOCKS FOR THE PUMP DOWN PROCEDURE MUST BE MET TO BEGIN PUMPING: COOLING WATER FOR MAIN CHAMBER ICP TURBO PUMP AND MASS SPECTROMETER TURBO PUMP MUST BE FLOWING AT 2.0-3.5GPM).
 - y. Check that all the flanges are tightened and all the valves are in the closed position.
 - z. Check all the cables are correctly connected.
 - aa. Check the oil level in the mechanical pump on the ion beam chamber load lock, which should be 2/3 full in view window.
 - bb. Check MP and its exhaust for liquid leaks. (oil, condensation, exhaust fluid).
 - cc. Check that the Baratron and thermocouple gauges are on.
 - dd. Turn on MP by turning on the switch on the power strip. The thermocouple gauge reading should start going down within 20 seconds. If not, turn off the pump and check connections to chamber and turbopumps for vacuum leaks. Ensure load lock 2.75" CF quartz door and roughing valve to mechanical pump are closed

- ee. Slowly open the manual gate valve between the 2.75" CF 6 way cross load lock and ion beam chamber.
 - ff. Slowly open the roughing valve on the load lock and wait for the chambers to reach base pressure (Baratron readout of ~ 0.037 , corresponding to 37mTorr).
- 4.

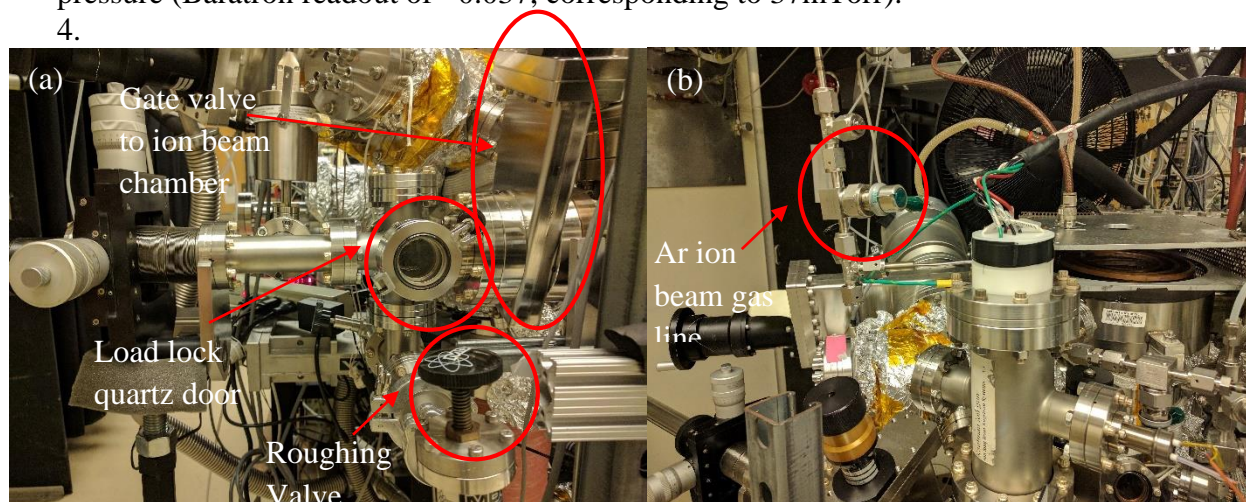


Figure A-0-10 (a) Roughing valve for load lock and ion beam chamber. (b) Ar gas line for ion source

- a. Close the gate valve between the load lock chamber and ion beam chamber and slowly open manual gate valve between ion gun and ICP main chamber, while keeping an eye on the ICP chamber Baratron gauge.
- b. Slowly open Ar ion beam gas line valve to pump out the gas line. Check the ICP Baratron gauge and ensure the pressure does not exceed 50mTorr.
- c. Once the ICP Baratron has reached below 1mTorr, turn on the ion gauges by pressing the IG1 and IG2 buttons on the ion gauge controller. If the pressure reads above 5.0×10^{-5} Torr, shut off ion gauge by pressing the IG1 button and wait several minutes before turning the gauge back on.

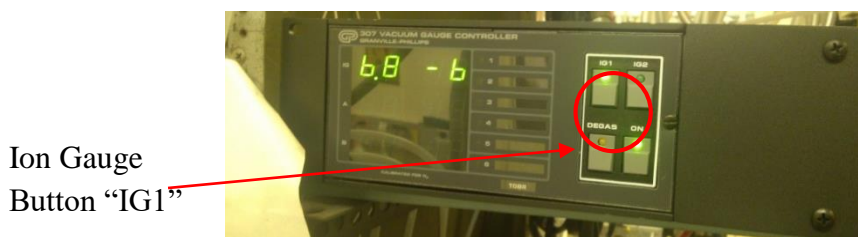


Figure A-0-11 ICP Chamber Ion gauge

5. Turning on the ion source controller (Note: the sample must already be loaded and the chamber must be already pumped down).

- q. Ensure the Ar gas line valve is open.
- r. Leave IG1 on the ICP ion gauge turned on

- s. Set the set point on the Ion Beam MFC to 0.50 and monitor the ion gauge until it reaches about 5×10^{-6} Torr
- t. Turn on left source beam switch. Do not turn on the right source beam switch yet.
- u. Hold down discharge switch to the voltage setting and adjust the discharge dial until the monitor reads 40.0 V.
- v. Hold up discharge switch to the current setting and adjust the cathode dial until the monitor reads 0.25 mA.
- w. Turn on right source beam switch.
- x. Hold neutralizer switch to the emission setting and adjust the neutralizer dial until the monitor reads a value close to the value displayed on the beam display. This value should be about 5 mA.

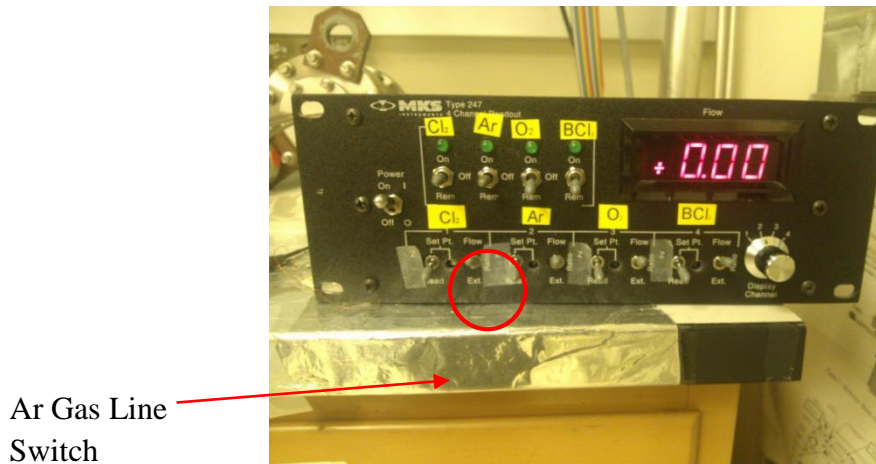


Figure A-0-12 MFC with Ar gas line switch.

6. Turning off the ion source controller.

6. Turn off the right beam switch
7. Turn the neutralizer, cathode, and discharge dials counter-clockwise until they stop.
8. Then the left source switch.
9. Turn off the power switch.
10. Turn off Ar gas switch on MFC.
11. Turn on ion gauges by pressing the IG1 and IG2 buttons on the ion gauge controller.

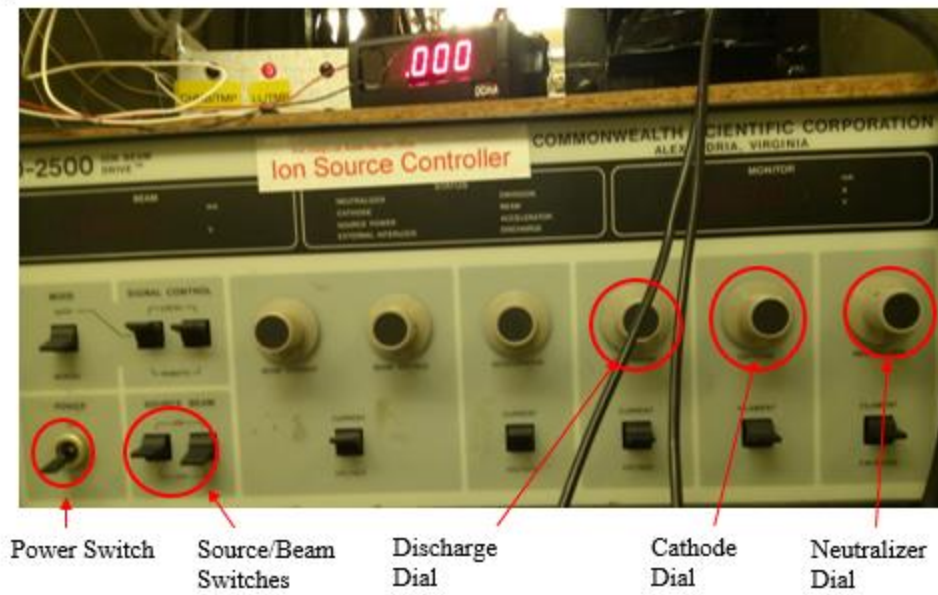
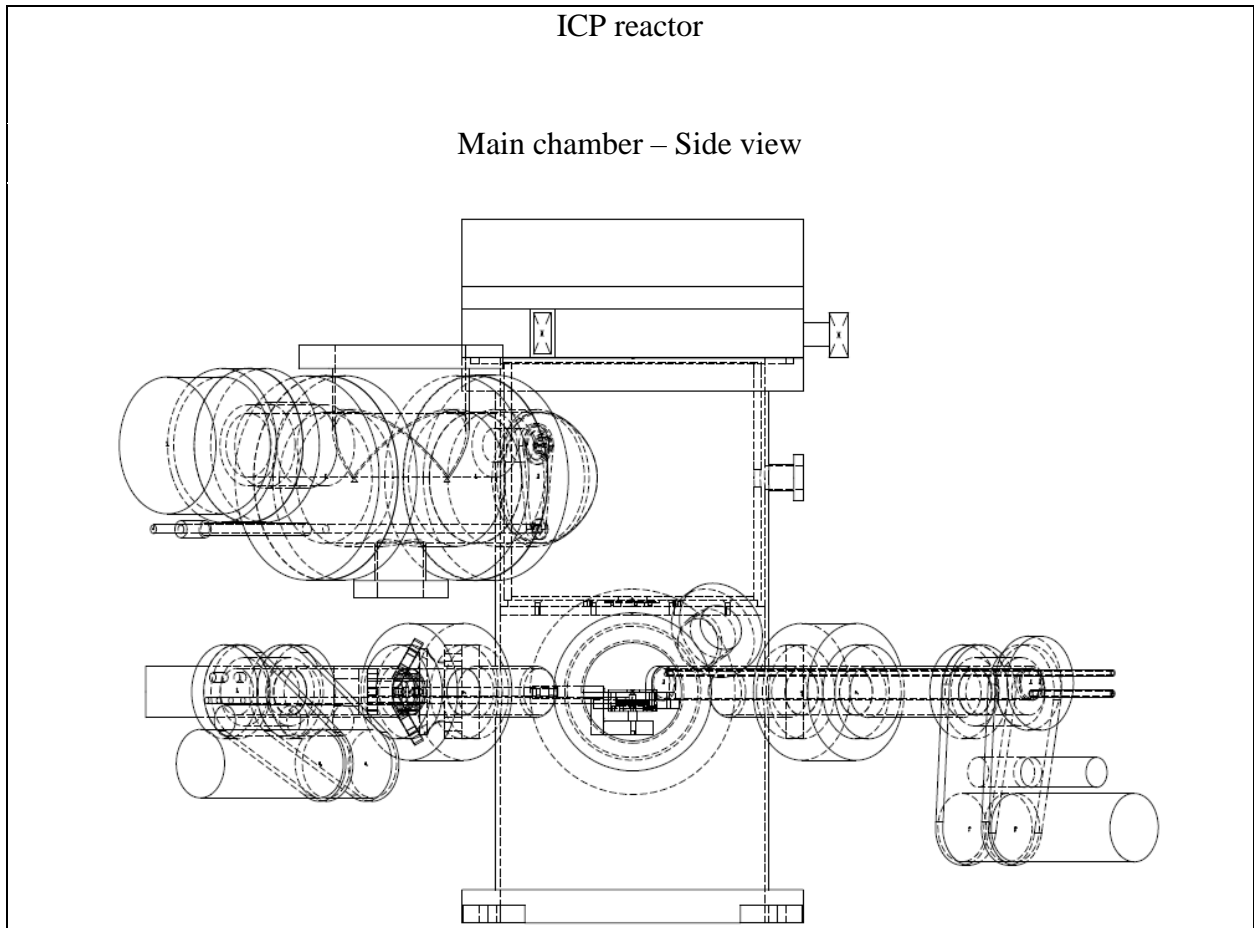


Figure A-0-13 Ion source controller.

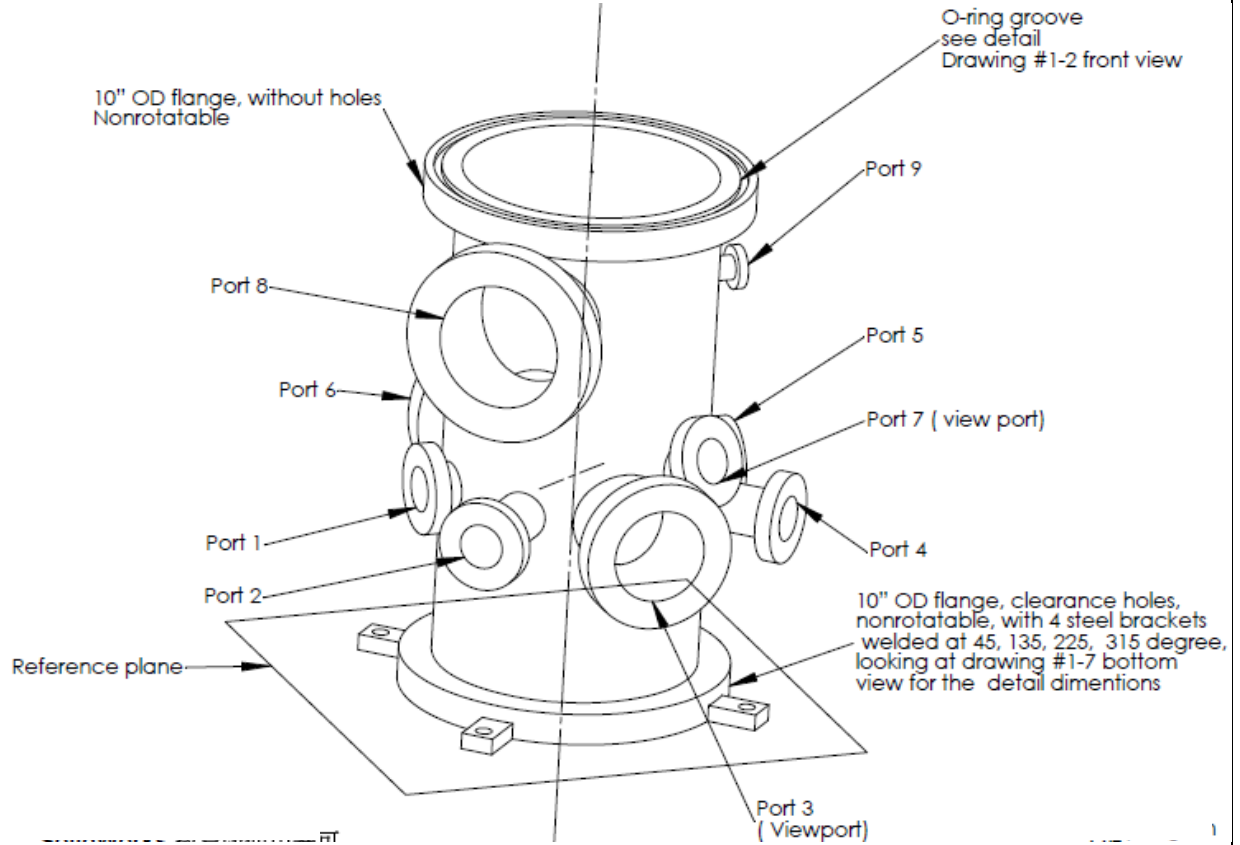
A.3. Schematics



University of California, Los Angeles, Department of Chemical and Biomolecular Engineering							
Part		Material	Stainless steel				
Filename		Scale	Yes	Units	inch	Quantity	1
Designer	Yunpeng Yin(MIT)	Date	6/11/2003				
Revised by		Date					
Contractor	Applied Vacuum Technologies	Date	6/11/2003				
Comments			Tolerance			+/- .0001	

ICP reactor

Main chamber – Isometric view

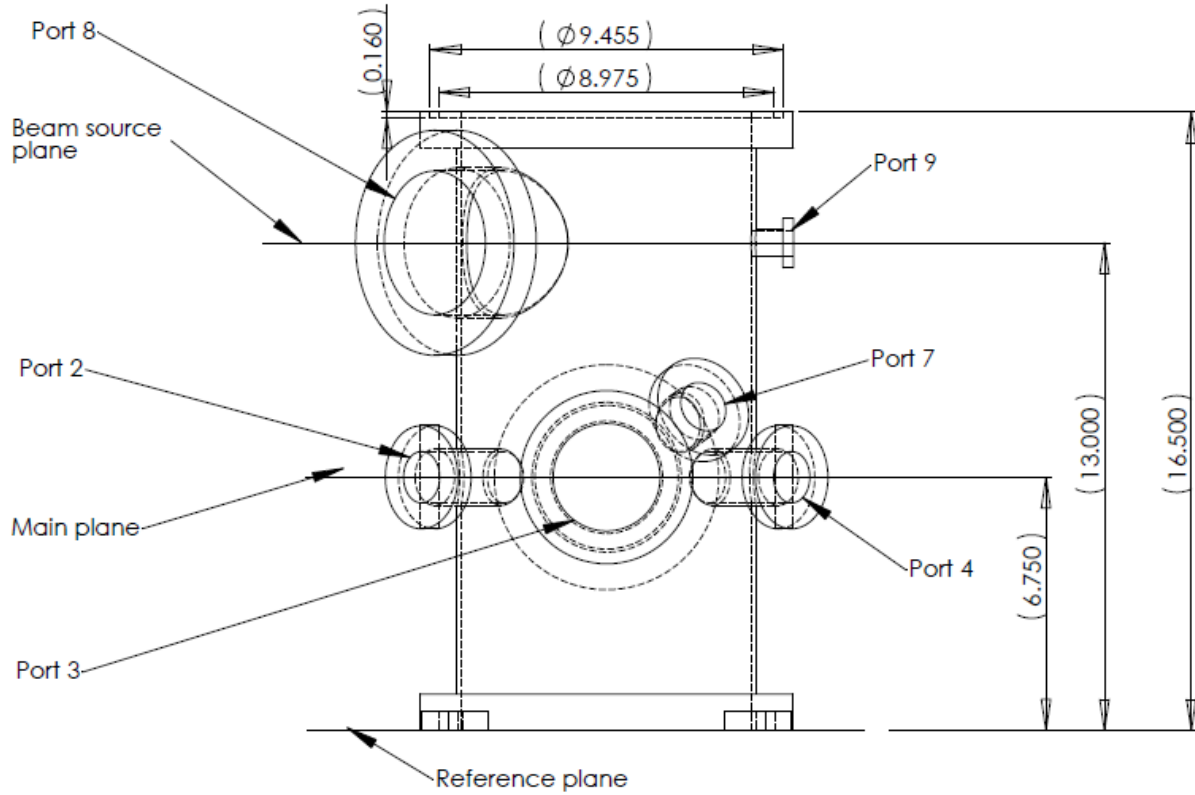


University of California, Los Angeles, Department of Chemical and Biomolecular Engineering

Part		Material	Stainless steel			
Filename		Scale	Yes	File name		Yes
Designer	Yunpeng Yin(MIT)	Date	6/11/2003			
Revised by		Date				
Contractor	Applied Vacuum Technologies	Date	6/11/2003			
Comments		Tolerance	+/- .0001			

ICP reactor

Main chamber – Front view

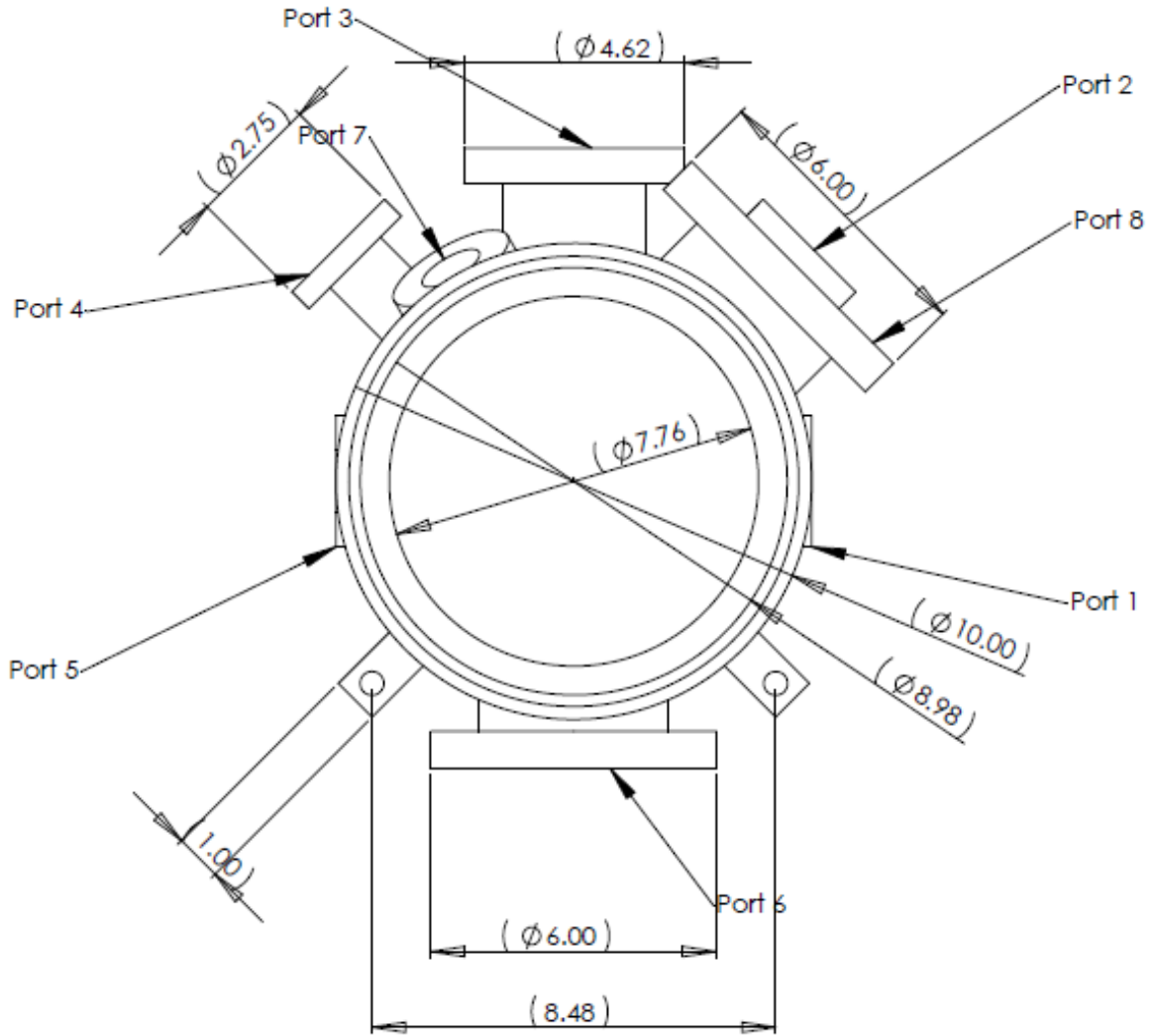


University of California, Los Angeles, Department of Chemical and Biomolecular Engineering

Part		Material	Stainless steel			
Filename		Scale	Yes	File name	Scale	Yes
Designer	Yunpeng Yin(MIT)	Date	6/11/2003			
Revised by		Date				
Contractor	Applied Vacuum Technologies	Date	6/11/2003			
Comments			Tolerance	+/- .0001		

ICP reactor

Main chamber – Top view

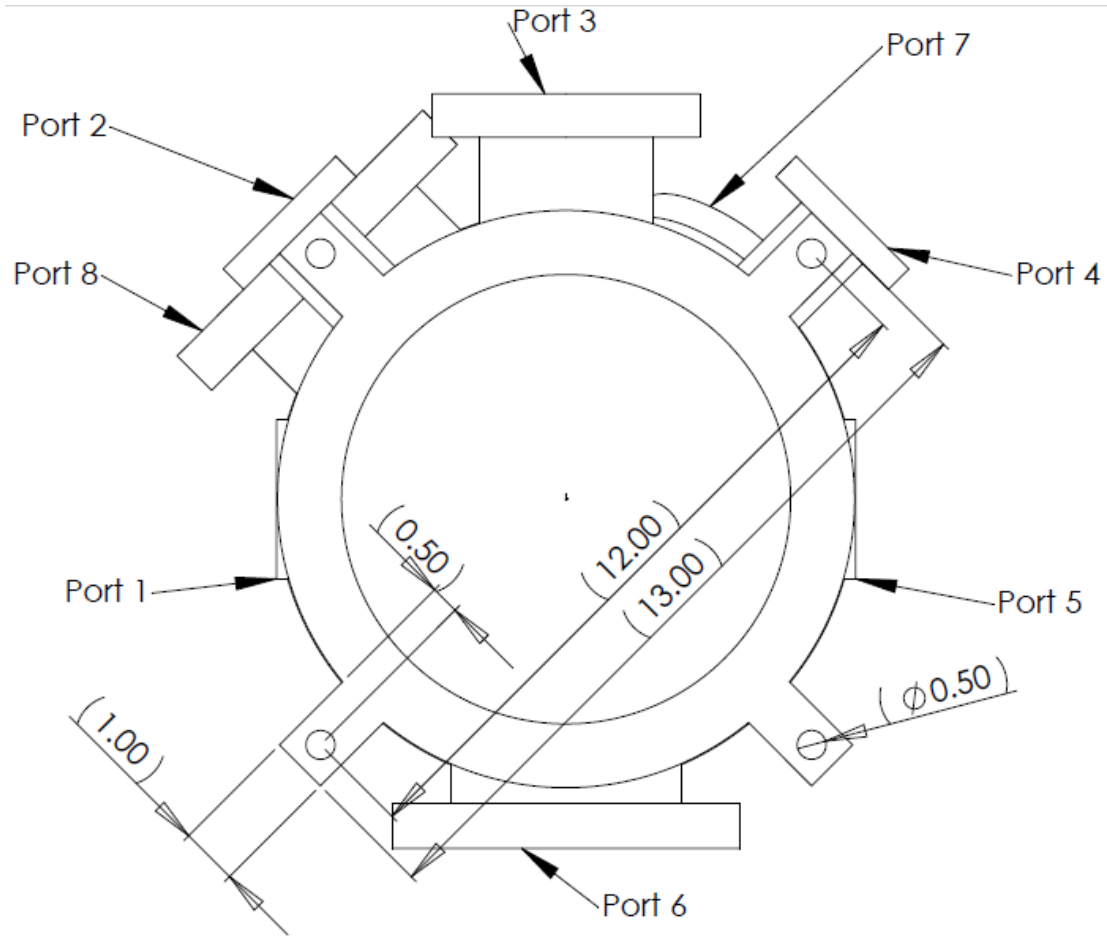


University of California, Los Angeles, Department of Chemical and Biomolecular Engineering

Part		Material	Stainless steel				
Filename		Scale	Yes	Filename		Scale	Yes
Designer	Yunpeng Yin(MIT)	Date	6/11/2003				
Revised by		Date					
Contractor	Applied Vacuum Technologies	Date	6/11/2003				
Comments			Tolerance		+/- .0001		

ICP reactor

Main chamber – Button view

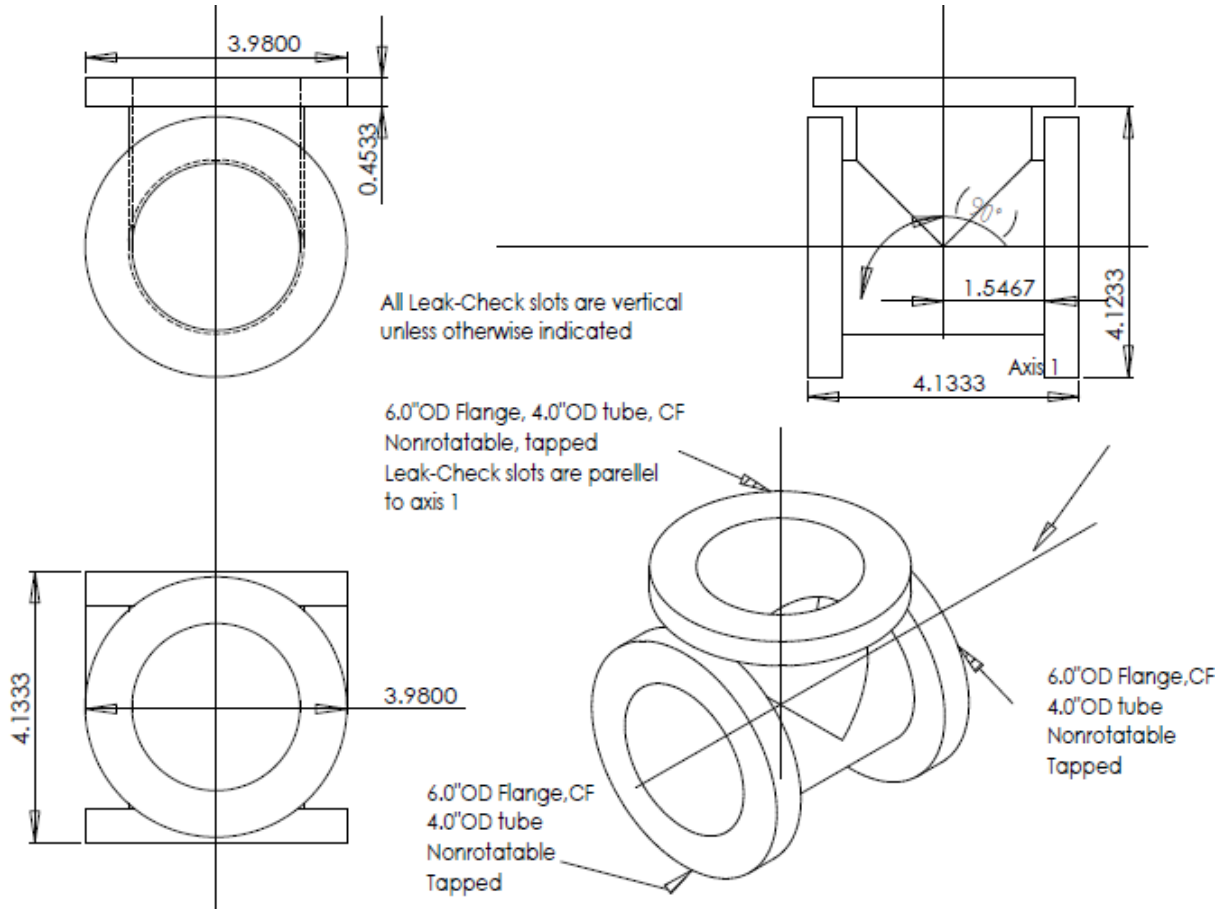


University of California, Los Angeles, Department of Chemical and Biomolecular Engineering

Part		Material	Stainless steel				
Filename		Scale	Yes	Filename		Scale	Yes
Designer	Yunpeng Yin(MIT)	Date	6/11/2003				
Revised by		Date					
Contractor	Applied Vacuum Technologies	Date	6/11/2003				
Comments			Tolerance	+/- .0001			

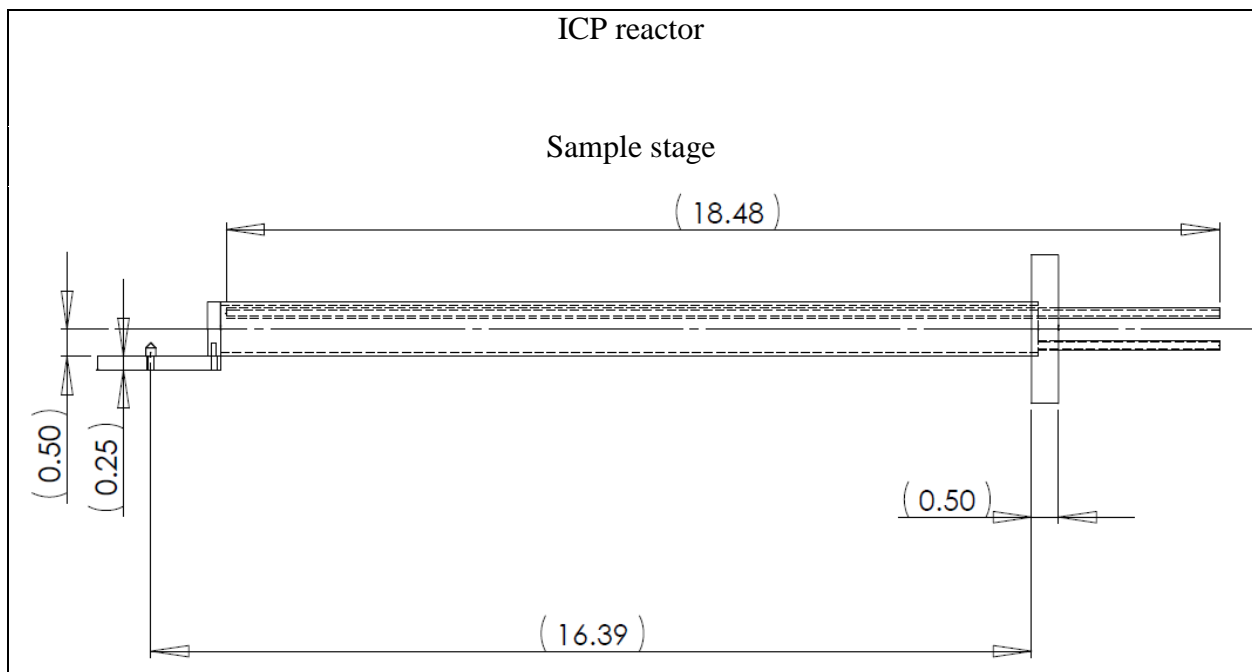
ICP reactor

Main chamber – QMS chamber



University of California, Los Angeles, Department of Chemical and Biomolecular Engineering

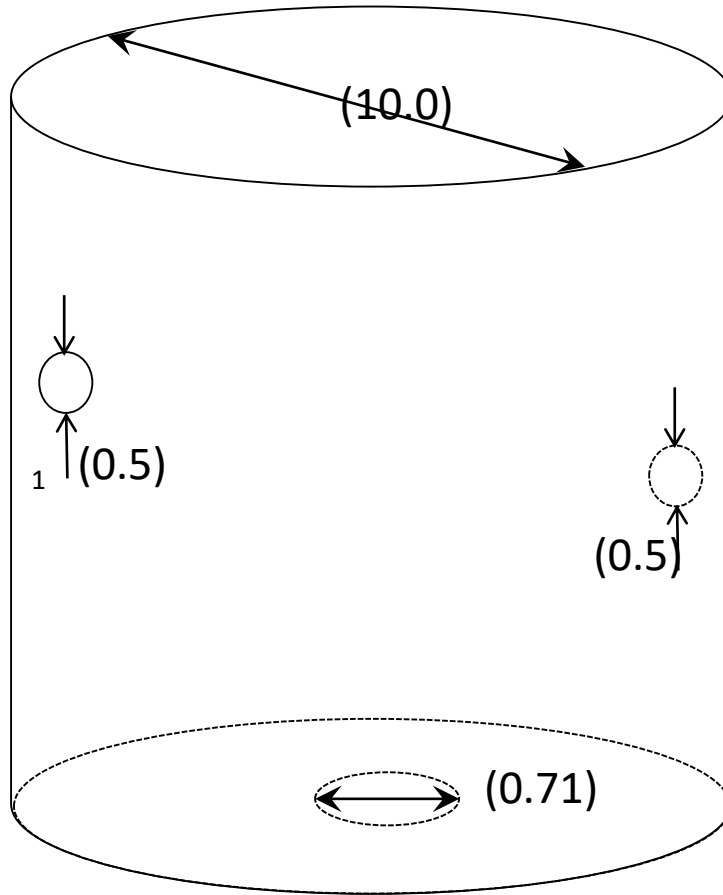
Part		Material	Stainless steel			
Filename		Scale	Yes	Filename	Scale	Yes
Designer	Yunpeng Yin(MIT)	Date	6/11/2003			
Revised by		Date				
Contractor	Applied Vacuum Technologies	Date	6/11/2003			
Comments		Tolerance	+/- .0001			



University of California, Los Angeles, Department of Chemical and Biomolecular Engineering							
Part		Material	Stainless steel				
Filename		Scale	Yes	Filename		Scale	Yes
Designer	Yunpeng Yin(MIT)	Date	6/11/2003				
Revised by		Date					
Contractor	Applied Vacuum Technologies	Date	6/11/2003				
Comments			Tolerance		+/- .0001		

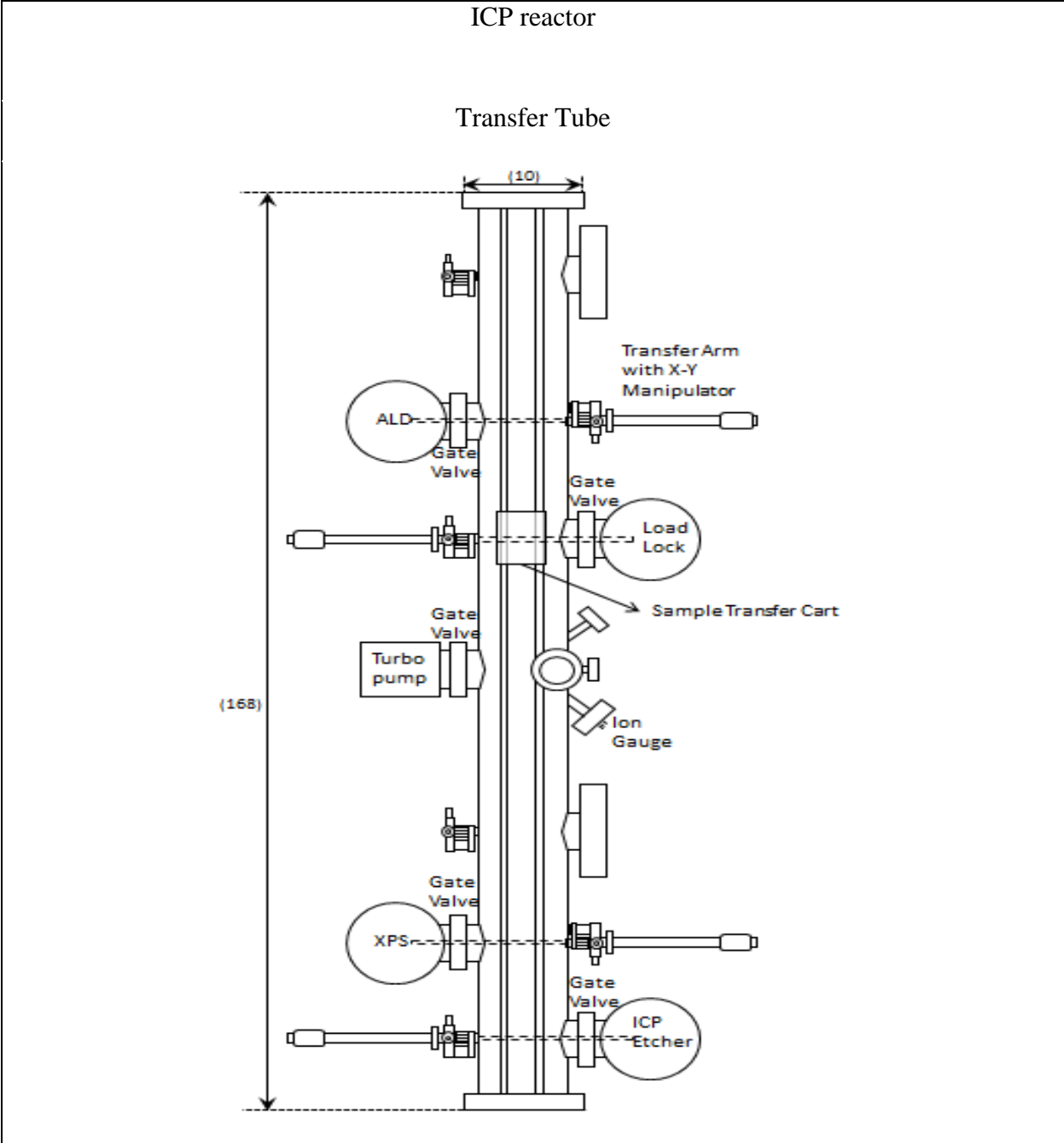
ICP reactor

Quartz in the ICP chamber



University of California, Los Angeles, Department of Chemical and Biomolecular Engineering

Part		Material	Stainless steel				
Filename		Scale	Yes	Filename		Scale	Yes
Designer	Yunpeng Yin (MIT)	Date	6/11/2003				
Revised by		Date					
Contractor	Applied Vacuum Technologies	Date	6/11/2003				
Comments			Tolerance			+/- .0001	



University of California, Los Angeles, Department of Chemical and Biomolecular Engineering

Part		Material	Stainless steel				
Filename		Scale	Yes	Filename		Scale	Yes
Designer	Jane Chang (MIT)	Date	1994				
Revised by		Date					
Contractor	Applied Vacuum Technologies	Date	1994				

B. Quadrupole Mass Spectrometer

B.1. Emergency Shutdown Procedures

1. Turn off the UTI100C Electronics Controller by following the sequence labeled below in the order indicated.

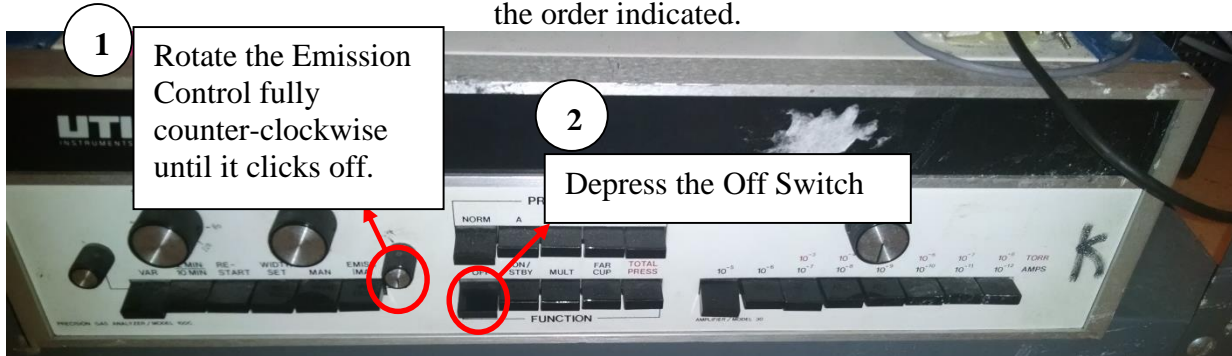


Figure B-1 QCM panel.

2. Turn off the oscilloscope by pressing the power button:

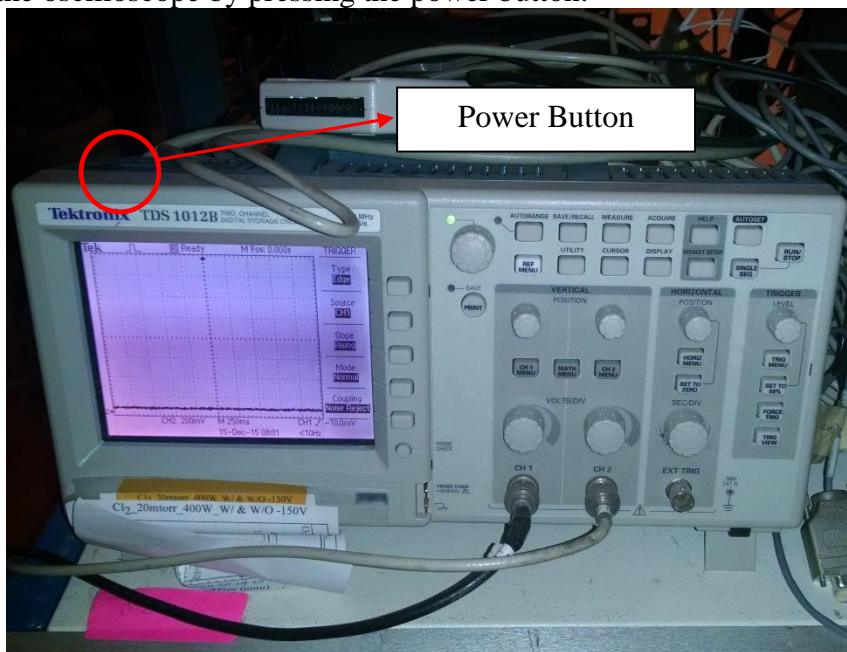


Figure B-2 Oscilloscope panel.

B.2. Schematics

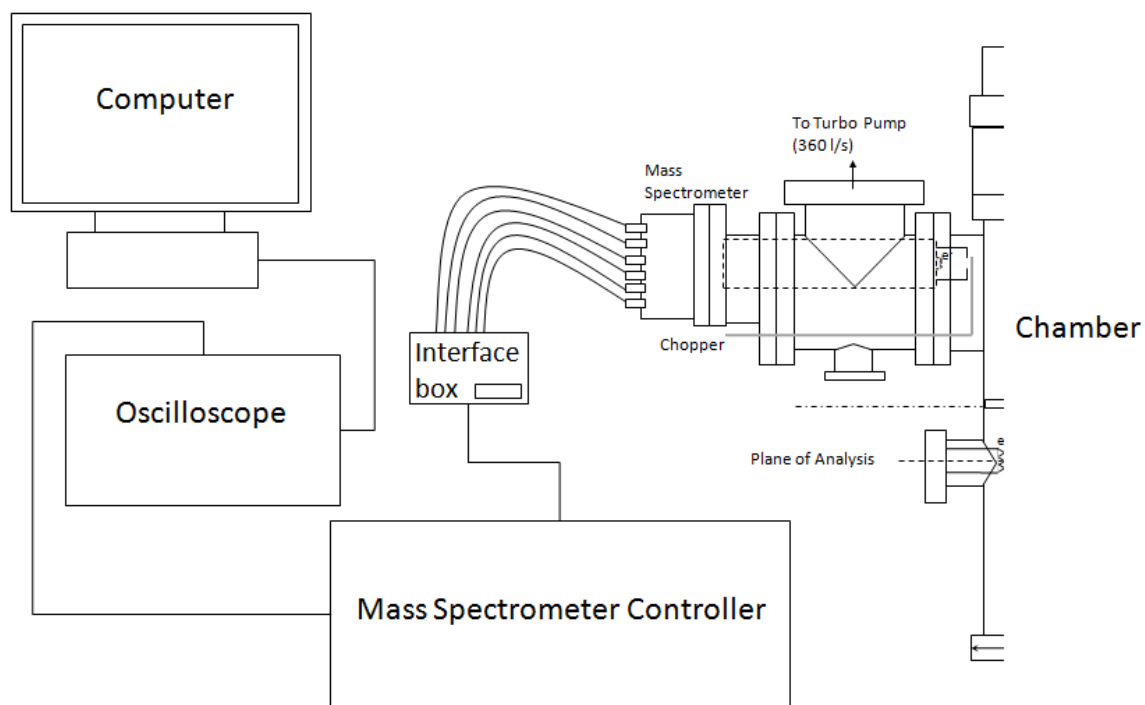


Figure B-3 QMS schematics.

B.3. Operating Procedures

1. Check the base pressure of the system, which should be about 2.8×10^{-8} Torr. Write the base pressure in the logbook.
2. Check the connections between the Spectrometer and the Interface Box, the Interface Box and the Spectrometer Control Unit (SCU), the SCU and the Oscilloscope, and the Oscilloscope and the Computer (Illustrated below). Turn on the computer.

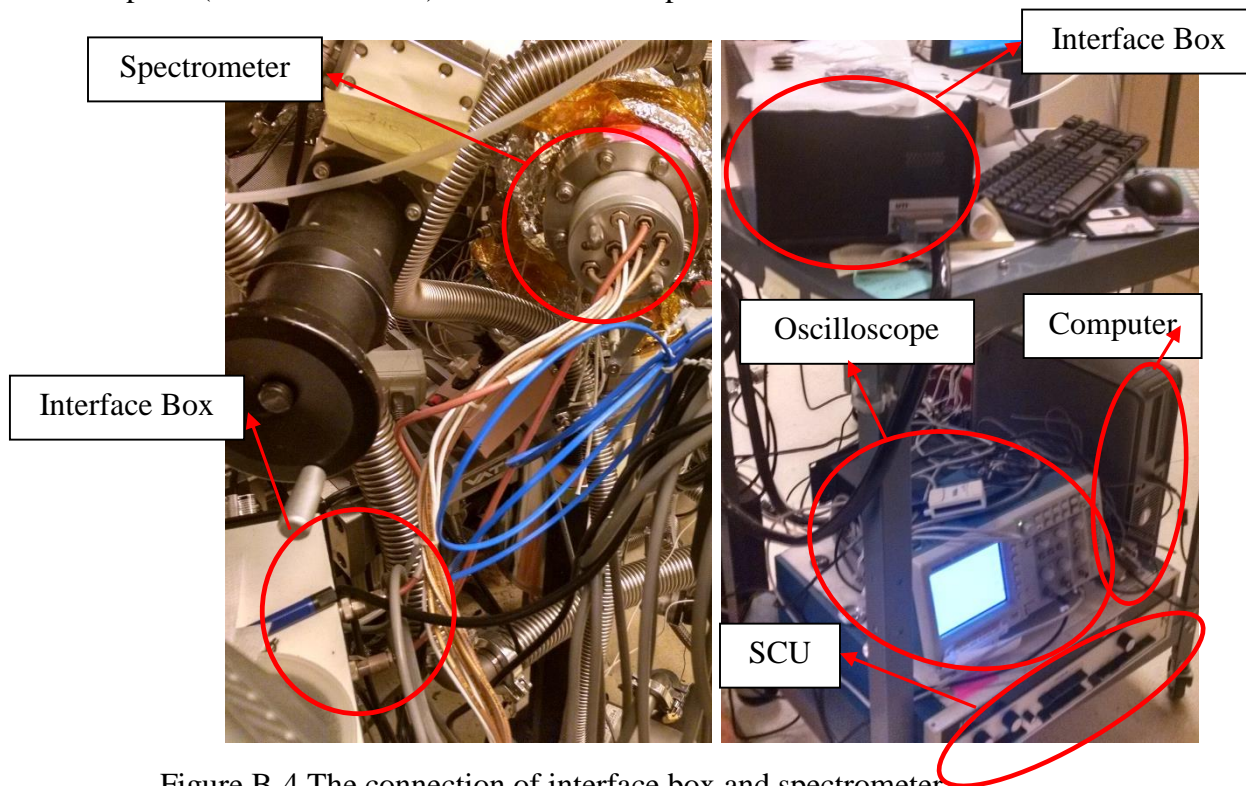


Figure B-4 The connection of interface box and spectrometer

3. Ensure that the power cable into the SCU is plugged in. Check that the follow switches are depressed (labeled below): “Var” and “Man” in the Scan section, “Norm” in the Program Section, “Off” in the Function Section and “ 10^{-5} ” in the Damper Section. Also make sure the emission control is off (rotated fully counter-clockwise).

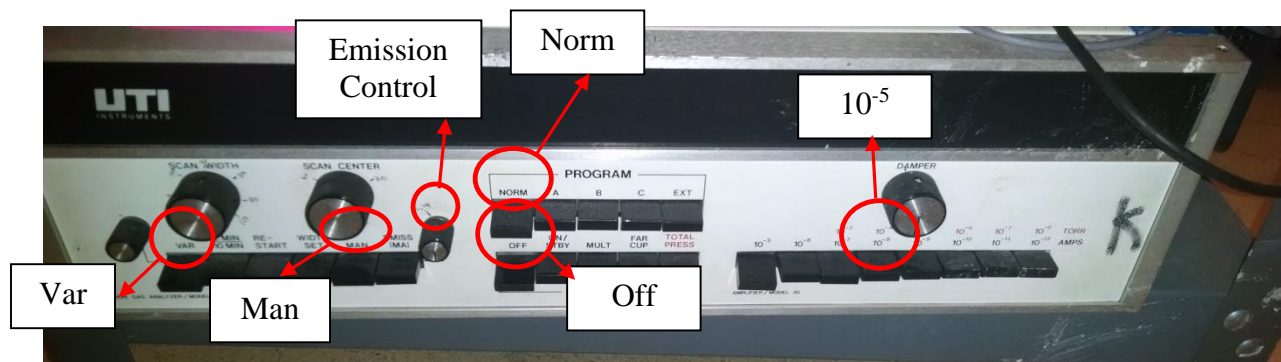


Figure B-5 QCM panel.

4. Depress the “On/Stby” switch on the SCU directly to the right of the “Off” switch. Let the electronics warm up for 30 minutes. Power on the oscilloscope by pressing its power button. Windows should indicate that new USB device has been plugged in and you need to select the software option to view the device.
5. Select TekDesktopAcquisition (the TDS 1012B should be selected as device by default).
6. After the electronics have warmed up set the scan center and width using the Scan Control section of the SCU. To set the center “Man” has to be depressed. To set the width, “Width Set” has to be depressed and “Man” should be released. Both of these values are set by using the corresponding rotary controls above the switches (can be seen in the preceding image).
7. Flow gas and strike plasma as required by your experiment.
8. Monitor the QMS pressure. The maximum operating pressure for QMS is $5 \cdot 10^{-6}$ Torr.
9. Start the QMS scan by releasing the “Man” switch, and depressing “Emiss (mA) and “Mult” switches at the same time. Adjust the emission current using the rotary control (max = 0.5 mA). If no signal is seen adjust the Damper (max = 10^{-9}).
10. Monitor the scan on the oscilloscope and adjust the visual as necessary using the controls for the y- and x-axis. A visual can be captured using the Tektronic software “Data Capture” button.
11. After finishing all the experiments, close the software and transfer all the data files to the server.
12. Turn off the power to the SCU by using the steps outlined below:

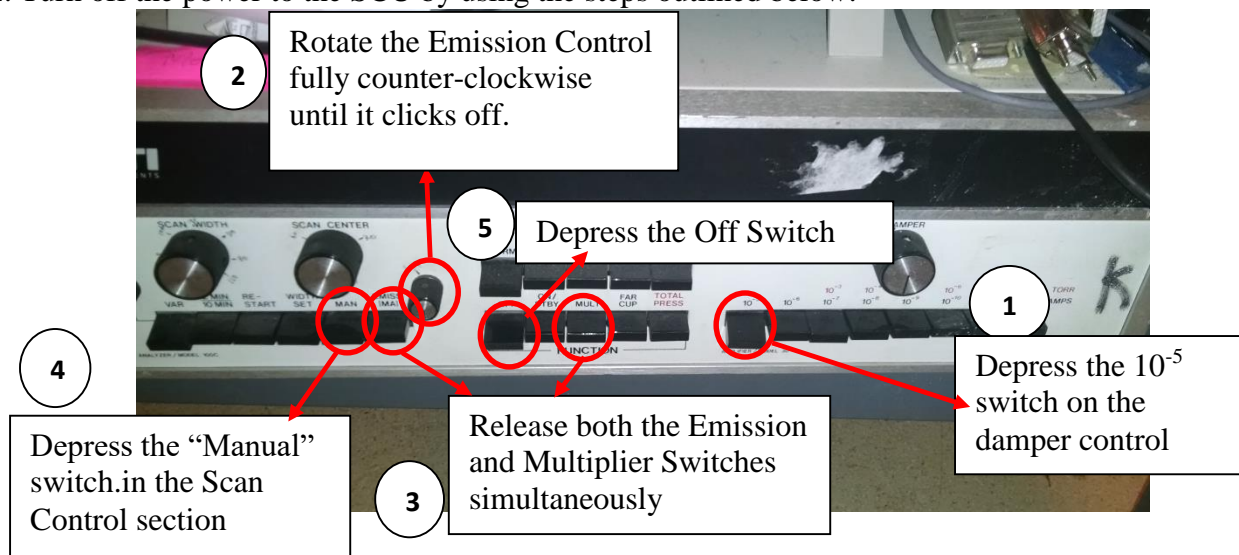


Figure B-6 QMS control electronics panel panel.

- a. Turn off the oscilloscope by pressing its power switch.
- b. Finish the logbook.

B.4. Troubleshooting

This section details major problems occurring on the QMS and the steps taken to fix them.

1/2018:

Problem: QMS not used for > 2 years, upon powering on and flowing gas, could not observe mass spectrum

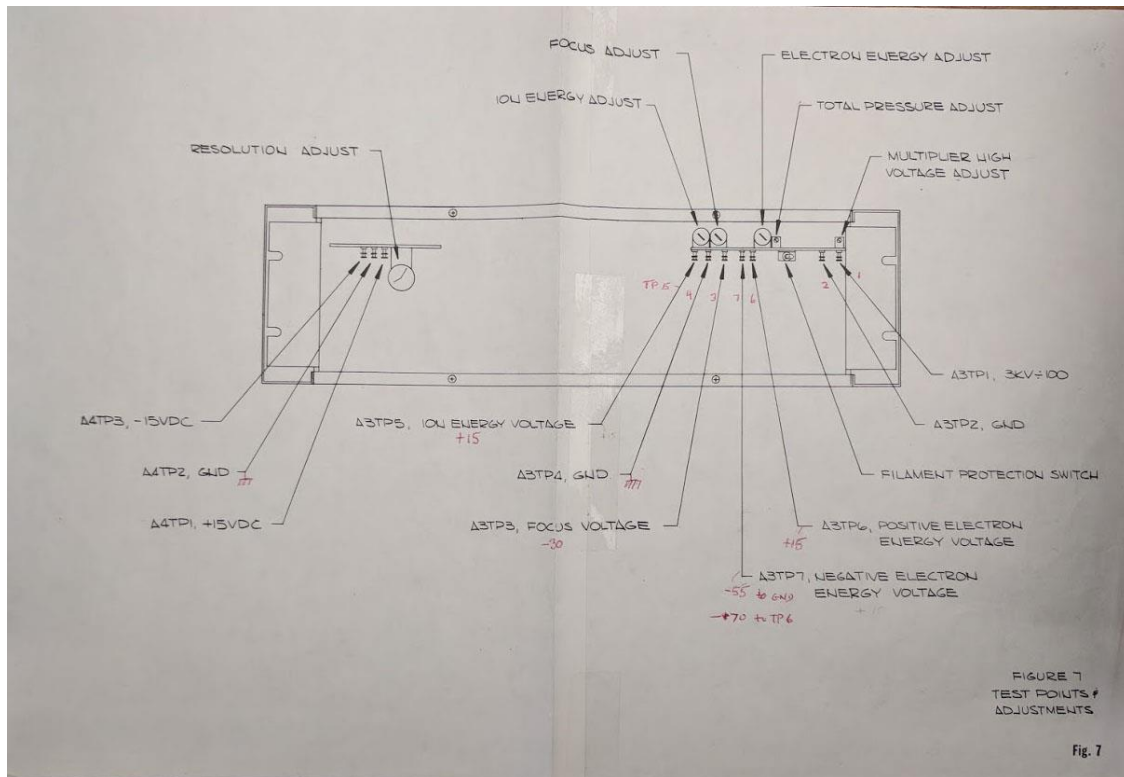


Figure B-7 Diagram of test points present under front cover of QMS control electronics.

Solution:

1. Contacted Dr. Taeseung Kim (former postdoctoral researcher in lab). Suggested contacting Stan Sheldon (UCR Prof. Zaera's group, retired instrument technician)
2. Visited Stan at UCR on Friday, January 26th, spent day troubleshooting instrument with bench top setup in Prof. Zaera's lab.
3. Adjustments were made to bring QMS control electronics back into specified settings laid out in operation manual and fault-finding guide (located in QMS Operation Manuel binder, stored in dry lab shelf next to ICP reactor/QMS probe)

4. A multimeter was used to measure the DC voltage between test points (Figure B-7). Negative electron energy voltage was shown to be severely out of spec. Recommended set point (TP7 to TP2 (ground)): -55 Vdc, measured value pre-tune was -15Vdc. (TP7 to TP6, negative electron energy voltage: -70 Vdc, measured value pre-tune was -30 Vdc. Adjusted using Electron Energy Adjust potentiometer.
5. Multiplier voltage was found to also be out of spec. Recommended value of 3kV (read as 30, as actual value is divided by 100). Measured value was 18 (1.8kV, suggesting insufficient multiplier voltage). Tuned using Multiplier High Voltage Adjust potentiometer.
6. Remainder of test point analysis suggested set points were at or near operating specifications

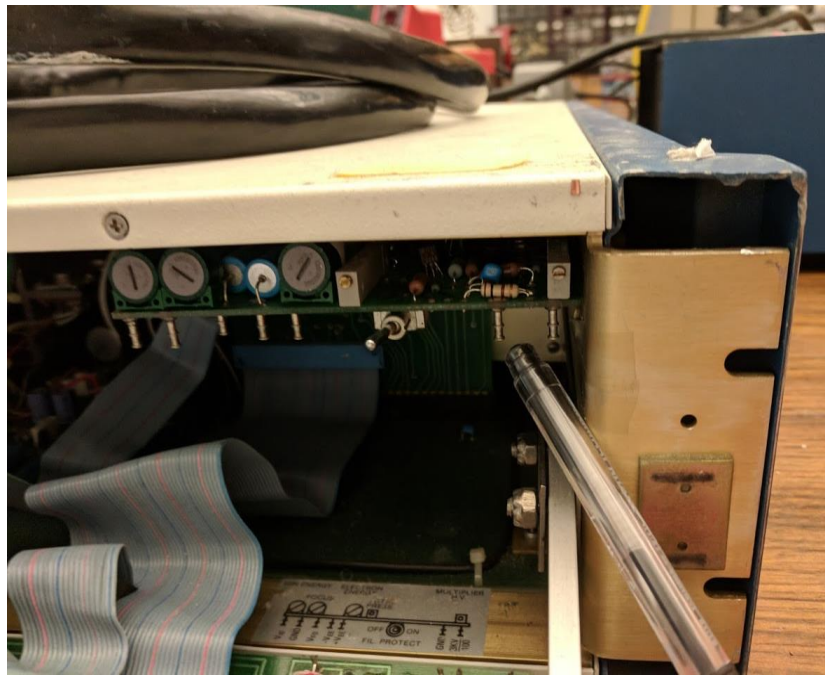


Figure B-8. Image of QMS control electronics front panel with corresponding test points (TP) #1-7. Pointer showing location of test point 2 (TP2) which serves as the chassis ground (GND) test point.

7. After test point verification, observed no signal on attached oscilloscope readout. Presence of gas phase species confirmed using second, functioning UTI-100C QMS unit, ruling out oscilloscope or chamber test setup malfunction
8. Mechanical switches for Program, Amplifier, and Scan Settings groups were lubricated and tuned through mechanical toggling. Stan indicated that due to age of instrumentation as well as exposure to humidity and dust, the mechanical components of the switch can become stuck or slightly corroded, thus requiring “exercise”. Three rounds of complete shutdown and

startup as well as increasing and decreasing the amplifier settings were deemed sufficient for mechanical switch functionality.

C. Langmuir Probe Operation Procedure

C.1. Emergency Shutdown Procedures

I. In case of an emergency overpressure situation in the plasma etcher

1. Stop any current scans using the Hiden ESPsoft software: STOP SCAN
2. If necessary, pull the probe tip out of the etcher main chamber and back it's housing unit by homing the z-stage: Probe → Home ZStage.
3. Exit the Hiden ESPsoft program: File → Exit.
4. Turn off the Langmuir probe electronics by pressing the "OFF" switches on the front panels of both electronics units.

II. In case probe has been driven into the closed gate valve

1. Immediately stop the motor of the z-stage by pressing "Cancel" on the "Probe Positioning" window of the ESPsoft software.
2. Home the z-stage.
3. At this point, the Langmuir probe housing will need to be disassembled off the etcher system in order to assess damage to the probe.

C.2. Schematics

The Hiden Analytical Langmuir Probe system consists of the following components:

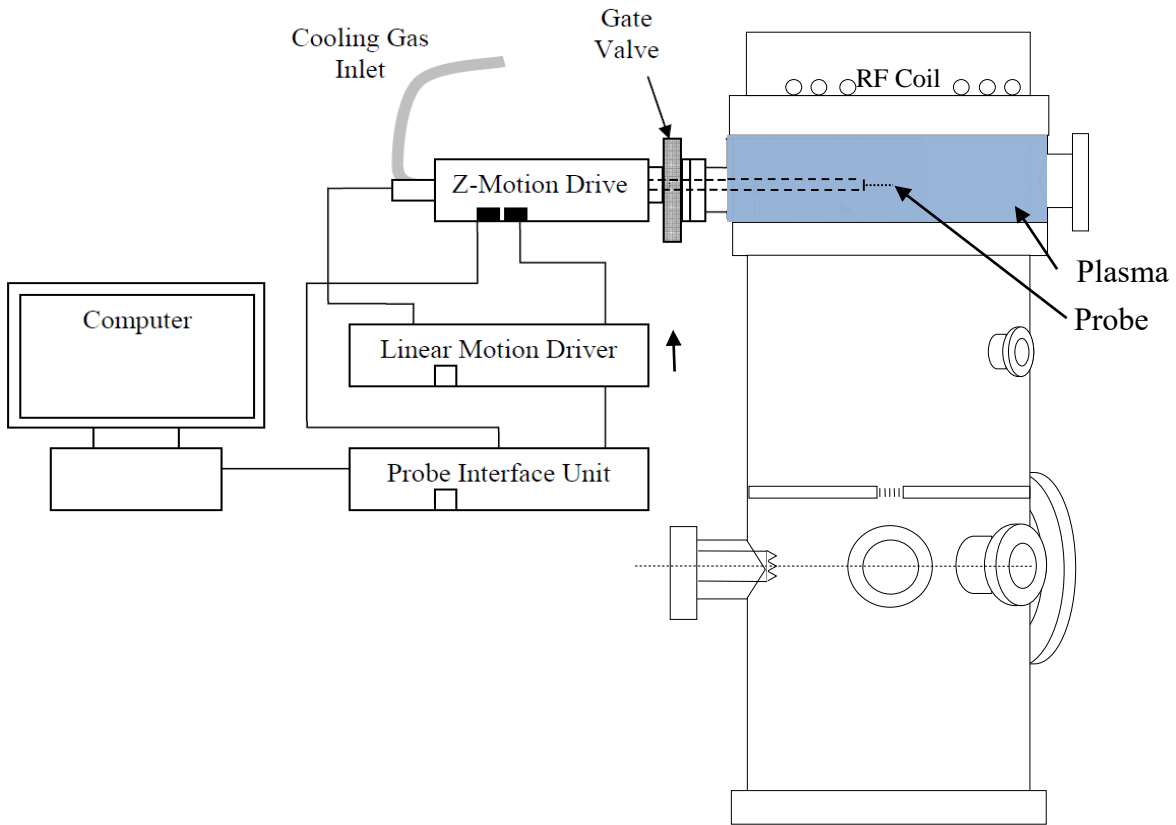


Figure C-1 Schematic of Langmuir Probe System and ICP chamber connection.

C.3. Operating Procedures

I. Install Langmuir probe into upper ICP chamber

This section details how to install probe into chamber.

1. Replace the window in upper chamber with Langmuir Probe:

Prepare the adaptor, gate valve, Cu gasket, nuts, bolts and screws beforehand, calculate the length of the bolt for each adaptor and valve. The following is the necessary component for the connection:

Component	Quantity	Component	Quantity	Component	Quantity
Adaptor 4 5/8"	1	Nuts 2 3/4"	6	Cu gasket 2 3/4"	3
Extension 2 3/4"	1	Nuts 1 5/8"	10	Cu gasket 4 5/8"	1
Gate Valve	1	Nuts 2"	6		

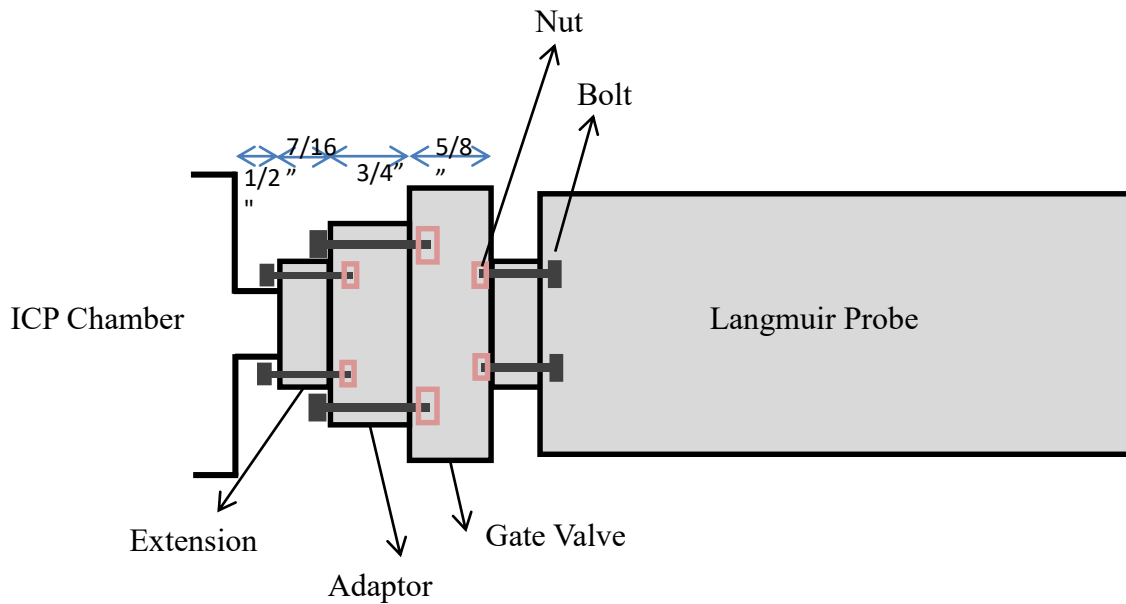


Figure C-2 Schematic of Langmuir Probe System showing connection of components.

2. Find a stand to support the Langmuir probe main body.

II. Probe Operation and Data Collection

This section details how to set up and perform scans for plasma analysis.

1. Check that the etcher system is at base pressure. Then slowly open the Langmuir probe gate valve. If the Langmuir probe housing has been isolated for a long time, a significant amount of gas may have accumulated in the Langmuir probe bellow and the pressure in the chamber will rise once the gate valve seal has been cracked open. Slowly opening the valve will help protect the etcher main chamber turbo pump.
2. Turn on the Langmuir probe and z-drive electronics units and warm up for 30 minutes before acquiring data.
3. Open the ESP soft program on the diagnostics computer.
4. With the gate valve is open, advance the probe into the main chamber by selecting Probe → Z-Stage, then entering the desired insertion distance (in cm) in the Park position prompt, then

selecting “Move Now” and “Ok”. (parking the probe tip at the center of the main chamber requires a position of 26-27 cm)

5. Set the desired parameters for acquisition by selecting Probe → Edit, and then inputting all desired parameters.
6. Once a plasma is struck, data can be acquired by selecting Probe → Run, then entering the amount of acquisitions, naming the file, and selecting “Start”.

III. Probe Tip Replacement

This section details how to uninstall the Langmuir probe from the vacuum chamber and replace the probe tip

1. Home the z-drive and close the manual gate valve connecting the Langmuir probe house from the main chamber.
2. Remove screws holding the outer housing to the z-drive chassis, then take off the outer housing.
3. Disconnect the cables connecting the back end of the 2 3/4” CF flange (the end that the probe is attached to on the inside), then, while holding the flange (and probe) in place, remove the bolts connecting the CF flange to the bellow valve.
4. While *carefully* and *firmly* holding the bellow valve in place with one hand, and holding the CF flange/probe in the other, advance the z-drive forward in small (~2 cm) increments until the probe can be safely removed from the bellow. It is *very important* to secure the bellow valve while doing this as when it is compressed it want to spring out sideways! Allowing this to happen could damage the fragile bellow weldings and cause a leak.
5. Replace the probe tip using gloves and clean tongs.
6. To replace the probe, follow this procedure in reverse order, making sure to hold the probe steady while retracting the z-stage. Colliding the probe tip with the bellow while retracting could damage the new tip!
7. Once the probe CF flange is reattached to the bellow and the housing cover is replaced, the bellow volume will have to be opened to the etcher while it is isolated from all turbopumps in order to protect them (remember the bellow volume will be at atmospheric pressure!).
8. Rough pump the chamber and then pump down with the turbopump, as instructed in the etcher system operation procedures.

IV. Troubleshooting

This section details major problems occurring on the Langmuir probe and the steps taken to fix them.

Spring 2007:

It was found that some plasma conditions (e.g. BCl₃-containing chemistries) lead to rapid degradation of the collected current. This is due to deposition on the probe tip while it is idle. In order to avoid deposition on the tip and prolong the lifetime of each probe tip, the following procedures are suggested:

- a. Always keep the Langmuir probe retracted into the housing with the gate valve closed for any experiments that do not require data acquisition using the Langmuir probe.
- b. Keep experiments as short as possible whenever the Langmuir probe is in use (this applies to all plasma conditions!)
- c. If a potentially depositing plasma chemistry will be in use, always set the “Idle Park Potential” of probe (in the Probe → Edit menu) to a high negative voltage (~-80 V) right before striking

plasma, and return the idle park potential to 0 V once the plasma has been turned off. This will induce ion bombardment of the probe with the plasma on which will prevent a deposition layer from developing.

- d.* In addition, in the Probe → Edit menu, turn on the automatic cleaning during for data acquisition in depositing plasmas by selecting the checkbox next to “Automatic Cleaning On” as well as “20 ms clean/5 ms data acq.”, and set the “Cleaning *Potential*” to a high negative voltage (~ -80 V).

D. Optical Emission Spectrometer Operation Procedures

D.1 Emergency Shutdown Procedures

1. Stop the program, and no further shutdown procedure is required.
2. The modules needed to be moved are optical fibers and the S2000 module where the fibers are attached.
3. The ADC1000-USB module is used for the computer on the ECR etcher (or other computers with the software properly installed if needed).

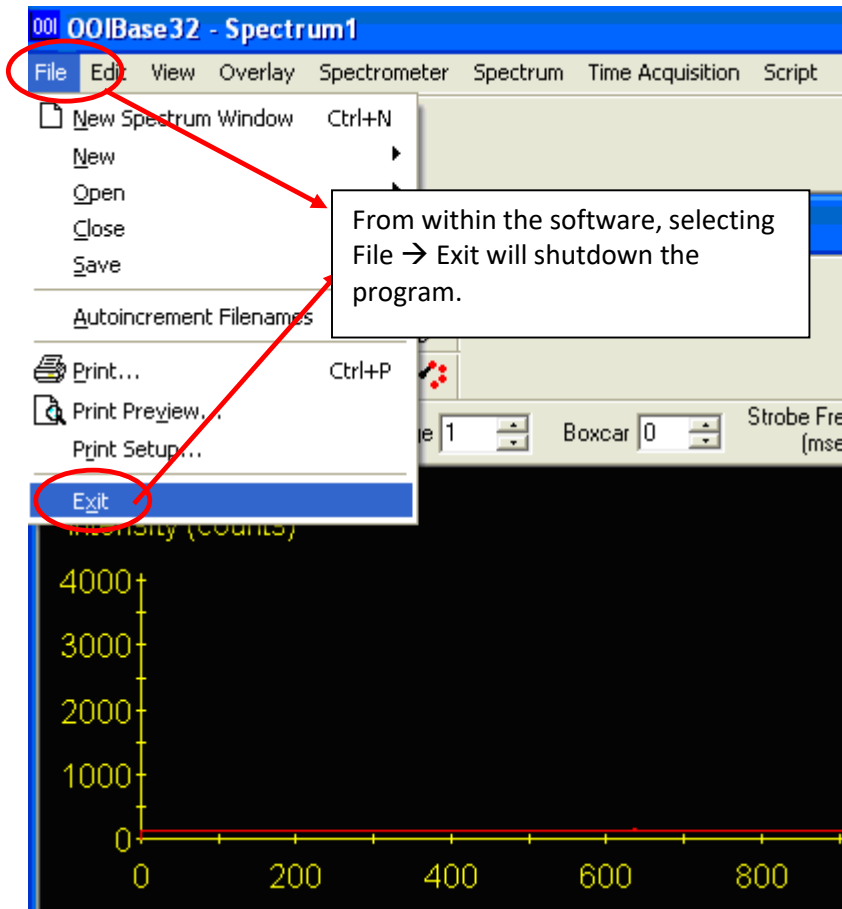


Figure D-1 OES operating software.

D.2. Schematic

The Ocean Optics S2000 System consists of 5 fiber optic cables (Labeled Master, Slave 1-4) connected to an analyzer which interfaces with a computer workstation so that data can be collected. The fiber optic cables are attached to a viewport in the ECR reactor through a machined cover held in place by screws

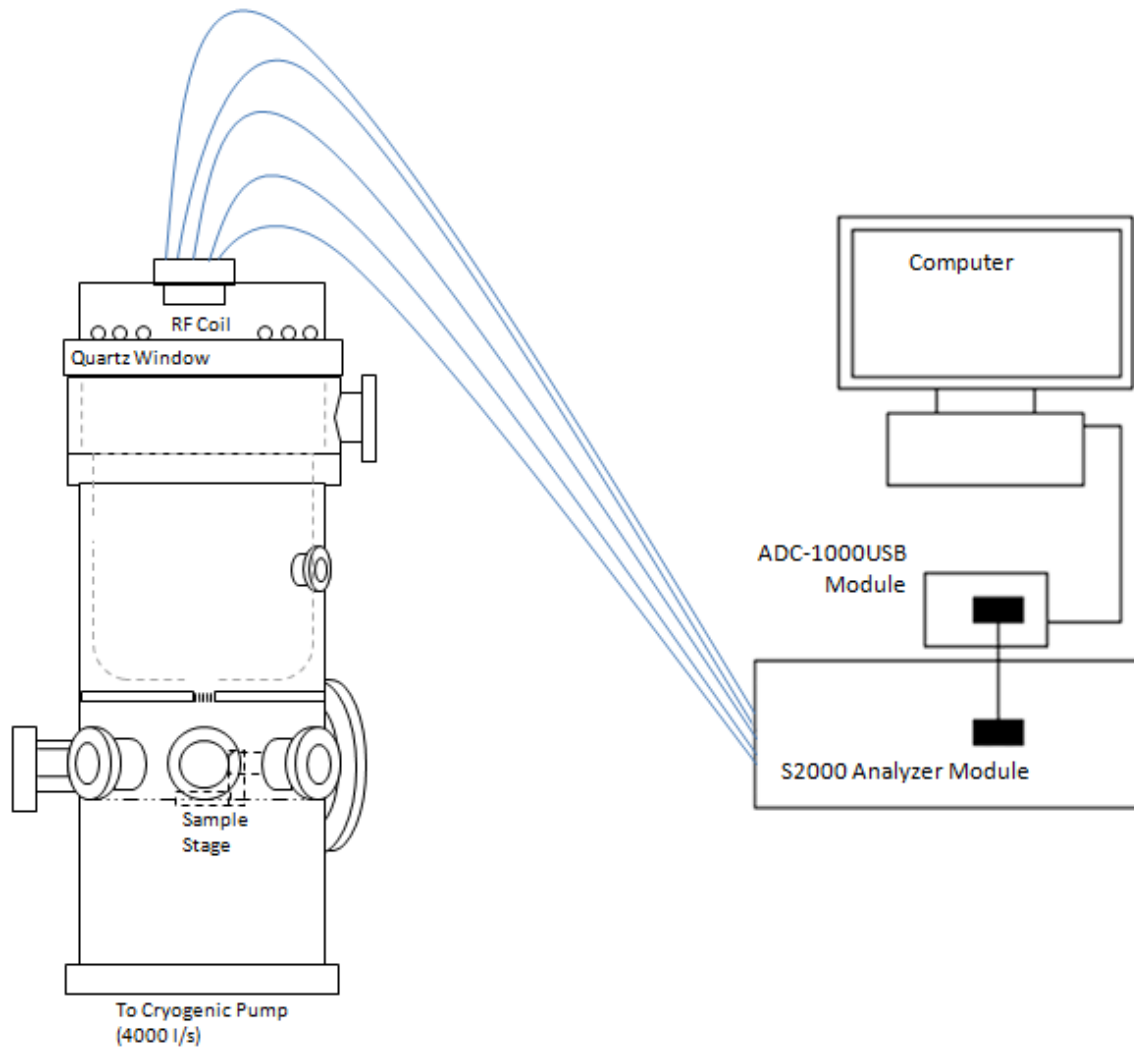


Figure D-2 Schematic of Optical Emission Spectrometer showing connection of components.

D.3. Safety and Operating Procedures

1. Have Optical fiber and cable connections ready

- i. One end of the fiber points to the light source (plasma)
- ii. The other side of the fiber plugged into the S2000 module.
- iii. S2000 module connects to ADC1000-USB (S/N ADUD6666) converter
- iv. USB cable goes from ADC1000-USB to the computer USB port

2. Start the OOIBase 32 program

3. Load the configuration file:

- a. Go to Spectrometer → Open Configuration
- b. Load c:\Program Files\Ocean Optics\OOIBase32\Default.spec

4. Enable channels:

- a. Go to Spectrometer → Configure
- b. Select Wavelength Calibration → Spectrometer Channel
- c. For Master, Slave 1, Slave 2, Slave 3, and Slave 4: check Channel Enabled Box.
- d. Click OK

5. Set proper integration time and time of average required.

D.4. Wavelength Calibration Settings:

These calibrations are set in the *.spec, the file that currently loads properly is located in Jerry's directory in the main Ocean Optics\OES folder.

Settings for Each Channels

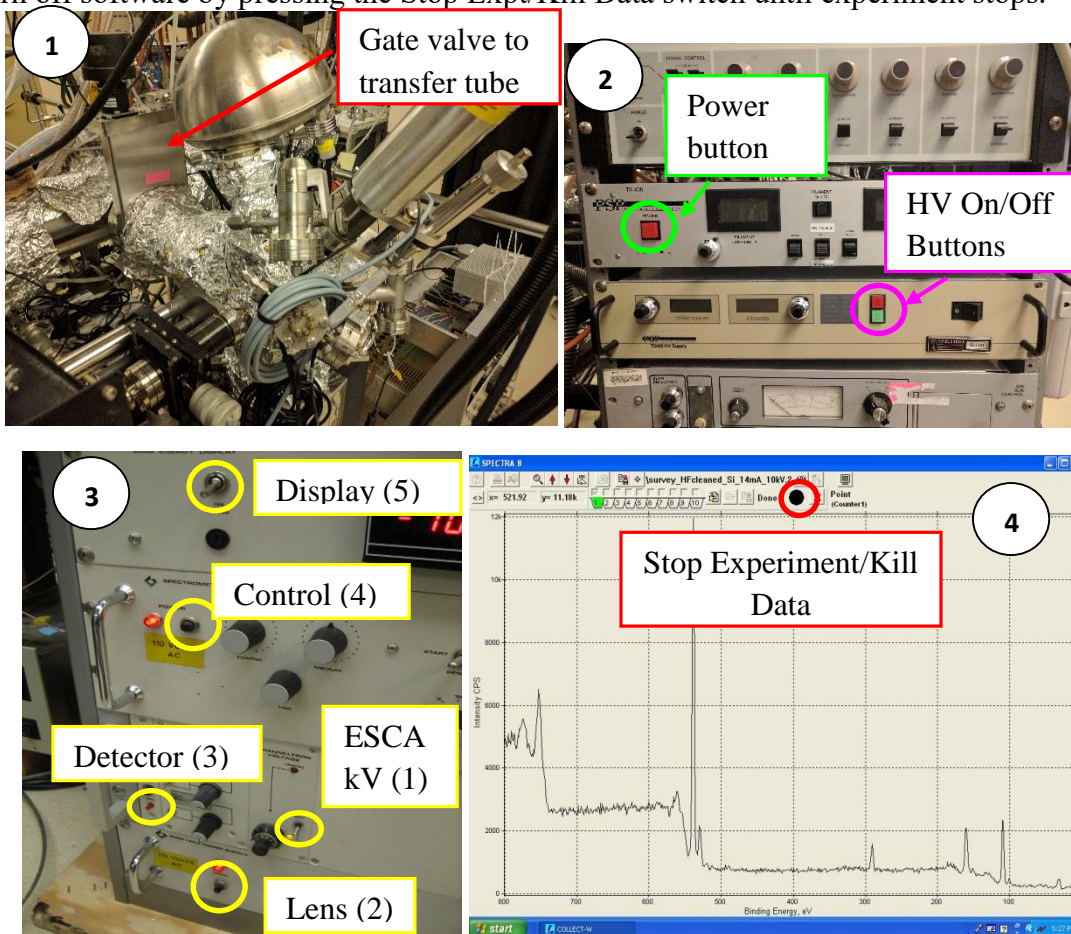
Channel	Coefficient	
Master	First Coefficient	0.09149
	Second Coefficient	-6.95276e-6
	Third Coefficient	8.21743e-11
	Intercept	195.774872
Slave 1	First Coefficient	0.08122
	Second Coefficient	-6.12735e-6
	Third Coefficient	-4.10603e-10
	Intercept	327.208588
Slave 2	First Coefficient	0.10891
	Second Coefficient	-9.05373e-6
	Third Coefficient	-3.54458e-10
	Intercept	437.932098
Slave 3	First Coefficient	0.16705
	Second Coefficient	-1.29450e-5
	Third Coefficient	-5.23387e-10
	Intercept	585.628601
Slave 4	First Coefficient	-0.15435
	Second Coefficient	-1.47189e-5
	Third Coefficient	-1.54958e-10

	Intercept	786.201172
--	-----------	------------

E. X-ray Photoelectron Spectroscopy Operational Guidelines

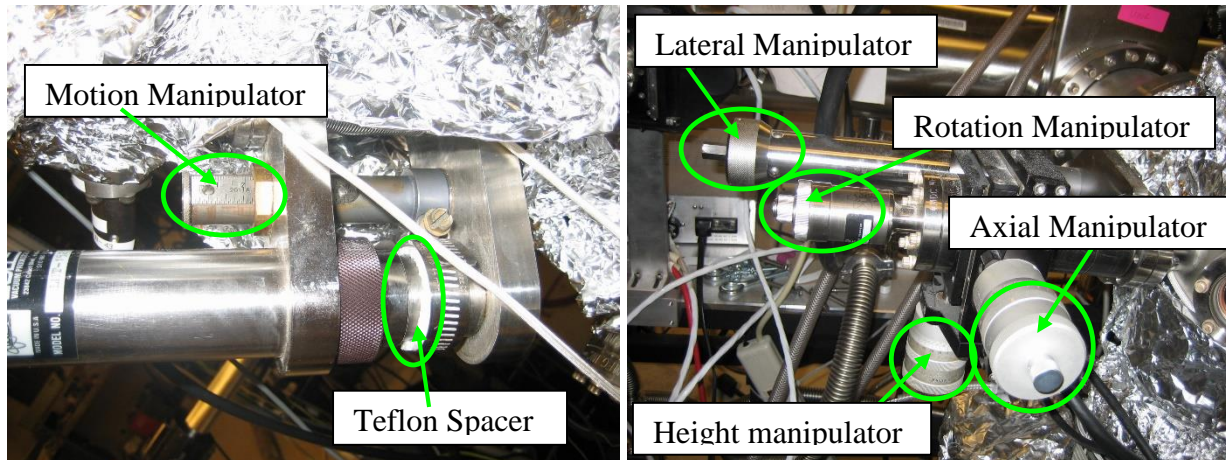
E.1 Emergency Shutdown Procedures

1. Make sure the transfer loading arm from the tube is all the way out of the XPS chamber and then close the gate valve to the transfer tube.
2. Turn off X-ray source by pressing “Power” button on TX-400 unit (should be lit, light will turn off when pressed) and then “HV Off” button (“HV On” button will be illuminated, will turn “HV Off” button green when pressed) on the SL600 unit. If there is time, wait for water to flow to cool the anode for ~ 1 minute. Then, turn off the chiller power.
3. Turn off energy analyzer by turning off ESCA kV and power switches on boxes from bottom to top (lens, detector, control and display)
4. Turn off software by pressing the Stop Exp/Kill Data switch until experiment stops.

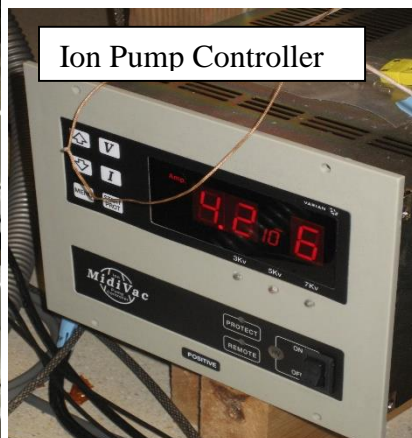


E.2. Safety and Operating Procedures

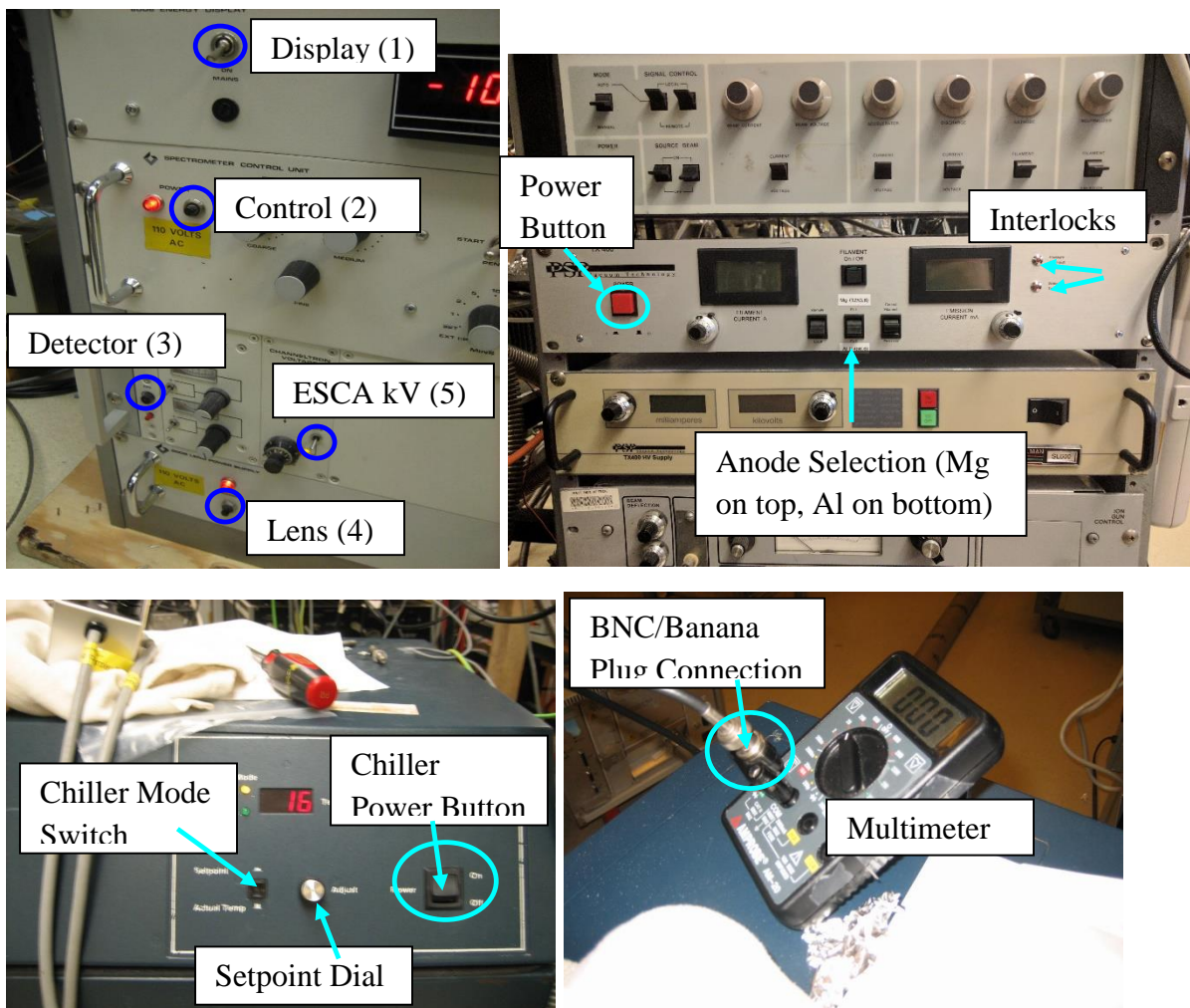
1. Before transferring the sample, make sure the x-ray gun is backed out to a setting of about 1.5 mm on the motion manipulator (~1 cm from the Teflon spacer). Move the sample stage towards the gate valve to a setting of 1-2 on the corresponding manipulator). Lower the stage to a setting of ~4 on the corresponding manipulator. Ensure the stage is vertical. **Be careful as the stage rotates easily.**



2. Check the pressure on the XPS using the ion gauge controller (base is $\sim 5 \times 10^{-10}$ Torr, but anything below 3×10^{-9} Torr is acceptable. If the pressure is above the 10^{-9} Torr range check the ion pump controller for current reading – should read $\sim 10^5 - 10^6$ A). Check the pressure on the TT using its ion gauge controller, pressure should be $\sim 4 \times 10^{-9}$ Torr (if it is higher check that the gate valve between the cryo and the TT is open, if it is not, then open it using the controller box (trace the cable to be sure)). Once both pressures are in the requisite range open the gate valve between the TT and XPS using the corresponding controller box (trace the cable if unsure).

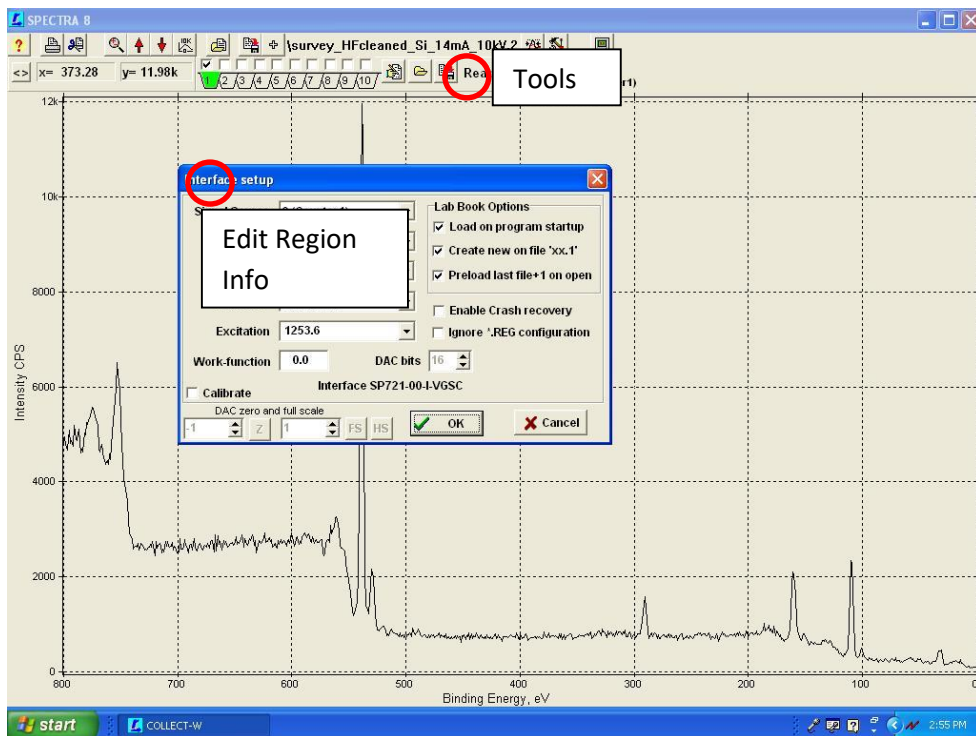


3. Slide the transfer arm into the tube **slowly**, checking the viewport occasionally to make sure that you do not collide with the stage or x-ray source. The manipulator settings on the arm should be X-setting = 4 (black) and Y-setting = 6.25 (black). Make sure the stage is aligned with the sample using the lateral manipulator (pictured in Step 1 on previous page). At this point you may have to raise the sample or lower the stage to provide the necessary vertical clearance. Lower the sample onto the stage. You may have to lower the loading arm to a Y-setting of 3-4 in order to remove the fork from the sample – slowly pull out the fork and after each small movement, increase the Y-setting slightly to avoid excessive straining. Retract the fork completely, being cautious to clear the transfer cart, and close the gate valve between the tube and the XPS.
4. Move the sample stage closer to the source and move source in until it is at a spacing of about 2.2cm. Select the angle theta, which is the angle between the sample surface and the detector axis, using the rotational control - 240° corresponds to a 90° take off angle and 270° to a 60° take-off angle.
5. Move x-ray source closer if desired and adjust the stage position using the various manipulators until you are satisfied that the beam will illuminate the sample. Check the pressure in the XPS chamber – it should be at or below 3×10^{-9} Torr. Turn on the analyzer by turning on the switches labeled in the left picture below – from top to bottom: Display, Control, Detector, Lens, then ESCA kV. Turn on the x-ray source by pressing the Power button on the TX-400 unit. Select the Mg or Al anode, and turn on the NESLAB HX-75 Chiller (This should result in the Water Trip Fault light becoming unlit). Press “FILAMENT On/Off” (this should result in the button lighting up with a green light to indicate that the filament is on). At this point neither the Pressure Trip Fault nor Water Trip Fault interlock lights should be lit. If they are seek assistance from a senior lab member or cautiously check all connections from electronics to the unit.

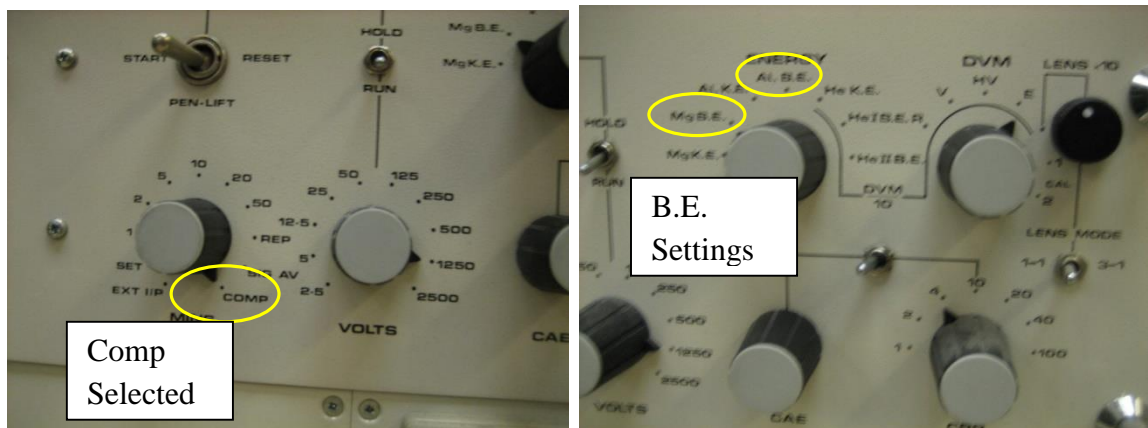


Check the chiller setpoint by pushing in the chiller mode switch. This should read 17 degrees. If it has changed adjust the setpoint dial while keeping the mode switch depressed. Check the flow rate by plugging in the BNC/Banana Plug connection to the multimeter. When set to measure DC Voltage the multimeter should give a reading of over 3.4 V. Allow all the electronics to warm up for 10 minutes before running an experiment.

6. Launch the software program SPECTRA by double clicking the icon labeled SPECTRA in the center of the desktop. To save time before the experiment begins you can define your regions (survey, detailed, etc) by clicking the Edit Region Info Button. Also confirm that the software is configured for the anode you selected in Step 5, by clicking the Tools Button, then clicking “Setup Card” in the menu that pops up. In the dialogue box that pops up you can select either Mg (1253.6 eV) or Al (1486.6 eV) in the Excitation field.



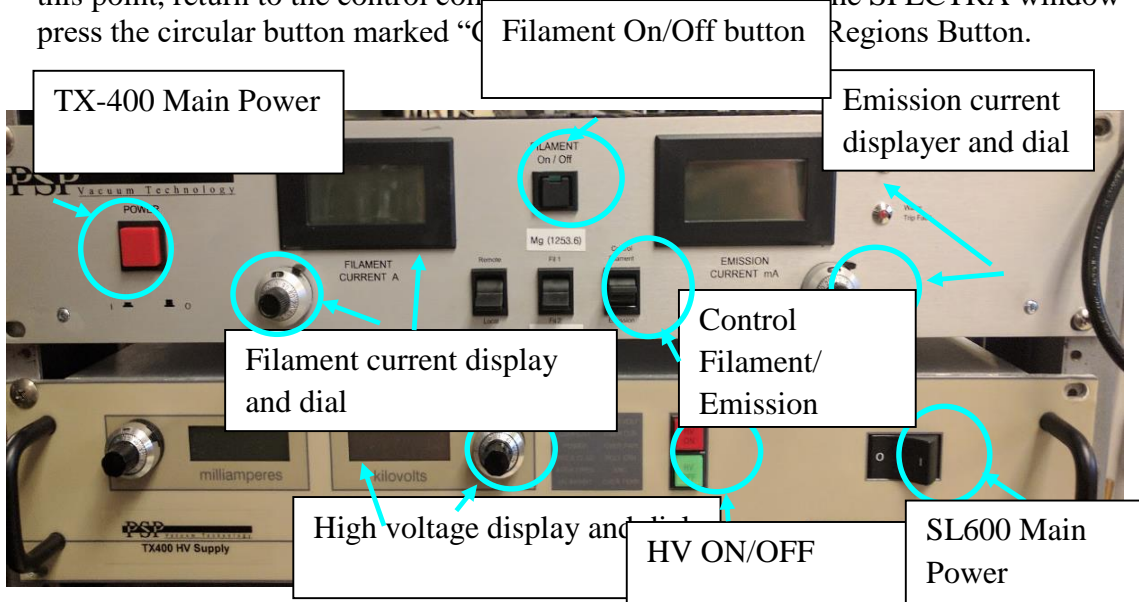
- Once the electronics have warmed up, check that the Spectrometer Control Unit is set to COMP mode and that the Energy Selector corresponds to the Binding Energy (BE) of the anode you selected earlier in Step 5.



- On the TX-400 unit, check to ensure that the “FILAMENT On/Off button” is illuminated. Slowly turn the “FILAMENT CURRENT” potentiometer (dial) located on the left of the panel, below the “FILAMENT CURRENT” display up to 1.75A, being careful to do this

over the course of 2-3 minutes to ensure slow warming up of the filament. The pressure can, at times, spike to up to 2×10^{-8} Torr, especially upon reaching $\sim 1.0A$, but should decrease quickly. When it has returned to 10^{-9} Torr, go to the SL600 unit *below* the TX-400 unit and press the red “HV ON” button and adjust the voltage potentiometer (right-hand dial) so that the “kilovolts” display reads 10.0kV. At this point, the “EMISSION CURRENT” display on the TX-400 unit (right-hand display) should read between 3.0-5.0 mA. Upon first use, a 1.75A and 10kV setting may not accomplish this level of emission current, in which case, slowly increase the “FILAMENT CURRENT”

9. Monitor the pressure throughout this process, which should still be in the 10^{-9} range. Once the “EMISSION CURRENT” display reads between 3.0 and 5.0mA, turn the “EMISSION CURRENT” potentiometer (right-hand dial on TX-400 unit) to 120%. This is accomplished upon full clockwise rotation of the dial to display a white “1” at the top edge of the dial and corresponding “20” in black lettering on the dial itself (which is graduated into increments of 2%).
10. Locate the toggle switch, labeled “Control Filament” on top and “Emission” on bottom, immediately to the right of the anode selection switch on the TX-400 unit. Upon powering up, this should be set to “Control Filament”. Once 10kV and between 3-5mA has been achieved, and the “EMISSION CURRENT” potentiometer is set to 120%, flip this switch down to “Emission”. This will put the two units into Emission control mode for x-ray source operation. The voltage on the SL600 unit will remain constant; however, you may see a small change in the “EMISSION CURRENT” and “FILAMENT CURRENT” display.
11. Slowly increase the “kilovolt” potentiometer on the SL600 unit up to 15.00kV. Rarely, some arc-over may occur and the unit will decrease voltage. Once 15.00kV is reached on the “kilovolt” display, return to the “EMISSION CURRENT” potentiometer and slowly increase this up to 20.00mA while simultaneously monitoring the pressure. The setting of 20mA and 15kV is the **MAXIMUM** allowable power for the x-ray source. **DO NOT** increase past this point on the control units, otherwise there is risk of filament failure. At this point, return to the control computer and begin the run. In the SPECTRA window press the circular button marked “Regions Button”.



12. Once the scans are finished, first ramp down the “EMISSION CURRENT” to 5.0mA and “kilovolts” to 10kV by turning down the dials slowly. Flip the toggle switch back to “Control filament” and continue decreasing the “kilovolts” potentiometer down to 0. Press “HV OFF” (the light should turn green on that button) and then decrease the “FILAMENT CURRENT” potentiometer to 0. Press the “FILAMENT On/Off” button to turn off the filament. The green light should then become unlit. You can leave the “EMISSION CURRENT” potentiometer dial set to where it is for all future runs, as this is the set point that you will use when turning the unit from “Control Filament” mode to “Emission” mode.
13. If you are going to do more scans but the pressure has increased significantly over the course of your run, the system can be left in this state while it pumps down. If the pressure has not increased significantly, you can adjust the region info and then run more scans at your discretion without having to turn off the HV/I_E switches.
14. If you will not run anymore scans, leave the chiller on for a 5-10 minutes after finished to ensure complete cooling of the anode. After waiting the allotted time, you may then press the main I/O power switch on the SL600 unit and red “Power” button on the TX-400 unit to completely turn off the power to both units. Turn off the chiller. Turn off the analyzer electronics by turning off ESCA kV first, then the boxes from bottom to top (in reverse order from Step 5). Remove your sample from the chamber if desired.

F. Spectroscopic Ellipsometer Operational Guidelines

F.1 Emergency Shutdown Procedures

1. Turn off the power of LPS-400 light source.
2. Shut off the circuit breaker of the power controller.

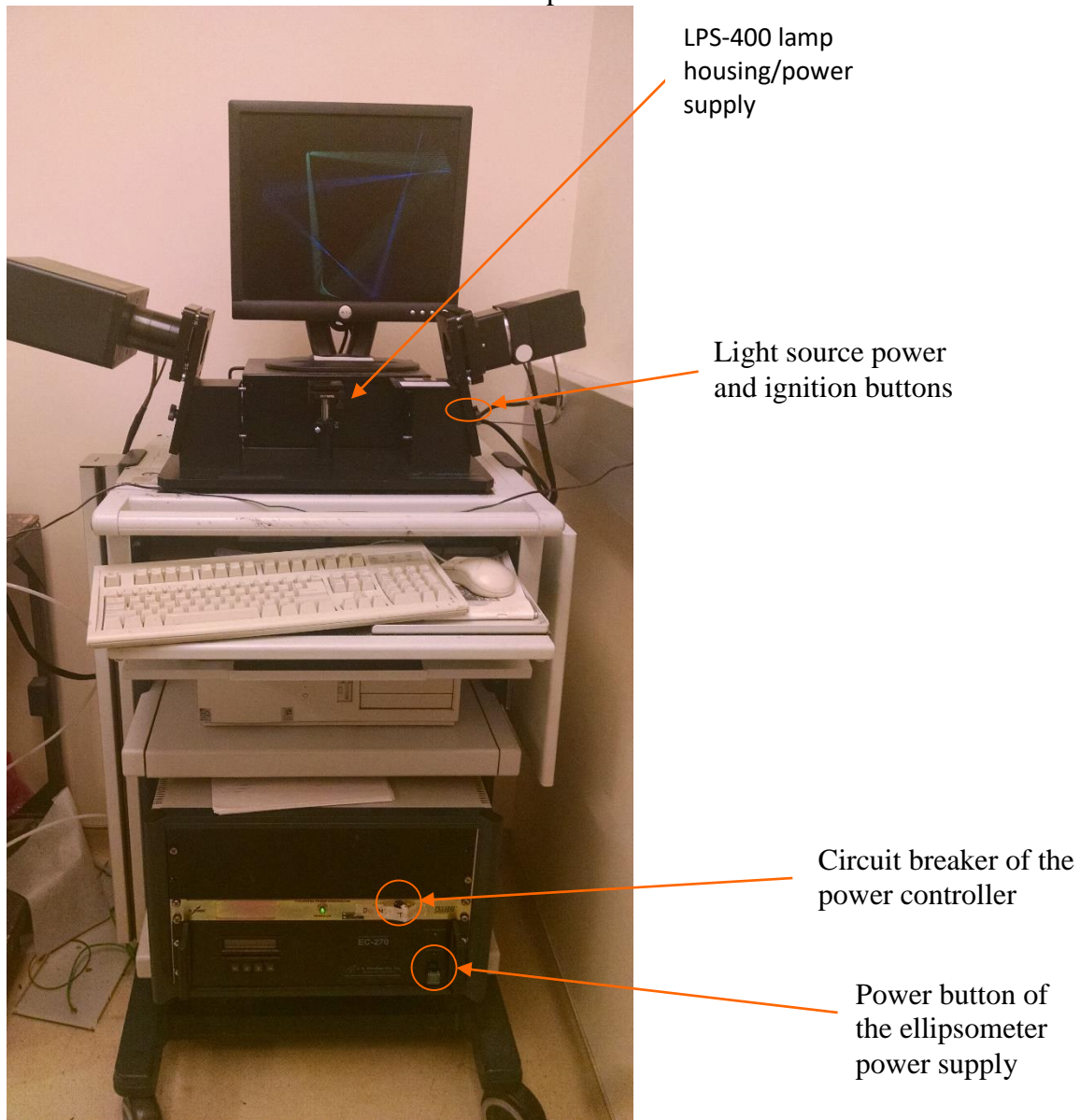


Figure F-1 Ellipsometer apparatus.

F.2. Safety and Operating Procedures

Turn-on procedure

1. Turn on the circuit breaker of the power controller.
2. Turn on the power of the ellipsometer power supply (Electronics Control Module EC-270).
3. Turn on the light source (LPS-400). Press “power” button, and wait a few seconds, then press “ignition” button.
4. Flip on the sign that reads “Lamp ON!”

Turn-off procedure

<For short time off>

1. Turn off the light source (LPS-400).
2. Flip on the sign that reads “Lamp OFF but Power ON!”

<For system off at the end of the day>

1. Turn off the light source (LPS-400).
2. Turn off the circuit breaker of the power controller.
3. Flip on the sign that reads “Power OFF!”

Do not leave the light source on for extended time periods.

F.3. Software Operation

1. Load the software (WVASE32).
2. Press “Window” on the menu bar, and select “Hardware”.
The “Hardware” window pops up, showing a message “Status:Hardware NOT Initialized”
3. Press “Initialize”.
You will hear motor-running sound from the ellipsometer.
4. Place your sample on the stage. Make sure the beam is hitting the area you want to probe.
5. Press “Align”. The window for alignment will pop up. Your goal is to align the red cross to the center of the reference frame.
6. Adjust two tuning knobs underneath the sample stage until the red cross appears on the center of the reference frame.
7. Once alignment is done, press “Esc” key on the keyboard to exit the window.
8. Press “Ellipsometric data”. A new window of “In-situ real-time scan” will appear.
9. Press “Acquire Single Scan”. Data will be collected. It takes only a second.
10. To see the graphical results, press “Window” to select “Graph”.

It will show Ψ and Δ .

You can see other parameters (such as ϵ_1 , ϵ_2 , n , k , etc.) by pressing “Type” and selecting the parameter you want to see.

To estimate layer thickness (Sequence: choose a model → fit the data)

1. Choose a model

- 1) Press “Window” and select “Model”.

- 2) Press “Addlayer” and select a proper material file (*.mat) for substrate.
You can set substrate thickness to 1 mm. Contact Woolam if the material you are interested in is not in the data base.
- 3) Press “Addlayer” and select a proper material file (*.mat) for each layer.
 1. For files containing n and k data (tabulated-layer file), the initial layer thickness should be reasonably close to the actual thickness. Check the “Fit” box, and press “OK”.
 2. For functional files, you can fit other coefficients as well as layer thickness by checking the “Fit” boxes.

Recommended material-data file (*.mat): Files are located in C:\wvase32\mat\

Examples:

- Si: SI_JELL.mat (n,k data)
- SiO₂: Sio2.mat (n,k data)
- HfO₂: \mat\dielectr\Hfo2.mat (n,k data) or Hfo2_c.mat (Cauchy fit)
- ZrO₂: \ mat\dielectr\ Zro2_c.mat (Cauchy fit)
- Y₂O₃: \mat\dielectr\y2o3.mat (n,k data)
- SiC: \mat\semicond\sic.mat (n,k data)
- AlN: aln_final_nk.mat (n,k data) or aln_cauchy_final.mat (Cauchy fit)

2. Fit

- 1) Press “Window” and select “Fit”.
- 2) Press “Normal fit” several time until the result value conversed.

3. Save the data

- 1) Press “Experimental Data” window and go to “file” to save the data.
- 2) Press “Generated Data” window and go to “file” to save the data.

F.4. Hardware Calibration Procedure

1. Place a sample on the stage and align it.
2. Load the software (WVASE32).
3. window → hardware → calibrate
4. You will see a dialog box “Calibration Mode” with five selections, which are;
 - a. Normal
 - b. Coarse
 - c. Detector electronics (off sample)
 - d. Detector system (straight-through configuration)
 - e. Detector system (with calibration sample)
 - “Normal” or “coarse” calibration can be performed every time the system is turned on and the data acquisition is to be carried out. However, it is not necessary to perform it unless you suspect the system is not working correctly.
 - “Detector system (straight-through configuration)” calibration must be performed only once, when the instrument is first set up, and does not need to be performed every time the instrument is turned on. To perform it, please see the manufacturer’s manual.
5. For routine calibration, choose “normal” or ‘coarse” calibration, and press “OK”
6. To see the graph: window → graph

F.5. Installation of Compensator

Follow the manual for the JA Woollam Manual Retarder to remove the input module and install compensator in between the base and the input.



Figure F-2 Sample stage, light source and compensator of ellipsometer .

A Si wafer with a medium thickness SiO₂ film ~260 Å should be used for calibration.

9/7/04

After the Retarder is set to “IN”, be careful not to turn X and Y screws too far or they will come out and the compensator must be reassembled.

The screws should be adjusted so Psi lines up exactly and the Delta model should be shifted lower than the experimental value by 40-90deg.

Problems: On Step 10 in the manual for the JA Woollam Manual Retarder, when doing the Detector System Calibration (Calibration Sample), it finished acquiring the data. Then at Channel #87 an Error Message appeared “Error bars on calibration parameters exceed suggested limits. Verify instrument is operating properly and then repeat the straight through calibration procedure.”

Solution: Increased error tolerances in the “mmx-cal.cnf” file in the WVASE32 folder. Repeated Step 10. The calibration finished. Entered delta offsets in the “hardware.cnf” file according to the manual. In “Ellipsometric Data”, the High Accuracy Mode option needs to be checked. Took data on several SiC and Si samples. Much cleaner data. Better fit. Delta is much smoother, near 90deg. Unsure if it is still very accurate for SiC...

9/29/04

Problem: Tried to measure SiC samples. Delta for the model was extremely noisy for all samples and would not fit the data.

Solution: Tried to repeat Steps 10,11. No Change.

Repeating entire calibration procedure.

Performed normal calibration (out)

Acquired dynamic data (in) and aligned psi and offset delta.

Guessed delta offset parameters in Model Options

Performed Detector System Calibration (with Calibration Sample)

DelOff1 = 78.014

DelOff2 = -1.9517e-2

F.6. Replacement of Protection Device

On March 11, 2005 the WVASE 32 program would not load. When clicking on the WVASE 32 icon on the desktop, the message "Protection Device Not Found!" was given. After contacting J.A. Woollam (phone # (402) 477-7501) and speaking to Ping He, it was determined that the protection device plugged into one of the parallel ports in the back of the computer was no longer working. J.A. Woollam sent us a replacement protection device, and the WVASE 32 program is now working.

G. Transfer Tube

G.1 Emergency Shutdown Procedures

1. Ensure that all transfer arms are in the fully withdrawn position (i.e. they are not extended into any reactor chambers).
2. Close all electrically operated gate valves on the system using the control boxes located on the transfer tube table. (In the event of a power outage, this should automatically happen). Visually inspect that this has taken place whenever possible by looking through the appropriate windows on the transfer tube. In the event that a manual gate valve is present, close it by hand.

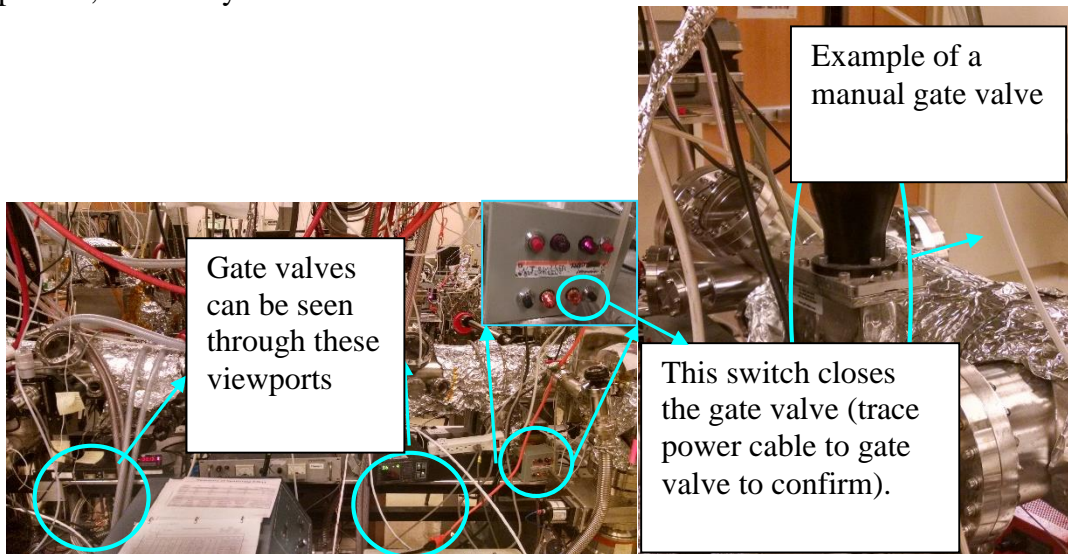


Figure G-1 Windows, gate valve and gate valve controller of transfer tube.

3. Press the stop button on all the turbo pump controllers (in the event of the power outage the controllers should all turn off).



Figure G-2 Controller of TMP.

4. If power is still available, allow the turbo pumps 10-15 minutes to wind down and then close all the roughing valves between the turbo pumps and their backing mechanical pumps. In the event of power loss close these valves immediately.

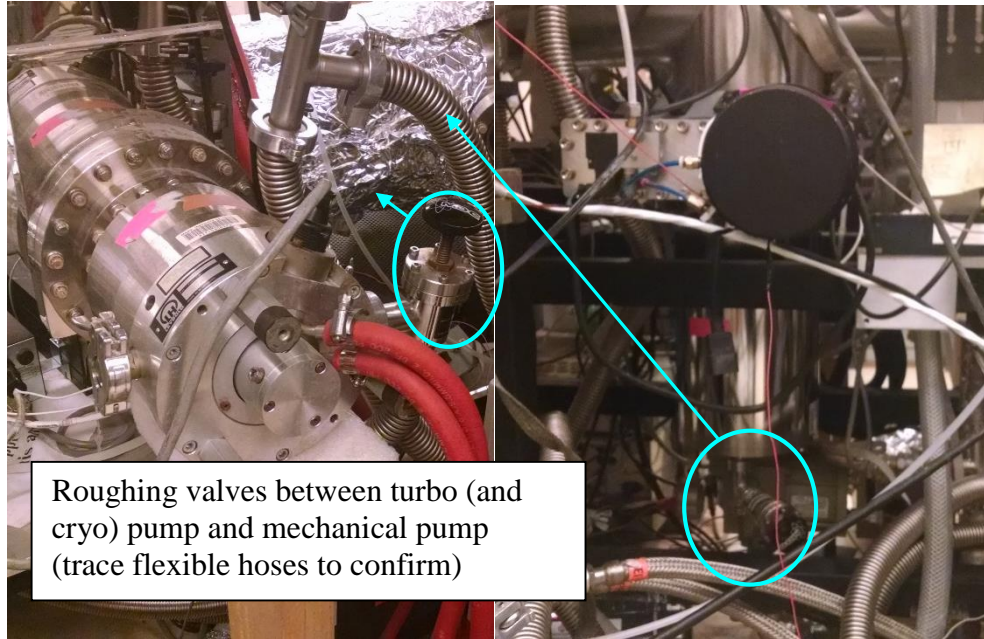


Figure G-3 Roughing valve of TMP and cryopump.

5. Use your discretion to turn off the mechanical pump on the tube, situated under the table.

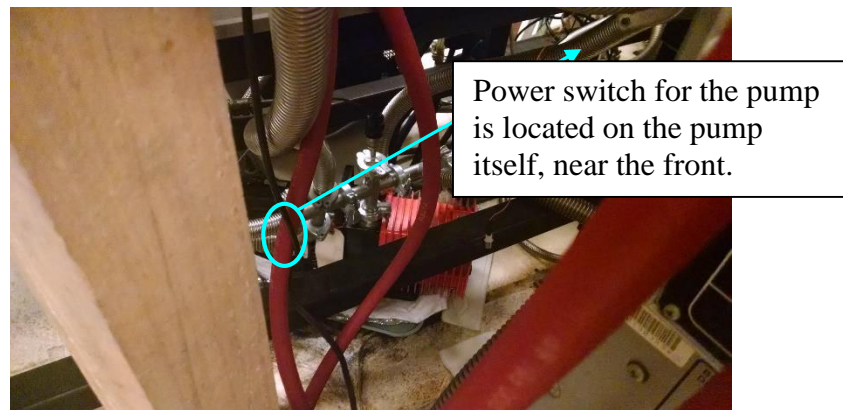


Figure G-4. Mechanical pump of TMP.

6. The pressure of the transfer tube is displayed on a readout/controller located on the tube table next to the loadlock (this controller monitors the loadlock and transfer tube pressure), facing the north side of the room. Monitor the pressure regularly.

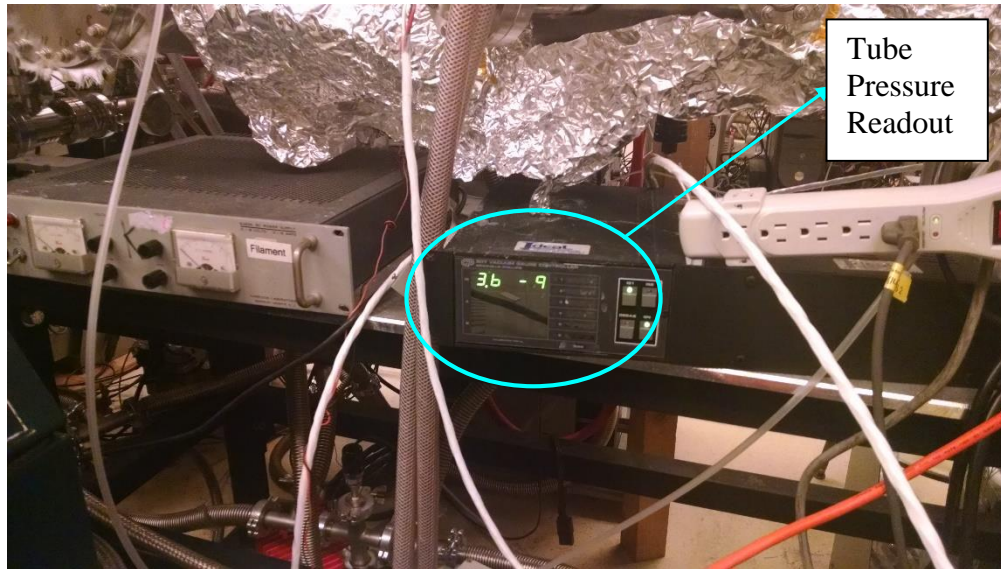


Figure G-5. Ion gauge of transfer tube system.

7. Double check that the gate valve above the cryopump is shut and the rough valve between the cryopump and the mechanical pump is closed (this should have been done in the previous steps). Turn off the CTI 9600 Compressor connected to the cryopump by flipping the white circuit breaker to the “off” position.

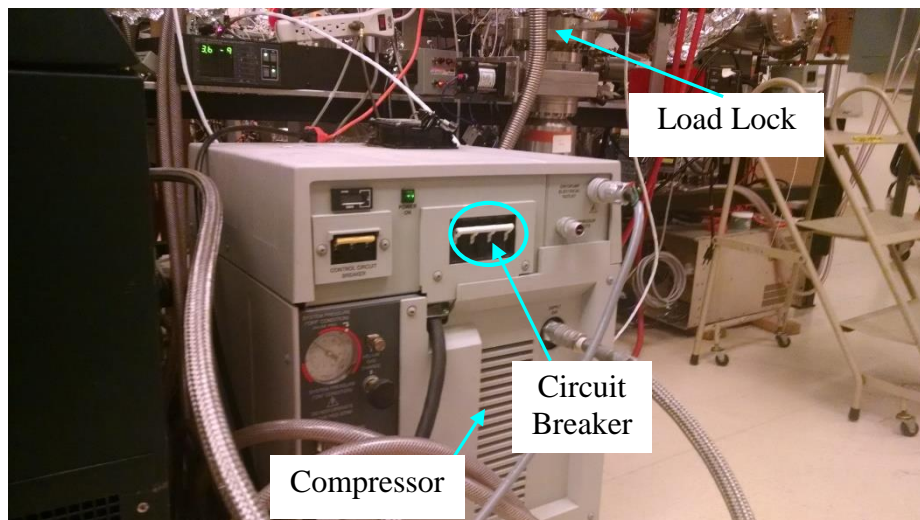


Figure G-6 Compressor of cryopumps.

G.2. Safety and Operating Procedures

Please refer to the following labeled picture when performing Steps 1 and 2.

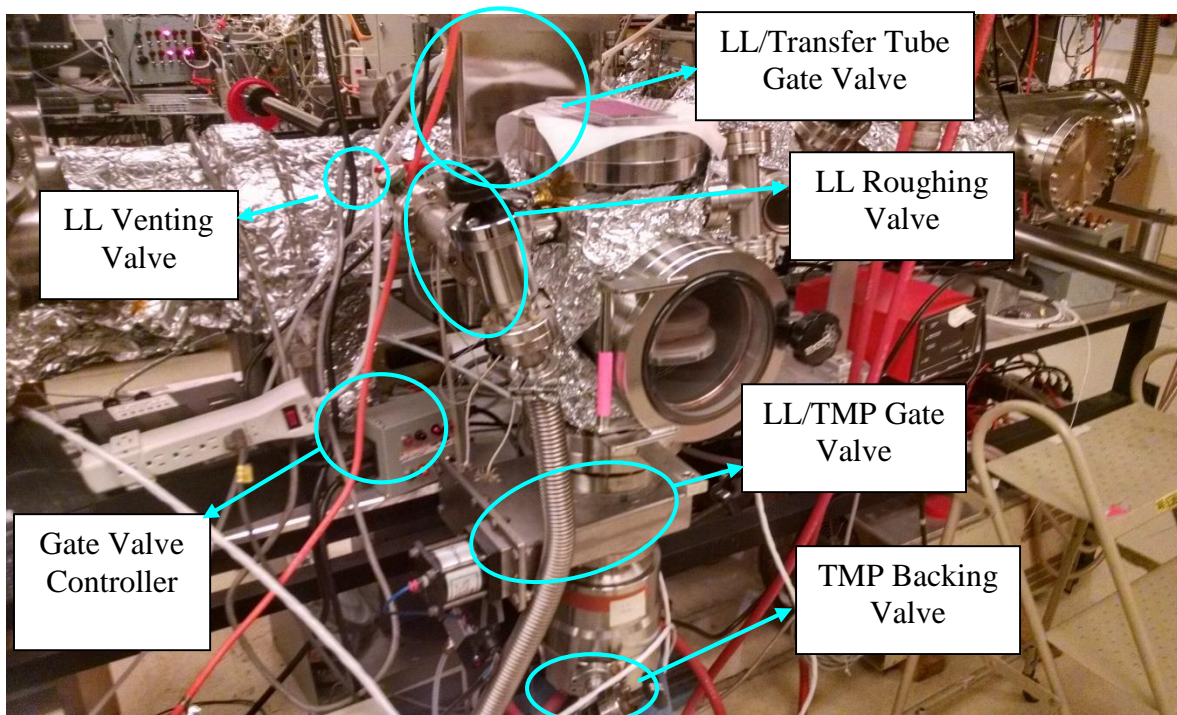


Figure G-7 Components of load lock.

1. To load a sample, the loadlock must first be vented. Ensure that the gate valve between the load lock and the transfer tube is CLOSED. Close the gate valve between the LL turbo and the LL. Ensure that the roughing valve between the LL and its mechanical pump is also closed. Vent the load lock by SLOWLY opening the green venting valve. Within a short time period the load lock door should open easily. Close the green venting valve. DO NOT UNDER ANY CIRCUMSTANCES OPEN THE GATE VALVE BETWEEN THE LL AND ITS TURBO WHILE THE LOAD LOCK IS VENTED! Place your sample holder on the pin holder inside of the load lock. If you used screws to secure your sample, ensure that the screws are facing you.
2. Close the LL door and slightly tighten the handle. Isolate the LL turbo pump and the TT turbo pump by closing the roughing valve between these pumps and their backing mechanical pump (trace the flexible hoses to confirm the pump identity). Open the roughing valve between the load lock and the mechanical pump while pressing in the door. Readjust the tightness of the screw handle, but do not overtighten. Verify that the LL is pumping down by checking the pressure on the thermocouple gauge attached to the mechanical pump. Note that the turbopumps can only be isolated for ~5 minutes. When the pressure has dropped to ~60 mTorr, close the roughing valve to the LL, unisolate the LL and TT turbo pumps and open the gate valve to the LL turbo. Monitor the pressure using the LL ion gauge.
3. When the pressure in the LL is $\sim 5 \times 10^{-6}$ Torr, sample transfer is possible. In this case the pressure in the tube should be $\sim 10^{-8}$ Torr. (If the loadlock pressure is $\sim 5 \times 10^{-7}$ Torr, then the pressure in the tube can be $\sim 10^{-9}$ Torr). Accomplish this by closing the TT/Cryopump gate valve, then monitoring the pressure using the ion gauge. When the pressures are at the requisite levels open the gate valve between the LL and the transfer tube. Check for pressure spikes using the TT ion gauge. If you are uncomfortable about transferring by yourself you may close the gate valve between the LL and its turbo pump to prevent samples from hitting the TMP if they fall.

4. Use the transfer arm to place the sample holder onto the cart (recommended settings are on the transfer arm, but exercise caution when carrying out this operation). Try to ensure that the tines of the loading fork extend past the edge of the sample holder nearest to you. Also remember that the arm cannot be lifted to its maximum value if it is near the limit of its lateral extension. Make adjustment in small increments, consistently checking to ensure that nothing is strained. Retract the transfer arm completely and close the LL/TT gate valve.

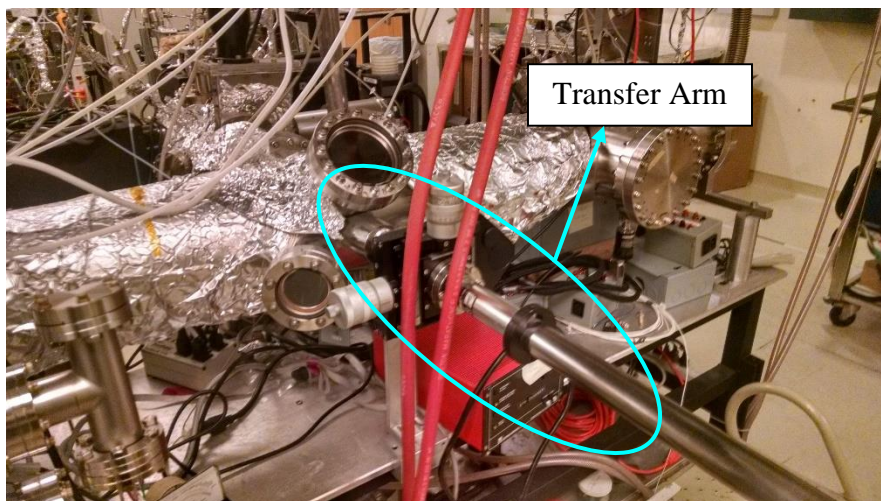


Figure G-8 Transfer arm on the transfer tube.

5. Use the motor control situated at the eastern end of the tube to move the cart to the desired chamber. If the cart is having problems moving, closing the gate valve between the tube and its turbo pump often rectifies this situation, as well as the gate valve between the tube and its cryopump. However, remember to reopen the valves after moving the cart into place. Once in place, close the gate valve between the transfer tube and its cryo pump, then open the gate valve to the transfer tube. Use the transfer arm to lift the sample holder off the cart and place it into the chamber. Retract the arm completely and then close the chamber/TT gate valve before reopening the TT/Cryopump gate valve.

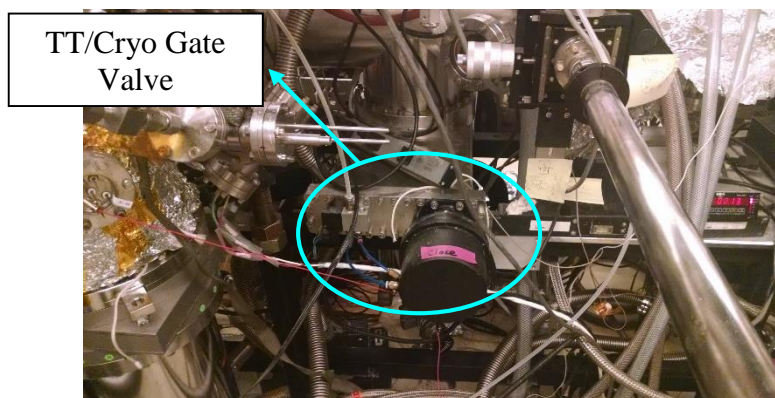


Figure G-9 Gate valve of cryopump to transfer tube.

6. To transfer samples from chambers to the transfer tube, first make sure the experiment has been fully halted (i.e. there is no gas flow, plasma, etc.) and that the chamber has been pumped down to its base pressure for ~15-30 minutes. Close the TT/Cryo gate valve first, then open the chamber/TT gate valve. Use the transfer arm to remove the sample from the chamber and place it into the transfer cart. Retract the transfer arm completely, close the chamber/TT gate valve and then reopen the TT/Cryo gate valve.

H. Vapor Etch Chamber

H.1. Emergency Shutdown Procedures

1. To Shut off the chamber in the event of an emergency:
 - a. Turn off vaporizer heater.
 - b. Close VV1.
 - c. Unplug vaporizer heater, LFC controller, and MFC controller.
 - d.

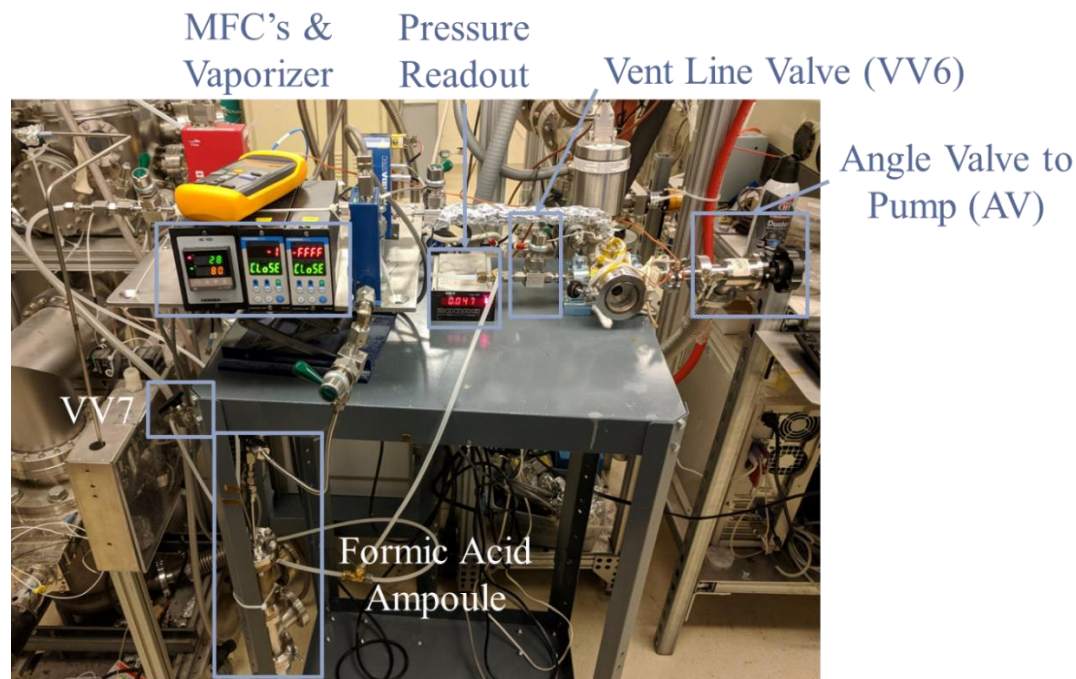


Figure H-1 Overview of Vapor Chamber Setup

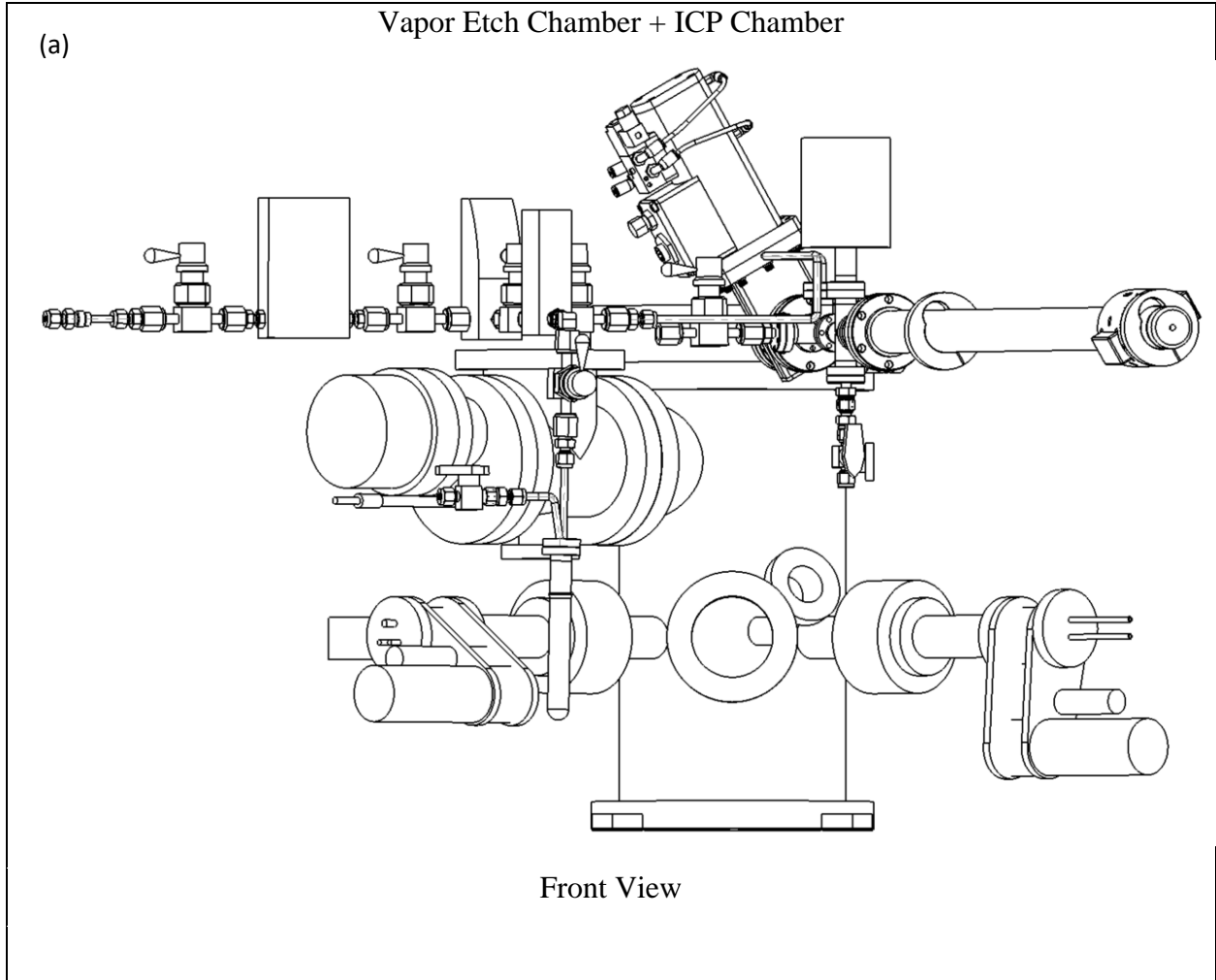
H.2. Operating Procedures

1. *Initial Check:* Make sure all the valves are closed, heaters are off, chamber is pumped down.
 - a. Heaters should be off, vaporizer heater and thermocouples should show room temperature.
 - b. Angle valve to mechanical pump (AV) should be open, baratron gauge readout should show ~ 40 mTorr.
2. *Prepare for Operation:*
 - a. Open valves before and after MFC's and before and after ampoule.
 - b. Turn on heaters. Allow approximately 30 minutes for the chamber to reach temperature, check with thermocouple.
 - i. For 80°C operation, set vaporizer heater to 80°C , line and chamber variacs to 28.
 - ii. For 100°C operation, set vaporizer heater to 100°C , line variac to 29, chamber variac to 36.
3. *Load Sample into Chamber:*
 - a. Check valve to vapor chamber is closed (VV1).

- b. Close the valve to the mechanical pump (AV).
 - c. Open vent line valve (VV6) slowly until viewport door opens. Pressure gauge should read approx. 750 Torr.
 - d. Loosen transfer arm lock and bring arm forward by turning the rack and pinion handle until the stage is out of the vapor chamber.
 - e. Attach sample to stage using copper tape.
 - f. Retract transfer arm into the chamber by turning the rack and pinion handle. Check that the sample will not collide with the doser. Position for stage to be beneath doser is 30. Tighten the transfer arm lock.
4. *Pump Down Chamber:*
- a. Check that vent line valve (VV6) is in the closed position. Close if not.
 - b. Check that viewport door is closed and secured.
 - c. Open valve to mechanical pump slowly. Pressure should drop at approx. 10 mtorr/sec. until gauge reads approx. ~40 Torr.
5. *Deliver Vapor to System:*
- a. Close valve (AV) to the mechanical pump
 - b. Check that VV6 is closed, VV1-5 are open. Pressurize the ampoule by briefly opening then closing VV7.
 - c. Baratron gauge should show an increase in pressure (up ~10 Torr). Press Cont on the vapor MFC and Open on the liquid MFC simultaneously.
 - d. Allow the chamber to fill to the desired pressure, then press Close on both MFC's and close the valve to the chamber (VV1) when the desired pressure is met. Allow the sample to sit in the chamber for the desired etch time. Condensation should occur on the viewport door. For longer times, small pools of formic acid may form by the viewport door, and it is advisable to lock the viewport door.
 - e. Once process is finished, open the valve to the mechanical pump (AV) and press Open on the vapor MFC to push out remaining formic acid (this should take ~1 minute). Press Off to stop vapor MFC flow.
6. *Unload Sample from Vapor Chamber:*
- a. Check valve to vapor chamber is closed (VV1).
 - b. Close the valve to the mechanical pump (AV).
 - c. Open vent line valve (VV6) slowly until viewport door opens. Pressure gauge should read approx. 750 Torr.
 - d. Loosen transfer arm lock and bring arm forward by turning the rack and pinion handle until the stage is out of the vapor chamber.
 - e. Remove sample from stage. If another sample needs to be processed, attach it to the stage now using copper tape.
 - f. Retract transfer arm into the chamber by turning the rack and pinion handle. Check that the sample will not collide with the doser. Position for stage to be beneath doser is 30. Tighten the transfer arm lock.
7. *Refill Ampoule:*
- a. Ampoule can sustain approximately 15 cycles before needing a refill.
 - b. If formic acid is suspected to still be in the liquid MFC line, check that VV1, VV2, and AV are open and press Open on the liquid MFC to pump out as much formic acid as possible.

- c. Check that VV3 and VV7 are closed. Disconnect the N₂ line leading to VV7 upstream of VV7. Disconnect the liquid formic acid line leading out of VV3 downstream of VV3.
- d. Fill formic acid or other volatile compounds in the fume hood. Disconnect the CF connection between the 1.33" CF liquid feedthrough and the 1.33" to 2.75" CF zero-length adapter. Refill the ampoule, leaving about ½ inch below the steel-quartz joint for the doser tubing. Be wary of liquid flowing back out of the doser once it is removed from the ampoule.
- e. Once ampoule is full, reconnect the liquid feedthrough to the rest of the ampoule assembly. Use the Ni CF gasket for corrosives, otherwise use a new Cu gasket.
- f. Reconnect the ampoule to the vapor chamber setup. The N₂ line does not need a gasket, but the liquid MFC line will need a new VCR gasket. A zip tie may be helpful in keeping the ampoule in place during the connection process.

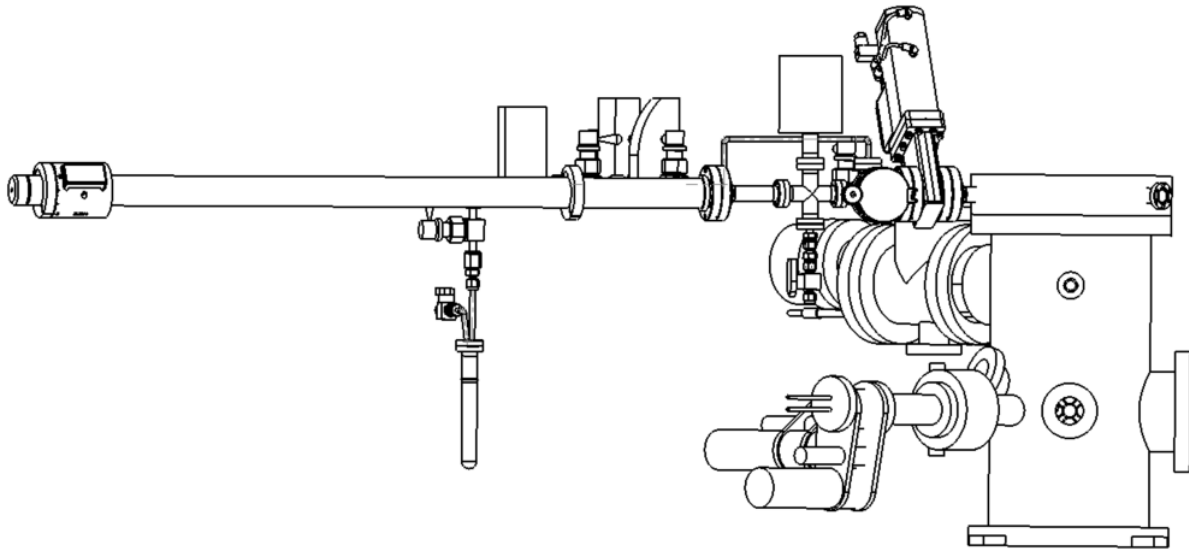
H.3. Schematics



University of California, Los Angeles, Department of Chemical and Biomolecular Engineering							
Part		Material	Stainless steel				
Filename		Scale	Yes	Units	inc h	Quantity	1
Designer	Jack Chen (UCLA)	Date	1/1/2015				
Revised by		Date					
Contractor		Date					
Comments			Tolerance			+/- .0001	

Vapor Etch Chamber + ICP Chamber

(b)



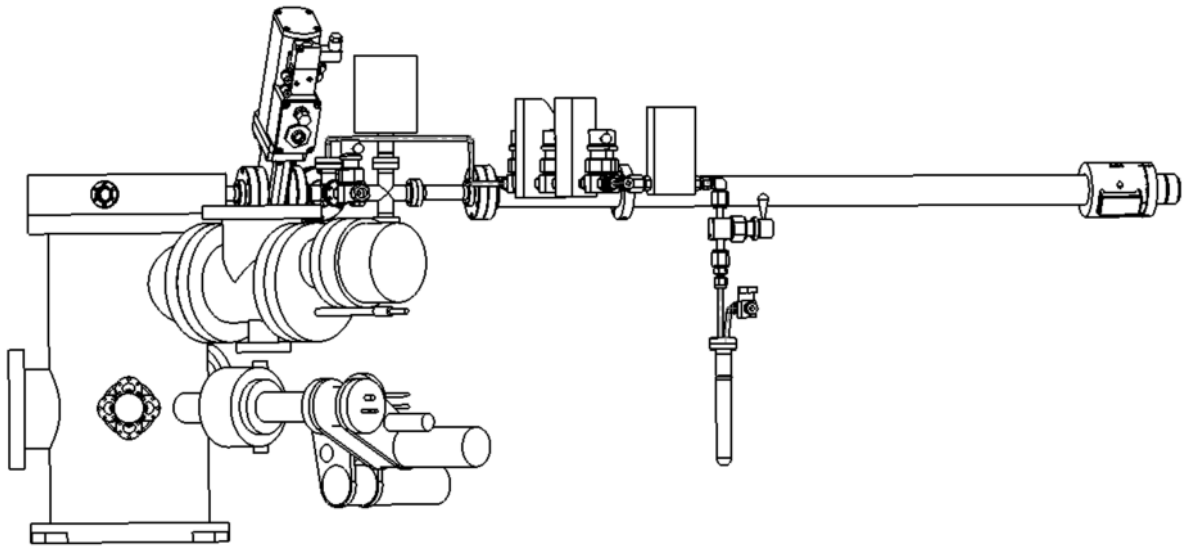
Side View

University of California, Los Angeles, Department of Chemical and Biomolecular Engineering

Part		Material	Stainless steel				
Filename		Scale	Yes	Units	inc h	Quantity	1
Designer	Jack Chen (UCLA)	Date	1/1/2015				
Revised by		Date					
Contractor		Date					
Comments			Tolerance			+/- .0001	

(c)

Vapor Etch Chamber + ICP Chamber

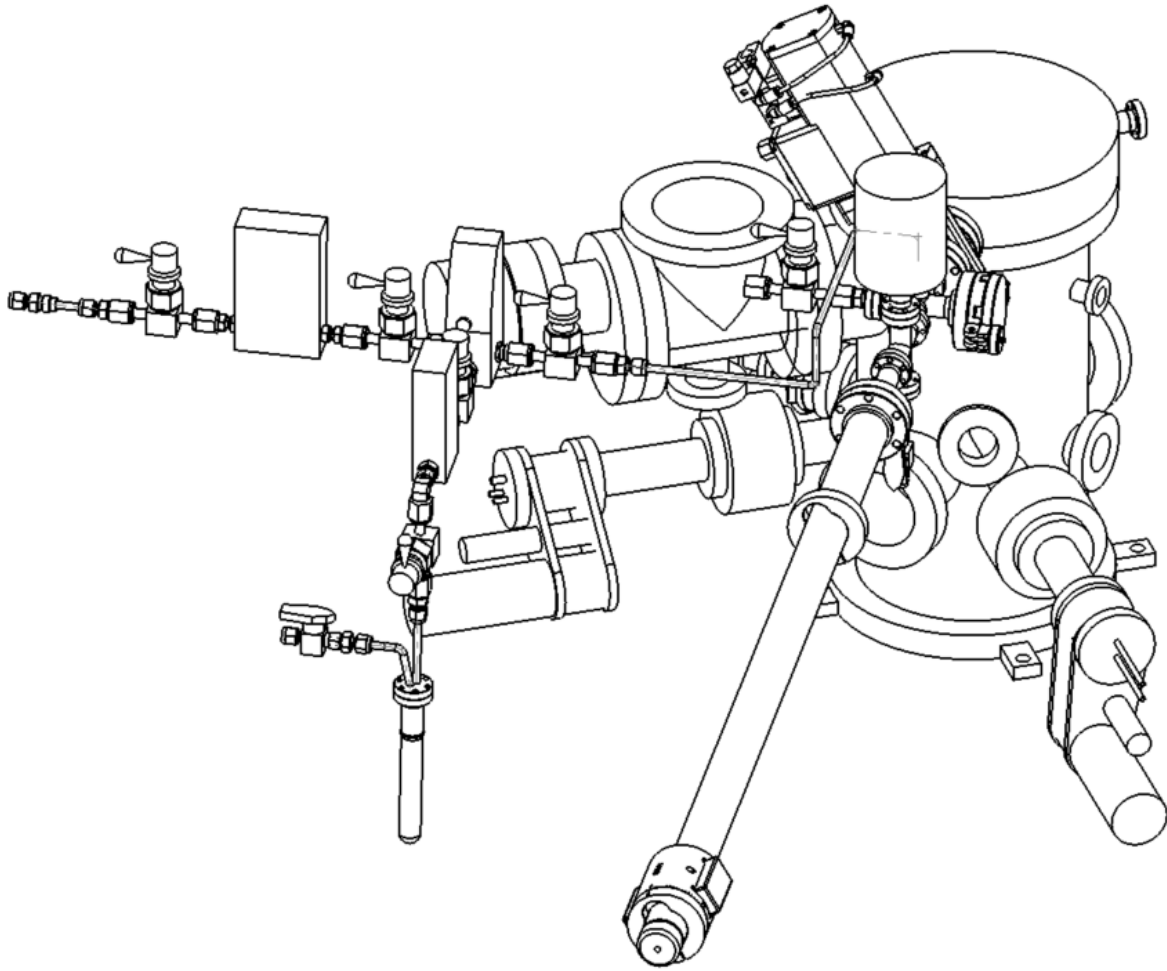


Side View

University of California, Los Angeles, Department of Chemical and Biomolecular Engineering							
Part		Material	Stainless steel				
Filename		Scale	Yes	Units	inc h	Quantity	1
Designer	Jack Chen (UCLA)	Date	1/1/2015				
Revised by		Date					
Contractor		Date					
Comments			Tolerance			+/- .0001	

(d)

Vapor Etch Chamber + ICP Chamber



Isometric View

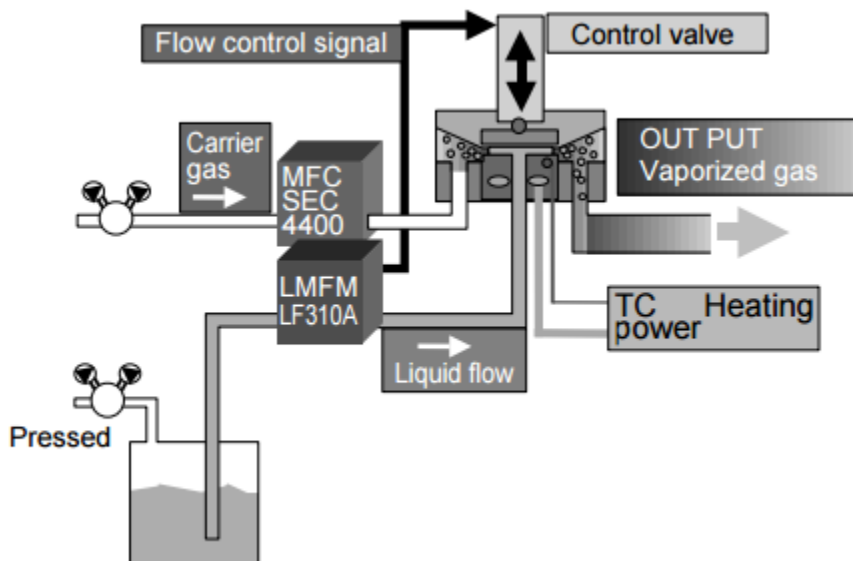
University of California, Los Angeles, Department of Chemical and Biomolecular Engineering

Part		Material	Stainless steel				
Filename		Scale	Yes	Units	inc h	Quantity	1
Designer	Jack Chen (UCLA)	Date	1/1/2015				
Revised by		Date					
Contractor		Date					
Comments			Tolerance			+/- .0001	

Figure H-3 Schematics of Vapor Etch System Attached to ICP Chamber (a-d).

H.4. Vaporizer Info

Chapter 7 Liquid phase etchant is first stored in a round bottom glass vial, 3/4" in diameter which is attached to a 1.33" to 1/4" VCR adapter for incorporation into the feed line. A metal tube protrudes into the glass vial as a channel for delivering the liquid phase etchant under reduced pressures to the liquid mass flow controller, a Horiba™ LF-F20M-A model fitted with 1/8" stainless steel Swagelok (capable of handling most corrosive chemicals except HCl and HF, generally) and 1/8" Swagelok to 1/4" VCR fittings for vacuum compatibility. This allows for metered feeding up to mass flow rates of 0.1 g/min of the liquid phase etchant at temperatures varying from 5-50°C into the vaporizing unit.



Chapter 8

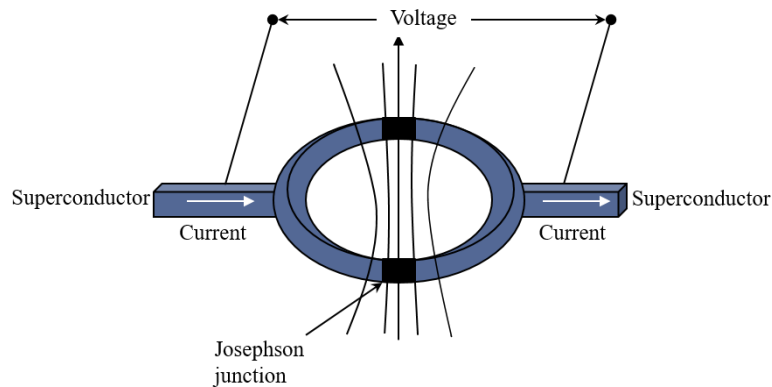
Figure H-4 Liquid injection method utilizing heating element to vaporize liquid flow and introduce to vacuum chamber (Image courtesy of STEC Inc)

To aid in the delivery of the vaporized gas output, an inert gas input is recommended as a secondary input to the vaporizer unit. For these studies, ultra-high purity N₂ will be used at flowrates controlled via a Horiba™ SEC-E40 gas MFC with maximum flowrates of 100 sccm. This MFC contains two 1/4" VCR connections, eliminating any need for adapters between the N₂ MFC and vaporizer. With both of these MFC units connected to the M1-1141-PN, resulting vapor can be delivered at flowrates of up to 3cm³/min (rated with isopropanol) at temperatures of up to 140°C. This delivery temperature is sufficient for complete vaporization of the organic chemicals of interest to the study.

I. Superconducting quantum interference device (SQUID)

I.1. Introduction

Chapter 9 Superconducting quantum interference device (SQUID) is a magnetometer that measures magnetization (M) as a function of the applied field (H). A hysteresis loop can be plotted to extract information regarding the magnetic properties of the film. For example, coercivity, H_c , is the horizontal intercept of the hysteresis curve. It is the applied field necessary to change the direction of magnetization within the domains of the material. It indicates the stability of magnetization in the material. The saturation magnetization, M_s , is the maximum magnetization of a material $dM/dH=0$. It indicates the magnetic strength a material. The enabling phenomenon behind SQUID is the Josephson junction.



Chapter 10

Figure J-1 Diagram of Josephson junction utilizing a superconducting loop with two parallel non-superconducting sections.

Chapter 11 The Josephson junction is a superconducting loop separated by two parallel pieces of non-superconducting material (Figure 1). Electrons tunnel through the non-superconducting material in the form of Cooper pairs, electrons that are bound together in a very low energy state that allows for long range interaction over hundreds of nanometers (Allender 1973). This interaction is very weak, on the order of 0.001 eV, and requires reduced temperatures since small amounts of thermal energy can break it.

Chapter 12 An applied current, I , is split equally across the two parallel branches. If a magnetic field is applied, a screening current, I_s , is circulates the loop resulting in a magnetic flux equal but opposite of the external magnetic flux (Bardeen 1957). This induced current travels in the same direction as current in one branch, and opposite in the other, causing two different currents across the parallel non-superconductors Equations 1 and 2.

$$I_1 = \frac{I}{2} + I_s \quad (1)$$

Chapter 13 and

$$I_2 = \frac{I}{2} - I_s \quad (2)$$

Chapter 14 Once a threshold current is reached, a measurable voltage appears across the junction. If the magnetic flux exceeds $\phi_0/2$, or half of the magnetic flux quantum, the system will energetically favor an increase in this value to an integer of ϕ_0 , which results in the current flipping

direction. This phenomenon causes the current to oscillate as a function of the applied magnetic flux. Equation 3 represents the magnetic flux quantum, where h is Planck's constant and e is the elementary charge.

$$\varphi_0 = \frac{h}{2e} = 2.067833 \times 10^{-15} \text{ tesla-m}^2 \quad (3)$$

Chapter 15 The SQUID device has two Josephson junctions, at either end of the device. By maintaining a constant current within the SQUID, the measurable voltage will fluctuate at each of the two Josephson junctions, allowing for the oscillation to be correlated to the amount of magnetic flux through the sample. Equation 4 is the resulting voltage change, which is dependent on the resistance, R , and the loop's inductance, L , as well as the change in the magnetic flux quantum, $\Delta\varphi$.

$$\Delta V = \frac{R}{L} \Delta\varphi \quad (4)$$

Chapter 16 To measure the magnetic properties via SQUID, the sample is first moved up and down between two electromagnets to change the applied field. A pair of sensory coils around the sample measures the voltage. For these measurements, a Quantum Design Magnetic Property Measurement System (MPMS) XL was used. This tool only measures the total magnetization, so data must be normalized by the volume of magnetic material, excluding the substrate. Due to the diamagnetic influence of air within the sample holder as well as the response generated from the silicon substrate, it is necessary to first perform a linear fit of the raw data at either very high or very low fields. The diamagnetic response can be subtracted from raw data to obtain the magnetic measurement of the sample.

I.2. SQUID Operating Procedure

Chapter 17 Sample preparation

1. Put on clean pair of gloves. Obtain drinking straw, remove wrapper.
2. Using diamond scribe, cleave sample of interest into a 5mm x 5mm square
3. Record dimension of sample using digital calipers
4. Calculate and make a note of the volume of magnetic film in cm^3 by taking product of calculated sample area and film thickness
5. Obtain a pill capsule, pull apart the two halves, and insert the sample into the inner half of the capsule. It may be necessary to gently squeeze the capsule to accommodate larger samples.
6. Once the sample has been placed inside, releasing the capsule should hold the sample upright by tension of the capsule wall. Rejoin the two halves and insert the capsule into the straw
7. Using a metal rod, gently push the capsule into an eye-balled center of the straw.
8. Using a fine-tipped permanent marker, label the very top of the straw with the date and sample information

Chapter 18 Sample loading

1. Check the MPMS MultiVu Application window at the bottom to determine the current state of the SQUID machine.
2. If the temperature is below 298 K, left-click System (see photo, outlined in red)
3. The "Temperature Parameters" window will appear.

- Under “Control” change “Set Point” value to 298. Change “Rate” to 10 K/min. Left-click “Set” button.

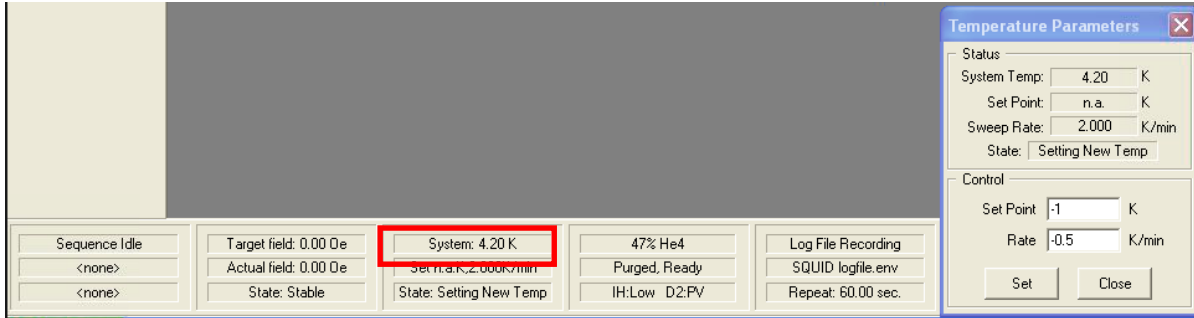


Figure J-2 Example SQUID MPMS MultiVu Application window. Outlined in red is the System temperature. Left-clicking here will bring up the Temperature Parameter window.

- The temperature must reach a minimum 100K before the sample can be loaded. Otherwise a “Remove Servo Sample” window will display saying that “The sample space is too cold to be safely opened.”

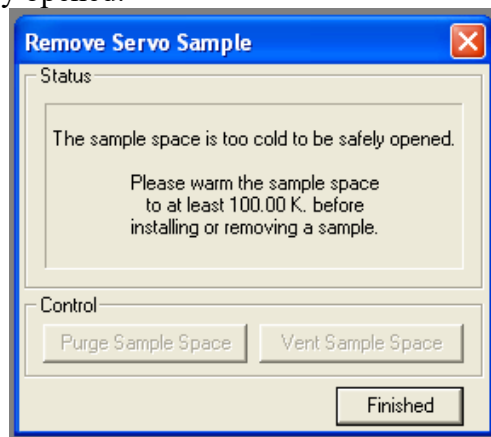


Figure J-3 Remove Servo Sample window will appear when the system temperature is below 100K while trying to remove a sample.

- The SQUID machine will make a clicking noise and while observing the loading port, the top of the sample insertion rod should become visible—generally the top consists of a small blue cylindrical piece at the top. This can be seen through the clear plastic housing.
- Remove the top piece sealing the loading port and turn it over.
- Screw the threaded white plastic portion into the top of the sample loading rod and carefully remove the rod from the SQUID chamber. If a sample was previously in the chamber, it will appear mounted to the end of the loading rod. Carefully remove it from the bottom of the rod and place it on the SQUID machine housing next to the computer.
- Before mounting on the rod, carefully pierce the straw, making three of holes radially around the sample. Do this two more times, each time making the set about 1.5 cm from the last.

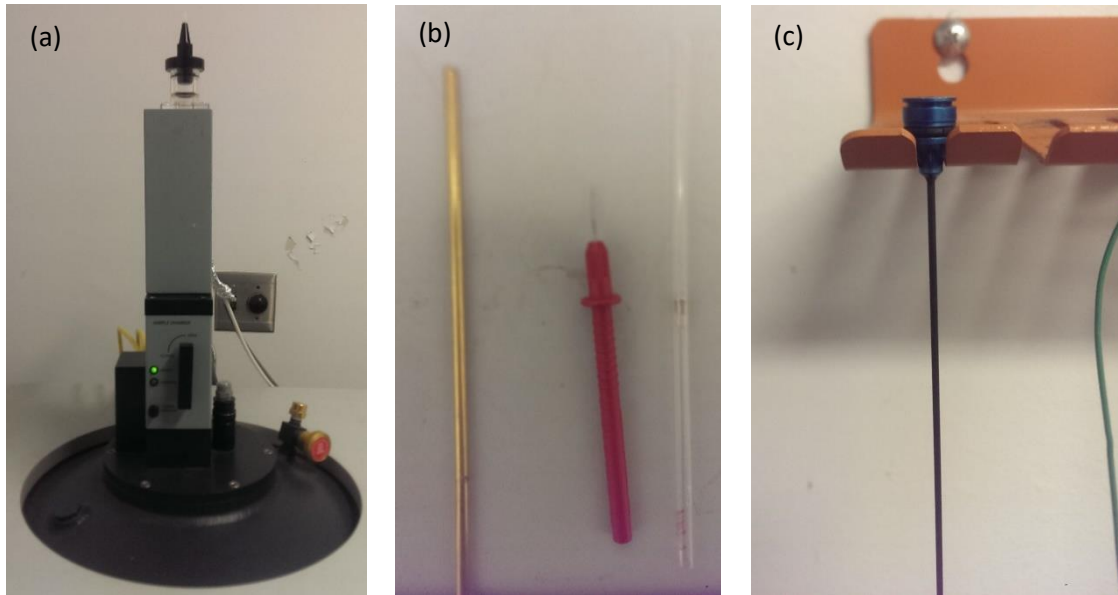


Figure J-4 (a) SQUID loading chamber with sealing top piece, (b) centering rod, piercing tool, and straw with inserted pill capsule and sample, and (c) loading rod with blue cylindrical top piece.

10. Avoid piercing the capsule as it can crack and break, releasing the sample and causing it to fall out of the straw.
11. Taking the sample to be scanned, gently push the top of the straw onto the peg at the bottom of the loading rod.
12. Insert the second plug on the bottom of the sample straw.
13. Re-insert the loading rod into the SQUID loading chamber until it is just barely visible, the exact same position was when it was unloaded.
14. Replace the sealing topper, ensuring that the o-ring makes good contact with the port.
15. Press the black button labeled "Purge". The SQUID will cycle through purging the chamber with helium until a green light is illuminated indicating that the port has been purge and is ready to load.
16. Left-click "Center" → "RSO..." → "Initialize Transport" to load the sample. The sample loading rod can be observed descending into the chamber.
17. Next the sample must be centered. Left-click "Center" to perform the centering scan. A window will appear showing both a fitted regression (blue) and the measured data (red). The key is to have the blue fit overlapping with red data in a Gaussian shaped peak at the ideal centered distance (x-axis).
18. Adjust the position manually to 3.5 and scan, this will seek out the more sensitive bottom coil and establish a lower limit to the position
19. Ensure that the box is checked, adjust the position manually again to 3.5 and scan
20. At this point, the program should have lined up the maximum or minimum from the scan.
21. Using the value automatically populated in the field, click Adjust position (without inputting 3.5)
22. The result should be that the fit and data should overlap and the sample will be sufficiently centered in between the coils.

J. Copper Volatility Diagram Construction

J.1. Introduction

A volatility diagram is a suitable method for studying the dry etching of solid materials, and it can be constructed from knowledge of the reaction thermodynamics of a particular system. For the etching of copper by chlorine, the relevant reactions can be found in Table K-1.

The relationship between the pressure of each gas phase Cu-Cl compound and the pressure of Cl₂ can be determined from expressions for the equilibrium constant of each reaction. Examples of this for each reaction listed in Table K-1 can be found below.

Table J-1 Table of relevant reaction for Cu-Cl systems, reproduced from (Kulkarni, et al., 2002).

Reaction		ΔH° (kJ/mol)			
		50C	100C	150C	200C
(1)	$Cu(c) + 1/2 Cl_2(g) \rightarrow CuCl(c)$	-137.01	-136.62	-136.17	-135.66
(2)	$CuCl(c) + 1/2 Cl_2(g) \rightarrow CuCl_2(c)$	-80.63	-80.30	-79.98	-79.70
(3)	$Cu(c) \rightarrow Cu(g)$	337.50	337.30	337.05	336.80
(4)	$CuCl(c) \rightarrow Cu(g) + 1/2 Cl_2(g)$	474.52	473.91	473.22	472.46
(5)	$CuCl_2(c) \rightarrow Cu(g) + Cl_2(g)$	555.15	554.20	553.20	552.16
(6)	$Cu(c) + 1/2 Cl_2(g) \rightarrow CuCl(g)$	91.06	90.72	90.37	90.01
(7)	$CuCl(c) \rightarrow CuCl(g)$	228.07	227.34	226.54	225.67
(8)	$CuCl_2(c) \rightarrow CuCl(g) + 1/2 Cl_2(g)$	308.70	307.64	306.52	305.37
(9)	$Cu(c) + Cl_2(g) \rightarrow CuCl_2(g)$	-43.31	-43.39	-43.49	-43.59
(10)	$CuCl(c) + 1/2 Cl_2(g) \rightarrow CuCl_2(g)$	93.22	93.22	92.68	92.07
(11)	$CuCl_2(c) \rightarrow CuCl_2(g)$	173.52	173.52	172.66	171.77
(12)	$3 Cu(c) + 3/2 Cl_2(g) \rightarrow Cu_3Cl_3(g)$	-246.47	-246.47	-246.55	-246.66
(13)	$3 CuCl(c) \rightarrow Cu_3Cl_3(g)$	163.38	163.38	161.95	160.32
(14)	$3 CuCl_2(c) \rightarrow Cu_3Cl_3(g) + 3/2 Cl_2(g)$	404.27	404.27	401.90	399.41

J.2. Example Calculations

For Cu(g) only:

$$\begin{aligned} \text{Cu}(c) + \frac{1}{2}\text{Cl}_2(g) \rightleftharpoons \text{CuCl}(c) \rightarrow \log(K_1) &= \log\left(\frac{a_{\text{CuCl}}}{a_{\text{Cu}}P_{\text{Cl}_2}^{\frac{1}{2}}}\right) \rightarrow \log(P_{\text{Cl}_2}) \\ &= -2\log(K_1) \end{aligned} \quad (1)$$

$$\begin{aligned} \text{CuCl}(c) + \frac{1}{2}\text{Cl}_2(g) \rightleftharpoons \text{CuCl}_2(c) \rightarrow \log(K_2) &= \log\left(\frac{a_{\text{CuCl}_2}}{a_{\text{CuCl}}P_{\text{Cl}_2}^{\frac{1}{2}}}\right) \rightarrow \log(P_{\text{Cl}_2}) \\ &= -2\log(K_2) \end{aligned} \quad (2)$$

$$\text{Cu}(c) \rightleftharpoons \text{Cu}(g) \rightarrow \log(K_3) = \log\left(\frac{P_{\text{Cu}}}{a_{\text{Cu}}}\right) \rightarrow \log(P_{\text{Cu}}) = \log(K_3) \quad (3)$$

$$\text{CuCl}(c) \rightleftharpoons \text{Cu}(g) + \frac{1}{2}\text{Cl}_2(g) \rightarrow \log(K_4) = \log\left(\frac{P_{\text{Cu}}P_{\text{Cl}_2}^{\frac{1}{2}}}{a_{\text{CuCl}}}\right) \rightarrow \quad (4)$$

$$\log(P_{\text{Cu}}) = \log(K_4) - \frac{1}{2}\log(P_{\text{Cl}_2})$$

$$\begin{aligned} \text{CuCl}_2(c) \rightleftharpoons \text{Cu}(g) + \text{Cl}_2(g) \rightarrow \log(K_5) &= \log\left(\frac{P_{\text{Cu}}P_{\text{Cl}_2}}{a_{\text{CuCl}_2}}\right) \rightarrow \log(P_{\text{Cu}}) \\ &= \log(K_4) - \log(P_{\text{Cl}_2}) \end{aligned} \quad (5)$$

For $\text{CuCl}_2(g)$ only:

Eq. 1 and 2.

$$\text{Cu}(c) + \frac{1}{2}\text{Cl}_2(g) \rightleftharpoons \text{CuCl}(g) \rightarrow \log(K_6) = \log\left(\frac{P_{\text{CuCl}}}{a_{\text{Cu}}P_{\text{Cl}_2}^{\frac{1}{2}}}\right) \quad (6)$$

$$\rightarrow \log(P_{\text{CuCl}}) = \log(K_6) + \frac{1}{2}\log(P_{\text{Cl}_2})$$

$$\begin{aligned} \text{CuCl}(c) \rightleftharpoons \text{CuCl}(g) \rightarrow \log(K_7) &= \log\left(\frac{P_{\text{CuCl}}}{a_{\text{CuCl}}}\right) \rightarrow \log(P_{\text{CuCl}}) \\ &= \log(K_7) \end{aligned} \quad (7)$$

$$\text{CuCl}_2(\text{c}) \rightleftharpoons \text{CuCl}(\text{g}) + \frac{1}{2}\text{Cl}_2(\text{g}) \rightarrow \log(K_8) = \log\left(\frac{P_{\text{CuCl}}P_{\text{Cl}_2}^{\frac{1}{2}}}{a_{\text{CuCl}}}\right) \quad (8)$$

$$\rightarrow \log(P_{\text{CuCl}}) = \log(K_8) - \frac{1}{2}\log(P_{\text{Cl}_2})$$

For $\text{CuCl}_2(\text{g})$ only:Eq. 1 and 2.

$$\text{Cu}(\text{c}) + \text{Cl}_2(\text{g}) \rightleftharpoons \text{CuCl}_2(\text{g}) \rightarrow \log(K_9) = \log\left(\frac{P_{\text{CuCl}_2}}{a_{\text{Cu}}P_{\text{Cl}_2}}\right) \rightarrow \log(P_{\text{CuCl}_2}) \quad (9)$$

$$= \log(K_9) + \log(P_{\text{Cl}_2})$$

$$\text{CuCl}(\text{c}) + \frac{1}{2}\text{Cl}_2(\text{g}) \rightleftharpoons \text{CuCl}_2(\text{g}) \rightarrow \log(K_{10}) = \log\left(\frac{P_{\text{CuCl}_2}}{a_{\text{CuCl}}P_{\text{Cl}_2}^{\frac{1}{2}}}\right) \rightarrow \log(P_{\text{CuCl}_2}) \quad (10)$$

$$= \log(K_{10}) + \frac{1}{2}\log(P_{\text{Cl}_2})$$

$$\text{CuCl}_2(\text{c}) \rightleftharpoons \text{CuCl}_2(\text{g}) \rightarrow \log(K_{11}) = \log\left(\frac{P_{\text{CuCl}_2}}{a_{\text{CuCl}_2}}\right) \rightarrow \log(P_{\text{CuCl}_2}) = \log(K_{11}) \quad (11)$$

For $\text{Cu}_3\text{Cl}_3(\text{g})$ only:Eq. 1 and 2.

$$3\text{Cu}(\text{c}) + \frac{3}{2}\text{Cl}_2(\text{g}) \rightleftharpoons \text{Cu}_3\text{Cl}_3(\text{g}) \rightarrow \log(K_{12}) = \log\left(\frac{P_{\text{Cu}_3\text{Cl}_3}}{a_{\text{Cu}}^3P_{\text{Cl}_2}^{\frac{3}{2}}}\right) \quad (12)$$

$$\rightarrow \log(P_{\text{Cu}_3\text{Cl}_3})$$

$$= \log(K_{12}) + \frac{3}{2}\log(P_{\text{Cl}_2})$$

$$3\text{CuCl}(\text{c}) \rightleftharpoons \text{Cu}_3\text{Cl}_3(\text{g}) \rightarrow \log(K_{13}) = \log\left(\frac{P_{\text{Cu}_3\text{Cl}_3}}{a_{\text{CuCl}}^3}\right) \rightarrow \log(P_{\text{Cu}_3\text{Cl}_3}) \quad (13)$$

$$= \log(K_{13})$$

$$\begin{aligned}
3\text{CuCl}_2(\text{c}) &\rightleftharpoons \text{Cu}_3\text{Cl}_3(\text{g}) + \frac{3}{2}\text{Cl}_2(\text{g}) \rightarrow \log(K_{14}) = \log\left(\frac{P_{\text{Cu}_3\text{Cl}_3} P_{\text{Cl}_2}^{\frac{3}{2}}}{a_{\text{CuCl}_2}^3}\right) \\
&\rightarrow \log(P_{\text{CuCl}_2}) \\
&= \log(K_{14}) - \frac{3}{2}\log(P_{\text{Cl}_2})
\end{aligned}
\tag{14}$$

Each of these equations can be plotted together to produce a volatility diagram for the system of Cu and the species in question. Volatility diagrams for each gas can be found below in Fig. K-1-K-4. A volatility diagram for all species can be found in Fig. K-5. MATLAB code for calculating and producing these plots can be found following Fig. K-5.

J.3. Volatility Diagrams

Figure K-1. Volatility diagram for Cu(g) only.

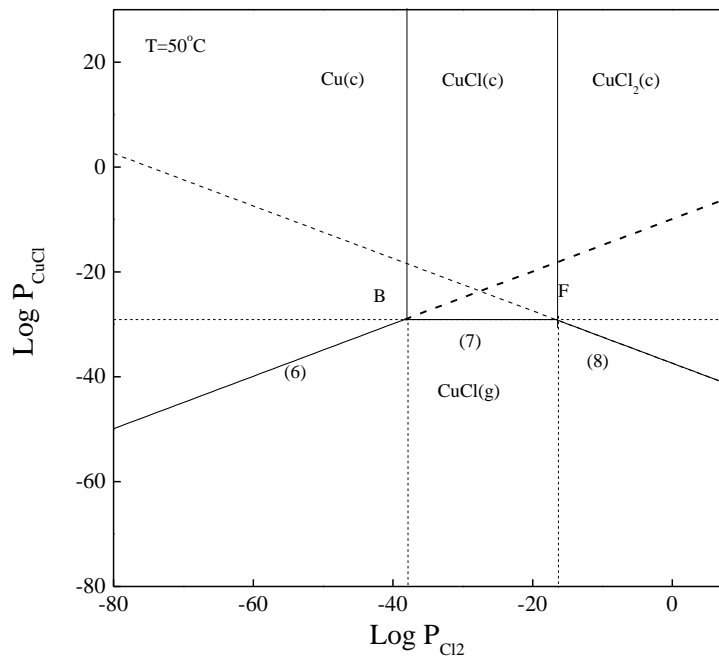


Figure J-2. Volatility Diagram for CuCl(g) only.

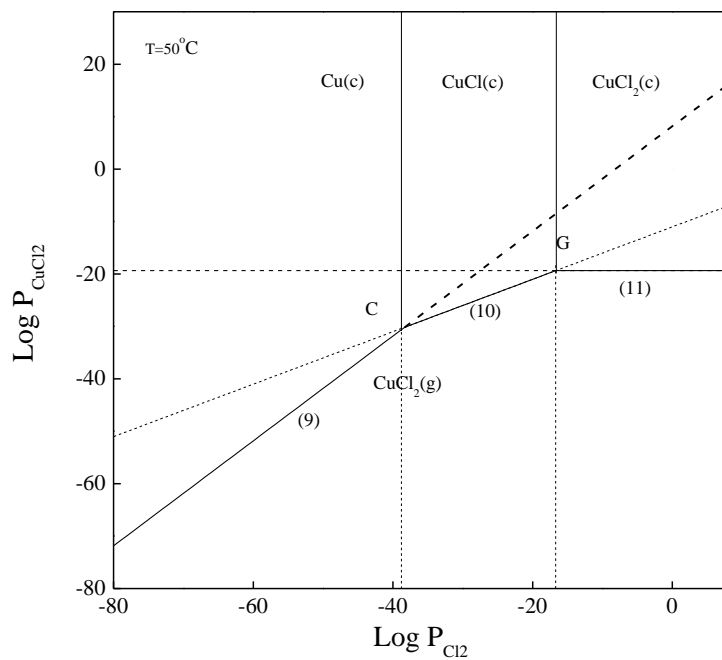


Figure J-3 Volatility diagram for $\text{CuCl}_2(\text{g})$ only.

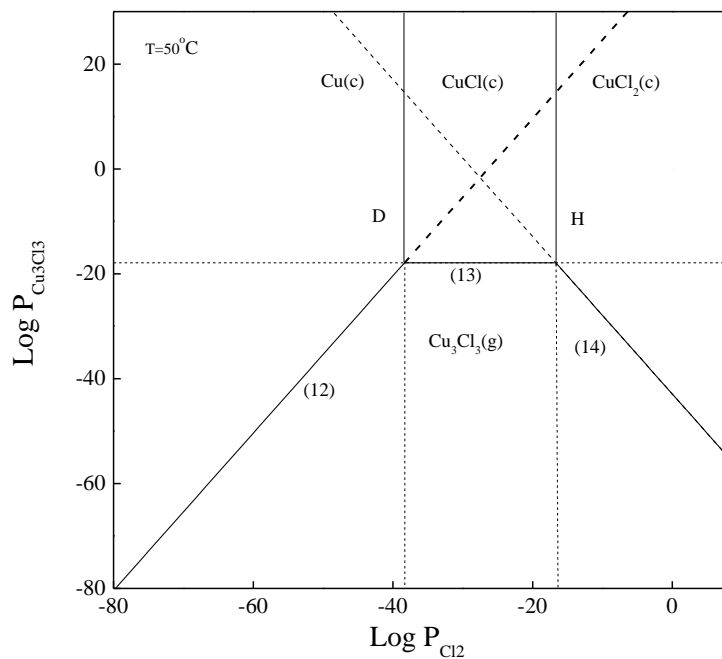


Figure J-4 Volatility diagram for $\text{Cu}_3\text{Cl}_3(\text{g})$ only.

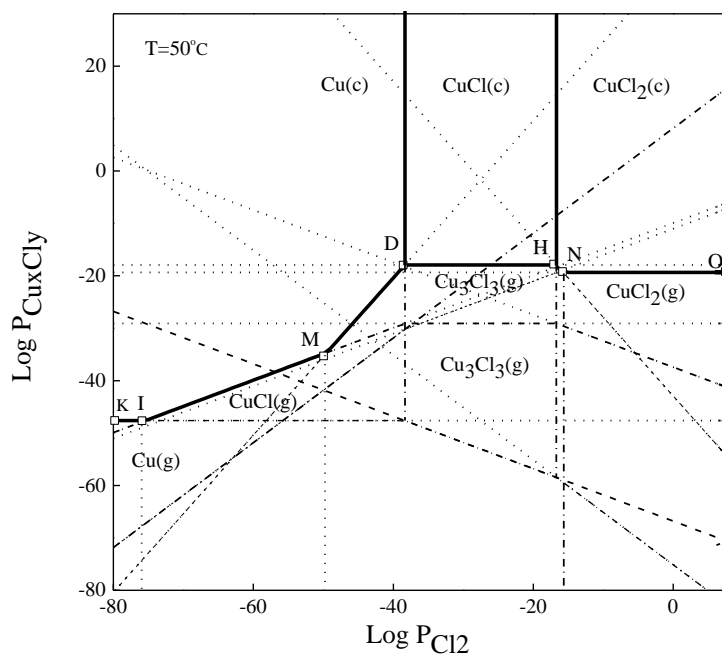


Figure J-5 Volatility diagram for entire Cu_xCl_y system.

J.4. Matlab Code

Matlab code for constructing these diagrams at $T = 50^\circ\text{C}$ can be found below:

```
%% Set up log(P_Cl2), log(K), and log(P_gas_species) (rxn)
logPCl2 = linspace(10,-80,1000);
logK = [19.17 8.34 -47.63 -66.80 -75.13 -9.91 -29.09 -37.43 8.16 -11.02 -19.36 39.61 -17.91 -
42.93];
rxn = {-2*logK(1); -2*logK(2); logK(3); logK(4)-0.5*logPCl2;
logK(5)-logPCl2; logK(6)+0.5*logPCl2; logK(7); logK(8)-0.5*logPCl2;
logK(9)+logPCl2; logK(10)+0.5*logPCl2; logK(11); logK(12)+1.5*logPCl2;
logK(13); logK(14)-1.5*logPCl2};

%% For Cu(g) only
xmin = -80;
xmax = 10;
```

```

ymin = -80;
ymax = 30;

rxn1 = ones(1,2).*cell2mat(rxn(1));
rxn2 = ones(1,2).*cell2mat(rxn(2));
rxn3 = ones(1,length(logPCl2)).*cell2mat(rxn(3));
rxn4 = cell2mat(rxn(4));
rxn5 = cell2mat(rxn(5));

[L1] = InterX([rxn1; [ymin ymax]],[logPCl2; rxn3]);
[L2] = InterX([rxn2; [ymin ymax]],[logPCl2; rxn4]);

l1x = [L1(1) L1(1)];
l1y = [L1(2) ymax];
l2x = [L2(1) L2(1)];
l2y = [L2(2) ymax];
l3x = [xmin L1(1)];
l3y = [L1(2) L1(2)];
l4x = [L1(1) L2(1)];
l4y = [L1(2) L2(2)];
l5x = [L2(1) xmax];
l5y = [L2(2) ymin];

plot(l1x,l1y,l2x,l2y,l3x,l3y,l4x,l4y,l5x,l5y);

axis([xmin xmax ymin ymax]);
xlabel('Log P_{Cl_2}99 (atm)');
ylabel('Log P_(Amorim) (atm)');
legend('Reaction 1','Reaction 2','Reaction 3','Reaction 4','Reaction 5','Location','NorthWest');

```

```

%% For CuCl(g) only
xmin = -80;
xmax = 10;
ymin = -80;
ymax = 30;

rxn1 = ones(1,2).*cell2mat(rxn(1));
rxn2 = ones(1,2).*cell2mat(rxn(2));
rxn6 = cell2mat(rxn(6));
rxn7 = ones(1,length(logPCl2)).*cell2mat(rxn(7));
rxn8 = cell2mat(rxn(8));

[L1] = InterX([rxn1; [ymin ymax]], [logPCl2; rxn6]);
[L2] = InterX([rxn2; [ymin ymax]], [logPCl2; rxn7]);

l1x = [L1(1) L1(1)];
l1y = [L1(2) ymax];
l2x = [L2(1) L2(1)];
l2y = [L2(2) ymax];
l3x = [xmin L1(1)];
l3y = [rxn6(length(rxn6)) L1(2)];
l4x = [L1(1) L2(1)];
l4y = [L1(2) L2(2)];
l5x = [L2(1) xmax];
l5y = [L2(2) rxn8(1)];

plot(l1x,l1y,l2x,l2y,l3x,l3y,l4x,l4y,l5x,l5y);

axis([xmin xmax ymin ymax]);
xlabel('Log P_{Cl_2} (atm)');

```

```

ylabel('Log P_{CuCl} (atm)');
legend('Reaction 1','Reaction 2','Reaction 6','Reaction 7','Reaction 8','Location','NorthWest');

%% For CuCl2(g) only
xmin = -80;
xmax = 10;
ymin = -80;
ymax = 30;

rxn1 = ones(1,2).*cell2mat(rxn(1));
rxn2 = ones(1,2).*cell2mat(rxn(2));
rxn9 = cell2mat(rxn(9));
rxn10 = cell2mat(rxn(10));
rxn11 = ones(1,length(logPCl2)).*cell2mat(rxn(11));

[L1] = InterX([rxn1; [ymin ymax]],[logPCl2; rxn9]);
[L2] = InterX([rxn2; [ymin ymax]],[logPCl2; rxn10]);

l1x = [L1(1) L1(1)];
l1y = [L1(2) ymax];
l2x = [L2(1) L2(1)];
l2y = [L2(2) ymax];
l3x = [xmin L1(1)];
l3y = [rxn9(length(rxn9)) L1(2)];
l4x = [L1(1) L2(1)];
l4y = [L1(2) L2(2)];
l5x = [L2(1) xmax];
l5y = [L2(2) rxn11(1)];

plot(l1x,l1y,l2x,l2y,l3x,l3y,l4x,l4y,l5x,l5y);

```



```

axis([xmin xmax ymin ymax]);
xlabel('Log P_{Cl_2} (atm)');
ylabel('Log P_{CuCl_2} (atm)');
legend('Reaction 1','Reaction 2','Reaction 9','Reaction 10','Reaction 11','Location','NorthWest');

%% For Cu3Cl3(g) only
xmin = -80;
xmax = 10;
ymin = -80;
ymax = 30;

rxn1 = ones(1,2).*cell2mat(rxn(1));
rxn2 = ones(1,2).*cell2mat(rxn(2));
rxn12 = cell2mat(rxn(12));
rxn13 = ones(1,length(logPCI2)).*cell2mat(rxn(13));
rxn14 = cell2mat(rxn(14));

[L1] = InterX([rxn1; [ymin ymax]], [logPCI2; rxn12]);
[L2] = InterX([rxn2; [ymin ymax]], [logPCI2; rxn13]);

l1x = [L1(1) L1(1)];
l1y = [L1(2) ymax];
l2x = [L2(1) L2(1)];
l2y = [L2(2) ymax];
l3x = [xmin L1(1)];
l3y = [rxn9(length(rxn12)) L1(2)];
l4x = [L1(1) L2(1)];
l4y = [L1(2) L2(2)];
l5x = [L2(1) xmax];

```

```

l5y = [L2(2) rxn14(1)];

plot(l1x,l1y,l2x,l2y,l3x,l3y,l4x,l4y,l5x,l5y);

axis([xmin xmax ymin ymax]);
xlabel('Log P_{Cl_2} (atm)');
ylabel('Log P_{Cu_3Cl_3} (atm)');
legend('Reaction 1','Reaction 2','Reaction 12','Reaction 13','Reaction 14','Location','NorthWest');

%% Total volatility diagram for Cu(g), CuCl(g), CuCl2(g), and Cu3Cl3(g)
xmin = -80;
xmax = 10;
ymin = -80;
ymax = 30;

[L1] = InterX([logPCl2; rxn3],[logPCl2; rxn6]);
l1x = [xmin L1(1)];
l1y = [L1(2) L1(2)];
[L2] = InterX([logPCl2; rxn12],[logPCl2; rxn6]);
l2x = [L1(1) L2(1)];
l2y = [L1(2) L2(2)];
[L3] = InterX([logPCl2; rxn12],[logPCl2; rxn13]);
l3x = [L2(1) L3(1)];
l3y = [L2(2) L3(2)];
[L4] = InterX([logPCl2; rxn13],[logPCl2; rxn14]);
l4x = [L3(1) L4(1)];
l4y = [L3(2) L4(2)];
[L5] = InterX([logPCl2; rxn14],[logPCl2; rxn11]);
l5x = [L4(1) L5(1)];
l5y = [L4(2) L5(2)];

```

l6x = [L5(1) xmax];

l6y = [L5(2) L5(2)];

l7x = [L3(1) L3(1)];

l7y = [L3(2) ymax];

l8x = [L4(1) L4(1)];

l8y = [L4(2) ymax];

plot(l1x,l1y,l2x,l2y,l3x,l3y,l4x,l4y,l5x,l5y,l6x,l6y,l7x,l7y,l8x,l8y);

axis([xmin xmax ymin ymax]);

xlabel('Log P_{Cl_2} (atm)');

ylabel('Log P_{Cu or CuCl or CuCl_2 or Cu_3Cl_3} (atm)');

legend('Reaction 3','Reaction 6','Reaction 12','Reaction 13','Reaction 14','Reaction 11','Reaction 1','Reaction 2','Location','NorthWest');

The function InterX is used to calculate the intersection and self-intersections between two curves within a particular range. It is authored by NS and is available online at the Matlab File Exchange (File ID #22441).

K. Gibbs Free Energy Minimization

K.1. Introduction

Total Gibbs free energy for a system is defined as:

$$G_{total}(T, P, \{n_j\}_{j=1}^k) = \sum_p \sum_j n_{pj} \mu_{pj} \quad (15)$$

Where n_{pj} defined as mols of species j in phase p , and μ_{pj} is defined as the chemical potential of species j in phase p . Chemical potential is defined by:

$$\mu_j = \left(\frac{\partial (nG(T, P, \{n_i\}_{i=1}^k))}{\partial n_j} \right)_{T, P, N_{i \neq j}} = G_j^o(T) + RT \ln \frac{\hat{f}_j}{f_j^o} \quad (16)$$

Where G^o is the heat of formation, R is the universal gas constant, T is temperature, \hat{f} is the species fugacity, and f^o is the reference fugacity.

For gasses:

$$\hat{f}_j = \hat{\Phi}_j y_j P \quad (17)$$

Where ϕ is the fugacity coefficient, $y_j P$ is the partial pressure of j.

$$f_j^o = P_0 \quad (18)$$

$$\mu_j = \Delta G_{fj}^o(T) + RT \ln \left(\frac{P}{P_0} \frac{n_j}{\sum n_j} \right) = \Delta G_{fj}^o(T) + RT \ln \left(\frac{P}{P_0} y_j \right) \quad (19)$$

For Solids:

$$\mu_j = G_j^o(T) + RT \ln \frac{f_j}{f_j^{sat}} \quad (20)$$

Where f_j^{sat} is the fugacity at P_j^{sat}

$$f_j = \phi_j^{sat} P_j^{sat} \exp \left(\frac{(V_j^{sat} (P - P_j^{sat}))}{RT} \right) \quad (21)$$

$$f_j^{sat} = P_j^{sat}$$

Where ϕ_j^{sat} is the fugacity coefficient at P_j^{sat} .

$$\phi_j^{sat} = \exp \left(\frac{B_{jj} P_j^{sat}}{RT} \right) \quad (22)$$

Where B_{jj} is the virial coefficient corresponding to volume occupied by molecules.

$$\mu_j = \Delta G_{fj}^o(T) + RT \ln \left(\exp \left(\frac{B_{jj} P_j^{sat} + (V_j^{sat} (P - P_j^{sat}))}{RT} \right) \right) \quad (23)$$

$$\mu_j = \Delta G_{fj}^o(T) + B_{jj} P_j^{sat} + (V_j^{sat} (P - P_j^{sat})) = \Delta G_{fj}^o(T) + (V_j^{sat} (P - P_j^{sat})) \quad (24)$$

The B_{jj} term goes to zero if it is assumed that gas molecules have negligible volume.

For a system at equilibrium:

$$\sum_j \frac{\partial(nG)}{\partial n_j} = \sum_j \mu_j = 0 \quad (25)$$

A generic atom balance is given as:

$$N_a - \sum_j \nu_{a,j} n_j = 0 \quad (26)$$

Where N_a is the total number of atom a, n_j are mols of species j, and ν_{aj} is the atoms of a in species j. Mols can be constrained to only positive values

$$n_j \geq 0 \quad \forall j = 1, 2, \dots, k \quad (27)$$

The most energetically favorable distribution of products at equilibrium is the product distribution that has minimum total Gibbs energy while satisfying mass balance and equilibrium constraints.

$$\left\{ \begin{array}{l} \min_{\{n_j\}_{j=1}^k} \left(G_{total} \left(T, P, \{n_j\}_{j=1}^k \right) \right) \\ j = 1, 2, \dots, k \\ \text{s. t.} \\ \sum_j \frac{\partial(nG)}{\partial n_j} = \sum_j \mu_j = 0 \\ N_a - \sum_j \nu_{a,j} n_j = 0 \\ n_j \geq 0 \quad \forall j = 1, 2, \dots, k \end{array} \right\} \quad (28)$$

K.2. Examples

Example: 1 kmol SiOCH₂ and 6 kmol CF₄ at P = 10⁻⁵ atm

1. Linear constraint of atomic mass conservation

$$\begin{pmatrix} n_{Si,SiOCH_2} & n_{Si,SiO_2} & n_{Si,CF_4} & n_{Si,SiF_4} & n_{Si,CO_2} & n_{Si,H_2} \\ n_{O,SiOCH_2} & n_{O,SiO_2} & n_{O,CF_4} & n_{O,SiF_4} & n_{O,CO_2} & n_{O,H_2} \\ n_{C,SiOCH_2} & n_{C,SiO_2} & n_{C,CF_4} & n_{C,SiF_4} & n_{C,CO_2} & n_{C,H_2} \\ n_{F,SiOCH_2} & n_{F,SiO_2} & n_{F,CF_4} & n_{F,SiF_4} & n_{F,CO_2} & n_{F,H_2} \\ n_{H,SiOCH_2} & n_{H,SiO_2} & n_{H,CF_4} & n_{H,SiF_4} & n_{H,CO_2} & n_{H,H_2} \end{pmatrix} \begin{pmatrix} n_{SiOCH_2} \\ n_{SiO_2} \\ n_{CF_4} \\ n_{SiF_4} \\ n_{CO_2} \\ n_{H_2} \end{pmatrix} = \begin{pmatrix} n_{Si,in} \\ n_{O,in} \\ n_{C,in} \\ n_{F,in} \\ n_{H,in} \end{pmatrix}$$

2. Define feed (1 kmol SiOCH₂, 6 kmol CF₄)

$$\begin{pmatrix} 1 & 1 & 0 & 1 & 0 & 0 \\ 1 & 2 & 0 & 0 & 2 & 0 \\ 1 & 0 & 1 & 0 & 1 & 0 \\ 0 & 0 & 4 & 4 & 0 & 0 \\ 2 & 0 & 0 & 0 & 0 & 2 \end{pmatrix} \begin{pmatrix} 1 \\ 0 \\ 6 \\ 0 \\ 0 \\ 0 \end{pmatrix} = \begin{pmatrix} 1 \\ 1 \\ 7 \\ 24 \\ 2 \end{pmatrix}$$

3. Minimize total Gibbs free energy function

$$\min_{n_j} \left\{ \frac{G_{Total}}{RT} = \sum_{phase} \sum_j \frac{n_{p,j} \mu_{p,j}}{RT} \right\}$$

The Gibbs free energy minimization scheme utilizes three separate MATLAB files “createSpeciesHSC.m”, “gibbsminsolve_Cr_phasecorrected.m”, and “gibbsInterface_solve.m”.

“createSpeciesHSC.m” is a list of possible species that can form in the system at equilibrium. The list is sorted into gas and solid phase components using the specs.gas and specs.solid tags. Each gas phase component has 3 variables:

specs.gas(n).name : gives the name in the form of the molecular formula

specs.gas(n).bal : elemental composition of each compound [Si O C F H N I]

specs.gas(n).Gf : Gibbs free energies of formation at temperatures defined in the temperature array contained in “gibbsInterface_solve.m”.

The data for these Gibbs free energies of formation can be taken in the form of ΔG_f reported in the NIST-JANAF databases or in the HSC software. Solid phase components, generally in the form of the thin film material of interest, contains an added variable:

specs.solid(n).molvol : this is the molar volume (i.e. inverse of the molar density) of the material of interest. These values can be calculated based off of the reported density of the material.

“gibbsminsolve_Cr_phasecorrected.m” is the portion of the MATLAB code which does the actual calculations for minimizing the objective function in the form of the total Gibbs free energy of the system. This file contains the gas constant (R), standard state pressure (Po), array of temperatures wherein the calculation is done at each element (T= [...]), and the operating pressure (P). The conditions used for the simulations done in this work are provided below.

R = 0.008314;

Po = 0.986923267;

```
T = [1 100 200 298.15 300 400 500...2000];
```

```
P = 1e-5;
```

Due to the numerical nature of the algorithm used in calculating the minimum, initial guesses must be provided in the form of an array (x0). Generally these values are held at unity for each species:

```
x0 = [1 1 1 1 1 1 1 1 1 1 1 1 1 1 1 1 1 1 1 1];
```

Additionally, a lower boundary must be established such as that seen in the solving criteria, depicting that one cannot have less than zero moles of any component, thus the lower bound is set to zero in the following array (LB = zeros...)

```
LB = zeros(1,lenGas+lenSol).
```

Finally, the “gibbsInterface_solve.m” file contains the vital information of the names of the gases and solids, for example:

```
gases = {'CO2(g)' 'SiF4(g)' 'COF2(g)' 'SiF3(g)' 'CO(g)' 'CF4(g)' 'SiF2(g)' 'N2(g)' 'CH4(g)'  
'CHF3(g)' 'CH2F2(g)' 'CH3F(g)' 'CH2O(g)' 'CIF3(g)' 'H2(g)' 'HF(g)' 'HCN(g)' 'H2O(g)' 'NH3(g)'  
'SiF(g)'};
```

```
solids = {'SiOCH2(s)'};
```

as well as the input feed of each mol of each atom. For this example a feed of 1 kmol of SiOCH₂(s) and 6 kmol of CF₄(g) was simulated. Converting this into a column vector of Si, O, C, F, H, N, and I atoms in kmol results in:

```
input = [1      % mol Si fed  
        1      % mol O fed  
        7      % mol C fed  
        24     % mol F fed  
        2      % mol H fed  
        0      % mol N fed  
        0];    % mol I fed
```

This is then handed as input into the aforementioned “gibbsminsolve_Cr_phasecorrected.m” file, which in turn matches each component name with the specific Gibbs free energy data contained in “createSpeciesHSC.m” and minimizes the total Gibbs free energy function.

The output can then be graphed to visualize the product distribution of components predicted to be present at equilibrium as a function of temperature—since the calculation was done at each temperature predefined in the $T = [\dots]$ array previously shown.

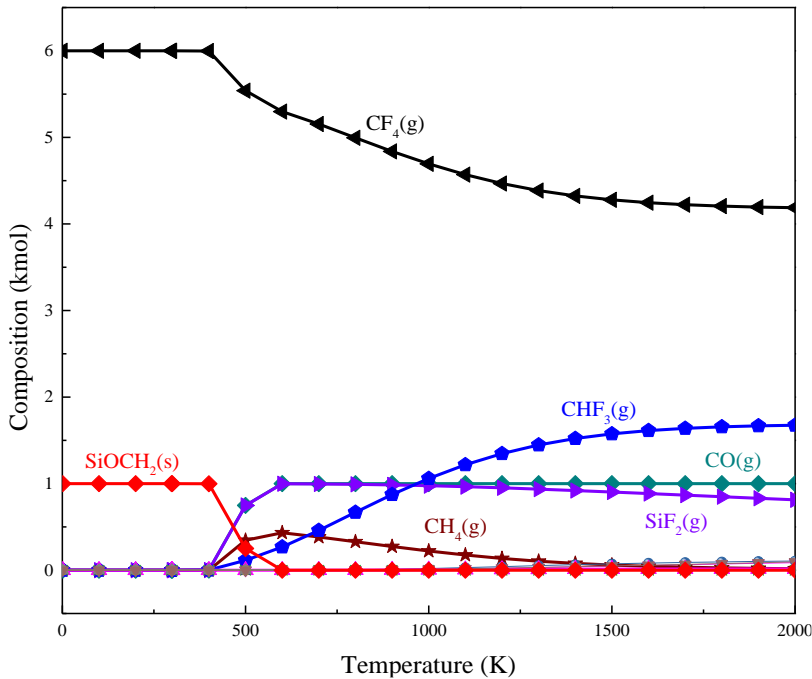


Figure L-1 The plot of composition as a function of temperature for the system of 1 kmol SiOCH_2 and 6 kmol CF_4 at $P = 10^{-5}\text{atm}$ based on the Gibbs free energy minimization.

K.3. Matlab Code

The full code for the “createSpeciesHSC.m” of this example is shown below:

```
function specs = createSpeciesHSC()
%Gases
specs.gas(1).name = 'CO2(g)';
specs.gas(1).bal = [0 2 1 0 0 0 0]'; %element composition of each compound [Si O C F H N I]
specs.gas(1).Gf = [-393.151
-393.683
-394.085
-394.389
```


-394.394
-394.675
-394.939
-395.182
-395.398
-395.586
-395.748
-395.886
-396.001
-396.098
-396.177
-396.24
-396.288
-396.323
-396.344
-396.353
-396.349
-396.333]';
specs.gas(2).name = 'SiF4(g)';
specs.gas(2).bal = [1 0 0 4 0 0 0]';
specs.gas(2).Gf = [-1609.428
-1599.596
-1586.418
-1572.711
-1572.449
-1558.165
-1543.75
-1529.287
-1514.816
-1500.354

-1485.91
-1471.484
-1457.077
-1442.686
-1428.308
-1413.941
-1399.58
-1385.222
-1370.418
-1353.088
-1335.767
-1318.454]';
specs.gas(3).name = 'COF2(g)';
specs.gas(3).bal = [1 1 0 2 0 0 0]';
specs.gas(3).Gf = [-635.798
-632.823
-628.302
-623.329
-623.232
-617.909
-612.454
-606.918
-601.329
-595.701
-590.046
-584.369
-578.676
-572.968
-567.247
-561.516

-555.774
-550.021
-544.258
-538.485
-532.7
-526.905]';
specs.gas(4).name = 'SiF3(g)';
specs.gas(4).bal = [1 0 0 3 0 0 0]';
specs.gas(4).Gf = [-1082.273
-1080.471
-1077.058
-1073.218
-1073.143
-1068.976
-1064.673
-1060.29
-1055.855
-1051.384
-1046.883
-1042.354
-1037.8
-1033.221
-1028.615
-1023.983
-1019.323
-1014.634
-1009.467
-1001.745
-994.005
-986.247]';

```
specs.gas(5).name = 'CO(g)';
specs.gas(5).bal = [0 1 1 0 0 0 0]';
specs.gas(5).Gf = [-113.805
-120.239
-128.526
-137.163
-137.328
-146.338
-155.414
-164.486
-173.518
-182.497
-191.416
-200.275
-209.075
-217.819
-226.509
-235.149
-243.74
-252.284
-260.784
-269.242
-277.658
-286.034]';
specs.gas(6).name = 'CF4(g)';
specs.gas(6).bal = [0 0 1 4 0 0 0]';
specs.gas(6).Gf = [-927.229
-916.822
-902.995
-888.507
```

-888.229
-873.107
-857.841
-842.523
-827.197
-811.884
-796.596
-781.337
-766.108
-750.909
-735.739
-720.597
-705.479
-690.383
-675.308
-660.251
-645.21
-630.184]';
specs.gas(7).name = 'SiF2(g)';
specs.gas(7).bal = [1 0 0 2 0 0 0]';
specs.gas(7).Gf = [-587.013
-590.839
-594.726
-598.278
-598.343
-601.733
-604.955
-608.046
-611.029
-613.918

-616.723

-619.449

-622.103

-624.685

-627.201

-629.651

-632.036

-634.359

-636.173

-635.401

-634.583

-633.72]';

specs.gas(8).name = 'N2(g)';

specs.gas(8).bal = [0 0 0 0 0 2 0]';

specs.gas(8).Gf = [0

0

0

0

0

0

0

0

0

0

0

0

0

0

0

0

```
0
0
0
0
0
0]';
specs.gas(9).name = 'CH4(g)';
specs.gas(9).bal = [0 0 1 0 4 0 0]';
specs.gas(9).Gf = [-66.911
-64.353
-58.161
-50.768
-50.618
-42.054
-32.741
-22.887
-12.643
-2.115
8.616
19.492
30.472
41.524
52.626
63.761
74.918
86.088
97.265
108.445
119.624
130.802]';
```

```
specs.gas(10).name = 'CHF3(g)';
specs.gas(10).bal = [0 0 1 3 1 0 0]';
specs.gas(10).Gf = [-690.096
-683.593
-673.566
-662.586
-662.372
-650.535
-638.317
-625.867
-613.274
-600.593
-587.861
-575.1
-562.325
-549.546
-536.77
-524
-511.239
-498.488
-485.747
-473.016
-460.296
-447.585]';
specs.gas(11).name = 'CH2F2(g)';
specs.gas(11).bal = [0 0 1 2 2 0 0]';
specs.gas(11).Gf = [-443.005
-439.137
-431.68
-423.076
```


-422.905
-413.261
-403.037
-392.424
-381.549
-370.494
-359.319
-348.062
-336.752
-325.407
-314.042
-302.665
-291.282
-279.9
-268.519
-257.142
-245.77
-234.404]';
specs.gas(12).name = 'CH3F(g);
specs.gas(12).bal = [0 0 1 1 3 0 0]';
specs.gas(12).Gf = [-226.275
-223.802
-217.703
-210.359
-210.21
-201.716
-192.515
-182.822
-172.783
-162.5

```
-152.045
-141.47
-130.81
-120.093
-109.338
-98.557
-87.761
-76.956
-66.147
-55.338
-44.53
-33.725]';
specs.gas(13).name = 'CH2O(g)';
specs.gas(13).bal = [0 1 1 0 2 0 0]; %element composition of each compound [Si O C F H N
I]
specs.gas(13).Gf = [-112.057
-112.63
-111.598
-109.921
-109.884
-107.615
-104.923
-101.917
-98.675
-95.259
-91.712
-88.068
-84.351
-80.578
-76.763
```

-72.914
-69.039
-65.141
-61.225
-57.292
-53.345
-49.385]';
specs.gas(14).name = 'CIF3(g)';
specs.gas(14).bal = [0 0 1 3 0 0 1]';
specs.gas(14).Gf = [-583.227
-581.659
-576.793
-571.109
-570.997
-564.51
-553.952
-540.717
-527.541
-514.427
-501.372
-488.371
-475.421
-462.516
-449.651
-436.822
-424.023
-411.25
-398.499
-385.766
-373.046

```
-360.336]';  
specs.gas(15).name = 'H2(g)';  
specs.gas(15).bal = [0 0 0 0 2 0 0]';  
specs.gas(15).Gf = [0  
0  
0  
0  
0  
0  
0  
0  
0  
0  
0  
0  
0  
0  
0  
0  
0  
0  
0  
0  
0  
0]';  
specs.gas(16).name = 'HF(g)';  
specs.gas(16).bal = [0 0 0 1 1 0 0]';  
specs.gas(16).Gf = [-272.499  
-273.266  
-273.947
```

-274.646
-274.659
-275.344
-275.981
-276.566
-277.102
-277.59
-278.036
-278.443
-278.816
-279.157
-279.471
-279.76
-280.027
-280.273
-280.502
-280.714
-280.911
-281.093]';
specs.gas(17).name = 'HCN(g)';
specs.gas(17).bal = [0 0 1 0 1 1 0]';
specs.gas(17).Gf = [135.529
131.784
128.187
124.725
124.66
121.192
117.769
114.393
111.063

107.775
104.525
101.308
98.12
94.955
91.812
88.687
85.579
82.484
79.403
76.333
73.274
70.226]';
specs.gas(18).name = 'H2O(g)';
specs.gas(18).bal = [0 1 0 0 2 0 0]';
specs.gas(18).Gf = [-238.921
-236.584
-232.766
-228.582
-228.5
-223.901
-219.051
-214.007
-208.812
-203.496
-198.083
-192.59
-187.033
-181.425
-175.774

-170.089
-164.376
-158.639
-152.883
-147.111
-141.325
-135.528]';
specs.gas(19).name = 'NH3(g)';
specs.gas(19).bal = [0 0 0 0 3 1 0]';
specs.gas(19).Gf = [-38.907
-34.034
-25.679
-16.367
-16.183
-5.941
4.8
15.879
27.19
38.662
50.247
61.91
73.625
85.373
97.141
108.918
120.696
132.469
144.234
155.986
167.725

```
179.447]';  
specs.gas(20).name = 'SiF(g)';  
specs.gas(20).bal = [1 0 0 1 0 0 0]';  
specs.gas(20).Gf = [-21.912  
-30.708  
-41.165  
-51.559  
-51.755  
-62.254  
-72.636  
-82.905  
-93.071  
-103.142  
-113.123  
-123.02  
-132.837  
-142.578  
-152.246  
-161.844  
-171.372  
-180.834  
-189.783  
-196.144  
-202.456  
-208.722]';  
specs.solid(1).name = 'SiOCH2(s)';  
specs.solid(1).bal = [1 1 1 0 2 0 0]';  
specs.solid(1).molvol = 0.0000226888218;  
specs.solid(1).Gf = [-556.4131  
-538.8001
```


-521.1871
-503.89994
-503.5741
-485.9611
-468.3481
-450.7351
-433.1221
-415.5091
-397.8961
-380.2831
-362.6701
-345.0571
-327.4441
-309.8311
-292.2181
-274.6051
-256.9921
-239.3791
-221.7661
-204.1531]';

end %creates structure "specs" that contains name, Gibbs energy of formation (from HSC data)

The full code for the “gibbsInterface_solve.m” of this example is shown below:

```
clear;

gases = {'CO2(g)' 'SiF4(g)' 'COF2(g)' 'SiF3(g)' 'CO(g)' 'CF4(g)' 'SiF2(g)' 'N2(g)' 'CH4(g)'
'CHF3(g)' 'CH2F2(g)' 'CH3F(g)' 'CH2O(g)' 'ClF3(g)' 'H2(g)' 'HF(g)' 'HCN(g)' 'H2O(g)' 'NH3(g)'
'SiF(g)'};

solids = {'SiOCH2(s)'};

n = 0;
% initial feed of 1 kmol SiOCH2(s), 6 kmol CF4(g)
input = [1      % mol Si fed
         1      % mol O fed
         7      % mol C fed
         24     % mol F fed
         2      % mol H fed
         0      % mol N fed
         0];    % mol I fed

moles = gibbsminsolve_Cr_phasecorrected(gases,solids,input,'HSC');
eqBal(1,n+1) = {[num2str(input(3)/2) ' mol O2']};
eqBal(2,n+1) = {moles};

figure;
markers = '+o*.xsd';
colors = 'rgbkmcy';

hold;
c = 1;
m = 1;

for z = 2:length(gases)+length(solids)+1
    plot(moles(:,1),moles(:,z),strcat(colors(c),markers(m)),'MarkerSize', 8);
```

```

c = c + 1;
if c == 8
    m = m + 1;
    c = 1;

```

```
end
```

```
end
```

```
legend([gases solids])
```

```
xlabel('Temperature (K)');ylabel('Number of Moles');
```

The full code for the “gibbsminsolve_Cr_phasecorrected.m” of this example is shown below:

```

function [moles] = gibbsminsolve_Cr_phasecorrected(gases,solids,beq,database)
global specs;
if strcmp(database,'NIST') == 1
    specs = createSpeciesNIST();
elseif strcmp(database,'HSC') == 1
    specs = createSpeciesHSC();
else
    error('Input name of thermodynamic database.');
```

```
end
```

```

R = 0.008314; % gas constant [kJ/mol*K]
Po = 0.986923267; % standard state pressure [atm]
T = [1 100 200 298.15 300 400 500 600 700 800 900 1000 1100 1200 1300 1400 1500 1600
1700 1800 1900 2000]; %temperature range in Kelvin
P = 1e-5; % Total operating pressure in atm
lenGas = length(gases);
lenSol = length(solids);
Ggas = zeros(length(gases),1);
Gsol = zeros(length(solids),1);
x0 = [1 1 1 1 1 1 1 1 1 1 1 1 1 1 1 1 1 1 1 1 1 1 1];

```

```

LB = zeros(1,lenGas+lenSol);
for t = 1:length(T);
    for n = 1:lenGas %make array of G_f/RT values for gases
        for m = 1:length(specs.gas)
            if strcmp(gases{n},specs.gas(m).name) == 1
                Aeq(:,n) = specs.gas(m).bal;
                Ggas(n) = specs.gas(m).Gf(t)/R/T(t);
                break;
            elseif m == length(specs.gas)
                str = gases{n};
                error(['Input compound ' str ' is not in list.']);
            end
        end
    end
end

for n = 1:lenSol %make array of Gf/RT values for solids
    for m = 1:lenSol
        if strcmp(solids{n},specs.solid(m).name) == 1
            Aeq(:,n+lenGas) = specs.solid(m).bal;
            Gsol(n) = specs.solid(m).Gf(t)/R/T(t) + specs.solid(m).molvol*101.325*(P-Po)/R/T(t);
            break;
        elseif m == length(specs.solid)
            str = solids{n};
            error(['Input compound ' str ' is not in list.']);
        end
    end
end

options = optimset('Algorithm','sqp');
[x,f] = fmincon(@gibbsArray,x0,[],[],Aeq,beq,LB,[],[],options);

```

```
moles(t,1) = T(t);  
moles(t,2:length(x)+1) = x;  
gibbs(t,1) = T(t);  
gibbs(t,2) = f*R*T(t);  
end
```

```
function F = gibbsArray(nj)  
    ntot = sum(nj(1:lenGas));  
  
    F = sum(nj(1:lenGas)'*(Ggas + log(nj(1:lenGas)'/ntot*P/Po))) +  
    sum(nj(lenGas+1:lenGas+lenSol)'*Gsol);  
end  
  
end
```

L. HSC Database

L.1. HSC Operating Procedure

1. Run HSC. The menu shown below in Fig. L-1 should appear.

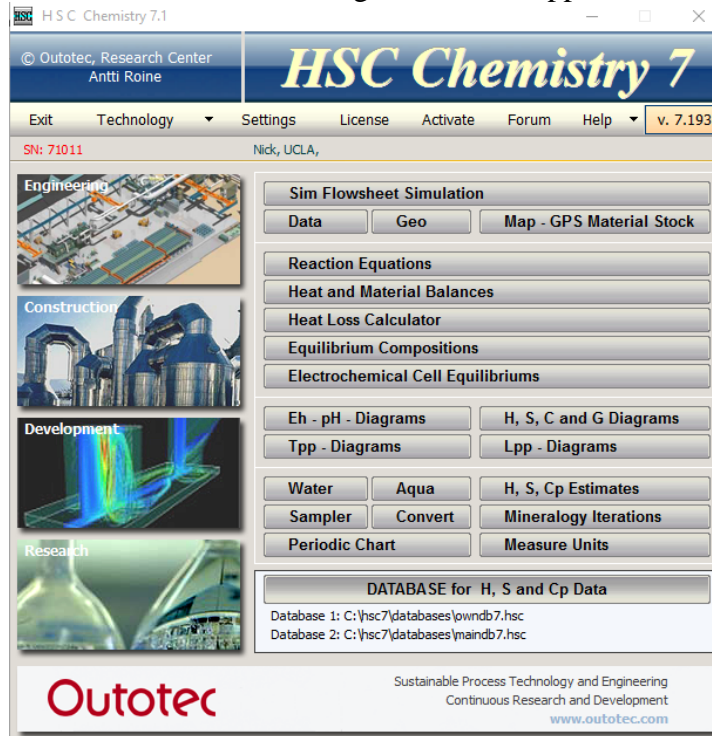


Figure M-1 Main Menu of HSC Chemistry 7.

2. Click on "DATABASE for H, S and Cp Data". The menu shown in Fig. L-2 below should appear.

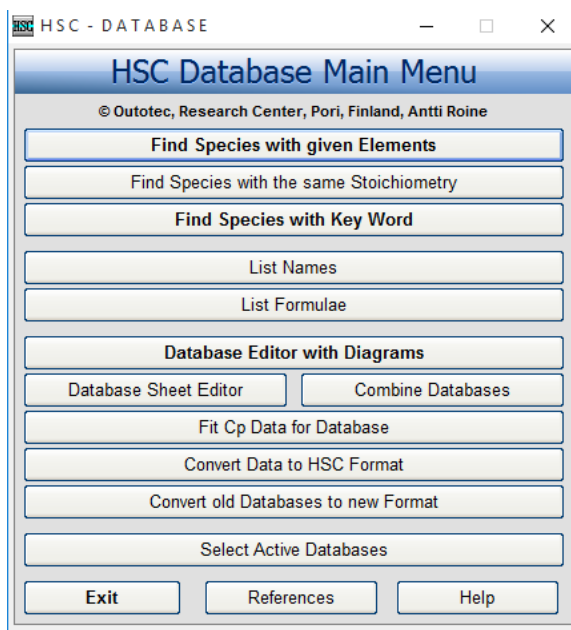


Figure L-2 HSC Database Main Menu.

- Click on “Database Editor with Diagrams”. The screen shown in Fig. L-3 below should appear.

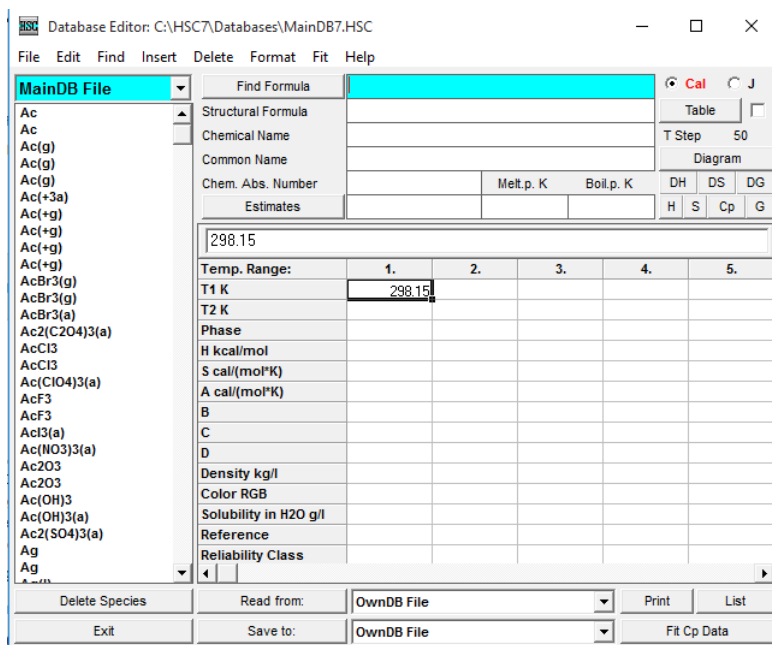


Figure L-3 Database Editor.

- Values can be set to be reported in joules and calories using the radio buttons in the top right hand corner. The database can be searched by entering a formula in the “Find Formula” field highlighted in teal and clicking on “Find Formula”. The desired species can be selected from the list on the left hand side.

- Once a desired species has been found, thermodynamic data can be displayed using the “Table” button in the upper right hand corner. Clicking “Table” should bring up two screens, shown below in Fig. L-4 and Fig. L-5. SiO₂ is being used as an example compound.

Figure L-4 Reaction Equations.

	T	Cp	H	S	G	Reference
1	SiO2					
2	T	Cp	deltaH	deltaS	deltaG	Reference
3	K	J/(mol*K)	kJ/mol	J/(mol*K)	kJ/mol	
4	100.000	-84.230	-905.412	-144.698	-890.942	Barin 89
5	100.000	-84.229	-905.412	-144.698	-890.942	Barin 89
6	150.000	-4.661	-908.450	-170.080	-882.938	Barin 89
7	200.000	23.557	-909.825	-178.121	-874.200	Barin 89
8	250.000	37.023	-910.520	-181.265	-865.204	Barin 89
9	298.150	44.540	-910.856	-182.505	-856.442	Barin 89
10	298.150	44.540	-910.856	-182.505	-856.442	Barin 89
11	300.000	44.769	-910.864	-182.533	-856.104	Barin 89
12	350.000	49.888	-910.998	-182.953	-846.965	Barin 89
13	400.000	53.672	-910.992	-182.939	-837.816	Barin 89
14	450.000	56.740	-910.881	-182.681	-828.675	Barin 89
15	500.000	59.417	-910.685	-182.270	-819.551	Barin 89
16	550.000	61.887	-910.412	-181.751	-810.450	Barin 89
17	600.000	64.261	-910.065	-181.147	-801.377	Barin 89
18	650.000	66.609	-909.642	-180.471	-792.336	Barin 89

Figure L-5 Thermodynamic Results.

- Results format can be cycled between Normal and Delta using the radio buttons beneath “Format of Results”. The table of values given in Fig. L-4 can be updated by pressing the

“Calculate” button in the lower right of Fig. L-4. The temperature range can be altered by changing the temperature values in Fig. L-4.

M. Vendors and Equipment Used

M.1. Vendor Contact Information

<i>Vendor</i>	<i>Contact name</i>	<i>Contact phone number</i>	<i>Contact email</i>	<i>Note</i>
Kurt J. Lesker	Clara DeMaio	1-800-245-1656	clarad@lesker.com	CSR for Lesker
UC Riverside	Stan Sheldon	1-951-922-6824 (home number, best to reach at, leave voicemail)	stan.sheldon@ucr.edu (likely not in use)	Retired technician, repaired UTI-100C QMS
PSP Vacuum (XPS x-ray source)	Ian Spender	+44 (0) 1625 500154	ianpspvacuum@btconnect.com	In UK
Vacuum Technology	William (Rob) Robinson	865-481-3342 (ext. 2265)	rrobinson@vacuumtechnology.com	Alternative for UTI-100C QMS repair
Consultant/Vendor, affiliated with Kaufman Robinson	Fred Van Der Linde	818-424-0324	fredvanderlinde@cs.com	Ion source parts/repair
Kaufman Robinson	Kent Rennie Chris Griffith	970-495-0187 (ext. 207) 970-495-0187 (ext. 206)	rennie@ionsources.com griffith@ionsources.com	Ion source parts/repair
PTB Sales	Arrigo Pueyo	626-385-3522	arrigo@ptbsales.com	Vacuum parts and pump/compressor repairs
Duniway Stockroom	Michael Marinello	650-969-8811 (ext. 107)	michael.m@duniway.com	Pump rebuild/repair/sales
University of Arizona ALEC, ICP-MS	Mary Kay Amistadi	520-626-9965	amistadi@ag.arizona.edu	ICP-MS services
RF Parts Co	Steve LaGaisse	760-744-0700 (ext. 316)	steve@rfparts.com	Doorknob capacitors for ICP coil
Sci-Tech Glassblowing	Glenn Gados	805-523-9790	stglass@sbcglobal.net	Cleaning/modification of ICP quartz components
USC Center for Electron Microscopy and Microanalyses	John Curulli (Director of Operations)	213-740-1990	curulli@usc.edu	Back up Kratos (identical to Chem XPS setup)

Tritool	Don Pangburn	Not available	d.pangburn@tritool.com	Facing tool repair for orbital welder
Tecan Precision Metal	Barry Eggington	+44 (0) 1305 765432	Barry.eggington@tecan.co.uk	Electroformed mesh for use in ion energy analyzer
Pasternack	Anthony Cerda	949-261-1920	sales@pasternack.com	Cabling for ICP coil

M.2. Electrical Equipment Parameters

<i>Equipment</i>	<i>Parameters</i>
Mechanical pump	115 VAC, single phase
Cryogenic pump compressor	208 VAC, 3 phase, 30 A min
Turbomolecular pump	115 VAC, single phase
Mass flow controller	120 VAC, single phase
XPS x-ray source	120 VAC, single phase Source up to 15kV, 20 mA

M.3. Water, Gas, and Chemical Equipment Parameters

<i>Equipment</i>	<i>Parameters</i>
Water to compressor	Flow rate = 2.8 GPM
Water to chiller (XPS)	Flow rate = 3.5 GPM
H ₂ cylinder to MFC (ICP)	Flowing H ₂
SF ₆ cylinder to MFC (ICP)	Flowing SF ₆
O ₂ cylinder to MFC (ICP)	Flowing O ₂
N ₂ cylinder to MFC (ICP)	Flowing N ₂
Ar cylinder to MFC (ICP/Kaufman source)	Flowing Ar
Formic acid (vaporizer chamber) (Sigma-Aldrich F0507)	Flowing 0.01-0.2 g/min

M.4. Specialty Electrical Equipment

<i>Equipment</i>	<i>Vendor</i>	<i>Part Number</i>
Doorknob Capacitor (ICP coil, 200 pF, 7.5 kV)	RF Parts Co.	CRL857-200
C male to C male BNC cable (connection from match network to ICP coil)	Pasternack	PE33098-36
Female connector solder attachment (for on top of cage)	Pasternack	PE44117

Bibliography

- Abe, T., Y. G. Hong and M. Esashi (2003). "High-selectivity reaction ion etching with CO/NH₃/Xe gas for micro/nanostructuring of 20% Fe-Ni, Au, Pt, and Cu." IEEE Int. C. Microelec.: 574-577.
- Abe, T., Y. G. Hong and M. Esashi (2003). "Highly selective reactive-ion etching using CO/NH₃/Xe gases for microstructuring of Au, Pt, Cu, and 20% Fe-Ni." J. Vac. Sci. Technol. B **21**(5): 2159.
- Agarwal, A. and M. J. Kushner (2009). "Plasma atomic layer etching using conventional plasma equipment." J. Vac. Sci. Technol. A **27**(1): 37.
- Allender, D., J. Bray and J. Bardeen (1973). "Model for an Exciton Mechanism of Superconductivity." Phys. Rev. B **7**(3): 1020-1029.
- Allender, D., J. Bray and J. Bardeen (1973). "Model for an Exciton Mechanism of Superconductivity." Physical Review B **7**(3): 1020-1029.
- Altieri, N. D., J. K.-C. Chen, L. Minardi and J. P. Chang (2017). "Review Article: Plasma-surface interactions at the atomic scale for patterning metals." J. Vac. Sci. Technol. A **35**(5): 05C203.
- Amorim, J., H. S. Maciel and J. P. Sudano (1991). "High-Density Plasma Mode Of An Inductively Coupled Radio-Frequency Discharge." Journal Of Vacuum Science & Technology B **9**(2): 362-365.
- Andriacos, P. C., C. Uzoh, J. O. Dukovic, J. Horkans and H. Deligianni (1998). "Damascene copper electroplating for chip interconnections." IBM J. Res. Dev. **42**(5): 567-574.
- Aoyagi, Y., K. Shinmura, K. Kawasaki, T. Tanaka, K. Gamo, S. Namba and I. Nakamoto (1992). "Molecular layer etching of GaAs." Appl. Phys. Lett. **60**(8): 968.
- Athavale, S. D. (1996). "Realization of atomic layer etching of silicon." J. Vac. Sci. Technol. B **14**(6): 3702.
- Athavale, S. D. (1996). "Realization of atomic layer etching of silicon." Journal of Vacuum Science & Technology B: Microelectronics and Nanometer Structures **14**(6): 3702.
- Athavale, S. D. and D. J. Economou (1995). "Molecular dynamics simulation of atomic layer etching of silicon." Journal of Vacuum Science & Technology A: Vacuum, Surfaces, and Films **13**(3): 966-971.
- Bardeen, J., L. N. Cooper and J. R. Schrieffer (1957). "Theory of Superconductivity." Physical Review **108**(5): 1175-1204.
- Bardeen, J., L. N. Cooper and J. R. Schrieffer (1957). "Theory of Superconductivity." Phys. Rev. **108**(5): 1175-1204.

Battistoni, C., G. Mattogno and E. Paparazzo (1985). "An XPS and Auger Study of some Polynuclear Copper Compounds." Inorg. Chim. Acta **102**: 1-3.

Bell, F. H. (1994). "Investigation of selective SiO₂-to-Si etching in an inductively coupled high-density plasma using fluorocarbon gases." J. Vac. Sci. Technol. A **12**(6): 3095.

Blackstock, J. J., Z. Li, M. R. Freeman and D. R. Stewart (2003). "Ultra-flat platinum surfaces from template-stripping of sputter deposited films." Surf. Sci. **546**(2-3): 87-96.

Blackstock, J. J., D. R. Stewart and Z. Li (2005). "Plasma-produced ultra-thin platinum-oxide films for nanoelectronics: physical characterization." Appl. Phys. A-Mater. **80**(6): 1343-1353.

Boris, D. R., G. M. Petrov, E. H. Lock, T. B. Petrova, R. F. Fernsler and S. G. Walton (2013). "Controlling the electron energy distribution function of electron beam generated plasmas with molecular gas concentration: I. Experimental results." Plasma Sources Sci T. **22**(6): 065004.

Bourhila, N., J. Torres, J. Palleau, C. Bernard and R. Madar (1997). "Copper LPCVD for advanced technology." Microelectron. Eng. **33**: 25-30.

Cabrera, N. and N. F. Mott (1949). "Theory of the oxidation of metals." Rep. Prog. Phys. **12**: 163-184.

Çakır, O. (2006). "Copper etching with cupric chloride and regeneration of waste etchant." Journal of Materials Processing Technology **175**(1-3): 63-68.

Çakır, O., H. Temel and M. Kiyak (2005). "Chemical etching of Cu-ETP copper." Journal of Materials Processing Technology **162-163**: 275-279.

Chae, H., S. A. Vitale and H. H. Sawin (2003). "Silicon dioxide etching yield measurements with inductively coupled fluorocarbon plasmas." J. Vac. Sci. Technol. A **21**(2): 381-387.

Chavez, K. L. and D. W. Hess (2001). "A Novel Method of Etching Copper Oxide Using Acetic Acid." J. Electrochem. Soc. **148**(11): G640.

Chen, C., O. Kitakami, S. Okamoto and Y. Shimada (2000). "Ordering and orientation of CoPt/SiO₂ granular films with additive Ag." Appl. Phys. Lett. **76**(22): 3218.

Chen, F. F. (2012). "Langmuir Probe Diagnostics."

Chen, J. K.-C., N. D. Altieri, T. Kim, E. Chen, T. Lill, M. Shen and J. P. Chang (2017). "Directional etch of magnetic and noble metals. II. Organic chemical vapor etch." J. Vac. Sci. Technol. A **35**(5): 05C305.

Chen, J. K.-C., N. D. Altieri, T. Kim, T. Lill, M. Shen and J. P. Chang (2017). "Directional etch of magnetic and noble metals. I. Role of surface oxidation states." J. Vac. Sci. Technol. A **35**(5): 05C304.

Chen, J. K. C., T. Kim, N. D. Altieri, E. Chen and J. P. Chang (2017). "Ion Beam Assisted Organic Chemical Vapor Etch of Magnetic Thin Films." J. Vac. Sci. Technol. A **35**(3): 031304.

Cheng, P. (2008). "Influence of substrates in ZnO devices on the surface plasma enhanced light emission." Opt. Exp. **16**(12): 8896-8901.

Chiang, M.-C., F.-M. Pan, H.-C. Cheng, J.-S. Liu, S.-H. Chan and T.-C. Wei (2000). "Dry etching of platinum films with TiN masks in an Ar/O₂ helicon wave plasma." J. Vac. Sci. Technol. A **18**(1): 181.

Choi, T. S. and D. W. Hess (2014). "Chemical Etching and Patterning of Copper, Silver, and Gold Films at Low Temperatures." ECS J. Solid State Sc. **4**(1): N3084-N3093.

Choi, T. S., G. Levitin and D. W. Hess (2013). "Low Temperature Cu Etching Using CH₄-Based Plasmas." ECS J. Solid State Sc. **2**(11): P506-P514.

Chou, C. H. and J. Phillips (1990). "Platinum metal etching in a microwave oxygen plasma." Journal of Applied Physics **68**(5): 2415.

Chung, C. W., W. I. Lee and J. K. Lee (1995). "Dry etching of Pt/PbZr_xTi_{1-x}O₃/Pt thin film capacitors in an inductively coupled plasma (ICP)." Integr. Ferroelectr. **11**(1-4): 259-267.

Coburn, J. W. and M. Chen (1980). "Optical emission spectroscopy of reactive plasmas: A method for correlating emission intensities to reactive particle density." Journal of Applied Physics **51**(6): 3134-3136.

Coburn, J. W. and H. F. Winters (1979). "Ion- and electron-assisted gas-surface chemistry—An important effect in plasma etching." J. Appl. Phys. **50**(5): 3189.

Coburn, J. W. and H. F. Winters (1984). "Plasma-assisted etching: ion-assisted surface chemistry." AIP Conf. Proc. **122**: 98-105.

Donahue, M. J. (2002). "Analysis of Switching in Uniformly Magnetized Bodies." IEEE T. Magn. **38**(5): 2468-2470.

Donnelly, V. M. and A. Kornblit (2013). "Plasma etching: Yesterday, today, and tomorrow." J. Vac. Sci. Technol. A **31**(5): 050825.

Donnelly, V. M. and M. V. Malyshev (2000). "Diagnostics of inductively coupled chlorine plasmas: Measurements of the neutral gas temperature." Appl. Phys. Lett. **77**(16): 2467.

Duffy, D. M. and A. M. Stoneham (1983). "Conductivity and 'negative U' for ionic grain boundaries." J. Phys. C Solid State **16**: 4087-4092.

DuMont, J. W., A. E. Marquardt, A. M. Cano and S. M. George (2017). "Thermal Atomic Layer Etching of SiO₂ by a "Conversion-Etch" Mechanism Using Sequential Reactions of Trimethylaluminum and Hydrogen Fluoride." ACS Appl. Mater. Inter. **9**(11): 10296-10307.

Ein-Eli, Y. and D. Starosvetsky (2007). "Review on copper chemical–mechanical polishing (CMP) and post-CMP cleaning in ultra large system integrated (ULSI)—An electrochemical perspective." Electrochim. Acta **52**(5): 1825-1838.

Evans, U. R. (1960). "The corrosion and oxidation of metals: scientific principles and practical applications."

Farrow, R. F. C., D. Weller, R. F. Marks, M. F. Toney, S. Hom, G. R. Harp and A. Cebollada (1996). "Growth temperature dependence of long-range alloy order and magnetic properties of epitaxial $\text{Fe}_x\text{Pt}_{1-x}$ ($x \approx 0.5$) films." Appl. Phys. Lett. **69**(8): 1166.

Fitzsimons, N. P. and W. Jones (1995). "Studies of Copper Hydride." J. Chem. Soc. Faraday T. **91**(4): 713-718.

Flamm, D. L. and V. M. Donnelly (1981). "The Design of Plasma Etchants." Plasma Chem. Plasma P. **1**(4).

Garay, A. A., J. H. Choi, S. M. Hwang and C. W. Chung (2015). "Inductively Coupled Plasma Reactive Ion Etching of Magnetic Tunnel Junction Stacks in a $\text{CH}_3\text{COOH}/\text{Ar}$ Gas." Electrochem. Solid St. **4**(10): P77-P79.

George, M. A. and D. W. Hess (1995). "Reaction of 1,1,1,5,5,5-Hexafluoro-2,4-pentanedione with CuO , Cu_2O , and Cu films." Journal of The Electrochemical Society **142**(3): 961-965.

Giannetti, J. P. and R. T. Sebulsy (1969). "Chlorinated platinum-alumina low temperature isomerization catalysts." Ind. Eng. Chem. Prod. RD **8**(4): 356-361.

Grezes, C., F. Ebrahimi, J. G. Alzate, X. Cai, J. A. Katine, J. Langer, B. Ocker, P. Khalili Amiri and K. L. Wang (2016). "Ultra-low switching energy and scaling in electric-field-controlled nanoscale magnetic tunnel junctions with high resistance-area product." Applied Physics Letters **108**(1): 012403.

Hagström, S., C. Nordling and K. Siegbahn (1964). "Electron spectroscopy for chemical analyses." Physics Letters **9**(3): 235.

Hoang, J., C.-C. Hsu and J. P. Chang (2008). "Feature profile evolution during shallow trench isolation etch in chlorine-based plasmas. I. Feature scale modeling." J. Vac. Sci. Technol. B **26**(6): 1911-1918.

Horiike, Y. (1990). "Digital chemical vapor deposition and etching technologies for semiconductor processing." Journal of Vacuum Science & Technology A: Vacuum, Surfaces, and Films **8**(3): 1844.

Hosoi, N. and Y. Ohshita (1993). "Lower-temperature plasma etching of Cu films using infrared radiation." Appl. Phys. Lett. **63**(19): 2703.

Howard, B. J. (1994). "Reactive ion etching of copper with BCl_3 and SiCl_4 : Plasma diagnostics and patterning." J. Vac. Sci. Technol. A **12**(4): 1259.

Howard, B. J. and C. Steinbrüchel (1991). "Reactive ion etching of copper in SiCl₄-based plasmas." Appl. Phys. Lett. **59**(8): 914.

Hsu, C.-C., J. Hoang, V. Le and J. P. Chang (2008). "Feature profile evolution during shallow trench isolation etch in chlorine-based plasmas. II. Coupling reactor and feature scale models." J. Vac. Sci. Technol. B **26**(6): 1919-1925.

Hwang, S. M., A. A. Garay, I. H. Lee and C. W. Chung (2014). "Etch characteristics of CoFeB thin films and magnetic tunnel junction stacks in a H₂O/CH₃OH plasma." Korean J. Chem. Eng. **31**(12): 2274-2279.

Ikeda, S., K. Miura, H. Yamamoto, K. Mizunuma, H. D. Gan, M. Endo, S. Kanai, J. Hayakawa, F. Matsukura and H. Ohno (2010). "A perpendicular-anisotropy CoFeB-MgO magnetic tunnel junction." Nat. Mater. **9**(9): 721-724.

Ismail, A. F., K. C. Khulbe and T. Matsuura (2015). Gas Separation Membranes Polymeric and Inorganic. Heidelberg, Springer.

Johnson, N. R. and S. M. George (2017). "WO₃ and W Thermal Atomic Layer Etching Using "Conversion-Fluorination" and "Oxidation-Conversion-Fluorination" Mechanisms." ACS Appl. Mater. Inter. **9**(39): 34435-34447.

Johnson, N. R., H. Sun, K. Sharma and S. M. George (2016). "Thermal atomic layer etching of crystalline aluminum nitride using sequential, self-limiting hydrogen fluoride and Sn(acac)₂ reactions and enhancement by H₂ and Ar plasmas." Journal of Vacuum Science & Technology A: Vacuum, Surfaces, and Films **34**(5): 050603.

Jung, K. B. (1997). "Patterning of Cu, Co, Fe, and Ag for magnetic nanostructures." J. Vac. Sci. Technol. A **15**(3): 1780.

Kamata, Y. (2004). "Ar ion milling process for fabricating CoCrPt patterned media using a self-assembled PS-PMMA diblock copolymer mask." J. Appl. Phys. **95**(11): 6705.

Kanarik, K. J., T. Lill, E. A. Hudson, S. Sriraman, S. S. H. Tan, J. Marks, V. Vahedi and R. A. Gottscho (2015). "Overview of atomic layer etching in the semiconductor industry." J. Vac. Sci. Technol. A **33**(2): 020802.

Kanarik, K. J., S. Tan, W. Yang, T. Kim, T. Lill, A. Kabansky, E. A. Hudson, T. Ohba, K. Nojiri, J. Yu, R. Wise, I. L. Berry, Y. Pan, J. Marks and R. A. Gottscho (2017). "Predicting synergy in atomic layer etching." J. Vac. Sci. Technol. A **35**(5): 05C302-301.

Kauppinen, C., S. A. Khan, J. Sundqvist, D. B. Suyatin, S. Suihkonen, E. I. Kauppinen and M. Sapanen (2017). "Atomic layer etching of gallium nitride (0001)." J. Vac. Sci. Technol. A **35**(6): 060603.

Kim, E. H., T. Y. Lee, B. C. Min and C. W. Chung (2012). "High density plasma reactive ion etching of CoFeB magnetic thin films using a CH₄/Ar plasma." Thin Solid Films **521**: 216-221.

- Kim, H.-w., B.-S. Ju, B.-Y. Nam, W.-J. Yoo, C.-J. Kang, T.-H. Ahn, J.-T. Moon and M.-Y. Lee (1999). "High temperature platinum etching using Ti mask layer." J. Vac. Sci. Technol. A **17**(4): 2151.
- Kim, J. H., I. W. Seong, B. Y. Nam and W. J. Yoo (1999). "Anisotropic Etching Characteristics of Platinum Electrode for Ferroelectric Capacitor." IEEE T. Electron Dev. **46**(5): 984-992.
- Kim, J. H. and S. I. Woo (1998). "Chemical Dry Etching of Platinum Using Cl₂/CO Gas." Chem. Mater. **10**: 3576-3582.
- Kim, S. H., S.-Y. Ju, J. H. Hwang and J. Ahn (2003). "Chemical Reaction During Pt Etching with SF₆/Ar and Cl₂/Ar Plasma Chemistries." Jpn. J. Appl. Phys. **42**(Part 1, No. 4A): 1581-1585.
- Kim, S. H., S. W. Lee, J. Hwang and J. Ahn (2003). "Characteristics of Platinum Films Etched with a SF₆/Ar plasma." J. Korean Phys. Soc. **42**(2): 196-199.
- Kim, T., J. K. C. Chen and J. P. Chang (2014). "Thermodynamic assessment and experimental verification of reactive ion etching of magnetic metal elements." J. Vac. Sci. Technol. A **32**(4): 041305.
- Kim, T., Y. Kim, J. K. C. Chen and J. P. Chang (2015). "Viable chemical approach for patterning nanoscale magnetoresistive random access memory." J. Vac. Sci. Technol. A **33**(2): 021308.
- Kim, W.-H., D. Sung, S. Oh, J. Woo, S. Lim, H. Lee and S. F. Bent (2018). "Thermal adsorption-enhanced atomic layer etching of Si₃N₄." J. Vac. Sci. Technol. A **36**(1): 01B104.
- Kinoshita, K., H. Utsumi, K. Suemitsu, H. Hada and T. Sugibayashi (2010). "Etching Magnetic Tunnel Junction with Metal Etchers." Jpn. J. Appl. Phys. **49**(8): 08JB02.
- Kulkarni, N. S. and R. T. DeHoff (2002). "Application of Volatility Diagrams for Low Temperature, Dry Etching, and Planarization of Copper." J. Electrochem. Soc. **149**(11): G620.
- Kumar, R., S. Roy, M. Rashidi and R. J. Puddephatt (1989). "New Precursors for Chemical Vapour Deposition of Platinum and the Hydrogen Effect on CVD." Polyhedron **8**(4): 551-553.
- Kuo, Y. and S. Lee (2001). "Room-temperature copper etching based on a plasma-copper reaction." Appl. Phys. Lett. **78**(7): 1002.
- Kuo, Y. and S. Lee (2004). "A new, room-temperature, high-rate plasma-based copper etch process." Vacuum **74**(3-4): 473-477.
- Kwon, K.-H. (1998). "Etching properties of Pt thin films by inductively coupled plasma." Journal of Vacuum Science & Technology A: Vacuum, Surfaces, and Films **16**(5): 2772.
- Kwon, K.-H. (1998). "Etching properties of Pt thin films by inductively coupled plasma." J. Vac. Sci. Technol. A **16**(5): 2772.

Laegreid, N. and G. K. Wehner (1961). "Sputtering Yields of Metals for Ar⁺ and Ne⁺ Ions with Energies from 50 to 600 eV." J. Appl. Phys. **32**(3): 365.

Lee, I. H., T. Y. Lee and C. W. Chung (2013). "Etch characteristics of CoFeB magnetic thin films using high density plasma of a H₂O/CH₄/Ar gas mixture." Vacuum **97**: 49-54.

Lee, J. W., Y. D. Park, J. A. Childress, S. J. Pearton, F. Sharifi and F. Ren (1998). "Copper Dry Etching with Cl₂/Ar Plasma Chemistry." J. Electrochem. Soc. **145**(7): 2585-2588.

Lee, Y., J. W. DuMont and S. M. George (2015). "Atomic Layer Etching of HfO₂ Using Sequential, Self-Limiting Thermal Reactions with Sn(acac)₂ and HF." ECS J. Solid State Sc. **4**(6): N5013-N5022.

Lee, Y., J. W. DuMont and S. M. George (2016). "Trimethylaluminum as the Metal Precursor for the Atomic Layer Etching of Al₂O₃ Using Sequential, Self-Limiting Thermal Reactions." Chemistry of Materials **28**(9): 2994-3003.

Lee, Y. and S. M. George (2015). "Atomic Layer Etching of Al₂O₃ Using Sequential, Self-limiting thermal reactions with Sn(acac)₂ and Hydrogen fluoride." ACS Nano **9**(2): 2061-2070.

Lee, Y. and S. M. George (2017). "Thermal Atomic Layer Etching of Titanium Nitride Using Sequential, Self-Limiting Reactions: Oxidation to TiO₂ and Fluorination to Volatile TiF₄." Chem. Mater.

Lemaire, P. C. and G. N. Parsons (2017). "Thermal Selective Vapor Etching of TiO₂: Chemical Vapor Etching via WF₆ and Self-Limiting Atomic Layer Etching Using WF₆ and BCl₃." Chem. Mater. **29**(16): 6653-6665.

Li, L., X. Chen, C.-H. Wang, J. Cao, S. Lee, A. Tang, C. Ahn, S. Roy, M. S. Arnold and H. S. P. Wong (2015). "Vertical and Lateral Copper Transport through Graphene layers." ACS Nano **9**(8): 8361-8367.

Li, X., H. Zhou, R. J. W. Hill, M. Holland and I. G. Thayne (2012). "A Low Damage Etching Process of Sub-100 nm Platinum Gate Line for III–V Metal–Oxide–Semiconductor Field-Effect Transistor Fabrication and the Optical Emission Spectrometry of the Inductively Coupled Plasma of SF₆/C₄F₈." Jpn. J. Appl. Phys. **51**(1): 01AB01.

Liang, J., S. Yeh, S. S. Wong and H. S. P. Wong (2012). "Scaling Challenges for the Cross-point Resistive Memory Array to sub-10nm node--an interconnect perspective." 2012 4th IEEE International Memory Workshop: 1-4.

Lim, W. S., Y. Y. Kim, H. Kim, S. Jang, N. Kwon, B. J. Park, J.-H. Ahn, I. Chung, B. H. Hong and G. Y. Yeom (2012). "Atomic layer etching of graphene for full graphene device fabrication." Carbon **50**(2): 429-435.

Lin, T., B. Kang, M. Jeon, C. Huffman, J. Jeon, S. Lee, W. Han, J. Lee, S. Lee, G. Yeom and K. Kim (2015). "Controlled Layer-by-Layer Etching of MoS₂." ACS Appl. Mater. Inter. **7**(29): 15892.

Lin, W., R. W. Zhang, S. S. Jang, C. P. Wong and J. I. Hong (2010). "'Organic aqua regia'--powerful liquids for dissolving noble metals." Angew. Chem. Int. Ed. Engl. **49**(43): 7929-7932.

Lou, V. L. K., T. E. Mitchel and A. H. Heuer (1985). "Graphical Displays of the Thermodynamics of High-Temperature Gas-Solid Reactions and Their Applications to Oxidation of Metals and Evaporation of Oxides." J. Am. Ceram. Soc. **68**(2): 49-58.

Magnuson, G. D. and C. E. Carlston (1963). "Sputtering Yields of Single Crystals Bombarded by 1- to 10-keV Ar⁺ Ions." J. Appl. Phys. **34**(11): 3267.

Marchack, N. and J. P. Chang (2011). "Perspectives in nanoscale plasma etching: what are the ultimate limits?" J. Phys. D. Appl. Phys. **44**(17): 174011.

Marchack, N., J. M. Papalia, S. Engelmann and E. A. Joseph (2017). "Cyclic Cl₂/H₂ quasi-atomic layer etching approach for TiN and TaN patterning using organic masks." J. Vac. Sci. Technol. A **35**(5): 05C314.

Markert, M., A. Bertz and T. Gessner (1997). "Copper dry etching technique for ULSI interconnections." Microelectron. Eng. **35**: 333-336.

Matsumoto, S., H. Nikou and S. Nakagawa (1996). Method of Dry Etching Platinum Using Sulfur Containing Gas. United States of America, Matsushita Electronics Corporation. **5,492,855**: 1-13.

Matsuura, T., J. Murota, Y. Sawada and T. Ohmi (1993). "Self-limited layer-by-layer etching of Si by alternated chlorine adsorption and Ar⁺ ion irradiation." Appl. Phys. Lett. **63**(20): 2803.

McKervey, M. A., D. E. Johnston and J. J. Rooney (1971). "Preparation of diamondoid hydrocarbons by rearrangement employing a chlorinated platinum-alumina catalyst." J. Am. Chem. Soc. **93**(11): 2798-2799.

McMorran, B. J., A. C. Cochran, R. K. Dumas, K. Liu, P. Morrow, D. T. Pierce and J. Unguris (2010). "Measuring the effects of low energy ion milling on the magnetization of Co/Pd multilayers using scanning electron microscopy with polarization analysis." J. Appl. Phys. **107**(9): 09D305.

Meguro, T., M. Hamagaki, S. Modaresi, T. Hara, Y. Aoyagi, M. Ishii and Y. Yamamoto (1990). "Digital etching of GaAs: New approach of dry etching to atomic ordered processing." Applied Physics Letters **56**(16): 1552.

Metzler, D., R. L. Bruce, S. Engelmann, E. A. Joseph and G. S. Oehrlein (2014). "Fluorocarbon assisted atomic layer etching of SiO₂ using cyclic Ar/C₄F₈ plasma." J. Vac. Sci. Technol. A **32**(2): 020603.

Metzler, D., C. Li, S. Engelmann, R. L. Bruce, E. A. Joseph and G. S. Oehrlein (2016). "Fluorocarbon assisted atomic layer etching of SiO₂ and Si using cyclic Ar/C₄F₈ and Ar/CHF₃ plasma." J. Vac. Sci. Technol. A **34**(1): 01B101.

Metzler, D., C. Li, S. Engelmann, R. L. Bruce, E. A. Joseph and G. S. Oehrlein (2017). "Characterizing fluorocarbon assisted atomic layer etching of Si using cyclic Ar/C₄F₈ and Ar/CHF₃ plasma." J. Chem. Phys. **146**(5): 052801.

Miyazaki, H. (1997). "Copper dry etching with precise wafer-temperature control using Cl₂ gas as a single reactant." J. Vac. Sci. Technol. B **15**(2): 237.

Murdock, E. S., R. F. Simmons and R. Davidson (1992). "Roadmap for 10 Gbit/in² Media: Challenges." IEEE T. Magn. **28**(5): 3078-3082.

Nemes, P., I. Marginean and A. Vertes (2007). "Spraying Mode Effect on Droplet Formation and Ion Chemistry in Electrosprays." Anal. Chem. **79**: 3105-3116.

Nguyen, H. V., I. An and R. W. Collins (1993). "Evolution of the optical functions of thin-film aluminum: A real-time spectroscopic ellipsometry study." Phys. Rev. B **47**(7): 3947-3965.

Nigg, H. L. (1998). "Surface-mediated reaction pathways of 2,4-pentanedione on clean and oxygen covered Cu (210)." J. Vac. Sci. Technol. A **16**(5): 3064.

Nigg, H. L. (1998). "Surface reaction mechanisms of trifluoroacetylacetone on clean and pre-oxidized Ni(110): An example where etching chemistry does not follow volatility trends." J. Vac. Sci. Technol. A **16**(6): 3259.

Nigg, H. L. and R. I. Masel (1998). "The surface chemistry of hexafluoroacetylacetone on clean and oxygen pre-covered Cu(210): a temperature-programmed desorption study." Surf. Sci. **409**: 428-434.

Nigg, H. L. and R. I. Masel (1999). "Surface reaction pathways of 1,1,1,5,5,5-hexafluoro-2,4-pentanedione on clean and pre-oxidized Ni(110) surfaces." J. Vac. Sci. Technol. A **17**(6): 3477.

Nishikawa, K., Y. Kusumi, T. Oomori, M. Hanazaki and K. Namba (1993). "Platinum etching and plasma characteristics in RF magnetron and electron cyclotron resonance plasmas." Japanese Journal of Applied Physics **32**: 6102-6108.

Ohtake, M., S. Ouchi, F. Kirino and M. Futamoto (2012). "L10 ordered phase formation in FePt, FePd, CoPt, and CoPd alloy thin films epitaxially grown on MgO(001) single-crystal substrates." J. Appl. Phys. **111**(7): 07A708.

Ono, K. and M. Tuda (1997). "Profile evolution during cold plasma beam etching of silicon." Jpn. J. Appl. Phys. **36**: 4854-4865.

Panias, D., M. Taxiarchou, I. Paspaliaris and A. Kontopoulos (1996). "Mechanisms of dissolution of iron oxides in aqueous oxalic acid solutions." Hydrometallurgy **42**: 257-265.

Park, J.-Y., S.-K. Kang, M.-H. Jeon, M. S. Jhon and G.-Y. Yeom (2011). "Etching of CoFeB Using CO/NH₃ in an Inductively Coupled Plasma Etching System." J. Electrochem. Soc. **158**(1): H1.

- Parkin, S. S., C. Kaiser, A. Panchula, P. M. Rice, B. Hughes, M. Samant and S. H. Yang (2004). "Giant tunnelling magnetoresistance at room temperature with MgO (100) tunnel barriers." Nat. Mater. **3**(12): 862-867.
- Petrov, G. M., D. R. Boris, T. B. Petrova, E. H. Lock, R. F. Fernsler and S. G. Walton (2013). "Controlling the electron energy distribution function of electron beam generated plasmas with molecular gas concentration: II. Numerical modeling." Plasma Sources Sci T. **22**(6): 065005.
- Posseme, N., O. Pollet and S. Barnola (2014). "Alternative process for thin layer etching: Application to nitride spacer etching stopping on silicon germanium." Applied Physics Letters **105**(5): 051605.
- Read, J. C., P. M. Braganca, N. Robertson and J. R. Childress (2014). "Magnetic degradation of thin film multilayers during ion milling." APL Mater. **2**(4): 046109.
- Rousseau, F., A. Jain, L. Perry, J. Farkas, T. T. Kostas, M. J. Hampden-Smith, M. Paffett and R. Muenchausen (1992). "New Approaches for Dry Etching Metal Oxides at low Temperature and High Rates." Mat. Res. Soc. Symp. Proc **268**: 57-62.
- Schwartz, G. C. and P. M. Schaible (1983). "Reactive Ion Etching of Copper Films." J. Electrochem. Soc.: Accelerated Brief Communication **130**(8): 1777-1779.
- Shibano, T. (1998). "Platinum etching in Ar/O₂ mixed gas plasma with a thin SiO₂ etching mask." Journal of Vacuum Science & Technology A: Vacuum, Surfaces, and Films **16**(2): 502.
- Shibano, T., K. Nakamura, T. Takenaga and K. Ono (1999). "Platinum etching in Ar/Cl₂ plasmas with a photoresist mask." J. Vac. Sci. Technol. A **17**(3): 799.
- Shibano, T., K. Nakamura, T. Takenaga and K. Ono (1999). "Platinum etching in Ar/Cl₂ plasmas with a photoresist mask." Journal of Vacuum Science & Technology A: Vacuum, Surfaces, and Films **17**(3): 799.
- Song, Y.-J., G. Jeong, I.-G. Baek and J. Choi (2013). "What Lies Ahead for Resistance Based Memory Technologies." Computer **46**(8): 30-36.
- Steger, R. and R. I. Masel (1999). "Chemical vapor etching of copper using oxygen and 1,1,1,5,5,5-hexafluoro-2,4-pentanedione." Thin Solid Films **342**: 221-229.
- Steigerwald, J. M. (1995). "Chemical processes in the chemical mechanical polishing of copper." Mater. Chem. Phys. **41**: 217-228.
- Suda, T., N. Toyoda, K. Hara and I. Yamada (2012). "Development of Cu Etching Using O₂ Cluster Ion Beam under Acetic Acid Gas Atmosphere." Jpn. J. Appl. Phys. **51**: 08HA02.
- Sugiura, K., S. Takahashi, M. Amano, T. Kajiyama, M. Iwayama, Y. Asao, N. Shimomura, T. Kishi, S. Ikegawa, H. Yoda and A. Nitayama (2009). "Ion Beam Etching Technology for High-

Density Spin Transfer Torque Magnetic Random Access Memory." Jpn. J. Appl. Phys. **48**(8): 08HD02.

Sugiyama, T., T. Matsuura and J. Murota (1997). "Atomic layer etching of Ge using an ultraclean ECR plasma." Appl. Surf. Sci. **112**: 187-190.

Sun, S., C. B. Murray, D. Weller, L. Folks and A. Moser (2000). "Monodisperse FePt Nanoparticles and Ferromagnetic FePt Nanocrystal Superlattices." Science **287**(5460): 1989-1992.

Tamirisa, P. A., G. Levitin, N. S. Kulkarni and D. W. Hess (2007). "Plasma etching of copper films at low temperature." Microelectron. Eng. **84**(1): 105-108.

Tanuma, S., C. J. Powell and D. R. Penn (1994). "Calculations of electron inelastic mean free paths. V. Data for 14 organic compounds over the 50–2000 eV range." Surf. Interface Anal. **21**: 165-176.

Tanuma, S., C. J. Powell and D. R. Penn (2011). "Calculations of electron inelastic mean free paths. IX. Data for 41 elemental solids over the 50 eV to 30 keV range." Surf. Interface Anal. **43**(3): 689-713.

Thurier, C. and P. Doppelt (2008). "Platinum OMCVD processes and precursor chemistry." Coordin. Chem. Rev. **252**(1-2): 155-169.

van Glabbeek, J. J., G. A. C. M. Spierings, M. J. E. Ulenaers, G. J. M. Dormans and P. K. Larsen (1993). "Reactive ion etching of Pt/PZT/Pt integrated ferroelectric capacitors." Mater. Res. Soc. Symp. P. **310**.

Walton, S. G., D. R. Boris, S. C. Hernandez, E. H. Lock, T. B. Petrova, G. M. Petrov and R. F. Fernsler (2015). "Electron Beam Generated Plasma for Ultra Low Te Processing." ECS J. Solid State Sc. **4**(6): N5033-N5040.

Walton, S. G., C. Muratore, D. Leonhardt, R. F. Fernsler, D. D. Blackwell and R. A. Meger (2004). "Electron-beam-generated plasmas for materials processing." Surf. Coat. Tech. **186**(1-2): 40-46.

Wang, J., Y. Yun and E. I. Altman (2007). "The plasma oxidation of Pd(100)." Surf. Sci. **601**(16): 3497-3505.

Williams, K. R., K. Gupta and M. Wasilik (2003). "Etch Rates for Micromachining Processing—Part II." J. Microelectromech S. **12**(6): 761-778.

Winters, H. F. (1978). "The role of chemisorption in plasma etching." J. Appl. Phys. **49**(10): 5165.

Winters, H. F. (1985). "Etch products from the reaction on Cl₂ with Al(100) and Cu(100) and XeF₂ with W(111) and Nb." J. Vac. Sci. Technol. B **3**(1): 9-15.

Winters, H. F. (1985). "The etching of Cu(100) with Cl₂." J. Vac. Sci. Technol. A **3**(3): 786.

Wu, F., G. Levitin and D. W. Hess (2010). "Low-Temperature Etching of Cu by Hydrogen-Based Plasmas." ACS Appl. Mater. Inter. **2**(8): 2175-2179.

Wu, F., G. Levitin and D. W. Hess (2010). "Patterning of Cu Films by a Two-Step Plasma Etching Process at Low Temperature." J. Electrochem. Soc. **157**(4): H474.

Wu, F., G. Levitin and D. W. Hess (2010). "Subtractive Etching of Cu with Hydrogen-based Plasmas." ECS Transactions **33**(12): 157-162.

Wu, F., G. Levitin and D. W. Hess (2011). "Mechanistic considerations of low temperature hydrogen-based plasma etching of Cu." J. Vac. Sci. Technol. B **29**(1): 011013.

Wu, F., G. Levitin and D. W. Hess (2012). "Temperature Effects and Optical Emission Spectroscopy Studies of Hydrogen-Based Plasma Etching of Copper." J. Electrochem. Soc. **159**(2): H121.

Xiao, Y. B., E. H. Kim, S. M. Kong and C. W. Chung (2011). "Evolution of etch profile in etching of CoFeB thin films using high density plasma reactive ion etching." Thin Solid Films **519**(20): 6673-6677.

Xie, W., P. C. Lemaire and G. N. Parsons (2018). "Thermally Driven Self-Limiting Atomic Layer Etching of Metallic Tungsten Using WF₆ and O₂." ACS Appl. Mater. Inter.

Yang, C. C., C. C. Ko, H. O. Yang, K. F. Chen, Y. Y. Peng, J. W. Liou, C. C. Chou, H. Y. Tsai, K. C. Lin, S. M. Jeng, H. J. Tao and M. Cao (2012). "Wet Clean Induce Pattern Collapse Mechanism Study." Solid State Phenomen. **187**: 253-256.

Yao, Z., C. Wang, H.-K. Sung and N.-Y. Kim (2014). "Defined micropatterns of platinum thin films by inductively coupled plasma etching using SF₆/Ar/O₂ mixture gas." Mat. Sci. Semicon. Proc. **27**: 228-232.

Yokoyama, S., Y. Ito, K. Ishihara, K. Hamada, S. Ohnishi, J. Kudo and K. Sakiyama (1995). "High-Temperature Etching of PZT-Pt-TiN Structure by High-Density ECR Plasma." Jpn. J. Appl. Phys. **34**: 767-770.

Yoo, W. J., J. H. Hahm, H. W. Kim, C. O. Jung, Y. B. Koh and M. Y. Lee (1996). "Control of etch slope during etching of Pt in Ar/Cl₂/O₂ plasmas." Jpn. J. Appl. Phys. **35**: 2501-2504.

Young, F. W. (1962). "Etching of Irradiated Copper." Journal of Applied Physics **33**(2): 749.

Zantye, P. B., A. Kumar and A. K. Sikder (2004). "Chemical mechanical planarization for microelectronics applications." Mater. Sci. Eng.: R: Reports **45**(3-6): 89-220.

Zeper, W. B., F. J. A. M. Greidanus, P. F. Carcia and C. R. Fincher (1989). "Perpendicular magnetic anisotropy and magneto-optical Kerr effect of vapor-deposited Co/Pt-layered structures." Journal of Applied Physics **65**(12): 4971.

Zhu, H., X. Qin, L. Cheng, A. Azcatl, J. Kim and R. M. Wallace (2016). "Remote Plasma Oxidation and Atomic Layer Etching of MoS₂." ACS Appl. Mater. Inter. **8**(29): 19119-19126.

Zywotko, D. R. and S. M. George (2017). "Thermal Atomic Layer Etching of ZnO by a "Conversion-Etch" Mechanism Using Sequential Exposures of Hydrogen Fluoride and Trimethylaluminum." Chem. Mater. **29**(3): 1183-1191.